University of New Mexico
UNM Digital Repository

Electrical and Computer Engineering ETDs | Engineering ETDs

Spring 4-15-2019

Transport in Mid-Wavelength Infrared (MWIR) p- and n-type InAsSb and InAs/InAsSb Type-II Strained Layer Superlattices (T2SLs) for infrared detection

Lilian K. Casias
Center for High Technology Materials

Follow this and additional works at: https://digitalrepository.unm.edu/ece_etds

Part of the Electrical and Computer Engineering Commons

Recommended Citation
Casias, Lilian K.. "Transport in Mid-Wavelength Infrared (MWIR) p- and n-type InAsSb and InAs/InAsSb Type-II Strained Layer Superlattices (T2SLs) for infrared detection." (2019). https://digitalrepository.unm.edu/ece_etds/456

This Dissertation is brought to you for free and open access by the Engineering ETDs at UNM Digital Repository. It has been accepted for inclusion in Electrical and Computer Engineering ETDs by an authorized administrator of UNM Digital Repository. For more information, please contact amywinter@unm.edu.

Lilian K. Casias
Candidate

Electrical and Computer Engineering (ECE)
Department

This dissertation is approved, and it is acceptable in quality and form for publication:

Approved by the Dissertation Committee:

Dr. Ganesh Balakrishnan, Chairperson

Dr. Francesca Cavallo

Dr. Sanjay Krishna

Dr. Christian Morath

Dr. Elizabeth Steenbergen

Transport in Mid-Wavelength Infrared (MWIR) *p*- and *n*-type InAsSb and InAs/InAsSb Type-II Strained Layer Superlattices (T2SLs) for infrared detection

by

Lilian K. Casias

B.S., Elect. Engineering, University of New Mexico, 2008
M.S., Elect. Engineering, University of New Mexico, 2015

DISSERTATION

Submitted in Partial Fulfillment of the
Requirements for the Degree of

Doctor of Philosophy
Engineering

The University of New Mexico
Albuquerque, New Mexico

May, 2019

DEDICATION

This work is dedicated to my dear husband, Miguel and my son, Ernesto "Nesto", thank you for all the support, motivation, patience and love you have given me.

Also, my parents for opening the door to the opportunity of education. Gracias queridos padres.

ACKNOWLEDGMENTS

I was very blessed and lucky to have great family, friends and colleagues during graduate school that helped and supported me throughout. First, I would like to thank my academic advisors, Dr. Sanjay Krishna and Dr. Ganesh Balakrishnan. Thank you, Dr. Krishna, for believing in me and opening the door to achieving this degree. All along you thought I could do it and I have learned so much from you. Thank you, Dr. Balakrishnan, for "adopting me" and taking me under your wing at UNM.

My dissertation committee: Prof. Cavallo, Dr. Chris Morath, and Dr. Elizabeth Steenbergen. Chris, you have been an excellent resource and inspired me to higher achievement and made me a stronger researcher. I still have much more to learn from you. Elizabeth, since I met you back in 2014, you have been an inspiration and a role model, both professionally and personally. Your strength and organization are what I wish to achieve one day. Thank you for believing in me. It has been an honor to work closely with the AFRL team: Elizabeth, Chris, Preston, Vince, Diana, John, Ben, Victor, Mark, Dan, David, Ian, Jerry, and PC as you all have been such a great support structure and I thank you all for the opportunity. Dr. John Hubbs, your words of encouragement since I joined AFRL have been greatly appreciated. Dr. Preston Webster, thanks for your advice and your positive attitude.

Thank you to the funding and collaboration from several resources for this work: AFRL, ARO, NRL, SNL, and UWA. Special thanks to Dr. Ed Aifer, Dr. Jerry Meyer, Dr. Chaffra Afouda, and Dr. Jill Noldes for welcoming me and training me at NRL for a few weeks and entrusting me with the software tool needed for my dissertation. The contribution from NRL MULTIBANDS® for my work has been of extreme importance. The growths of the samples were performed at Sandia National Laboratories and I am extremely thankful for the collaboration. Thank you to the CINT/SNL cleanroom staff as the tools and advice was invaluable (Denise Webb, John Nogan, Mike Lilly, and Don Bethke). Thank you, Dr. Gilberto Umana-Membreno at UWA for the collaboration and advice provided through my experiments, it has been such an honor and your contribution in vertical transport is greatly appreciated. Dr. Greg Savich, you were not scared to provide me with processing advice as I am extremely thankful for your advice. Dr. Alex Brown, your dissertation inspired mine and your willingness to answer my questions is appreciated.

It has been an honor for me to work with other students and staff at CHTM. Students who have been part of Office # 117 in the past and present: Stephen, Brianna, Happito, Emma, Mitch, Vinita, Marzieh, John, Ted, Zahra, Ali, Teressa, and Clark. Happito, thank you for years of unconditional friendship. I greatly appreciate Stephen Myers and Brianna Klein for being such good friends and mentors. I spent a lot of time with them learning processing and getting trained when I started this degree. Myers, I know I still bug you very much when I am confused. Thank you for being you!

My parents and my sister have always been supportive and cheered me on whenever I needed them. Thank you to my parents for risking it all and coming to a new country in search of a better future for us. They taught me the value of working hard. I love you, my wonderful parents! Sister "Yadi", I love you. You are my first best friend; I thank God for you and your family (Coraline: sky is the limit!). Thank you to my in-laws for their help as it's been a pleasure to also be a Casias and to have your unconditional support. To Benicio, Damion, Raiden, Joaquin, Aliyana, and Sofia, never give up!

My special thanks go to my husband, Miguel Casias. He has been my rock for the past six years of marriage and is my best friend. Even though we went through ups and downs during the last years, he never gave up and inspires me every day. I could not have done it without his support. I admire you so much Miguel, we are a team, you sacrificed as much as I did. Nesto, my son, you and your dad have been nothing but the whole reason why I have kept proceeding through this path. Your gorgeous smile and innocence inspire me to keep looking forward. Son, thank you, for sitting by me as I write this dissertation, patiently waiting and keeping me company, providing a hug when needed. Hope this effort echoes in your life -no matter what you may face, stand up tall and believe in yourself.

Finally, thank you God, for providing me with the strength and patience I needed.
The LORD is my strength and shield. I trust him with all my heart. He helps me, and my heart is filled with joy. I burst out in songs of thanksgiving. Ps 28:7

Transport in Mid-Wavelength Infrared (MWIR) *p*- and *n*-type InAsSb and InAs/InAsSb Type-II Strained Layer Superlattices (T2SLs) for infrared detection

by

Lilian K. Casias

B.S., Electrical Engineering, The University of New Mexico, 2008

M.S., Electrical Engineering, The University of New Mexico, 2015

Ph.D., Engineering, The University of New Mexico, 2019

ABSTRACT

III-V materials such as InAsSb alloys and InAs/InAsSb Type-II Strained Layer Superlattices (T2SLs) have significant potential for infrared (IR) detector applications, including space-based detection, when utilized in a unipolar barrier detector architecture (nBn). However, recent studies revealed the quantum efficiency in nBn detectors degrades significantly faster from proton-irradiation induced displacement damage as compared to HgCdTe photodiodes. Improving the quantum efficiency radiation-tolerance is theoretically possible by enhancing vertical hole mobility and thereby the vertical hole diffusion length. The vertical hole mobility of T2SLs materials differs significantly from the lateral mobility and measuring it is much less straightforward.

In order to tackle vertical transport, lateral transport must be better understood. There are added challenges to determining the lateral bulk carrier concentration in narrow bandgap materials due to the potential for electron accumulation at the surface of the

material and at its interface with the layer grown directly below it. Electron accumulation layers form high conductance electron channels that can dominate both resistivity and Hall-Effect transport measurements. Therefore, to correctly determine the lateral bulk concentration and mobility, temperature- and magnetic-field-dependent transport measurements in conjunction with Multi-Carrier Fit (MCF) analysis were utilized on a series of *p*-doped $InAs_{0.91}Sb_{0.09}$ samples on GaSb substrates. The samples are etched to different thicknesses, and variable-field measurements are utilized to assist in confirming whether a carrier species represents bulk, interface or surface conduction.

Secondly, *n*-type temperature- and magnetic-field dependent measurements on InAsSb and InAs/InAsSb T2SLs materials were performed to extract the lateral transport properties for all the carriers present in each sample under two different doping concentrations (Non-Intentionally Doped or *NID* and Silicon-doped). For lateral transport measurements, NRL MULTIBANDS® simulations were utilized to extract and compare the interface carriers for each sample. Lastly, substrate-removed, Metal-Semiconductor-Metal (MSM) devices were fabricated to extract vertical transport mobilities, while conventional Van der Pauw structures were used for lateral measurements. To accurately determine the lateral and vertical transport properties in the presence of multiple carrier species, Multi-Carrier Fit (MCF) and High-Resolution Mobility Spectrum Analysis (HR-MSA) were employed.

TABLE OF CONTENTS

DEDICATION iii

ACKNOWLEDGMENTS iv

ABSTRACT vi

LIST OF FIGURES xii

LIST OF TABLES xvii

CHAPTER 1 Introduction 1

1.1 Background 1

1.2 Infrared Spectrum and Applications 1

1.3 II-VI and III-V for Infrared Detectors 4

1.4 Type-II Strained Layer Superlattices (T2SLs) 6

1.5 Fundamental Limitations of III-V materials 9

1.6 Dissertation Overview 12

1.6.1 Significance of the Problem 12

1.6.2 Contributions of the Dissertation 13

1.6.3 Outline of the Dissertation 14

1.7 References 17

CHAPTER 2 Background 19

2.1 Introduction 19

2.2 Drift-Diffusion 19

2.3 Conductivity and Effective Mass 23

2.4 Hall Effect 27

2.5 Multi-Carrier Transport 30

2.5.1 Magneto-Transport 31

2.6 Transport Limitations in Superlattices (T2SLs) 34

2.7 Lateral Transport Measurements 36

2.8 Vertical Transport Measurements 39

2.9 Summary 41
2.10 References 43
CHAPTER 3 Methods **45**
3.1 Introduction 45
3.2 Epitaxial Growth 45
3.3 Experimental Methods by Collaborators 47
3.3.1 X-Ray Diffraction 47
3.3.2 Optical Characterization 49
3.4 Device Fabrication Overview 50
3.5 Experimental 52
3.5.1 Magneto-Transport Measurement Equipment 52
3.5.2 Lateral Transport Measurement 55
3.5.3 Vertical Transport Measurement 58
3.6 Modeling 60
3.6.1 NRL MULTIBANDS® 60
3.6.2 Multi-Carrier Analysis 61
3.6.2.1 Conductivity Tensors 61
3.6.2.2 Multi-Carrier Fit 63
3.6.2.3 Mobility Spectrum Analysis 65
3.7 Summary 70
3.8 References 71
CHAPTER 4 *p*-type InAsSb Lateral Transport **73**
4.1 Introduction 73
4.2 Sample and Methods 74
4.2.1 Device Structures, Fabrication and Characterization 74
4.2.2 Optical Characterization 76
4.2.3 Multi-Carrier Analysis 76
4.3 Simulations 78
4.4 Results and Analysis 80
4.4.1 Sheet Resistivity Characterization 80
4.4.2 Variable Field Characterization 82

4.4.2.1 Surface and Interface Components at 300 K 85
4.4.2.2 Variable Temperature 87
4.5 Substrate Removal Attempt 90
4.6 Conclusions 93
4.7 References 95
CHAPTER 5 *n*-type InAsSb and InAs/InAsSb T2SL Lateral Transport 97
5.1 Introduction 97
5.2 Surface Conductivity 99
5.3 Samples and Methods 102
5.3.1 Device Structures 102
5.3.2 Material Characterization 103
5.3.3 Fabrication and Electrical Characterization 105
5.4 Simulations 108
5.4.1 Undoped and Doped InAsSb Alloy Samples 109
5.4.2 Undoped and Doped InAs/InAsSb T2SLs 110
5.4.3 Interface Carriers Summary 113
5.5 Results and Analysis 114
5.5.1 Sheet Resistivity Characterization 114
5.5.2 Variable Field-Temperature Results for InAsSb 116
5.5.3 Variable Field-Temperature Results for T2SLs 123
5.5.3.1 Diffusion Length of Minority Carriers in T2SLs 129
5.6 Conclusions 131
5.7 Summary 139
5.8 References 140
CHAPTER 6 *n*-type InAs/InAsSb T2SL Vertical Transport 142
6.1 Introduction 142
6.2 Substrate Removal Background 144
6.3 Vertical Transport Review 146
6.3.1 Limitations 146
6.3.2 Vertical Transport Configuration for Magneto-Resistance 147

6.4 Samples and Methods 150
6.4.1 Device Structures 150
6.4.2 Material Characterization..151
6.4.3 Metal-Semiconductor-Metal (MSM) Fabrication............................153
6.4.3.1 Mesa Definition and Top Metal 155
6.4.3.2 Photoresist Protection 156
6.4.3.3 Bonding to Carrier 156
6.4.3.4 Lapping and Wet-Etching for Substrate Removal 157
6.4.3.5 Top Contacts 159
6.4.3.6 Acetone Release...161
6.4.3.7 Bonding to a Host Substrate 162
6.4.4 Electrical Characterization...163
6.5 Results..167
6.5.1 Variable Temperature Magneto-Resistance..167
6.5.2 InAs/InAsSb T2SL HR-MSA Vertical Transport.................................170
6.6 Summary 177
6.7 References..178
CHAPTER 7 Conclusions and Future Work 180
7.1 Transport to Improve III-V Detector Performance.......................................180
7.2 Conclusions..182
7.3 Future Work 185
7.3.1 Radiation Effects...185
7.3.2 Passivation in *p*-type Material 185
7.3.3 SdH Study and MSM Test-Structure 186
7.4 References..187
APPENDIX A OPTICAL MEASUREMENTS 188
A.1 Lateral Transport Samples 189
A.2 Vertical Transport Samples..190

LIST OF FIGURES

FIGURE PAGE

1.1 Atmospheric transmission of infrared radiation 3
1.2 The infrared band in the electromagnetic spectrum showing the different IR sub-bands....3
1.3 Type-I and Type-II energy bands for materials *A* and *B* that form a superlattice, with conduction and valence bands CB_A/CB_B and VB_A/VB_B, respectively. 7
1.4 Type-II Superlattice (T2SL) band alignment of the $InAs/InAs_{0.65}Sb_{0.35}$ structure, with InAs electron well (eW) and $InAs_{0.65}Sb_{0.35}$hole well (hW)....8
1.5 Approach, objective and steps for the work presented in this dissertation....13
2.1 Schematic of a *p-n* junction....21
2.2 Rectangular bar of semiconductor material with length, *L*, width, *w* and thickness, *t*. Cross-sectional area is known as A = *wt*....24
2.3 A theoretical graph of majority carrier concentration (either *n* or *p*) vs. reciprocal temperature (*1/T*) for an ideal extrinsic semiconductor sample 25
2.4 Schematic illustration of the Hall Effect 28
2.5 Illustration of magneto-resistance in a semiconductor....31
2.6 Cross-sectional illustration of configurations used for (a) lateral transport measurements to extract magneto-resistance and Hall coefficients and (b) vertical transport measurements to extract the geometrical magneto-resistance....32
2.7 Illustration of tilting a sample to extract the magneto-resisitivity in a semiconductor as a function of magnetic field magnitude and angle orientation....34
2.8 Schematic of the InAs/InAsSb degraded interface due to antimony segregation....36
2.9 $InAs_{0.58}Sb_{0.42}$ alloy layer with $Al_{0.74}In_{0.26}Sb$ barrier layer on a GaSb substrate grown by MBE 39
2.10 The *p*-type InAs/GaSb T2SL structure used by UWA for vertical transport measurements....40
3.1 X-Ray Diffraction (XRD) through crystal lattices showing the distance (*d*) between atomic crystal planes within the material....48
3.2 Block diagram of microwave apparatus used for Time-Resolved Microwave Reflectance (TMR) and frequency-modulated conductance....49
3.3 Wafer maps and histograms of the optical characterization used for photoluminescence (PL) and lifetime (LT) for undoped InAsSb sample....50
3.4 LakeShore Cryotronics Hall Measurement System, (a) Model 9509 cryogenic dewar with sample insert mounted in the dewar, (b) electronics equipment rack....52
3.5 HMS LakeShore software Current-Voltage (I-V) measurement taken by adjusting the current source level (positive and negative polarities) and measuring the voltage output....54
3.6 (a) Van der Pauw (VDP) patterned *n*-type InAs/InAsSb 5 mm x 5 mm sample with four 300 µm ohmic contacts placed on the perimeter of the sample with alignment marks, (b) Microscope picture shows one corner of the sample patterned with a 15 µm contact offset....56
3.7 Sample holder stick (or sample insert) showing a sample mounted and wire-bonded to a chip carrier....57
3.8 Vertical transport sample with top contact and metal-coated sapphire which acts as the bottom contact, sample is mounted on a non-magnetic chip carrier 58

3.9 (a) The vertical transport sample holder contains four indium posts which aid when soldering to the contacts located on the chip carrier; (b)-(c) vertical transport sample holder mounted to the HMS pedestal 59
3.10 Geometry of a VDP sample in the *x-y* plane with a perpendicular magnetic field applied (*z*-direction) 62
3.11 Sheet conductivity in the carrier mobility domain as extracted from mobility spectrum analysis techniques (e.g., HR-MSA), in which each peak conductivity represents a distinct carrier species 68
4.1 Schematics of the fabricated samples in Van der Pauw (VDP) configuration: (a) 2-dimensional InAsSb sample cross section with distinct conductive paths indicated (b) 3-dimensional etched InAsSb sample structure....75
4.2 Photoluminescence (PL) map at 80 K provided by SNL that shows the peak wavelength of every measurement across the whole *p*-type InAsSb wafer 76
4.3 LakeShore QMSA mobility spectrum for the *p*-type 1.4 μm InAsSb sample at 300 K 77
4.4 Energy band diagram vs. sample depth modeled using NRL MULTIBANDS® at 300 K 79
4.5 Carrier concentration vs. sample depth showing the different layers in the sample structure modeled using NRL MULTIBANDS® at 300 K....79
4.6 Sheet resistivity vs. B^2 for the 2 μm *p*-type InAsSb sample at (a) 77 K and (b) 300 K. The non-linear behavior indicates multiple-carrier conduction....81
4.7 Sheet resistivity as a function of magnetic field intensity for different InAsSb layer thickness at (a) 77 K and (b) 300 K....82
4.8 The sheet conductivity of the four carrier populations present in the *p*-type InAsSb structure at 77 K as a function of etched thickness on a (a) linear scale and (b) semilog scale 83
4.9 The average conductivity of the four carrier populations present in the *p*-type InAsSb structure at 300 K as a function of etched thickness on a (a) linear scale and (b) semilog scale with error bars 83
4.10 Variable-temperature analysis of the four resolved carrier populations in the *p*-type 2 μm thick InAsSb sample vs. (a) mobility and (b) carrier concentration 88
4.11 Bandgap and activation energy analysis for the bulk carrier (*h1*) in the *p*-type 2 μm thick InAsSb sample. Intrinsic, extrinsic and freeze-out regions of *h1* are indicated 89
4.12 Sheet conductivity vs. temperature of the four carrier populations present in the *p*-type 2 μm thick InAsSb sample 90
4.13 *p*-type InAsSb VDP processed sample in the HF-based solution....92
4.14 Steps and pictures taken on an attempt to remove the GaSb substrate, AlAsSb etch-stop, and the GaSb buffer for the *p*-type InAsSb lateral transport samples 92
5.1 Schematics of the fabricated *n*-type samples in Van der Pauw (VDP) configuration, (a) 2-dimensional InAsSb sample cross section (b) 2-dimensional InAs/InAsSb T2SL sample cross section with two doping concentrations (*NID* and Si-doped at 1×10^{16} cm^{-3})....102
5.2 XRD characterization for the *n*-type samples (a) InAsSb undoped (blue) and Silicon-doped (red), (b) InAs/InAsSb T2SL undoped (blue) and Silicon-doped (red) 103
5.3 Nomarski images comparing surface morphology of (a) Non-Intentionally Doped (*NID*) InAsSb (b) Si-doped InAsSb (c) *NID* InAs/InAsSb T2SL (d) Si-doped InAs/InAsSb T2SL 104
5.4 Photoluminescence (PL) and Lifetime (LT) measurements for Non-Intentionally Doped (*NID*) InAsSb sample....105

5.5 (a) Microscope and (b) SEM images of the *n*-type Si-doped InAsSb sample 106
5.6 SEM image of over-the-side (lateral) contacts deposited using e-beam evaporation on the Si-doped (1×10^{16} cm^{-3}) InAsSb sample 106
5.7 Current-voltage (I-V) behavior for the four *n*-type samples at 300 K, (a) InAsSb and (b) InAs/InAsSb T2SL samples under the two different absorber doping concentrations (*NID* and Si-doped) 107
5.8 Non-Intentionally Doped (*NID)* InAsSb sample, (a) Energy band diagram vs. sample depth (b) Carrier concentration vs. sample depth showing the different layers in the sample structure, modeled using NRL MULTIBANDS® at 300 K 109
5.9 Silicon-doped InAsSb sample, (a) Energy band diagram vs. sample depth (b) Carrier concentration vs. sample depth showing the different layers in the sample structure, modeled using NRL MULTIBANDS® at 300 K 109
5.10 Energy band alignment for the InAs/$InAs_{0.65}Sb_{0.35}$ T2SL sample. Modeled using NRL MULTIBANDS® at 300 K 110
5.11 Energy band structure of MWIR InAs/$InAs_{0.65}Sb_{0.35}$ T2SL showing the vertical *z*-direction (left portion) and lateral *x-y* direction (right portion) using NRL MULTIBANDS® 111
5.12 *NID* InAs/$InAs_{0.65}Sb_{0.35}$ T2SL sample, (a) Energy band diagram vs. sample depth (b) Carrier concentration vs. sample depth showing the different layers in the sample structure, modeled using NRL MULTIBANDS® at 300 K 112
5.13 Silicon-doped InAs/$InAs_{0.65}Sb_{0.35}$ T2SL sample, (a) Energy band diagram vs. sample depth (b) Carrier concentration vs. sample depth showing the different layers in the sample structure, modeled using NRL MULTIBANDS® at 300 K 113
5.14 Sheet resistivity vs. B^2 results for the 2 µm *n*-type InAsSb samples at 77 K and 300 K for (a) *NID* and (b) Si-doped at 1×10^{16} cm^{-3} 115
5.15 Sheet resistivity vs. B^2 results for the 2 µm *n*-type InAs/$InAs_{0.65}Sb_{0.35}$ T2SL samples at 77 K and 300 K for (a) *NID* and (b) Si-doped at 1×10^{16} cm^{-3} 115
5.16 Sheet concentrations of the four resolved carrier populations in the *n*-type $InAs_{0.91}Sb_{0.09}$ alloy samples as a function of temperature for (a) *NID* and (b) Si-doped at 1×10^{16} cm^{-3} 117
5.17 Mobilities of the four resolved carrier populations in the *n*-type $InAs_{0.91}Sb_{0.09}$ alloy samples as a function of temperature for (a) *NID* and (b) Si-doped at 1×10^{16} cm^{-3} 118
5.18 Sheet conductivities of the four resolved carrier populations in the *n*-type $InAs_{0.91}Sb_{0.09}$ alloy samples as a function of temperature for (a) *NID* and (b) Si-doped at 1×10^{16} cm^{-3} 118
5.19 Bandgap and activation energy analysis of the intrinsic region for the bulk electron carrier (*e1*) in the InAsSb alloy samples for (a) *NID* and (b) Si-doped 121
5.20 Sheet concentrations of the five resolved carrier populations in the *n*-type InAs/$InAs_{0.65}Sb_{0.35}$ T2SL samples as a function of temperature for (a) *NID* and (b) Si-doped at 1×10^{16} cm^{-3} 124
5.21 Mobilities of the five resolved carrier populations in the *n*-type InAs/$InAs_{0.65}Sb_{0.35}$ T2SL samples as a function of temperature for (a) *NID* and (b) Si-doped at 1×10^{16} cm^{-3} 124
5.22 Sheet conductivities of the five resolved carrier populations in the *n*-type InAs/$InAs_{0.65}Sb_{0.35}$ T2SL samples as a function of temperature for (a) *NID* and (b) Si-doped at 1×10^{16} cm^{-3} 125
5.23 Bandgap and activation energy analysis for the bulk carriers *e1* and *h1* found in InAs/$InAs_{0.65}Sb_{0.35}$ T2SL samples for (a) *NID* and (b) Si-doped at 1×10^{16} cm^{-3} 127

5.24 Lateral bulk (intrinsic) electron mobilities vs. temperature results for (a) *NID* and Si-doped InAsSb alloys and InAs/InAsSb T2SL samples. Figures (b) and (c) show the *NID* and Si-doped bulk electron mobility results vs. temperature, respectively, displaying the single-field mobility values at 77 and 300 K at a magnetic field (B) of 0.5 Tesla for each sample 132
5.25 Lateral bulk (intrinsic) electron concentrations vs. temperature results for (a) *NID* and Si-doped InAsSb alloys and InAs/InAsSb T2SL samples. Figures (b) and (c) show the *NID* and Si-doped bulk electron concentration results vs. temperature, respectively, displaying the single-field concentration values at 77 and 300 K at a magnetic field (B) of 0.5 Tesla for each sample 133
5.26 Lateral (a) mobilities and (b) concentration vs. temperature results for minority hole found in *NID* and Si-doped InAs/InAsSb T2SL samples 134
6.1 Typical device cross-section used for vertical transport measurements in T2SLs where an active region is sandwiched between two heavily doped contact layers, (a) device cross-section and (b) top view of typical device 148
6.2 Top view of a Corbino disk device geometry. A Corbino disk is a special case device geometry that shorts the Hall voltage, typical T2SL device structure is like the Corbino disk 148
6.3 Circuit diagram, R_{sh} represents the bottom contact layer sheet resistance and ρ_c represents the specific contact resistivity, which is the resistivity of the interface formed by the bottom contact layer and active region 149
6.4 Cross-section of the MBE grown $(n^+n^-n^+)$ InAs/$InAs_{0.65}Sb_{0.35}$ T2SL samples 150
6.5 XRD characterization for the two $(n^+n^-n^+)$ InAs/$InAs_{0.65}Sb_{0.35}$ T2SL samples 151
6.6 Nomarski images comparing surface morphology of the two InAs/$InAs_{0.65}Sb_{0.35}$ T2SL samples 152
6.7 Metal-Semiconductor-Metal (MSM) structure for vertical transport measurements (a) cross-section schematic and (b) top view 153
6.8 Schematic of the fabrication steps used for the Metal-Semiconductor-Metal (MSM) structure used for vertical transport measurements 154
6.9 Photolithography defined a 4.7 mm × 4.7 mm square for thick top metal application on the surface 155
6.10 Bonded sample to a sapphire carrier for lapping/polishing of the GaSb substrate, (a) shows the sample back (substrate side up) with Crystalbond™ 509 adhesive and (b) sample front showing through the sapphire carrier 157
6.11 Sample lapping and polishing, (a) shows the sample mounted on the lapping puck, (b) and (c) show the sample lapped and slightly polished and unmounted from lapping puck 158
6.12 Substrate removal by HF wet-etching 159
6.13 Sample “wrinkles” during an attempt to perform photolithography after substrate removal to fabricate top contacts 160
6.14 The use of a 6 mm × 6 mm square shadow mask with a 2 mm × 2 mm hole in the middle 160
6.15 Release in acetone bath and transfer to a sapphire carrier coated with metal 161
6.16 Au-Au bonding process of the released sample to sapphire substrate coated with Ti/Pt/Au 162
6.17 Experimental setup used with applied electric field (*E field*) and magnetic field (*B field*), (a) demonstrates the 3-dimensional and (b) the 2-dimensional four-wire setup used on the MSM structures. The top contacts are labeled as 1 and 2, while bottom contacts are 3 and 4 165

6.18 Testing configurations used with (a) applied current I (E *field*) and magnetic field (B *field*); where w, t and L are the width, thickness, and length of the sample under test and (b) a picture of the sample mounted for testing 165
6.19 Resistance versus square of magnetic field (B^2) for the *NID* InAs/InAsSb T2SL sample at temperatures (a) 20, (b) 50, (c) 130, (d) 250, (e) 300, and (f) 350 K under four resistance configurations..168
6.20 Resistance versus square of magnetic field (B^2) for the Si-doped InAs/InAsSb T2SL sample at temperatures (a) 20, (b) 50, (c) 77, (d) 130, (e) 250, and (f) 300 K under the four resistance configurations...169
6.21 Sheet conductance for *NID* InAs/InAsSb T2SL versus magnetic field (B) for the average magneto-resistance dataset, together with the fit obtained from HR-MSA, at (a) 20, (b) 77 and (c) 300 K 170
6.22 Mobility spectra for the *NID* InAs/InAsSb T2SL sample at selected temperatures from 20 to 350 K extracted using HR-MSA. High mobility/conductance carrier is assigned to an electron and low mobility/conductance to a hole.................................171
6.23 HR-MSA extracted coupled vertical mobility for (a) majority electron and (b) minority hole as a function of temperature for the *NID* InAs/InAsSb T2SL sample 172
6.24 Majority carrier electron comparison for lateral ($\mu_{||measured}$), coupled vertical ($\mu_{\perp coupled}$), and decoupled vertical ($\mu_{decoupled}$) results of mobility versus temperature for the *NID* InAs/InAsSb T2SL sample 173
6.25 (a) Minority carrier hole comparison for lateral ($\mu_{||measured}$), coupled vertical ($\mu_{\perp coupled}$), and decoupled vertical ($\mu_{decoupled}$) results of mobility versus temperature (T) for the *NID* InAs/InAsSb T2SL sample; (b) mobility versus temperature ($1/k_BT$) results for the vertical hole carrier (coupled and decoupled), where k_B is the Boltzmann constant (8.62×10^{-5} eV/K)..174

LIST OF TABLES

TABLE PAGE

1.1 Summary of the advantages and disadvantages of both II-VI (MCT) and III-V (InAsSb alloy and InAs/InAsSb T2SL) detector technologies 10

2.1 Summary of vertical mobility ($\mu_{\perp}$) measurements of InAsSb alloy, InAs/GaSb and InAs/InAsSb T2SLs grown on GaSb substrates by MBE, summarized in chronological order..42

3.1 Summary of the history of Mobility Spectrum Analysis (MSA) in chronological order and contribution 70

4.1 Pre- and post- surface treatment mobility and carrier concentration results for the 2.0 μm *p*-type InAsSb at 300 K..86

5.1 Summary of surface properties reported for InAs, $InAs_{1-x}Sb_x$ and InAs/ $InAs_{1-x}Sb_x$ T2SLs using different measurement techniques..101

5.2 Four *n*-type InAsSb alloy and InAs/InAsSb T2SL samples grown by MBE for lateral transport measurements...105

5.3 Summary of interface carrier concentrations for the *n*-type InAsSb and InAs/InAsSb T2SL samples modeled using NRL MULTIBANDS® at 300 K 113

5.4 Minority hole lateral diffusion lengths for the $InAs/InAs_{0.65}Sb_{0.35}$ T2SL samples 131

5.5 Summary of mobility and carrier concentration results found for the different carriers in the undoped (*NID*) $InAs_{0.91}Sb_{0.09}$ at 77 K 136

5.6 Summary of mobility and carrier concentration results found for the different carriers in the undoped (*NID*) $InAs_{0.91}Sb_{0.09}$ at 300 K 136

5.7 Summary of mobility and carrier concentration results found for the different carriers in the *n*-type Si-doped (1.0×10^{16} cm^{-3}) $InAs_{0.91}Sb_{0.09}$ at 77 K 136

5.8 Summary of mobility and carrier concentration results found for the different carriers in the *n*-type Si-doped (1.0×10^{16} cm^{-3}) $InAs_{0.91}Sb_{0.09}$ at 300 K 136

5.9 Summary of mobility and carrier concentration results found for the different carriers in the undoped (*NID*) $InAs/InAs_{0.65}Sb_{0.35}$ T2SL at 77 K.................................137

5.10 Summary of mobility and carrier concentration results found for the different carriers in the undoped (*NID*) $InAs/InAs_{0.65}Sb_{0.35}$ T2SL at 300 K...............................137

5.11 Summary of mobility and carrier concentration results found for the different carriers in the Si-doped (1.0×10^{16} cm^{-3}) $InAs/InAs_{0.65}Sb_{0.35}$ T2SL at 77 K 137

5.12 Summary of mobility and carrier concentration results found for the different carriers in the Si-doped (1.0×10^{16} cm^{-3}) $InAs/InAs_{0.65}Sb_{0.35}$ T2SL at 300 K 137

6.1 Two *n*-type ($n^+n^-n^+$) InAs/InAsSb T2SL samples grown by MBE for vertical transport measurements with structure, doping, lifetime (LT) at 100 K and Photoluminescence (PL) peak wavelength at 80 K summarized.................................153

6.2 Chronological summary of the vertical transport mobility results reported for III-V material (InAsSb alloy, InAs/GaSb, and InAs/InAsSb T2SLs), including the results presented in this dissertation from magneto-resistance characteristics of T2SL samples using the vertical MSM test-structures configuration, at 77 and 130 K..........176

Chapter 1

Introduction

1.1 Background

This chapter provides fundamental understanding of III-V InAsSb alloy ternaries and Type-II Strained Layer Superlattices (T2SLs) and compares them with state-of-the-art technology, namely II-VI Mercury Cadmium Telluride (MCT or HgCdTe), for infrared (IR) sensing applications. Before diving into the details of the III-V IR detectors, a brief description of the electromagnetic spectrum is provided, detailing the different parts of the infrared region. Next, III-V InAsSb alloy and T2SL material descriptions are provided while summarizing a comparison to MCT. Finally, the chapter ends with an outline of the dissertation and contributions of the work.

1.2 Infrared Spectrum and Applications

Infrared energy is light that is not visible due to the human eye's inability to detect long wavelengths. It is the part of the electromagnetic spectrum that is perceived as heat. In Latin "infra" means "below", therefore "infrared" means below red. In the perceivable visible light spectrum, red is the longest wavelength. Infrared light possess a longer wavelength, or lower frequency, than that of red [1].

Infrared photodetectors work by absorbing photons in the infrared spectrum and creating current, known as photovoltaic, or producing a change in the conductivity, known as photoconductive. For example, an infrared camera is a non-contact device that detects infrared energy in the form of heat and converts it to an electronic signal. Objects often emit infrared radiation across the wavelength spectrum; however, a limited region is of interest due to a sensor's limited ability to collect radiation within a specific bandwidth.

The first instance of using a thermometer to detect the "invisible light" was by Sir William Herschel (1738-1822), in 1800 [2]. He noticed that various filters produced different amounts of heat. He concluded that the amount of heat transmitted through a filter depended on the color of the filter. He employed a thermometer to measure the temperature under each filter color. He observed that the measured temperature continued to increase at the end of the visible spectrum with the red filter. As he continued to move the thermometer beyond the red region where no light was visible, the temperature still increased; hence, infrared radiation was discovered. Herschel went on to measure the solar radiation spectrum and originate the technique for measuring the transmission spectrum of the atmosphere using the sun as a source.

The spectral absorption of the Earth's atmosphere plays an essential role in the propagation of IR radiation. The Earth's atmosphere restricts how far light or photons of specific wavelengths can travel and be detected due to chemical and molecular absorption. This is known as the atmospheric window where only specific regions of high transmission exist as shown in Figure 1.1.

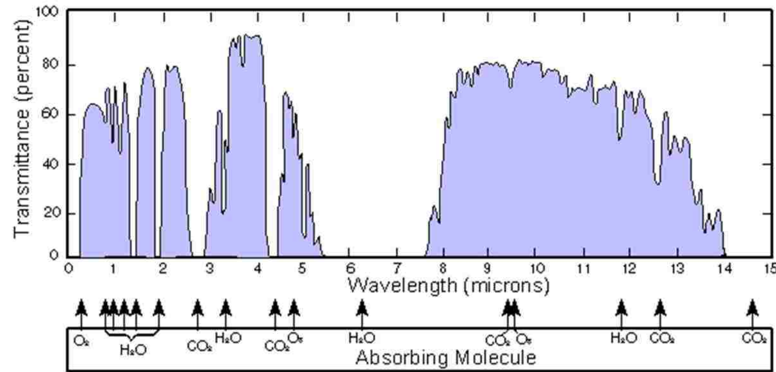

Figure 1.1: Atmospheric transmission of infrared radiation [3].

The infrared band is subdivided into smaller sections as shown in Figure 1.2: The Near-IR (NIR) from 0.75-1.4 µm, Short-Wavelength IR (SWIR) from 1.4-3 µm, Mid-Wavelength IR (MWIR) from 3-8 µm, Long-Wavelength IR (LWIR) from 8-15 µm, and Very-Long-Wavelength IR (VLWIR) from 15-1000 µm. Together, the MWIR and LWIR bands are referred to as the thermal IR bands.

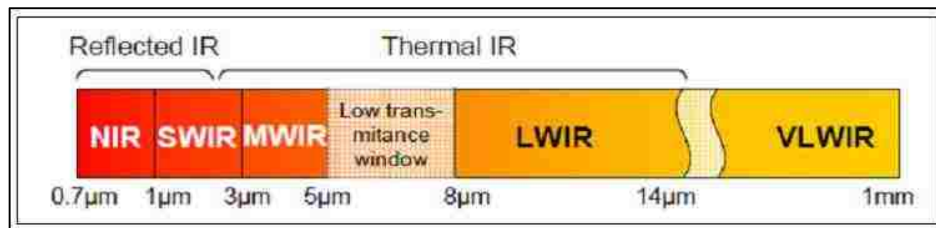

Figure 1.2: The infrared band in the electromagnetic spectrum showing the different IR sub-bands [1].

Since its discovery in the early 1800s, the technology that utilizes IR radiation has gained an immense amount of applications and consequently the research to develop and improve infrared detection technologies remains strong. The NIR region is employed in spectroscopy for the pharmaceutical field. The SWIR region is most known for being used in the telecommunications area. The MWIR region is employed in many military, industrial, and biomedical applications due to its high contrast, superior clear-weather performance, higher transmissivity in high humidity, and higher resolution. This region is

vital for detection as it is where blackbody radiation peaks for hot objects. The LWIR region is employed in cases where higher immunity to atmospheric turbulence, such as fog, dust, and winter haze, are required. This region is where peak blackbody emission resides for objects near room temperature. Infrared sensors are characteristically classified as either cryogenically cooled or uncooled. In many cases, cooling is necessary for the operation of the semiconductor materials employed in infrared photodetectors. Most modern cooled detectors operate in the 60-100 K temperature range. This dissertation's primary focus is to study the MWIR region.

1.3 II-VI and III-V for Infrared Detectors

Interest in II-VI materials (such as MCT) and III-V semiconductor materials (such as InSb, InAsSb and Type-II Strained Layer Superlattices (T2SLs)), has been ongoing through many years for infrared detector applications. Sensing applications spanning from the SWIR to the LWIR have been dominated by MCT detectors [4], since MCT devices have proven high quantum efficiencies and operating temperatures [5]. However, there are several fundamental material challenges. For example, low electron effective mass ($\sim 0.009m_o$) results in large dark-currents due to tunneling [6], and lattice-matched Cadmium-Zinc-Telluride (CdZnTe) substrates for epitaxial growth are expensive [5]. Regardless of its drawbacks, MCT material has been studied extensively since the 1960s and remains as a prominent, mature material for IR detector applications. MCT is still regarded as the state-of-the-art material even though younger technologies utilizing quantum confinement and heterostructure engineering exist.

The concept of heterostructures paved the way for many new types of semiconductor materials, such as quantum wells, quantum wires, quantum dots, and T2SLs. There is significant interest in the development of III-V IR detectors due to their low-cost substrates as well as mature processing and fabrication techniques.

III-V IR detector materials of interest include ternary alloy $InAs_{1-x}Sb_x$ [7], InAs/GaSb T2SLs [8] and $InAs/InAs_{1-x}Sb_x$ T2SLs [9], [10] . Some of the potential benefits of using III-V materials compared to MCT detectors include reduced Auger recombination [11] and the larger effective mass (~ $0.04m_o$) in T2SLs which leads to a reduction of tunneling currents compared with MCT detectors of the same bandgap [12]. Auger recombination occurs by the transfer of energy and momentum released by the recombination of an electron-hole pair to a third particle (either an electron or a hole carrier). Auger recombination is a prominent source of noise in MCT detectors; however, in T2SLs, due to the splitting of the light and heavy-hole bands plus larger effective masses, it has been reduced [13]. This dissertation's materials of interest are the III-V MWIR absorbers composed of the ternary $InAs_{0.91}Sb_{0.09}$ alloy or $InAs/InAs_{0.65}Sb_{0.35}$ T2SL.

III-V antimonide-based (Sb-based) materials, such as $InAs_{0.91}Sb_{0.09}$ lattice-matched to a GaSb substrate can be an alternative to MCT detectors in the MWIR 3-5 μm wavelength range [14], [15]. The ternary InAsSb is an alloy between InAs and InSb, it contains the lowest direct bandgap of any III-V semiconductor [16], with a bandgap of only 0.27 eV for $InAs_{0.91}Sb_{0.09}$ at room temperature [17]. MWIR InAsSb material applications include, but are not limited to, thermal imaging plus Light Detection and Ranging (LIDAR). Also, InAsSb alloys can reach the LWIR regions [18]–[21]. The performance of $InAs_{0.91}Sb_{0.09}$ detectors, especially at high temperatures, has been improved by utilizing

wide-bandgap barrier layers ($Al_{0.15}In_{0.85}As_{0.91}Sb_{0.09}$) [15]. The barrier layers tend to reduce the thermal diffusion currents [14] and allow an efficient photogenerated electron-hole separation [15]. Wide-bandgap barrier layers are lattice-matched to GaSb and can typically be epitaxially grown by alloying Al or P to form ternary or quaternary layers [15], [22].

1.4 Type-II Strained Layer Superlattices (T2SLs)

Sb-based Type-II Strained Layer Superlattices (T2SLs) have gained significant attention since their development in the late 70s and 80s by Esaki and other researchers [8], [23]. The technology to grow these superlattices has matured in recent decades which led to the realization of complex heterostructures with unipolar barriers [24]. Unipolar barrier structures resulted in improved T2SL performance by increasing the quantum efficiency and decreasing the dark current.

Superlattices (SLs) consist of two or more semiconductor materials epitaxially grown together. The materials are repeated periodically and together form conduction and valence minibands. In a superlattice (SL), the Brillouin zone splits into smaller minizones consisting of a series of allowed and forbidden energy bands. The energy bandgap (E_g) of a SL is determined by the separation between the upper edge of the valence miniband and the lower edge of the conduction miniband. Optical absorption in a T2SL requires an overlap of the electron and hole wavefunctions, which occurs primarily at the interfaces between the SL materials. The absorption properties change with SL layer thickness. Thinner layers (shorter SL period) will increase the wave function overlap and improve the optical absorption which is related to the quantum efficiency of the detector.

Several research groups, including some of the pioneers of the MCT technology, see the potential in SL material. There are two main types of superlattices: (1) Ga-bearing

(InAs/GaSb) [25]–[27] and (2) Ga-free (InAs/InAsSb) SL [9], [10], [28]. Both types of superlattices possess a Type-II band alignment as shown in Figure 1.3. Superlattices are categorized into two main groups: Type-I and Type-II superlattices. In Figure 1.3, materials *A* and *B* form a superlattice with conduction and valence bands CB_A/CB_B and VB_A/VB_B, respectively. The red (holes) and blue (electrons) dotted lines represent carrier confinement location.

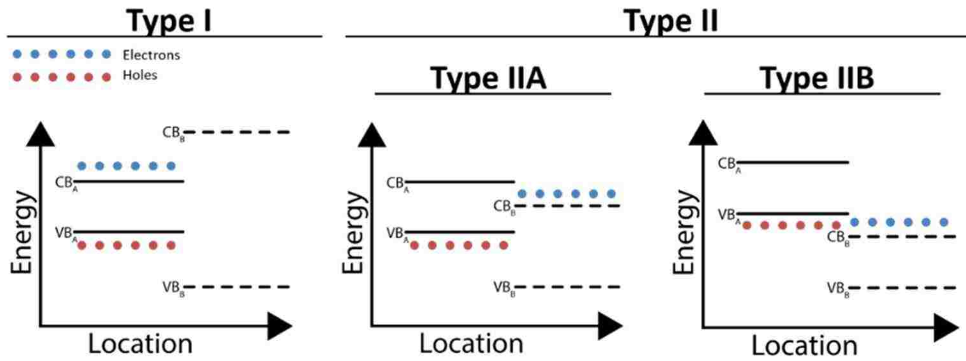

Figure 1.3: Type-I and Type-II energy bands for materials *A* and *B* that form a superlattice, with conduction and valence bands CB_A/CB_B and VB_A/VB_B, respectively. Type-IIA is the "staggered" superlattice energy band while Type-IIB is the "misaligned" or "broken gap" energy band. The red (holes) and blue (electrons) dotted lines represent carrier confinement location.

Type-I superlattices have the conduction and valence band of one material encompassed by the conduction and valence band of the other material. Type-II superlattices are subcategorized into Type-IIA and Type-IIB. Type-IIA alignment has a conduction and valence band offset, but the bands overlap. Type-IIB has a complete separation of the conduction and valence bands. Type-IIA is known as the "staggered" superlattice energy alignment while Type-IIB is known as the "misaligned" or "broken gap." The critical difference between the band alignments is the way the electrons and holes are confined as shown in Figure 1.3. For Type-I superlattices, the electrons and holes

are confined in material *A*, the smallest bandgap material. For Type-II superlattices electrons and holes are confined in separate materials.

Figure 1.4 shows the Type-II Superlattice (T2SL) band alignment of the two-layer $InAs/InAs_{0.65}Sb_{0.35}$ structure employed for this dissertation work, with the InAs electron well (eW) and the InAsSb hole well (hW). Figure 1.4 displays the optical transition between the conduction and valence band as well as the bandgap formation (E_g), modeled using Naval Research Laboratory (NRL) MULTIBANDS® software at 300 K. In the InAs/InAsSb T2SL, the optical transition occurs only when the probability distribution functions overlap because the conduction band electrons are confined to the InAs layer, whereas the heavy holes are confined to the InAsSb layer [29]. The bandgap can be controlled and shifted through much of the MWIR to LWIR through variation of the SL period, as well as the composition of the $InAs_{1-x}Sb_x$ layer.

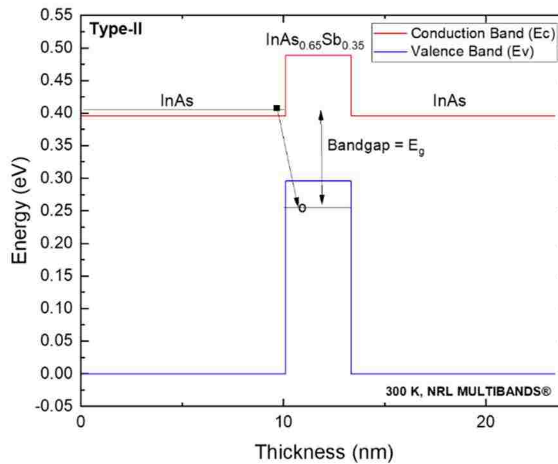

Figure 1.4: Type-II Superlattice (T2SL) band alignment of the $InAs/InAs_{0.65}Sb_{0.35}$ structure, with InAs electron well (eW) and $InAs_{0.65}Sb_{0.35}$hole well (hW). The optical transition between the conduction and valence band as well as the bandgap formation are shown, modeled using NRL MULTIBANDS® at 300 K.

The absence of Gallium in InAs/InAsSb T2SL hole wells can eliminate potential Gallium-related defect states. To minimize the occurrence of defects, the InAs/InAsSb

T2SL is lattice-matched to a GaSb substrate. The InAs/GaSb T2SL have short lifetimes (30-100 ns) [11], but the minority carrier lifetime improved in InAs/InAsSb (9 μs with a 4 μm cut-off) [9]. Hence, the InAs/InAsSb T2SL has shown considerable potential as an IR detector material due to the longer minority carrier lifetime. The MWIR T2SL absorber layers employed for this dissertation work are composed of alternating layers of InAs and $InAs_{0.65}Sb_{0.35}$.

1.5 Fundamental Limitations of III-V materials

Despite the progress of III-V material properties, such as stronger optical absorption characteristics [30] and relatively improved minority carrier lifetimes [9], IR detectors using these materials have yet to reach their full theoretical potential. Some of their most significant limitations remain: surface passivation of *p*-type materials [31] and Shockley-Read Hall (SRH) recombination [32]. As a result, the dark current in InAs/InAsSb T2SLs is higher than MCT detectors due to SRH recombination. Although InAs/InAsSb SRH is reduced compared to InAs/GaSb T2SLs, it is not eliminated. For InAs/$InAs_{0.66}Sb_{0.33}$ T2SL material, the minority carrier lifetimes are dominated by SRH recombination at low temperatures and by intrinsic Auger recombination at near room temperature [32]. SRH does not demonstrate a dominant contribution on $InAs_{0.91}Sb_{0.09}$ alloys, as lifetimes were found to be limited by radiative and Auger recombination through the entire temperature range. Recent fabrication developments resulted in improved lifetimes which has prompted increased interest in T2SLs as an alternative to MCT technology [33], [34]. Table 1.1 provides a summary of the advantages and disadvantages of both II-VI (MCT) and III-V (InAsSb alloy and InAs/InAsSb T2SL) detector technologies.

Table 1.1: Summary of the advantages and disadvantages of both II-VI (MCT) and III-V (InAsSb alloy and InAs/InAsSb T2SL) detector technologies.

	II-VI: Mercury Cadmium Telluride (MCT)	III-V: InAsSb, Type-II Strained Superlattice (T2SL)
Pros	✓High quantum efficiency	✓Wavelength flexibility
	✓Low dark-current	✓Reduced Auger recombination
	✓Wavelength flexibility	✓Reduced tunneling current
	✓High operation temperature	✓Good uniformity
	✓Radiation Tolerance	✓Mature processing
		✓Mature growth technology
Cons	× CdZnTe substrates	×Absorption Coefficient
	×Low uniformity over large area	×Sensitivity to the interfaces
	×Large tunneling currents	×Passivation for *p*-type
	×Material Stability - blinkers	×Shockley-Read-Hall (SRH)
		×Radiation tolerance

Minority carrier recombination lifetime is defined as the average time it takes for a minority carrier to recombine. Carrier lifetime while being a vital material parameter for detectors, does not solely determine their performance. Once charge is generated in a detector, it must be extracted from the device as photocurrent. Hence, understanding carrier transport parameters are therefore fundamentally important in advancing III-V IR photodetectors. Vertical transport of carriers is parallel to the epitaxial growth direction and is particularly important because this is the direction of photogenerated carrier flow in IR detectors. The holes in *n*-type T2SL absorbers are expected to be extremely heavy and theoretically should not contribute to conduction in the growth direction [35]. However, unipolar devices, such as the nBn, have demonstrated good carrier transport [36]–[38].

In the InAs/InAsSb T2SLs, the transport problem is exacerbated since the holes are confined to a thin layer of InAsSb and the exact mechanism for carrier transport is not fully understood. For example, a cross-sectional Scanning Tunneling Microscopy (STM) study [39], indicated a roughening of the InAs/InAsSb interface and antimony (Sb) segregation. One of the crucial questions is if sharper interfaces will adversely affect the transport of the holes due to better confinement in the InAsSb regions or not. Localization of minority carrier holes in *n*-type absorbers remains a limiting factor [40]. Hole localization is often associated to the very large effective mass along growth direction resulting in low vertical mobility. In contrast, recently reported heavy-hole/light-hole mixing demonstrated that while a hole carrier with a large effective mass moves very slowly along the vertical direction, it can be scattered into a state that can support much higher vertical velocity [35].

Transport studies on III-V IR materials have been the subject of continued research [7], [28], [41]–[43] and it is the topic of interest of this dissertation. To fully understand the transport in III-V materials, in-plane or lateral transport measurements need to be better understood. Lateral transport properties are usually extracted using Hall Effect measurements and are challenging to perform in InAsSb alloys and InAs/InAsSb T2SLs due to the parallel conduction in the highly conductive GaSb substrate as well as surface electron accumulation layers. Further development demands a better understanding of lateral (in-plane) and vertical (out-of-plane) carrier transport mechanisms and extraction of all the carrier species responsible for conduction. However, before further transport discussion of III-V materials is commenced in Chapter 2, an overview of the dissertation and the importance of the problem is described in Section 1.6.

1.6 Dissertation Overview

One major challenge is that fundamental transport properties, such as background carrier concentration and carrier mobility, of III-V absorbers such as InAsSb alloys and InAs/InAsSb T2SLs, are not fully understood. Background carrier concentration determines the minority carrier lifetime, whereas, vertical and lateral carrier mobilities affect the extraction of the photogenerated electron-hole pairs. The highly conductive GaSb substrate employed for the growth of these III-V materials can create an unwanted conduction path. Hence, the separation of conduction paths in a multi-carrier system such as InAsSb and InAs/InAsSb T2SLs is required to provide accurate lateral and vertical transport measurements. Removal of the GaSb substrate and transfer of absorber layers to insulating substrate materials can enable a thorough electrical transport properties investigation.

1.6.1 Significance of the Problem

III-V materials such as the T2SL, have been significantly hampered by: (1) the lack of a straightforward experimental technique to gain insight into the fundamental properties of carrier transport in the direction perpendicular to the superlattice plane (vertical transport), (2) the difficulties of making lateral transport measurements when an electrically conductive buffer or substrate is employed, and (3) the lack of insight or knowledge into correlations between lateral and vertical transport properties. Currently, no direct vertical transport measurement technique has been presented due to the difficulty in separating lateral and vertical transport properties.

1.6.2 Contributions of the Dissertation

This dissertation's tasks are to: (1) report the lateral/vertical transport properties of carriers in III-V MWIR detectors to understand carrier collection efficiency better, and (2) extract vertical transport mobilities in InAs/InAsSb T2SL material via a novel Metal-Semiconductor-Metal (MSM) processing technique. The work was divided into three steps as shown in Figure 1.5, which required magneto-transport measurements, Multi-Carrier Fitting (MCF), and High-Resolution Mobility Spectrum Analysis (HR-MSA). The primary objective was to extract lateral and vertical transport parameters using temperature- and magnetic-field-dependent (*B-field-dependent*) measurements.

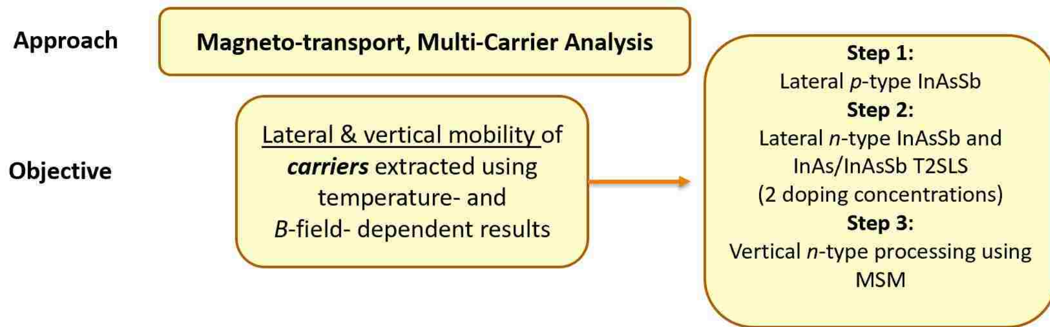

Figure 1.5: Approach, objective and steps for the work presented in this dissertation.

Step 1 incorporates a theoretical and experimental investigation of the lateral transport properties of the different carriers present in MWIR *p*-type $InAs_{0.91}Sb_{0.09}$ material. Step 2 follows a similar process, but the lateral transport measurements of *n*-type $InAs_{0.91}Sb_{0.09}$ and $InAs/InAs_{0.65}Sb_{0.35}$ T2SL materials are reported and compared. In step 2, results are presented for alloy and T2SL epitaxial structures with absorber regions grown with doping concentrations: (1) 1×10^{15} cm^{-3} or Non-Intentionally Doped (*NID*), and (2) 1×10^{16} cm^{-3} intentionally Si-doped (*n*-type). Note that lateral transport measurements enable a better understanding of the different conduction paths present in the materials.

Step 3 demonstrates for the first time, a Metal-Semiconductor-Metal (MSM) test-structure process to enable vertical transport measurements of III-V materials. The magneto-resistance properties of *n*-type ($n^{+}n^{-}n^{+}$) InAs/$InAs_{0.65}Sb_{0.35}$ T2SLs grown on GaSb substrates were determined using the MSM processing technique and variable-temperature. The decoupling of vertical transport mobilities in the *NID* InAs/$InAs_{0.65}Sb_{0.35}$ T2SL was performed using the lateral transport results taken in Step 2.

1.6.3 Outline of the Dissertation

The transport properties of InAsSb and InAs/InAsSb T2SLs are determined using theoretical modeling, Van der Pauw (VDP) processing, substrate-removal fabrication processes (MSM), and experimental verification. The theoretical modeling includes extraction of the interface carrier sheet concentrations using NRL MULTIBANDS®, transport properties using Multi-Carrier Fit (MCF), and High-Resolution Mobility Spectrum Analysis (HR-MSA). As-grown materials are characterized using photoluminescence (PL) and Time-Resolved Microwave Reflectance (TMR) to quantify optical parameters. Finally, the experimental effort involves temperature- and magnetic-field-dependent transport measurements.

In Chapter 1, the introduction describes III-V IR sensing material with a comparison to II-VI material, applications, and benefits of InAsSb as well as InAs/InAsSb T2SLs. The dissertation outline and significance are addressed.

In Chapter 2, the background presents a detailed description of drift-diffusion transport mechanisms and multi-carrier transport using magneto-resistance method for III-V materials. This chapter provides a descriptive history of lateral and vertical transport measurements.

In Chapter 3, the methodology reviews the experimental measurements and theoretical models employed for this work. MBE growth, optical measurements, and the lateral/vertical magneto-resistance configurations are explained with a summary of the equipment used for the experimental methods. The NRL MULTIBANDS®, Multi-Carrier Fit (MCF) and High-Resolution Mobility Spectrum Analysis (HR-MSA) are summarized as the theoretical models.

In Chapter 4, the lateral transport measurements on *p*-type (Beryllium-doped) InAsSb and extraction of all the carrier species present in the sample are presented. The extraction of the lateral transport properties required step-wise etching, surface experiment, modeling of interface carriers using NRL MULTIBANDS® and temperature- plus magnetic-field-dependent measurements analyzed by the MCF method.

In Chapter 5, the lateral transport measurements on *n*-type InAsSb alloys and InAs/InAsSb T2SLs under two doping concentrations: (1) Non-Intentionally Doped (*NID*) and (2) Silicon-doped (Si-doped) are performed. It focuses on the distinction of the different carriers present in each sample by providing a thorough comparison of the alloy and superlattice lateral transport results using variable temperature- and magnetic-field-dependent measurements in conjunction with the MCF method.

In Chapter 6, a novel Metal-Semiconductor-Metal (MSM) test-structure process enables vertical transport measurements of III-V materials. Using the MSM processing and variable-temperature, the magneto-resistance properties of *n*-type ($n^+n^-n^+$) InAs/$InAs_{0.65}Sb_{0.35}$ T2SLs were determined. To isolate the effect of the conducting substrate from the electrical measurements, samples were fabricated and transferred onto metal-coated sapphire substrates. The magnetic-field-dependent magneto-resistance

characteristics measured at different temperatures, were analyzed using the High-Resolution Mobility Spectrum Analysis (HR-MSA) methodology, which allowed the identification of two distinct carriers contributing to vertical conduction. The decoupling of vertical transport mobilities in the *NID* InAs/InAsSb T2SL was performed using the lateral transport results presented in Chapter 5.

In Chapter 7, the summary and conclusions are presented for lateral and vertical transport measurements. Recommendations for potential solutions, improvements, and future work are discussed.

1.7 References

[1] M. K. Bhowmik *et al.*, "Thermal Infrared Face Recognition - a Biometric Identification Technique for Robust Security System," 2011. [Online]. Available: www.intechopen.com.

[2] W. Herschel, "Royal Society," *Philos. Transcations R. Soc. London*, vol. 90, 1800.

[3] "Infrared window." [Online]. Available: https://en.wikipedia.org/wiki/Infrared_window.

[4] A. Rogalski, J. Antoszewski, and L. Faraone, "Third-generation infrared photodetector arrays," *J. Appl. Phys.*, vol. 105, no. 9, 2009.

[5] M. Kopytko and A. Rogalski, "HgCdTe barrier infrared detectors," *Prog. Quantum Electron.*, vol. 47, pp. 1–18, 2016.

[6] A. Rogalski, "HgCdTe infrared detector material: History, status and outlook," *Reports Prog. Phys.*, vol. 68, no. 10, pp. 2267–2336, 2005.

[7] Y. Lin, D. Wang, D. Donetsky, and G. Kipshidze, "Transport properties of holes in bulk InAsSb and performance of barrier long-wavelength infrared detectors," *Semicond. Sci. Technol*, vol. 29, no. 112002, 2014.

[8] D. L. Smith and C. Mailhiot, "Proposal for strained type II superlattice infrared detectors," *J. Appl. Phys.*, vol. 62, no. 6, 1987.

[9] E. H. Steenbergen *et al.*, "Significantly improved minority carrier lifetime observed in a long-wavelength infrared III-V type-II superlattice comprised of InAs/InAsSb," *Appl. Phys. Lett.*, vol. 99, no. 25, pp. 1–4, 2011.

[10] H. S. Kim *et al.*, "Long-wave infrared nBn photodetectors based on InAs/InAsSb type-II superlattices," *Appl. Phys. Lett.*, vol. 101, no. 16, pp. 1–4, 2012.

[11] C. H. Grein, M. E. Flatté, J. T. Olesberg, S. A. Anson, L. Zhang, and T. F. Boggess, "Auger recombination in narrow-gap semiconductor superlattices incorporating antimony," *J. Appl. Phys.*, vol. 92, no. 12, pp. 7311–7316, 2002.

[12] A. G. Thompson and J. C. Woolley, "Energy-Gap Variation in Mixed III–V Alloys," *Can. J. Phys.*, vol. 45, no. 2, 1967.

[13] C. H. Grein, P. M. Young, M. E. Flatte, and H. Ehrenreich, "Long wavelength InAs/InGaSb infrared detectors: optimization of carrier lifetimes," *J. Appl. Phys.*, vol. 78, no. 12, 1995.

[14] W. S. A. Krier, "Uncooled photodetectors for the spectral range 3-5 μm based on III – V heterojunctions," *Appl. Phys. Lett.*, vol. 89, no. 083512, 2006.

[15] M. Carras, J. L. Reverchon, G. Marre, C. Renard, B. Vinter, and X. Marcadet, "Interface band gap engineering in InAsSb photodiodes," *Appl. Phys. Lett.*, vol. 87, no. 102103, 2005.

[16] D. Lackner, "InAsSb / InAs STRAIN BALANCED SUPERLATTICES FOR PHOTODETECTOR APPLICATIONS," Simon Fraser University, 2011.

[17] I. Vurgaftman, J. R. Meyer, and L. R. Ram-Mohan, "Band parameters for III – V compound semiconductors and their alloys," *J. Appl. Phys.*, vol. 89, no. 11, 2001.

[18] G. Belenky *et al.*, "Metamorphic InAsSb/AlInAsSb heterostructures for optoelectronic applications," *Appl. Phys. Lett.*, vol. 102, no. 11, pp. 1–5, 2013.

[19] D. Wang *et al.*, "Metamorphic InAsSb-based barrier photodetectors for the long wave infrared region region," *Appl. Phys. Lett.*, vol. 051120, no. 103, 2013.

[20] S. P. Svensson *et al.*, "Band gap of InAs1-xSbx with native lattice constant," *Phys. Rev. B*, vol. 86, no. 24, 2012.

[21] P. T. Webster *et al.*, "Measurement of InAsSb bandgap energy and InAs / InAsSb band edge positions using spectroscopic ellipsometry and photoluminescence spectroscopy," *J. Appl. Phys.*, vol. 118, no. 24, 2015.

[22] O. J. Pitts, D. Lackner, Y. T. Cherng, and S. P. Ã. Watkins, "Growth of InAsSb / InPSb heterojunctions for mid-IR detector applications," *J. Cryst. Growth*, vol. 310, 2008.

[23] G. A. Sai-Halasz, R. Tsu, and L. Esaki, “A new semiconductor superlattice,” *Appl. Phys. Lett.*, vol. 30, no. 12, 1977.

[24] P. Martyniuk, M. Kopytko, and A. Rogalski, “Barrier infrared detectors,” *Opto-electronics Rev.*, vol. 22, no. 2, 2014.

[25] B. Klein *et al.*, “Carrier lifetime studies in midwave infrared type-II InAs/GaSb strained layer superlattice,” *J. Vac. Sci. Technol. B Microelectron. Nanom. Struct.*, vol. 32, no. 2, p. 02C101, Mar. 2014.

[26] B. V. Olson, L. M. Murray, J. P. Prineas, M. E. Flatte, J. T. Olesberg, and T. F. Boggess, “All-optical measurement of vertical charge carrier transport in mid-wave infrared InAs/GaSb type-II superlattices,” *Appl. Phys. Lett.*, vol. 102, no. 20, 2013.

[27] S. Mou, J. V Li, and S. L. Chuang, “Quantum Efficiency Analysis of InAs-GaSb Type-II Superlattice Photodiodes,” *Quantum Electron. IEEE J.*, vol. 45, no. 6, 2009.

[28] D. Zuo *et al.*, “Direct minority carrier transport characterization of InAs/InAsSb superlattice nBn photodetectors,” *Appl. Phys. Lett.*, vol. 106, no. 7, pp. 2–6, 2015.

[29] D. Lackner, M. Steger, M. L. W. Thewalt, O. J. Pitts, and Y. T. Cherng, “InAs / InAsSb strain balanced superlattices for optical detectors : Material properties and energy band simulations,” *J. Appl. Phys.*, vol. 111, no. 3, 2012.

[30] A. Rogalski, “New material systems for third generation infrared photodetectors,” *Opto-electronics Rev.*, vol. 16, no. 4, pp. 458–482, 2008.

[31] S. Mallick, K. Banerjee, S. Ghosh, J. B. Rodriguez, and S. Krishna, “Midwavelength infrared avalanche photodiode using InAs-GaSb strain layer superlattice,” *IEEE Photonics Technol. Lett.*, vol. 19, no. 22, pp. 1843–1845, 2007.

[32] B. V. Olson *et al.*, “Identification of dominant recombination mechanisms in narrow-bandgap InAs/InAsSb type-II superlattices and InAsSb alloys,” *Appl. Phys. Lett.*, vol. 103, no. 5, 2013.

[33] L. Höglund *et al.*, “Influence of radiative and non-radiative recombination on the minority carrier lifetime in midwave infrared InAs / InAsSb superlattices,” *Appl. Phys. Lett.*, vol. 103, no. 22, 2013.

[34] C. M. Ciesla, “Suppression of Auger recombination in arsenic-rich InAs1 − x Sb x strained layer superlattices,” *J. Appl. Phys.*, vol. 80, no. 5, 1996.

[35] D. Z. Ting, A. Soibel, and S. D. Gunapala, “Type-II superlattice hole effective masses,” *Infrared Phys. Technol.*, vol. 84, pp. 102–106, 2017.

[36] D. Z. Ting *et al.*, “Carrier transport in unipolar barrier infrared detectors,” in *Proceedings of SPIE*, 2015, vol. 9451.

[37] E. Plis *et al.*, “Infrared Physics & Technology Dual color longwave InAs / GaSb type-II strained layer superlattice detectors,” *Infrared Phys. Technol.*, vol. 70, pp. 93–98, 2015.

[38] J. B. Rodriguez, “nBn structure based on InAs/GaSb type-II strained layer superlattices,” *Appl. Phys. Lett.*, vol. 91, no. 4, 2007.

[39] M. R. Wood *et al.*, “Monolayer-by-monolayer compositional analysis of InAs/InAsSb superlattices with cross-sectional STM,” *J. Cryst. Growth*, vol. 425, 2015.

[40] B. V. Olson *et al.*, “Vertical Hole Transport and Carrier Localization in InAs/InAs1−xSbx Type-II Superlattice Heterojunction Bipolar Transistors,” *Phys. Rev. Appl.*, vol. 7, no. 2, 2017.

[41] C. Cervera *et al.*, “Transport measurements on InAs/GaSb superlattice structures for mid-infrared photodiode,” *J. Phys. Conf. Ser.*, vol. 193, no. 012030, 2009.

[42] Y. Lin *et al.*, “Effect of hole transport on performance of infrared type-II superlattice light emitting diodes,” *J. Appl. Phys.*, vol. 117, no. 16, pp. 1–5, 2015.

[43] G. A. Umana-Membreno *et al.*, “Vertical minority carrier electron transport in p-type InAs/GaSb type-II superlattices,” *Appl. Phys. Lett.*, vol. 101, no. 25, 2012.

Chapter 2

Background

2.1 Introduction

This chapter provides the background for understanding carrier transport in semiconductor materials, specifically III-V Infrared (IR) materials. It begins with a review of drift-diffusion, conductivity, effective mass and the Hall Effect measurement. An explanation for multiple-carrier (multi-carrier) transport is provided with an emphasizes on magneto-transport measurements. Isotropic InAsSb and Anisotropic InAs/InAsSb Type-II Strained Layer Superlattice (T2SL) properties are described followed with a discussion of the T2SL transport limitations. In addition to Hall Effect measurements at a single magnetic field, the variable magnetic field method is summarized. The background section concludes with a review of the different methods employed to measure lateral and vertical transport properties in III-V IR materials, specifically anisotropic T2SL material.

2.2 Drift and Diffusion

Electrons and holes are charged particles with an effective mass (m^*) that transport through a semiconductor material. The charge carrier transport consists of two main types of mechanisms: (1) diffusion and (2) drift. For the transport of charge carriers to occur, either a concentration gradient (diffusion) or an electric field (drift) is required. Due to thermally

induced random motion, mobile particles tend to move from a region of high concentration to a region of low concentration. The proportionality constant (D) is known as the diffusion constant D_p and D_n for holes and electrons, respectively. Diffusion current within a semiconductor consists of the addition of the hole ($J_{p,diff}$) and electron ($J_{n,diff}$) components to equal the total diffusion current density ($J_{Total,diff}$):

$$J_{p,diff} = -qD_p \frac{dp}{dx} \tag{2.1}$$

$$J_{n,diff} = qD_n \frac{dn}{dx} \tag{2.2}$$

$$J_{Total,diff} = q(D_n \frac{dn}{dx} - D_p \frac{dp}{dx}) \tag{2.3}$$

whereas q is the electron charge, n and p correspond to the electron and hole concentrations, respectively. In the presence of an applied electric field (E), the charged particles move due to a process called drift. Mobility (μ) describes how fast the charge carriers move. The hole velocity (v_p) and the electron velocity (v_n) equations are described as:

$$v_p = \mu_p E \tag{2.4}$$

$$v_n = -\mu_n E \tag{2.5}$$

whereas μ_p and μ_n are the hole and electron drift mobilities, respectively. One of the critical parameters in transport is mobility. Drift mobilities are dependent on temperature, and in extrinsic semiconductors, also depend on the doping or impurity concentration. Mobility is directly proportional to temperature and carrier scattering; it decreases with increasing temperature if lattice (phonon) scattering is dominant and decreases with decreasing temperature if impurity scattering is dominant. Drift current is proportional to

the carrier velocity and carrier concentration. Drift current density components for holes ($J_{p,drift}$) and electrons ($J_{n,drift}$) are described by:

$$J_{p,drift} = qpv_p = qp\mu_p E \tag{2.6}$$

$$J_{n,drift} = qnv_n = qp\mu_n E \tag{2.7}$$

In a semiconductor, both electrons and holes conduct current, and the total drift current density becomes:

$$J_{Total,drift} = qE(p\mu_p + n\mu_n) = \sigma E \tag{2.8}$$

A *p*-*n* junction is shown in Figure 2.1 to provide a visual explanation of drift and diffusion currents. A *p*-*n* junction consists of *p*- and *n*-type semiconductor material joined together during epitaxial growth. The majority carriers from each side diffuse as shown in Figure 2.1, where the holes diffuse towards the *n*-doped region while the electrons diffuse towards the *p*-doped region. Due to diffusion, the atoms near the *p*-*n* junction become ionized and create a "built-in" electric field that gives rise to a space charge (depletion) region. In the depletion region, the electric field goes from the *n*- doped region to the *p*-doped region.

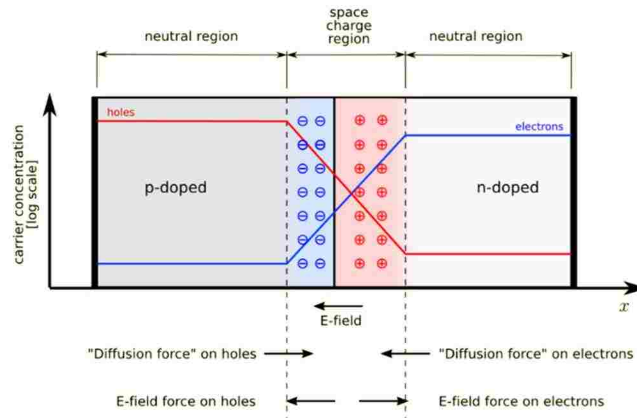

Figure 2.1: Schematic of a *p*-*n* junction [1].

Whenever incident photons create electron-hole pairs, the electric field accelerates each carrier by applying a force with each carrier type drifting toward opposite neutral regions. This may cause the carrier to end up being on the other side of the depletion region. These drifting of charge carriers is known as the drift current and it is associated to the minority carriers.

Equations 2.3 and 2.8 list the total current flowing in a semiconductor as the sum of drift and diffusion current densities. Einstein Relations relate the characteristic constants for drift and diffusion as:

$$D_p = \frac{k_B T \mu_p}{q} \tag{2.9}$$

$$D_n = \frac{k_B T \mu_n}{q} \tag{2.10}$$

written for holes and electrons, respectively, whereas k_B is the Boltzmann constant, T the temperature, and q is known as the fundamental electron charge constant. It is worth noting that Einstein relations are only valid for equilibrium conditions but are widely used as an approximation. The average distance that a charge carrier moves in the semiconductor before recombination is usually referred to as the minority carrier diffusion length L_p and L_n for holes and electrons, respectively. The diffusion length is related to the diffusion coefficient $D_{p,n}$ and lifetime $\tau_{p,n}$ as:

$$L_p = \sqrt{D_p \tau_p} \tag{2.11}$$

$$L_n = \sqrt{D_n \tau_n} \tag{2.12}$$

for minority holes and electrons, respectively.

In a material with both excess electrons and holes, the carriers do not move independently, but diffuse and drift with an effective mobility and diffusion coefficient. This phenomenon is known as ambipolar transport with the general equation as:

$$D_A \frac{\partial^2(n)}{\partial x^2} + \mu_A E \frac{\partial(n)}{\partial x} + G - R = \frac{\partial(n)}{\partial t} \quad (2.13)$$

whereas E is the applied electric field, and G and R are the generation and recombination rates, respectively. The ambipolar mobility and diffusion coefficients are μ_A and D_A. In a doped semiconductor (strongly p-type) under low injection ($\Delta n << n_o$), the ambipolar constants become $D_A = D_n$ and $\mu_A = \mu_n$, where the transport and recombination parameters are those of the minority carriers. However, when the concentration of excess carriers is much larger than the equilibrium concentration ($\Delta n >> n_o, p_o$), the carrier concentrations are almost equal ($p \sim n$), and the ambipolar constants become:

$$D_A = \frac{2D_n D_p}{D_n + D_p} \quad (2.14)$$

$$\mu_A = 0 \quad (2.15)$$

Hence, as shown by Equations 2.14 and 2.15, current under high injection conditions is dominated by diffusion.

2.3 Conductivity and Effective Mass

The conductivity ($\boldsymbol{\sigma}$) of a semiconductor depends on the mobile charge carrier concentrations and mobilities and is defined to be the current density (J) divided by the applied electric field:

$$\sigma = \frac{J}{E} = qp\mu_p + qn\mu_n \quad (2.16)$$

The resistivity (ρ) of a semiconductor is the conductivity reciprocal, namely:

$$\rho = {}^{1}/_{\sigma} \tag{2.17}$$

resistivity is commonly used to specify the doping level, in an *n*-type semiconductor with a donor doping concentration of N_d:

$$\rho_n = \frac{1}{qN_d\mu_n} \tag{2.18}$$

In a *p*-type semiconductor with an acceptor doping concentration of N_a:

$$\rho_p = \frac{1}{qN_a\mu_p} \tag{2.19}$$

Both the conductivity and resistivity are material properties. The electrical resistance of the rectangular bar of semiconductor material shown in Figure 2.2 is described by Ohm's law ($V = IR$).

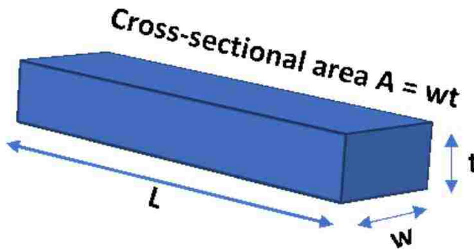

Figure 2.2: Rectangular bar of semiconductor material with length, L, width, w and thickness, t. Cross-sectional area is known as A = wt.

The resistance (R) of the bar is described by Ohm's law as:

$$R = \frac{V}{I} = \rho\,\frac{L}{A} = \rho\,\frac{L}{wt} \tag{2.20}$$

where V is the voltage, I is the current, and A, L, w, t are the cross-sectional area, length, width and thickness of the rectangular bar. The sheet resistance (R_{sh}) of a uniformly doped layer with constant carrier densities and mobilities is known as:

$$R_{sh} = \frac{\rho}{t} = \frac{1}{(qp\mu_p + qn\mu_n)t} \tag{2.21}$$

while strictly speaking the units of the sheet resistance is in ohms (Ω), one refers to it as being in Ohms per square (Ω/sq). This terminology comes in handy when the resistance of a rectangular piece of material similar to Figure 2.2 must be obtained, with length, L, and width, w. The sheet resistance is a meaningful descriptor not only for uniformly doped layers but also for non-uniformly doped layers, where both carrier densities and mobilities are depth dependent [2].

Extrinsic semiconductors have concentrations that depend on temperature, as shown in Figure 2.3. Figure 2.3 shows a theoretical graph of majority carrier concentration (either n or p) vs. reciprocal temperature (*1/T*) for an ideal semiconductor sample.

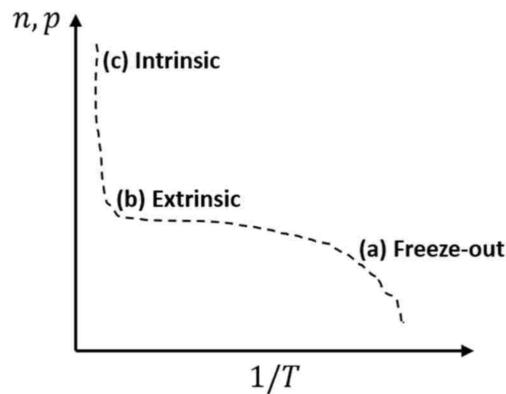

Figure 2.3: A theoretical graph of majority carrier concentration (either n or p) vs. reciprocal temperature (*1/T*) for an ideal extrinsic semiconductor sample. Phase (a), freeze-out, conductivity increases with temperature due to charge carriers being produced from impurity atoms within the sample. Phase (b), extrinsic region, there is no increase in conductivity with increasing temperature. Phase (c), intrinsic region, the conduction band begins to populate as charge carriers transition from the valence band at high temperatures.

For an n-type doped semiconductor, in phase (a), freeze-out, the thermal energy is insufficient to release the weakly-bound electrons from the donor sites and inadequate to excite them across the bandgap. In phase (b), extrinsic region, the temperature increase

frees almost all the electrons leading to the concentration being closer to that of the donors (n ~ N_d). More electrons are excited across the bandgap, but the number of electrons supplied in this region stays comfortably below or close to the *n*-type donor concentration N_d. In phase (c), the intrinsic region, the conduction band begins to populate due to the transition of electron charge carriers from the valence band to the conduction band ($n = n_i$) due to high temperatures. For phase (c), the temperature dependence of conductivity can be displayed as an exponential function [3]:

$$\sigma = \sigma_0 \, e^{\frac{-E_g}{2k_B T}} \tag{2.22}$$

whereas σ_0 is the undoped conductivity, E_g is the bandgap energy, k_B is the Boltzmann constant and T is the temperature. A plot of ln(σ) as a function of $1/T$ will yield a straight-line graph with a gradient given as:

$$b = -\frac{E_g}{2k_B} \tag{2.23}$$

from which the bandgap energy can be extracted.

Carrier transport in semiconductors is affected by various factors, effective mass, m^*, is one of the most influential parameters in transport. In order to fully understand mobility, the microscopic behavior of a carrier must be understood, the effective mass. Electrons have lighter effective masses relative to holes and hence are faster and possess higher mobility. The effective mass is inversely proportional to the curvature of the energy band. Even without an applied field, charged carriers are always moving with a thermal velocity (v_{th}) which is given by the thermodynamic relation:

$$\frac{1}{2} m^* v_{th}^2 = \frac{3}{2} k_B T \tag{2.24}$$

Furthermore, each carrier does not continue with a specific path indefinitely. A fundamental phenomenon called scattering occurs when a carrier collides with a scattering center. The scattering centers can be of many origins. The possible scattering mechanisms include (1) phonons, (2) ionized impurities, (3) neutral impurities, and (4) other charge carriers. In III-V materials, scattering can be generally divided into lattice (or phonon) scattering and impurity scattering. For a typical III-V semiconductor with moderate doping level at high temperatures, mobility is dominated by lattice scattering, and it has a $T^{-3/2}$ temperature dependence. At low temperature, mobility is controlled by impurity scattering, with a $T^{3/2}$ temperature dependence [4].

2.4 Hall Effect

In 1879, Edwin Hall discovered the Hall Effect [5]. Hall Effect measurements are of extreme importance as they are employed often in semiconductors to (1) distinguish if the conductivity type of a material is *n*-type or *p*-type, (2) measure the majority carrier concentration, (3) determine the majority carrier mobility, (4) calculate resistivity, and (5) perform magneto-resistance measurements. Illustration of the Hall Effect can be seen in Figure 2.4, with a semiconductor material of width (w), length (l), and depth or thickness (d), biased with a voltage (V_x) that induces a current (I_x). The applied magnetic field (B_z) in the z-direction causes the carriers to deflect in the y-direction due to the Lorentz force, and this build-up of carriers gives rise to a second electric field, the Hall field (E_H), oriented in the positive y-direction ($E_y = E_H$). The Hall field produces a Hall voltage, V_H, and once steady state is fully established, carriers are no longer deflected as the Lorentz force is balanced by the Hall field [2].

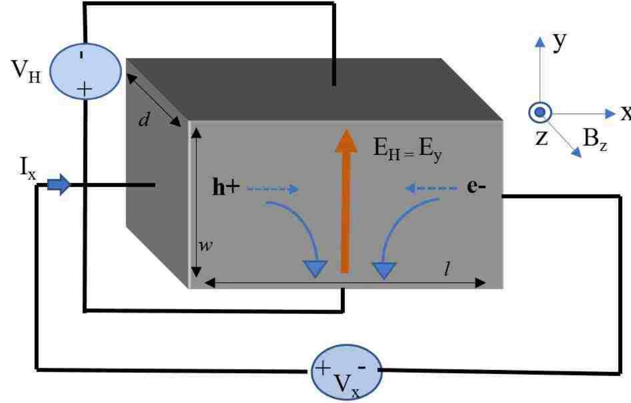

Figure 2.4: Schematic illustration of the Hall Effect. A semiconductor material of width (*w)*, length (*l)*, and depth (*d)* is biased with a voltage (V_x) that induces a current (I_x). The applied magnetic field (B_z) in the *z*-direction causes the carriers to deflect in the negative *y*-direction due to the Lorentz force, and this build-up of carriers gives rise to a second electric field, the Hall field, oriented in the positive *y*-direction ($E_y = E_H$).

The Lorentz force ($\vec{F}$) experienced by a particle with a charge q moving with a velocity ($\vec{v}$) in the *x*-direction in a magnetic field ($\vec{B}$) applied in the *z*-direction is given by:

$$\vec{F} = q\left(\vec{E} + \vec{v}\, x\, \vec{B}\right) \tag{2.25}$$

The Hall electric field produces the Hall voltage (V_H), and the polarity of the Hall voltage reveals whether an extrinsic semiconductor is *p*-type or *n*-type (positive for *p*-type and negative for *n*-type):

$$V_H = \pm E_H w \tag{2.26}$$

To find the carrier concentration for a *p*-type semiconductor, the Hall voltage can be written as:

$$V_H = \ +E_H w = \frac{B_z\, I_x}{qdp} \tag{2.27}$$

from which, solving for hole (*p*) concentration becomes:

$$p = \frac{B_z\, I_x}{qd\ \ _H} = \frac{r}{q\, R_H} \tag{2.28}$$

where the Hall coefficient (R_H), is defined by R_{Hp} and R_{Hn} for holes and electrons as:

$$R_{Hp} = \frac{1}{qp} \tag{2.29}$$

$$R_{Hn} = -\frac{1}{qn} \tag{2.30}$$

In Equation 2.28, the Hall scattering factor (r) is used. For an *n*-type semiconductor, the same idea applies except the Hall voltage, Hall coefficient, and carrier concentration are negative. Considering the current density (J_x) and using the *x-y* configuration shown in Figure 2.4, the Hall coefficient can be written as:

$$R_H = \frac{E_y}{J_x B_z} \tag{2.31}$$

Once the majority carrier concentration is resolved, the majority carrier mobility can be determined. A quantity frequently of interest is the Hall mobility μ_H:

$$\mu_H = \frac{|R_H|}{\rho\ (B=0)} = |R_H|\sigma \tag{2.32}$$

whereas (R_H) is the Hall coefficient, $\rho\ (B = 0)$ is the electrical resistivity at zero applied magnetic field and (σ) is the conductivity. The Hall mobility differs from but relates to the conductivity mobility with Hall scattering factor (r) as:

$$\mu_H = r\mu_p \tag{2.33}$$

If a single carrier dominates the transport, only a single magnetic field Hall Effect measurement is needed. However, in the case of mixed-conduction, or multi-carrier conduction, then the method of variable magnetic field measurements is commonly employed. There is a basic strategy of characterizing multiple carrier species in a semiconductor [6] by measuring and analyzing the conductivity tensor as a function of magnetic field. Variable magnetic field analysis is used to resolve different carriers within a semiconductor, and the background will be further explained in the next sections: (1)

multi-carrier transport and (2) methods employed to characterize multi-carrier conduction in III-V materials.

2.5 Multi-Carrier Transport

This section will introduce the concept of multi-carrier transport. Multi-carrier conduction occurs due to the charge, mobility, and energy of the carriers, and their interaction with the host material is different for various energy bands (multi-band) or various conduction paths (multi-layers) in multi-layered structures. Information provided by the Hall Effect measurement at a single field and temperature will only provide the average mobility and carrier concentration of all carriers, which will not be reliable information for a multi-carrier system. Thus, variable temperature- and magnetic-field-dependent transport measurements must be employed. If the variable magnetic-field Hall Effect technique is employed at different temperatures, information on the freeze-out of carriers and scattering mechanisms can also be deduced.

The first report of multi-carrier characterization method to estimate the mobility and carrier densities of semiconductors using variable magnetic-field measurements was published in 1993 by Leslie-Pelecky *et al.* [7]. They reported separation of carrier components in single crystal narrow bandgap materials by using a variable magnetic-field Hall technique at various temperatures. Their analysis was based on energy-independent relaxation times and showed how each carrier concentration component and corresponding transverse conductivity changed with temperature.

2.5.1 Magneto-Transport

Multiple carrier types due to *n*- and *p*-doped regions, thermally generated minority carriers, and two-dimensional accumulation populations at the surface and interface layers tend to make significant contributions to the conduction process in III-V IR detector structures [8]. In multi-carrier systems, standard Hall measurements at a single magnetic field assume that only one carrier is present, which results in an average value of the carrier concentration and mobility. Therefore, magneto-transport experiments as a function of the magnetic field are needed to provide more information in such systems for each carrier type. The concept of magneto-resistance or magneto-transport was first introduced in 1956 [9] for *p*-type germanium, where the conductivity tensor elements and their dependence on the magnetic field for light and heavy holes was studied.

A Magneto-resistance measurement is well described by its name, where one can record the resistance of the material as different magnetic fields are applied. Figure 2.5 illustrates the concept of magneto-resistance: (1) an electric field across a semiconductor structure generates carrier motion, (2) application of a magnetic field perpendicular to carrier motion produces a Lorentz force which acts on those carriers, and (3) the Lorentz force deviates the carrier path and thus alters the resistance.

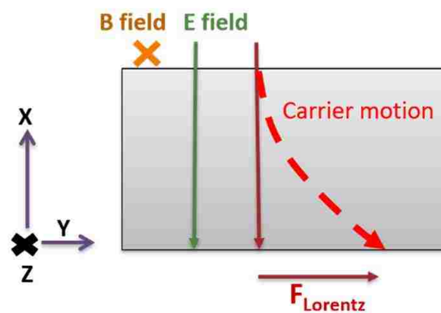

Figure 2.5: Illustration of magneto-resistance in a semiconductor.

Isotropic material such as an InAsSb alloy is described by a single mobility, where the magneto-resistance will follow the equation:

$$R(B) = R(0)(1 + \mu B^2) \tag{2.34}$$

whereas $R(B)$ is the measured resistance at a specific magnetic field (magneto-resistance), μ is the single discrete carrier mobility contributing to conduction, $R(0)$ is the zero-field resistance, and B is the applied magnetic field intensity. Equation 2.34 predicts measured resistance, $R(B)$, to be linear with respect to B^2 if a single carrier species is present [10], [11]. However, if the measured resistance is non-linear with respect to B^2, the presence of multiple carriers with distinct mobility values is theorized, as is the case with anisotropic materials like Type-II Strained Layer Superlattices (T2SLs). The anisotropy is accounted for by changing equation 2.34 to the following equation:

$$R(B) = R(0)(1 + \mu_{\parallel}\mu_{\perp} B^2) \tag{2.35}$$

whereas $\mu_{\parallel}$ is the lateral mobility, $\mu_{\perp}$ is vertical mobility, and B is the applied magnetic field intensity in the direction perpendicular to both $\mu_{\parallel}$ and $\mu_{\perp}$.

Lateral (in-plane) magneto-resistance and Hall coefficient measurements as a function of magnetic field are typically performed under the cross-sectional configuration shown in Figure 2.6 (a). The geometrical magneto-resistance configuration used for vertical transport measurements is shown in Figure 2.6 (b).

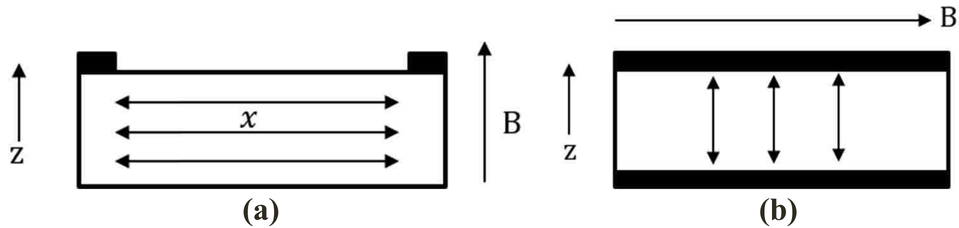

Figure 2.6: Cross-sectional illustration of configurations used for (a) lateral transport measurements to extract magneto-resistance and Hall coefficients and (b) vertical transport measurements to extract the geometrical magneto-resistance.

In Figure 2.6 (a), the current is applied in the x-direction through the top contacts and a magnetic field applied in the z-direction. In this configuration, the transverse magneto-resistivity, ρ_{xx}(B), for an isotropic material is described as:

$$\rho_{xx}(B) = \rho_{xx}(0)(1 + \mu B^2) \tag{2.36}$$

whereas $\rho_{xx}(0) = \frac{1}{qp\mu}$, is the zero-field resistivity which is similar to Equation 2.34 for an isotropic material where only a single mobility parameter describes the x, y and z- motion of a single carrier species. However, since T2SL structures are anisotropic, Equation 2.36 must be altered to account for both vertical and lateral components of mobility. Hence, the mobility parameter changes to the product of vertical and horizontal mobility. This may seem like a benign change; however, the extracted mobility from magneto-resistivity measurements is a coupled term with vertical and lateral mobility [11]. A vertical transport configuration is needed as shown in Figure 2.6 (b), where the current is applied through top and bottom contacts in the z-direction while a magnetic field is applied perpendicular to the current. The configuration shown in Figure 2.6 (b) is employed to extract magneto-resistivity $\rho_{zz}(B)$ as:

$$\rho_{zz}(B) = \rho_{zz}(0)(1 + \mu_{\parallel}\mu_{\perp}B^2) \tag{2.37}$$

It is worth noting that in 2014, Swartz *et al.* [11] decoupled vertical ($\mu_{\perp}$) and lateral ($\mu_{\parallel}$) mobilities of InAs/GaSb T2SLs by employing a magnetic field which varied in magnitude and angle orientation with the configuration shown in Figure 2.7. The current is applied in the z-direction through the top contacts and bottom contacts, where the bottom contact is on the side of the mesa. The measurement extracted $\rho_{zz}(B)$ vs. B vs. B-angle.

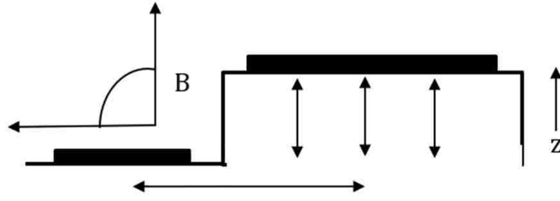

Figure 2.7: Illustration of tilting a sample to extract the magneto-resistivity in a semiconductor as a function of magnetic field magnitude and angle orientation. The current is applied in the *z*-direction through the top contacts and bottom contacts, where the bottom contact is on the side of the mesa.

2.6 Transport Limitations in Superlattices (T2SLs)

Superlattices are considered anisotropic as they possess different characteristics along the in-plane (lateral) or out-of-plane (vertical or growth) directions. T2SLs behave as an anisotropic *3-D* semiconductor in the case of miniband conduction. In miniband conduction, the effective mass determines whether the carriers transport is through miniband conduction or along the growth direction of the superlattice [12]. This anisotropy characteristic originates from different effective masses in the two directions. The tunneling probability depends on the effective mass as well as lighter carriers such as electrons can move much faster than the heavier carriers like holes, which can lead to hole localization. Olson *et al.* [13] confirmed that in InAs/GaSb T2SLs, localization of the heavy holes to the GaSb layers is realistic and that it is likely that the vertical hole transport proceeds via phonon-assisted tunneling (i.e., hopping transport) between adjacent GaSb wells.

Phonon-induced random fluctuations of atomic positions can change the transport mechanism from miniband transport to phonon-assisted tunneling, also called Wannier Stark (WS) hopping conduction, by disturbing the strict periodicity of the lattice [12]. The induced phonon-scattering enhances hopping while inhibiting miniband conduction. Phonon emission and absorption processes are temperature-dependent. Also, scattering is

proportional to the tunneling probability defined by the phonon scattering time (τ) which has a strong temperature dependence. As a result, the transport mechanism can change from miniband conduction to hopping conduction between disorder localized states as a function of temperature [14], which affects the mobility substantially. The vertical minority carrier hole transport has been recently reported in *n*-type $InAs/InAs_{0.55}Sb_{0.45}$ T2SL Heterojunction Bipolar Transistor (HBT) structures and demonstrated that at low temperatures, the holes are localized, and the dominant transport mechanism is hopping transport or phonon-assisted tunneling [15]. The cause of hole localization in the InAs/InAsSb T2SL is hypothesized by the disorder in the group-V alloy in the InAsSb hole well which leads to fluctuation of the valence-band energy. Also, vertical transport in InAs/InAsSb T2SLs photodetectors has been reported using Electron Beam Induced Current (EBIC) [16], but no particular picture was deduced on how the vertical hole transport proceeds in such material.

Localization is one of the main influential factors that affect mobility and degrades vertical carrier transport. Measurements of roughness parameters are crucial and continue to be the focus of different studies, both theoretically and experimentally [17]–[19]. For instance, Safa *et al*. [17] investigated the effect of Interface Roughness Scattering (IRS) on transport in InAs/GaSb T2SLs by calculating the lateral and vertical mobilities; results indicated that the mobility increased with increasing InAs well width. Also, carrier localization at low temperatures has been observed in minority carriers of MWIR InAs/InAsSb T2SL material when using the Time-Resolved Photoluminescence (TRPL) technique [20]. It was concluded that localization is more severe in shorter period

superlattices than the longer period ones due to disorder at the InAs/InAsSb interfaces. In thin layer superlattice structures, IRS has shown to dominate transport [18], [19], [21].

In InAs/InAsSb T2SLs, the composition of antimony (Sb) and the thickness fluctuation in the interfaces are of extreme importance in transport. Antimony segregation occurs during Molecular Beam Epitaxial (MBE) growth and has been shown to affect carrier transport [22]. Antimony tends to segregate and is more pronounced for longer wavelength structures which require higher Sb content and thinner periods and are grown at lower temperatures to enhance Sb incorporation. Antimony-segregation is interface-dependent in both InAs/InAsSb and InAs/GaSb T2SLs and leads to non-abrupt and asymmetrical interfaces. Figure 2.8 shows a schematic of the InAs/InAsSb degraded interface due to Sb segregation compared against the intended profile for a single bulk period using Scanning Tunneling Microscopy (STM) [23].

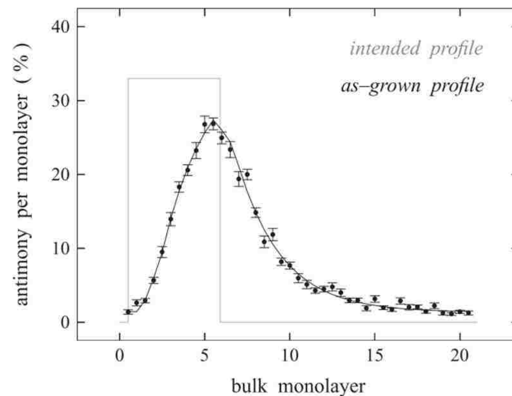

Figure 2.8: Schematic of the InAs/InAsSb degraded interface due to antimony (Sb) segregation. Intended Sb profile (gray) with compositionally abrupt interfaces, contrasted against the compositionally-graded as-grown profile (black) reconstructed from Scanning Tunneling Microscopy (STM) [23].

2.7 Lateral Transport Measurements

Mobility values are dependent on the transport direction, with lateral (in-plane) mobility exceeding mobility in the growth or vertical direction [24]. Conventional Hall Effect

measurements can obtain the lateral mobility and background carrier concentration of T2SLs when they are properly electrically isolated from other conducting layers in the structure. In 1983, the first Hall Effect and resistivity measurement on T2SLs [25] was performed to obtain electron mobilities of uniformly-doped and modulated-doped $In_{0.2}Ga_{0.8}As$/GaAs samples grown by MBE. The uniformly-doped sample mobilities were dominated by impurity scattering and only increased slightly with increasing temperature. Experimental work on superlattices before 1983 emphasized measurements of structural properties (electron microscopy, X-Ray Diffraction, Ion channeling) and optical properties(photoluminescence, absorption, and photocurrent); however, electrical transport results for superlattices were non-existent until 1983 [25].

Investigations of electrical transport of InAs/GaSb T2SLs grown on an undoped GaSb substrate have been reported [26], where resistivity and Hall coefficients were measured using Van der Pauw (VDP) configuration. To separate the effects of the GaSb substrate and the superlattice region, the superlattice was mechanically removed, and separate measurements were made on the substrate only. Their results indicated that the superlattice contributed a single electron species at 300 K with a mobility of $\sim 10^4$ cm^2/Vs. Also, a few other groups [19], [27] have published lateral transport of T2SLs on GaSb substrates. Cervera *et al*. [27] examined undoped InAs/GaSb T2SLs on semi-insulating GaAs and *n*-type GaSb substrates. For both substrates, resistivity and Hall coefficient measurements were performed under variable temperatures. The GaSb substrate was mechanically and chemically removed to compare the behavior of the superlattice carriers to the results obtained for the same structure grown on GaAs substrate. For the InAs/GaSb T2SL sample with the GaAs substrate, carrier-type switch occurred, mobility in the range

of 48 cm^2/Vs at 77 K (*p*-type), and 1720 cm^2/Vs at 300 K (*n*-type) was measured. For the InAs/GaSb T2SL sample with GaSb substrate, the mobilities were found higher at 270 cm^2/Vs at 77 K (*p*-type) and 3850 cm^2/Vs at 300 K (*n*-type). Consequently, the low mobilities in the GaAs-based T2SL sample were attributed to the high density of threading dislocations due to the superlattice and GaAs substrate lattice-mismatch.

In addition to the InAs/GaSb T2SL structures discussed, lateral transport on InAs/InAsSb superlattices grown on GaSb substrates has been investigated. Brown *et al.* [28] investigated the influence of dopant concentration on both mobility and minority carrier lifetime in Long-Wavelength Infrared (LWIR) *p*-type $InAs/InAs_{0.5}Sb_{0.5}$ T2SL material. A variable temperature- and magnetic-field dependent measurement enabled the extraction of hole and surface electron transport properties. The lateral hole mobility ranged from 800-1600 cm^2/Vs across the 40-90 K temperature range. In addition, Steenbergen *et al.* [29] reported an $InAs/InAs_{0.60}Sb_{0.40}$ superlattice structure grown on GaSb with thin AlSb barriers to determine the effect of the barriers on the electrical and optical properties of the T2SL. It was confirmed that variable magnetic field measurements are required to understand the multi-carrier behavior in such structures.

Lateral InAs/InAsSb T2SL transport can be similar to that of alloy material such as InAsSb [24], [28], [30]. The main challenge for Hall Effect measurements of small bandgap materials grown on GaSb substrates is the separation of the substrate, interface, and surface conduction channels from the actual superlattice or alloy material of interest. A previous study of $InAs_{0.58}Sb_{0.42}$ with $Al_{0.74}In_{0.26}Sb$ barrier grown on a GaSb substrate found that performing variable magnetic field measurements of the step-wise etched bulk film was necessary to assign different carriers to various regions of the structure, including

the surface, bulk, and interface [31]. The different conduction channels of the InAsSb alloy structure are shown in Figure 2.9 where electron concentrations and mobilities of the surface, bulk material ($InAs_{0.58}Sb_{0.42}$) and the barrier/bulk interface were extracted.

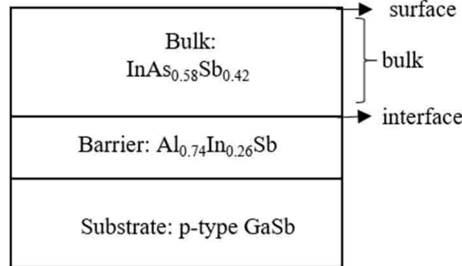

Figure 2.9: $InAs_{0.58}Sb_{0.42}$ alloy layer with $Al_{0.74}In_{0.26}Sb$ barrier layer on a GaSb substrate grown by MBE. Hall Effect measurements of a step-wise etched bulk film was necessary to assign different carriers to various regions of the structure, including the surface, bulk, and interface regions shown.

As mentioned in earlier sections, the highly anisotropic nature of the T2SL makes the correlation of lateral and vertical mobilities particularly challenging. Consequently, lateral Hall Effect measurements provide results that do not necessarily reflect the electronic vertical transport parameters of relevance to superlattice or alloy detector operation. Unlike lateral transport, vertical transport in III-V material is significantly different.

2.8 Vertical Transport Measurements

There have been several studies published on vertical transport in T2SLs over the past years under various techniques such as magneto-resistance, ultrafast optical time-of-flight, Electron Beam Induced Current (EBIC), and the quantum-efficiency technique [32]–[34]. Suchalkin *et al.* [32] employed magneto-transport in conjunction with cyclotron resonance measurements to investigate lateral and vertical electron cyclotron effective masses in InAs/GaSb T2SLs. By using these two different experimental methods, the carrier effective mass, background conductivity type, and carrier concentrations were determined.

Efforts from the University of Western Australia (UWA) group led by Umana-Membreno *et al.* [33] and the University of New Mexico (UNM), characterized for the first time the vertical transport of multiple carriers in *p*-type LWIR InAs/GaSb T2SL using magneto-transport measurements and multi-carrier analysis. Figure 2.10 shows the heterostructure employed for such measurement along with the magneto-transport measurement setup.

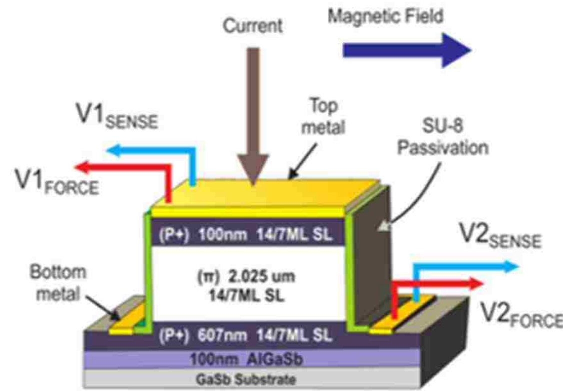

Figure 2.10: The *p*-type InAs/GaSb T2SL structure used by UWA and UNM for vertical transport measurements [33]. The structure consisted of a lightly *p*-type absorber layer sandwiched between two p^+ doped superlattice layers. The schematic of the fabricated device is shown along with the magneto-transport measurement setup.

The vertical transport results concluded that the conductivity was dominated by three distinct carriers: (1) majority holes (μ = 280 ± 27 cm^2/Vs), (2) minority electrons (μ = 2,460 ± 75 cm^2/Vs), and (3) parasitic sidewall inversion layer electrons (μ = 930 ± 55 cm^2/Vs) from 80 – 150 K. Recently, Taghipour *et al.* [35] reported the vertical transport properties of an nBp MWIR InAs/GaSb T2SL using EBIC measurements. Combined results of minority carrier lifetime in conjunction with EBIC diffusion length measurements at 80 K, extracted vertical electron mobility at ~ 200 cm^2/Vs under 20 keV beam energies.

As previously mentioned, the InAs/InAsSb T2SL has received increased attention compared to InAs/GaSb due to the longer minority carrier lifetimes. Hence, the *n*-type InAs/InAsSb T2SL is the subject of interest in this dissertation. In this system, localization of vertical minority holes has recently been revealed [15]. Although the InAs/InAsSb T2SL system has seen a recent elevated investigation of vertical transport properties, to the best of our knowledge, there have only been a few vertical transport measurements performed on such material from years 2015-2017 [15], [16], [34], emphasizing the need for further investigation. In 2015, minority carrier transport characterization of MWIR nBn $InAs/InAs_{0.81}Sb_{0.19}$ photodetectors using EBIC in conjunction with the lifetime measured via Time-Resolved Photoluminescence (TRPL) extracted a minority hole carrier mobility of 60 cm^2/Vs at 6 K [16]. In 2017, Heterojunction Bipolar Transistors (HBTs) were employed to measure the minority vertical hole mobility in undoped (*n*-type ~ 10^{15} cm^{-3}) $In_{0.97}As_{0.03}/InAs_{0.55}Sb_{0.45}$ T2SLs. Vertical hole mobilities (μ_h) are reported and found to decrease rapidly from 360 cm^2/Vs at 120 K to approximately 2 cm^2/Vs at 30 K, providing evidence of hole localization [15].

Table 2.1 at the end of this Chapter chronologically summarizes the vertical transport mobility results reported for III-V material (InAsSb alloy, InAs/GaSb, and InAs/InAsSb T2SLs) using different methods. In Table 2.1, μ_e and μ_h are the vertical ($\mu_\perp$) electron and hole mobilities, respectively. The cited works reference the original studies wherein the results were reported, to aid the reader access to such information and details.

2.9 Summary

This chapter provides the background for understanding carrier transport in semiconductor materials, specifically III-V Infrared (IR) materials. It begins with a review of drift-

diffusion, conductivity, effective mass and the Hall Effect measurement. An explanation for multiple-carrier (multi-carrier) transport is provided with an emphasizes on magneto-transport or magneto-resistance measurements. Isotropic InAsSb and Anisotropic InAs/InAsSb Type-II Strained Layer Superlattice (T2SL) properties are described, followed by a discussion of the transport limitations in T2SLs. In addition to Hall Effect measurements at a single magnetic field, the variable magnetic field method is summarized. The background section concludes with a review of the different methods employed to measure lateral and vertical transport properties in III-V IR materials, specifically anisotropic T2SL material. In Chapter 3, the experimental methods are discussed.

Table 2.1: Summary of vertical mobility ($\mu_\perp$) measurements of InAsSb alloy, InAs/GaSb and InAs/InAsSb T2SLs grown on GaSb substrates by MBE, summarized in chronological order.

Method	Material	Vertical $\mu_\perp$ (cm^2/Vs)	Temperature (K)	Ref., Year
Cyclotron Resonance	MWIR *p*-type InAs/GaSb	$\mu_e = 7.6\times10^3$	4	[32],
	LWIR *p*-type InAs/GaSb	$\mu_e = 1.5\times10^4$	4	2011
Magneto-Resistance	LWIR *p*-type InAs/GaSb	$\mu_h = 280 \pm 27$	80-150	[33],
		$\mu_e = 2.4\times10^3 \pm 75$	80-150	2012
TRDT	MWIR *n*- & *p*-type InAs/GaSb	$\mu_e = 700 \pm 80$	77	[13],
		$\mu_h = 6 \pm 5$	77	2013
Transient Response	LWIR *n*-type $InAs_{0.60}Sb_{0.40}$	$\mu_h = 800$	77	[36], 2014
EBIC/TRPL	MWIR nBn $InAs/InAs_{0.81}Sb_{0.19}$	$\mu_h = 60$	6	[16], 2015
EBIC/TRPL	MWIR nBn $InAs/InAs_{0.65}Sb_{0.35}$	$\mu_h = 1.2$	80	[34], 2017
HBT/PL	MWIR *n*-type $InAs/InAs_{0.55}Sb_{0.45}$	$\mu_h = 360$	120	[15],
		$\mu_h = 2$	30	2017
EBIC/TMR	MWIR nBp InAs/GaSb	$\mu_e = 150\text{-}200$	80	[35], 2019

2.10 References

[1] "p-n junction diagram." [Online]. Available: https://en.wikipedia.org/wiki/P–n_junction.

[2] D. K. Schroder, *Semiconductor material and device characterization*, 3rd Editio. John Wiley & Sons, Inc, 2006.

[3] H. Mirza and D. Morris, "Hall effect measurements for determining the band gap energy of undoped germanium , including the conductivity , charge carrier type , concentration and mobility for n-type and p-type doped germanium," 2013.

[4] K. K. Ng, "Physical phenomena," in *Complete Guide to Semiconductor Devices*, Wiley-IEEE Press, 2002.

[5] E. H. Hall, "On a New Action of the Magnet on Electric Currents," *Am. J. Math.*, vol. 2, no. 3, 1879.

[6] J. R. Meyer, C. a Hoffman, F. J. Bartoli, D. a Arnold, S. Sivananthan, and J. P. Fauri, "Methods for magnetotransport characterization of IR detector materials," *Semicond. Sci. Technol.*, vol. 8, no. 6S, 1993.

[7] D. L. Leslie-Pelecky, F. VanWijland, C. N. Hoff, J. A. Cowen, A. Gavrin, and C.-L. Chien, "Electron-spin-resonance linewidth of multilayered CuMn/Cu spin glasses: Residual width an therma-broadening coefficient," *Phys. Rev. B*, vol. 48, no. 10, 1993.

[8] J. Antoszewski, D. J. Seymour, L. Faraone, J. R. Meyer, and C. A. Hoffman, "Magneto-transport characterization using quantitative mobility-spectrum analysis," *J. Electron. Mater.*, vol. 24, no. 9, pp. 1255–1262, 1995.

[9] J. W. McClure, "Field dependence of magnetoconductivity," *Phys. Rev.*, vol. 101, pp. 1642–1646, 1956.

[10] V. H. J. Lippmann and F. Kuhrt, "Der Geometrieeinflub Auf Den Transversalen Magnetischen Widerstandseffekt Bei Rechteckformigen Halbleiterplatten," *Zeitschrift fur Naturforsch. - Sect. A J. Phys. Sci.*, vol. 13, no. 6, pp. 462–474, 1958.

[11] C. H. Swartz and T. H. Myers, "Method for the simultaneous determination of vertical and horizontal mobilities in superlattices," *Phys. Rev. B - Condens. Matter Mater. Phys.*, vol. 89, no. 7, pp. 1–5, 2014.

[12] A. Patanè and M. Fromhold, "Novel regimes of electron dynamics in superlattices," *Philos. Transcations R. Soc. London*, vol. 364, no. 1849, 2006.

[13] B. V. Olson, L. M. Murray, J. P. Prineas, M. E. Flatte, J. T. Olesberg, and T. F. Boggess, "All-optical measurement of vertical charge carrier transport in mid-wave infrared InAs/GaSb type-II superlattices," *Appl. Phys. Lett.*, vol. 102, no. 20, 2013.

[14] H. T. Grahn, K. Von Klitzing, K. Ploog, and G. H. Dohler, "Electrical transport in narrow-miniband semiconductor superlattices," *Phys. Rev. B*, vol. 43, no. 14, 1991.

[15] B. V. Olson *et al.*, "Vertical Hole Transport and Carrier Localization in InAs/InAs1−xSbx Type-II Superlattice Heterojunction Bipolar Transistors," *Phys. Rev. Appl.*, vol. 7, no. 2, 2017.

[16] D. Zuo *et al.*, "Direct minority carrier transport characterization of InAs / InAsSb superlattice nBn photodetectors," *Appl. Phys. Lett.*, vol. 106, no. 7, 2015.

[17] S. Safa, A. Asgari, and L. Faraone, "A study of vertical and in-plane electron mobility due to interface roughness scattering at low temperature in InAs/GaSb type-II superlattices," *J. Appl. Phys.*, vol. 114, no. 5, 2013.

[18] F. Szmulowicz, "Demonstration of interface-scattering- limited electron mobilities in InAs/GaSb superlattices," *J. Appl. Phys.*, vol. 101, no. 4, 2007.

[19] F. Szmulowicz, H. Haugan, S. Elhamri, and G. J. Brown, "Carrier mobility as a function of carrier density in type-II InAs/ GaSb superlattices," *J. Appl. Phys.*, vol. 105, no. 7, 2009.

[20] Z. . Lin, S. Liu, E. H. Steenbergen, and Y. H. Zhang, “Influence of carrier localization on minority carrier lifetime in InAs/InAsSb type-II superlattices,” *Appl. Phys. Lett.*, vol. 107, no. 20, 2015.

[21] M. J. . Hoffman, C A, “Interface Roughness Scattering in Semiconducting and semimetallic InAs-GaInSb Superlattices,” *Appl. Phys. Lett.*, vol. 63, no. 16, 1993.

[22] H. Kim, Y. Meng, J. L. Rouviére, D. Isheim, D. N. Seidman, and J. M. Zuo, “Atomic resolution mapping of interfacial intermixing and segregation in InAs/GaSb superlattices: A correlative study,” *J. Appl. Phys.*, vol. 113, no. 10, 2013.

[23] M. R. Wood *et al.*, “Monolayer-by-monolayer compositional analysis of InAs/InAsSb superlattices with cross-sectional STM,” *J. Cryst. Growth*, vol. 425, 2015.

[24] A. E. Brown, “Application of Mobility Spectrum Analysis to Modern Multi-layered IR Device Material,” University of Illinois at Chicago, 2015.

[25] I. J. Fritz, L. R. Dawson, and T. E. Zipperian, “Electron mobilities in In0.2Ga0.8As/GaAs strained-layer superlattices,” *Appl. Phys. Lett.*, vol. 43, no. 9, pp. 846–848, 1983.

[26] T. V. Chandrasekhar Rao, J. Antoszewski, J.-B. Rodriguez, E. A. Plis, S. Krishna, and L. Faraone, “Quantitative mobility spectrum analysis of carriers in GaSb/InAs/GaSb superlattice,” *J. Vac. Sci. Technol. B Microelectron. Nanom. Struct.*, vol. 26, no. 3, 2008.

[27] C. Cervera, J. B. Rodriguez, J. P. Perez, R. Chaghi, and L. Konczewicz, “Unambiguous determination of carrier concentration and mobility for InAs / GaSb superlattice photodiode optimization,” *J. Appl. Phys.*, vol. 106, no. 3, 2009.

[28] A. E. Brown, N. Baril, D. Zuo, L. A. Almeida, J. Arias, and S. Bandara, “Characterization of n-Type and p-Type Long-Wave InAs/InAsSb Superlattices,” *J. Electron. Mater.*, vol. 46, no. 9, pp. 5367–5373, 2017.

[29] E. H. Steenbergen, Z. Lin, S. Elhamri, W. C. Mitchel, Y.-H. Zhang, and R. Kaspi, “Effects of AlSb interfaces on InAs/InAsSb type-II infrared superlattice material properties,” in *Proceedings of SPIE*, 2015, vol. 9451.

[30] D. Lackner, “InAsSb / InAs STRAIN BALANCED SUPERLATTICES FOR PHOTODETECTOR APPLICATIONS,” Simon Fraser University, 2011.

[31] S. P. Svensson *et al.*, “Background and interface electron populations in InAs 0.58 Sb 0.42,” *Semicond. Sci. Technol.*, vol. 30, no. 3, p. 35018, 2015.

[32] S. Suchalkin *et al.*, “In-plane and growth direction electron cyclotron effective mass in short period InAs/GaSb semiconductor superlattices,” *J. Appl. Phys.*, vol. 110, no. 4, 2011.

[33] G. A. Umana-Membreno *et al.*, “Vertical minority carrier electron transport in p-type InAs/GaSb type-II superlattices,” *Appl. Phys. Lett.*, vol. 101, no. 25, 2012.

[34] N. Yoon *et al.*, “Modified electron beam induced current technique for in(Ga)As/InAsSb superlattice infrared detectors,” *J. Appl. Phys.*, vol. 122, no. 7, 2017.

[35] Z. Taghipour *et al.*, “Temperature-Dependent Minority-Carrier Mobility in p -Type InAs / GaSb Type-II-Superlattice Photodetectors,” *Phys. Rev. Appl.*, vol. 11, no. 024047, 2019.

[36] Y. Lin, D. Wang, D. Donetsky, and G. Kipshidze, “Transport properties of holes in bulk InAsSb and performance of barrier long-wavelength infrared detectors,” *Semicond. Sci. Technol*, vol. 29, no. 112002, 2014.

Chapter 3

Methods

3.1 Introduction

This chapter describes the primary growth technique, optical measurements, and fabrication as well as the equipment used to implement temperature- and magnetic-field-dependent transport measurements. A description of the modeling methods employed to analyze the variable-field Hall Effect data is summarized. The NRL MULTIBANDS® software employed to obtain band-diagrams plus estimate carrier concentration build-up at the interfaces of the samples is described. Multi-carrier fitting programs available are defined with an emphasizes to understand the fitting methods; Multiple-Carrier Fit (MCF) used in Chapter 4-5 and High-Resolution Mobility Spectrum Analysis (HR-MSA) used in Chapter 6.

3.2 Epitaxial Growth

Epitaxy is the growth of crystalline material whose structure and orientation are imparted by the underlying substrate's crystallinity. The word epitaxy has Greek roots, "epi" means "above", and "taxis" means "ordered." Epitaxial growth takes place due to the interaction of the material's fundamental constituents on the surface of a substrate. Molecular Beam Epitaxy (MBE) is a technique for epitaxial growth that produces high-quality materials.

Heteroepitaxy means that the substrate and material being epitaxially grown are different such as InAsSb grown on a GaSb substrate. The basic MBE technique was developed around 1968 at Bell Laboratories with important contributions added by Leo Esaki and Ray Tsu at IBM [1]. Since then, many other researchers have developed and refined the growth process. For instance, Alfred Cho was awarded the inaugural nanotechnology international prize in 2009 for work in developing MBE technology. Since then, MBE has evolved as one of the most prominent epitaxial growth techniques for advanced, high-quality semiconductor material structures for research and industrial production levels. MBE provides a high level of growth rate control, high material purity and enables the growth of complex multilayer structures with atomically abrupt interfaces.

In terms of the principles of operation, the MBE growth takes place in an ultra-high vacuum ($10^{-8} - 10^{-12}$ Torr) environment. Shutters covering the source material crucibles allow the user to finely control the thickness of the growing films: atomic layer by layer. A freshly prepared substrate is transferred to the preparation chamber which is under Ultra-High-Vacuum (UHV). Here, it is baked to remove atmospheric contaminants adhered to the exposed surfaces. Afterward, the substrate is moved to the growth chamber, which holds the group-III and group-V elemental sources or effusion cells. Once a substrate has been loaded into the growth chamber, it is heated while under group-V flux to remove the wafer's native oxide prior to growth (oxide removal). The growth rates are calibrated, and surface quality is monitored with the use of Reflection High-Energy Electron Diffraction (RHEED) in-situ and X-ray diffraction measurements post-growth. Specific growth temperatures and V/III flux ratios are utilized for each material system to yield the highest optoelectronic properties.

The MBE system provides control of the composition and doping of the structure by changing the incoming molecular beams rate, which are turned on and off abruptly by opening and closing the mechanical shutters. The beam that comes from the effusion cells consists of evaporated atoms or molecules that do not interact with each other or with other vacuum chamber gases until they reach the wafer substrate. All the multilayer structures used for this dissertation, including InAsSb alloys and InAs/InAsSb Type-II Strained Layered Superlattices (T2SLs), were grown on *n*-type GaSb substrates (Te-doped with $n \sim 5\times10^{17}$ cm^{-3}) at Sandia National Laboratories' (SNL) Veeco Gen 930 MBE system. For doping in the MBE system, the *p*-type structures were grown using beryllium (Be) while *n*-type structures were grown using silicon (Si).

3.3 Experimental Methods by Collaborators

This dissertation includes results by experimental methods that were obtained through collaborations with SNL. Details for X-Ray Diffraction and optical measurements regarding specific experimental conditions are documented in this section, while results are found in their respective chapters.

3.3.1 X-Ray Diffraction

X-Ray Diffraction (XRD) is a potent tool employed for material characterization of III-V materials. It provides information related to the strain and crystalline quality of the structures before any electrical characterization is performed. In 1913, Lawrence Bragg and his father William Henry Bragg discovered the relationship between the wavelength of an X-Ray, the angle of diffraction and the distance between internal planes of a crystal. This discovery is called Braggs Law which is known as $n\lambda = 2d\sin\theta$ and is vital in

understanding XRD, where the wavelength (λ) is proportional by integer *n*, and *d* is the distance separation between atomic crystal planes.

Figure 3.1 demonstrates the basic XRD operation: (1) the X-Rays exit a tube and are incident on the sample, (2) the X-Rays incident at an angle *θ* are diffracted from internal crystal planes into a detector, (3) the X-Rays can have destructive or constructive interference which is dependent on the material properties and the angle of incidence and diffraction (4) the inter-planar spacing of a material that is free from strain will produce a characteristic diffraction pattern.

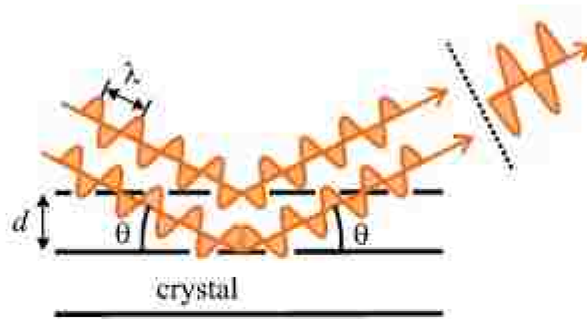

Figure 3.1: X-Ray Diffraction (XRD) through crystal lattices showing the distance (*d*) between atomic crystal planes within the material plus the angle of incidence and diffraction (*θ)* [2].

Each XRD spectrum possesses a peak pertaining to the substrate, in this case the GaSb, and a main or zeroth order peak for a superlattice or alloy material. The amount by which the peak locations differ indicate the lattice mismatch and incidentally strain in the structure. The breadth of the main peak is an indicator of the roughness of the interfaces between each layer, and thus the Full-Width-at-Half-Maximum (FWHM) is often quoted when describing the crystalline quality of material. The superlattice sample's XRD pattern includes several satellite peaks due to the numerous repeating period layers. The spacing between peaks indicates the period of the different layers which is used to confirm growth conditions and layer thicknesses. The material quality of the as-grown samples used was

evaluated via XRD measurements carried out at SNL using Philips Panalytical X'Pert3 MRD.

3.3.2 Optical Characterization

Time-Resolved Microwave Reflectance (TMR) was employed to obtain lifetime measurements at SNL. TMR utilizes a pulsed laser to excite electron-hole pairs in the InAsSb alloy and T2SL material. The excess charge creates a change of conductivity in the material, which results in a change in reflection of continuous-wave microwave radiation. Therefore, the recombination of charge carriers can be temporally monitored by measuring the change in power of reflected microwave radiation after optical excitation. The TMR operating principles are discussed in detail elsewhere [3], and a schematic of the setup employed at SNL is shown in Figure 3.2.

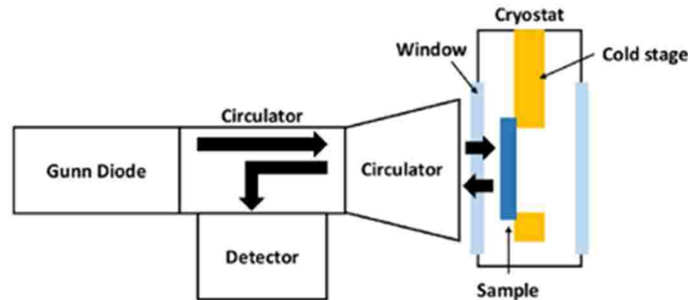

Figure 3.2: Block diagram of microwave apparatus used for Time-Resolved Microwave Reflectance (TMR) and frequency-modulated conductance [3].

Photoluminescence (PL) was done using double modulation Fourier-Transform Infrared Spectroscopy (FTIR) with a pump laser at 1550 nm and a 2.4 μm long pass filter. A skewed gaussian was employed to fit the PL spectra. To obtain PL and Lifetime (LT) wafer maps, measurements were obtained in 5mm increments.

TMR at 94 GHz was employed to obtain LT wafer maps, with a pump laser at 1535 nm. The TMR signal was averaged over 5,000-30,000 waveforms to generate the final data

to be fitted automatically. An example of the PL and LT wafer maps and histograms provided by SNL for each sample is shown in Figure 3.3. The histograms display the peak wavelength, or lifetime (τ) for a sample. Both, the PL and LT measurements were performed at SNL. The LT data is used to calculate the diffusion length in the lateral measurements discussed in Chapter 5. PL data is employed to confirm Mid-Wave Infrared (MWIR) operation and compare their respective modeled NRL MULTIBANDS® bandgap information.

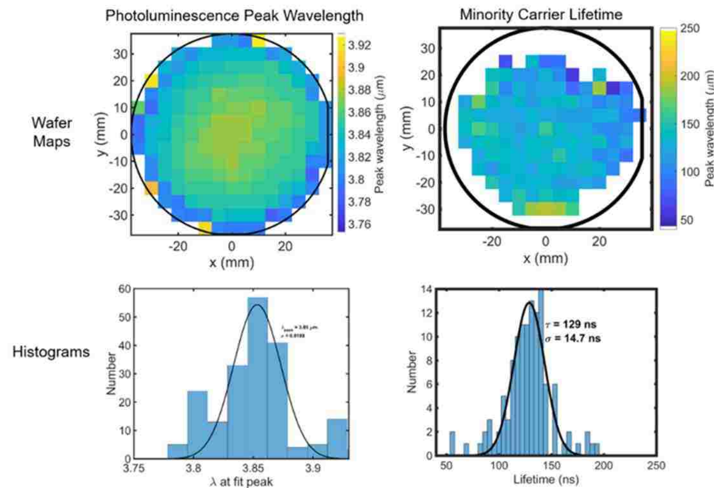

Figure 3.3: Wafer maps and histograms of the optical characterization used for photoluminescence (PL) and lifetime (LT) for undoped InAsSb sample. To obtain PL and LT maps, measurements are taken in 5mm steps. The histograms display the peak wavelength, or the lifetime of every measurement done across the whole wafer. **Provided by SNL*

3.4 Device Fabrication Overview

Fabrication is required before electrical characterization of the samples. This process was performed at the fabrication site at SNL's Center for Integrated Nano Technologies (CINT). Standard photolithography is used to define the patterns for mesa wet-etch and deposit contact metallization. The basic procedure for Van der Pauw (VDP) fabrication is

emphasized in this section. Detailed device fabrication for lateral and vertical transport samples is provided in Chapters 4, 5 (lateral transport) and 6 (vertical transport).

Wet-etching was employed to define mesas using a citric acid based etch (citric acid: H_2O_2(30%) = 5:1) at room temperature. The citric acid based solution selectively etches InAsSb or InAs/InAsSb T2SLs against AlAsSb layers as described in further detail by Dier *et al*. [4]. The anhydrous citric acid was mixed overnight with a composition of 1 ml H_2O with 1 g of citric acid crystals. The mesa thicknesses were confirmed using an Alpha-Step 500. No surface passivation treatment was used for any of the samples in this work.

One of the main challenges of VDP fabrication is to make good electrical ohmic contacts. Indium metal is employed for Hall Effect measurements in III-V materials since the contacts can be positioned on the four corners of the sample in VDP geometry configuration without patterning [5], [6]. For the materials in this work, photolithography patterning was used to create more uniform ohmic contacts on the samples, then, wire-bonding was utilized for external connection. For both *p*- and *n*-type InAsSb plus *n*-type InAs/InAsSb T2SLs, the ohmic top contacts were deposited by e-beam evaporation using Ti/Pt/Au (500/500/3000Å). This combination has proven to make good ohmic contacts in *n*- and *p*-type InAs and T2SL material [7]. It is essential to perform a pre-metallization acid dip in (1:10) (HCl:H_2O) right before the metal deposition to remove native oxide that builds on the surface of the sample [8].

For vertical transport samples, a mechanical lapping tool was employed to thin the GaSb substrate followed by a chemical wet-etch using an HF solution composed of (2:1:20) (HF:H_20_2:H_20) at room temperature. Upon removal of the GaSb substrate, AlAsSb etch-

stop, and GaSb buffer layers via chemical wet-etch, the T2SL material becomes freestanding. It then can be bonded to an alternative host substrate (sapphire) coated with metal using Au-Au cold welding technique commonly used in solar cells [9], [10]. In Chapter 6, more details about the substrate removal technique employed for this dissertation work is provided.

3.5 Experimental

3.5.1 Magneto-Transport Measurement Equipment

As mentioned in the fabrication section, all samples were contacted using Ti/Pt/Au, mounted and wire-bonded onto chip carriers acquired from Spectrum Semiconductors (LCC03263 and LCC02861). The Hall Effect measurement equipment used for this work is the LakeShore Cryotronics Model 9509 Hall Measurement System (HMS) equipped with a 9-Tesla superconducting magnet. The HMS setup used is located at Kirtland Air Force Research Laboratory (AFRL) and is shown in Figure 3.4.

Figure 3.4: LakeShore Cryotronics Hall Measurement System, (a) Model 9509 cryogenic dewar with sample insert mounted in the dewar, (b) electronics equipment rack.

In Figure 3.4 (a), the cryogenic liquid helium (LHe) 40-Liter dewar is pictured while the standard Model 9500 Flow cryostat sample insert is mounted in the dewar. The sample space in the dewar is pumped through a solenoid valve assembly attached to a vacuum pump. The system dewar hosts a superconducting solenoid magnet that sits on the bottom. The magnet consists of niobium-titanium (NbTi) embedded in a copper matrix. Superconducting magnet needs to be kept under cryogenic temperatures for operation. Stable operation at a range of temperatures is made possible by balancing the cooling power provided by the LHe taken from the surrounding dewar against two heater circuits powered by a temperature controller. The magnetic field direction is stationary for this setup and is, therefore, always applied in the vertical direction (e.g., parallel to the dewar sidewalls). A needle valve between the helium reservoir and the sample space is used to regulate the gas flow from the helium boil-off. The following descriptions summarize the components located on the electronics equipment rack pictured in Figure 3.4 (b) of the HMS System:

(1) LakeShore 625 Magnetic Power Supply (MPS): controls the magnetic field strength (0-9 Tesla). The Model 625 provides two analog outputs to monitor the output current and voltage.

(2) LakeShore 775 switch matrix: runs to the triaxial connectors which are connected to the indium posts located on the sample holder.

(3) LakeShore 241 Liquid Helium Level Monitor: a microcontroller-based instrument which measures the level of liquid helium using a hollow sensor with a superconductive Niobium-Titanium (NbTi) wire within it. The sensor, equipped with small liquid access holes, is placed in the cryogenic dewar.

(4) Model 340 Temperature Controller: used to control the temperature in a range from 2 K to 400 K.

(5) The electrical setup: consists of a Keithley 220 programmable current source, Keithley 485 autoranging picoammeter, and a Keithley 2182A nanovoltmeter.

(6) The HMS LakeShore V3.10 software controls the electrical equipment for each run and provides resistivity, carrier concentration, Current-Voltage (I-V) characterization, and other Hall properties. Both, temperature and magnetic field can be modified during each measurement and can be programmed to run. The variable field data is recorded for further processing with multi-carrier analysis. For I-V characterization, the system adjusts the current source level and measures the voltage output, usually across the same contacts as R_{1212}; R_{2323}; R_{3434}; R_{4141} using a $R_{I+I-V+V-}$ configuration, where R, V and I represent resistance, voltage, and current. Linear I-V characteristics are crucial to confirm ohmic contacts; an example of an I-V measurement provided by the HMS V3.10 software is shown in Figure 3.5.

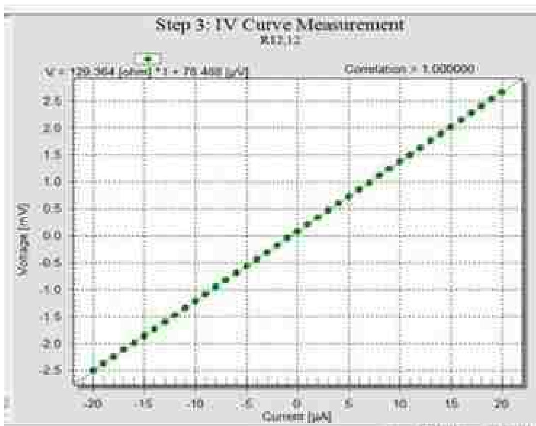

Figure 3.5: HMS LakeShore software Current-Voltage (I-V) measurement taken by adjusting the current source level (positive and negative polarities) and measuring the voltage output.

The system takes voltage measurements at both polarities of the same current (positive and negative values) and then calculates the slope from the two measurements to obtain the resistance as shown in Figure 3.5. The LakeShore software obtains the slope of the I-V relationship, or resistance value, via a pair of contacts. The contacts were verified to be ohmic for all temperatures of interest in each sample.

(7) Advanced Technology Liquefier (ATL160): is not pictured but is employed to recover the LHe boil-off from the HMS dewar and provides a Helium Recovery of 80-90%. It can hold up to 160 liters and was used to transfer LHe into the system throughout this work.

The number and magnitude of the magnetic field points are carefully chosen as too many magnetic field points can complicate the fitting process while too few can lose valuable information [11]. The Hall Effect measurement settings employed for this work contain 52 magnetic field values from -9-T to 9-T and temperatures ranging from 15 - 390 K. Further details for the LakeShore HMS system can be found in the reference [12]. For this work, two types of electrical configurations were used for lateral and vertical transport measurements. This is the subject in the next sections.

3.5.2 Lateral Transport Measurement

In 1958, Van der Pauw [13] simplified Hall bar fabrication and measurements with the 4-contact Van der Pauw (VDP) geometry. Lateral Hall Effect measurements use other different types of sample geometries such as Greek cross and Hall Bar. Greek cross configuration has shown to be better than VDP in terms of effects associated with contacts. However, for narrow bandgap materials, they demand very good sidewall passivation

otherwise the sidewall leakage creates discrepancies in the resistivity and Hall voltages measured, and at this point, it becomes harder to apply any multi-carrier fit analysis. Hence, a 4-contact VDP configuration, which is one of the most popular techniques for semiconductor samples was employed in this work.

The VDP technique requires four small ohmic contacts to be positioned at each corner of the square test structure. As emphasized, high-quality ohmic contacts are vital, and these must be positioned exactly at the corners of the sample. To ensure that this requirement was satisfied, Layout Editor (LE) was used to create a set of processing masks for the fabrication of the lateral transport samples. Lateral dimension of metal contacts was made less than 1/10th of the lateral dimension of the sample (e.g., 0.3 mm contacts for a 5 mm sample). Contact offsets of 15 or 25 µm are an option in the mask to account for any wet-etching uniformities of the mesa sidewalls. The 5 mm x 5 mm *n*-type InAs/InAsSb T2SL sample with four 300 µm ohmic contacts placed on the perimeter of the sample, was aligned using the alignment marks shown in Figure 3.6(a). Figure 3.6 (b) shows one corner of the sample patterned with a 15 µm contact offset.

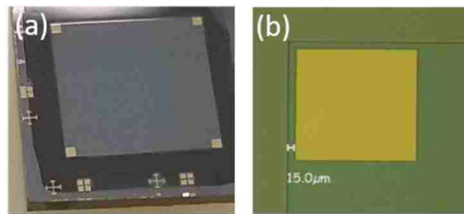

Figure 3.6: (a) Van der Pauw (VDP) patterned *n*-type InAs/InAsSb 5 mm x 5 mm sample with four 300 µm ohmic contacts placed on the perimeter of the sample with alignment marks, (b) Microscope picture shows one corner of the sample patterned with a 15 µm contact offset.

Using the VDP method, resistivity measurements are taken around the periphery of the sample before Hall voltage measurements are performed. These measurements are very similar in that they both use four contacts and involve forcing a current and sensing a

voltage; however, there are some key underlying differences. In the Hall Effect measurement, a current is injected across the diagonal of the sample, and then a voltage is measured on the opposite diagonal while a perpendicular magnetic field is imposed. In resistivity measurements, a current is forced on the adjacent contacts, and a voltage is measured on opposing adjacent contacts. To obtain reliable results and minimize any measurement errors with the VDP geometry used for lateral transport measurements reported in this work, several tests were performed which involved using two Hall Effect configurations and reversing source current and magnetic field polarity.

The sample holder, or sample insert, of the LakeShore HMS system with a sample mounted and wire-bonded to a chip carrier is shown in Figure 3.7. A sapphire plate is employed to separate the copper sample holder from the chip carrier. Six indium posts are surrounding the circular copper mount and are soldered to the appropriate contacts. For lateral transport measurements, a magnetic field is applied parallel to the growth axis.

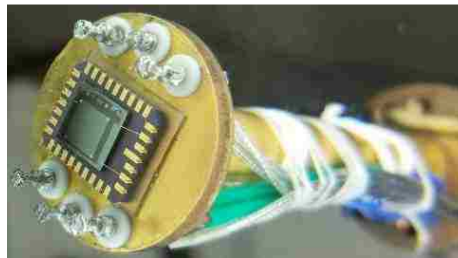

Figure 3.7: Sample holder stick (or sample insert) showing a sample mounted and wire-bonded to a chip carrier. A sapphire plate is used to separate the copper sample holder from the chip carrier. Six indium posts are surrounding the circular copper mount and soldered to the appropriate contacts. For lateral transport measurements, a magnetic field is applied parallel to the growth axis.

The chip carrier is mounted on a sapphire plate using rubber cement to avoid contact with the circular copper mount. As shown, the sample mount supports up to six contacts which can be employed for VDP, Greek Cross, and 6-contact Hall Bar configurations.

Temperature control is achieved by using two sensor readings that couple to resistive heating elements. The two sensor and resistors are located on the bottom of the circular sample holder and below a temperature block located on the sample insert. Using the VDP configuration, the lateral transport measurements extract the sheet resistance (R_s) and the Hall Coefficient (R_H) as a function of magnetic field (B).

3.5.3 Vertical Transport Measurement

For vertical transport measurements, a geometrical magneto-resistance approach is employed. The method measures sheet resistance (R_s) as a function of magnetic field (B). Similarly, to lateral transport measurements, the samples used for vertical transport are also mounted onto a sample chip carrier and wire-bonded. However, unlike the lateral transport measurement that contains four contacts (VDP geometry) on the surface of the sample, the vertical configuration uses a top and bottom contact as shown in Figure 3.8. For the bottom contact, metal-coated sapphire was employed.

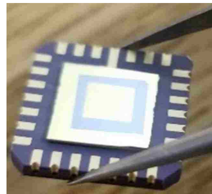

Figure 3.8: Vertical transport sample with top contact and metal-coated sapphire which acts as the bottom contact, sample is mounted on a non-magnetic chip carrier (LCC02861).

Lithography masks were utilized to pattern the sample mesa and bottom contact before any substrate removal. After substrate removal, the top contact application was performed using a shadow mask. A sapphire carrier coated with Ti/Pt/Au was used as a host substrate. Au-Au cold-welding technique was employed to bond the sample to the metal-coated sapphire carrier. Documented processing details with pictures can be found

in Chapter 6, Section 6.4.3, which further describes the fabrication of the Metal-Semiconductor-Metal (MSM) magneto-resistance test-structures.

For geometrical magneto-resistance measurements, the resistance ($R_{I+I-V+V-}$) is extracted as a function of magnetic field. The experimental data was obtained by measuring resistance (R) using top (1,2) and bottom (3,4) contact configurations. The four resistance configurations ($R_{I+I-V+V-}$) were measured by applying a 700 μA current and sensing the voltage; the four resistances are thus labeled R_{1324}, R_{1423}, R_{2314}, R_{2413}. For vertical transport measurements, the applied field must be perpendicular to the growth axis. Hence, since the HMS system is unable to alter the angle that the magnetic field is applied, a different sample mount was used to reorient the sample which in effect changes the magnetic field angle of incidence. The copper sample mount with four indium posts is shown in Figure 3.9 (a) and called the vertical transport sample holder.

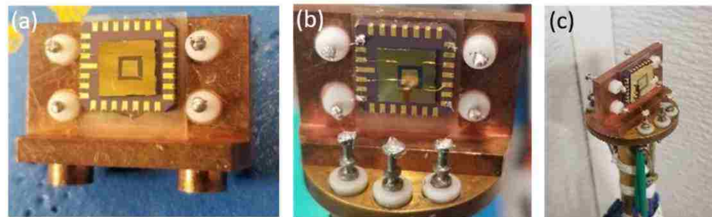

Figure 3.9: (a) The vertical transport sample holder contains four indium posts which aid when soldering to the contacts located on the chip carrier; (b)-(c) vertical transport sample holder mounted to the HMS pedestal. For vertical transport measurements, the magnetic field is applied perpendicular to the growth axis.

The vertical transport sample holder screws onto the HMS sample pedestal as shown in Figure 3.9 (b) and (c). The vertical transport sample holder contains four indium posts which aid when soldering to the contacts located on the chip carrier. Finally, four of the indium posts on the HMS sample pedestal are soldered to the indium posts located on the vertical transport sample holder.

Vertical transport mobility is obtained from magneto-resistance measurements of an InAs/InAsSb T2SL sample using High-Resolution Mobility Spectrum Analysis (HR-MSA). Access to HR-MSA was facilitated via collaboration links with the Microelectronic Research Group, headed by Prof. Faraone, at the University of Western Australia (UWA). Further details of the electrical characterization employed for vertical transport measurements is provided in Chapter 6, Section 6.4.4.

3.6 Modeling

3.6.1 NRL MULTIBANDS®

The first critical step in understanding infrared detectors transport properties and building reliable theoretical models to explain experimentally observed phenomena is electronic bandstructure knowledge for each specific sample type. Hence, comparison of experimental results to bandstructure theory is crucial. The 8x8 k·p perturbation method is a commonly utilized method. Although its application to bulk semiconductors is straightforward, modeling periodic structures such as superlattices is still under further improvement. Bandstructure calculations are performed using the Naval Research Laboratory (NRL) MULTIBANDS® 8x8 k·p perturbation theory software [14] which is an approximated semi-empirical approach employed for calculating the semiconductor's bandstructure and other optical properties.

The k·p perturbation theory method is commonly utilized in transport and optical properties studies in common semiconductors [15]. NRL MULTIBANDS® extracts the effective medium band properties such as the effective masses in lateral and vertical directions as well as lateral bandgaps. The eigenstates of the material are calculated using the z-dependent envelope-function approximations while the bandgap is defined as the

energy separation of the lowest energy electron and hole sub-bands. In addition to the k·p model, NRL MULTIBANDS® includes a drift-diffusion model for parabolic bands that use Fermi-Dirac statistics to calculate carrier concentrations [14].

3.6.2 Multi-Carrier Analysis

Mobility Spectrum Analysis (MSA) and Multiple Carrier Fit (MCF) are extensively employed for analyzing variable magnetic-field Hall Effect data [16], [17] to acquire the concentration and mobility of each carrier species present in the sample. Although conventional Hall Effect analysis at a single magnetic field is routinely employed to characterize transport properties in III-V materials, the need for a multi-carrier analysis in alloy material, as well as superlattices, is evident when the magnetic-field-dependent resistivity and Hall coefficient characteristics indicate the presence of more than one carrier species. There are various models available to analyze the experimental data in a multi-carrier conduction system. Using the experimentally measured resistivity and Hall coefficient data gathered from temperature- and magnetic-field-dependent transport measurements, one can deduct additional information about all present carriers. To better comprehend multi-carrier analysis and the different contributions of the conductivity, an introduction of conductivity or resistivity tensors is provided in Section 3.6.2.1.

3.6.2.1 Conductivity Tensors

Magneto-resistance measurements extract the changes in the components of the conductivity tensors of a material caused by an applied magnetic field. The conductivity tensors of a multi-carrier system and the importance of understanding them for variable-magnetic-field Hall Effect measurements are presented in this section.

A VDP sample for lateral transport measurements consisting of a thin film of width (w) in the x-y plane with a perpendicular magnetic field applied (z-direction) is shown in Figure 3.10. The magnetic field (B) is applied parallel to the z-direction (i.e., $B = (0,0, B_z)$), while the current (I_x) is driven through the sample in the x-direction. Then, the voltage drop across the contacts is measured so that the electric fields in the x-y plane (E_x and E_y) can be deduced as $E_x = V_x/w$ and $E_y = V_y/w$. The total conduction from the current carriers in the x-y plane results in a current density (J) which can be described by a two-dimensional conductivity tensor (σ). The conductivity tensor shows that, with an applied magnetic field, the total current density no longer flows parallel to the applied electric field (E_x). Instead, it now contains both x and y components (J_x and J_y).

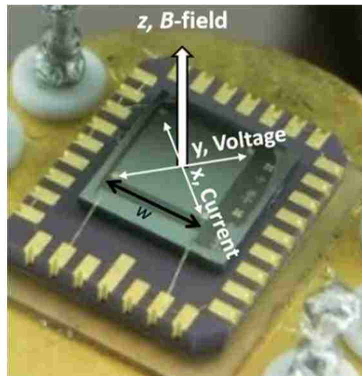

Figure 3.10: Geometry of a VDP sample in the x-y plane with a perpendicular magnetic field applied (z-direction). The magnetic field B is applied parallel to the z-direction (i.e., $B = (0,0, B_z)$) while the current I_x is driven through the sample in the x-direction.

The current carriers flowing in the y-direction will experience a Lorentz force produced by the magnetic field. This backflow of carriers will act to change the apparent resistivity; this is known as the magneto-resistance. The application of the magnetic field makes the conductivity anisotropic; which means that the conductivity, or resistivity, becomes a tensor, rather than a scalar. The current density ($\vec{J}$) is related to the conductivity tensor and applied electric field ($\vec{E}$) as:

$$\vec{J} = \sigma\vec{E} \tag{3.1}$$

In the *x-y* plane, the conductivity tensor components can be written as:

$$\begin{pmatrix} J_x \\ J_y \end{pmatrix} = \begin{pmatrix} \sigma_{xx} & \sigma_{yx} \\ \sigma_{xy} & \sigma_{yy} \end{pmatrix} \begin{pmatrix} E_x \\ E_y \end{pmatrix} = \begin{pmatrix} \sigma_{xx} & \sigma_{xy} \\ -\sigma_{xy} & \sigma_{xx} \end{pmatrix} \begin{pmatrix} E_x \\ E_y \end{pmatrix} \tag{3.2}$$

whereas σ_{xx} is the longitudinal component of the conductivity tensor and σ_{xy} is the transverse component of the conductivity tensor. As mentioned, the lateral transport experiments conducted in this dissertation measure voltage drop in the *x-y* plane between two pairs of contacts. Since the current is forced along the *x*-direction, then the electric field will have components in both *x*- and *y*- directions. Hence, the resistivity tensor component ($\rho_{xx}(B)$) can be described as a function of magnetic field as:

$$\rho_{xx}(B) = \frac{E_y}{J_x} \tag{3.3}$$

whereas E_y is the electric field in the *y*-direction and J_x is the applied magnetic field current density in the *x*-direction.

A lateral transport measurement obtains the resistivity (ρ_{xx}) and the Hall coefficient (R_H) as a function of magnetic field and temperature. The extracted experimental data allows a fit of the longitudinal and transverse components of the conductivity(resistivity) tensors, this relationship is discussed in section 3.6.2.2 for Multi-Carrier Fit (MCF) and section 3.6.2.3 for Mobility Spectrum Analysis (MSA).

3.6.2.2 Multi-Carrier Fit

Multi-Carrier Fit (MCF) analysis has been extensively utilized for analyzing variable magnetic-field data. In MCF, results can be expressed only in terms of a discrete number of carrier species with discrete mobilities [18]. Basically, MCF performs a least-squares fit

of the experimentally measured data to extract the number of carriers present. The disadvantage of the MCF technique is that it requires a prior guess of the number of electron and hole carriers present in the sample. By performing a least-squares fit simultaneously to the conductivity tensors as a function of applied magnetic field, the extraction of a discrete set of contributing electrical carriers at each temperature can be resolved. In MCF, the experimental Hall coefficient ($\boldsymbol{R_H}$) and resistivity ($\boldsymbol{\rho_{xx}}$) are related to the longitudinal and transverse conductivity tensor components ($\boldsymbol{\sigma_{xx}}$ and $\boldsymbol{\sigma_{xy}}$) via Equations 3.4 and 3.5:

$$R_H(B) = \frac{\sigma_{xy}/B}{\sigma_{xx}^2 + \sigma_{xy}^2} \tag{3.4}$$

$$\rho_{xx}(B) = \frac{\sigma_{xx}}{\sigma_{xx}^2 + \sigma_{xy}^2} \tag{3.5}$$

If multiple carriers are present, each with discrete mobilities μ_i, then the conductivities of the individual carriers are additive, and the values of the conductivity tensors (of an *N*-carrier system) are given by the summation expressions given in Equations 3.6 and 3.7:

$$\sigma_{xx}(B) = \sum_{i=1}^{N} \frac{q n_i \mu_i}{1+\mu_i^2 B^2} \tag{3.6}$$

$$\sigma_{xy}(B) = \sum_{i=1}^{N} S_i \frac{q n_i \mu_i^2 B}{1+\mu_i^2 B^2} \tag{3.7}$$

whereas S_i is +1 for holes and -1 for electrons. Note that in Equations 3.6 and 3.7, it is the denominator terms which primarily differentiates the contributions from individual carriers in the variable-field measurements and determines the overall shape of the measured R_H and ρ_{xx} or consequently the σ_{xx} and σ_{xy} curves. The denominator in Equations 3.6 and 3.7, manifest with the contributions from the higher mobility carriers being the first to quench with the increasing magnetic field (*i.e.,* $\mu B >> 1$), causing those carriers to have less influence on the measured Hall coefficient and resistivity [18].

Higher magnetic fields ultimately enable the determination of the lower mobility carriers contributing to conduction that are otherwise unobservable [19]. The maximum magnetic field strength of the Hall Effect measurement system becomes essential in the analysis; it specifically dictates the lowest possible measurable mobility.

A maximum of eight carrier species was imposed on the fitting algorithm employed for the lateral transport work. However, the LakeShore MCF routine always returned fewer than eight carriers which are specified for each experiment set in their respective chapters. Due to the reliability of the MCF to analyze lateral transport data and identify low mobility carriers in our samples, all lateral transport experimental data analysis presented in this dissertation was undertaken using MCF technique. The LakeShore Quantitative Mobility Spectrum Analysis (QMSA) was employed in Chapter 4, Section 4.2.3, but due to the system's magnetic field intensity limitations, resolving low mobility carriers was impossible. For vertical transport measurements, the High-Resolution Mobility Spectrum Analysis (HR-MSA) was facilitated via collaboration links with the Microelectronic Research Group at UWA. Mobility Spectrum Analysis (MSA) techniques are summarized in the next section.

3.6.2.3 Mobility Spectrum Analysis

The downside of the MCF technique is that it requires prior knowledge of the number and the type carriers (electrons and holes), and an initial guess is required to fit the experimental data. In an effort to overcome the deficiencies of MCF, Beck and Anderson [16] proposed the Mobility Spectrum Analysis (MSA) technique, based on earlier work by McClure *et al.* [20], as a method for analyzing and interpreting magnetic field-dependent Hall Effect data. Using generalized integral transforms representation, MSA analyses the longitudinal

and transverse conductivity tensor components in the magnetic-field domain which are calculated from the measured magnetic-field-dependent resistivity ($\rho_{xx}(B)$) and Hall resistivity ($\rho_{xy}(B) = BR_H(B)$). The analysis, effectively a solution to an inverse transform problem, yields the sample conductivity in the mobility domain. Although in principle the "mobility" transform are continuous functions, computational expedience requires the representation in a discretized form, as expressed in Equations 3.8 and 3.9, in which, *N* represents the total number of "analysis" grid points in the mobility space.

$$\sigma_{xx}(B_j) = \int_0^\infty \frac{s_p(\mu)+s_n(\mu)}{1+\mu^2 B^2} d\mu = \sum_{\mathrm{i=1}}^{\mathrm{N}} \frac{S_p(\mu_i)+S_n(\mu_i)}{1+\mu_i{}^2 B_j{}^2} \tag{3.8}$$

$$\sigma_{xy}(B_j) = \int_0^\infty \frac{[s_p(\mu)+s_n(\mu)]\mu B}{1+\mu^2 B^2} d\mu = \sum_{\mathrm{i=1}}^{\mathrm{N}} \frac{[S_p(\mu_i)+S_n(\mu_i)]\mu_i B}{1+\mu_i{}^2 B^2} \tag{3.9}$$

In equations 3.8 and 3.9, $s_n(\mu_i)$ and $s_p(\mu_i)$ are the mobility-dependent conductivity density functions for electrons and holes, respectively, μ_i is the carrier mobility, and q and B_j are the electron charge and the specific magnetic field intensity, respectively. Note that the density functional forms in Equations 3.8 and 3.9 are represented in lower case literals, whereas in the discretized electron and hole mobility spectra are presented in upper case literal. For representational convenience, the electron and hole conductivity in the "mobility spectrum" representation are defined as:

$$S_n(\mu_i) = \int_{\mu_i}^{\mu_i+d\mu} s_n(\mu)\, d\mu \; = q\, n(\mu_i)\, \mu_i, \tag{3.10}$$

$$S_p(\mu_i) = \int_{\mu_i}^{\mu_i+d\mu} s_p(\mu)\, d\mu \; = q\, p(\mu_i)\, \mu_i, \tag{3.11}$$

where $n(\mu_i)$ and $p(\mu_i)$ represent the sheet density of electrons and holes, respectively. Beck and Anderson [16] transformed the integrals over k space to integrals over the mobility and introduced the conductivity density functions $s_{n,p}(\mu_i)$. In their solution to the

mobility transform problem, the experimental Hall Effect and resistivity measurements are deemed not to uniquely define $S_{n,p}(\mu_i)$, but yet the solution advanced by Beck and Anderson which provides a unique envelope (or upper-bound) that contains all physical sets of solutions [11]**.** The Beck and Anderson approach is the first of many subsequent methods to solve the mobility transform problem (Equations 3.8 and 3.9). In general, such methods are now commonly referred to as MSA.

Meyer *et al*. [21] developed a Hybrid-Mixed-Conduction Analysis (HMCA) procedure. In HMCA, the number of carriers and their densities plus mobilities are extracted using Beck-Anderson MSA envelope approach, and then the MCF analysis is used to obtain a quantitative fit. Similarly, Brugger and Kosser reported another technique for combining MSA and MCF [22]. These quantitative methods sought to combine the meaningful spectral representation of MSA with the quantitative accuracy of conventional least-squares MCF optimization procedures [18].

As a product of a collaborative project between UWA and the Naval Research Laboratory (NRL), Antoszewski *et al.* [18] reported the development of an MSA technique known as Quantitative Mobility Spectrum Analysis (QMSA). QMSA represents a significant improvement in the implementation of MSA, as it incorporates the iterative procedure proposed by Dziuba and Gorska, [23] to find a solution that uses the Beck-Anderson MSA as a 'first trial' function to obtain a mobility spectrum, and thus gain information about the carrier species present in the sample. The final output from QMSA is a spectrum of conductivity as a function of mobility.

QMSA was licensed and made available commercially by LakeShore Cryotronics, because it was widely employed to study III-V semiconductors. Using the feedback from

the characterization of different III-V materials, Meyer *et al.* [24] reported a further optimized the QMSA technique. In 1998, improved-Quantitative Mobility Spectrum Analysis (i-QMSA) procedure was reported by Vurgaftman *et al.* [19]. The i-QMSA had the dual purpose of reducing the error in the fit to the conductivity tensors and simplifying the shape of the spectra. Rao *et al*. [25] employed the i-QMSA procedure to analyze magnetic-field-dependent measurements, and thus discriminate between carriers in the substrate and those in the superlattice layer.

A few different approaches to MSA-based algorithms were proposed in the 2000s. Several variants of the Maximum-Entropy Mobility Spectrum Analysis (ME-MSA) [26] that computes the mobility spectra using a maximum-entropy approach to determine the most feasible solution. In 2010, Umana-Membreno *et al.* [27] introduced the High-Resolution Mobility Spectrum Analysis (HR-MSA). In comparison to previously reported MSA approaches, HR-MSA does not interpolate the measured conductivity tensor components and does not use their derivatives; thus it is less sensitive to noise in the measured data and has demonstrated improved robustness and higher resolution than the iQMSA [28]. As with other MSA approaches, the aim of the HR-MSA algorithm is to find the electron and hole spectral functions $S_n(\mu_i)$ and $S_p(\mu_i)$, as defined by Equation 3.10 and 3.11, that provide the best fit to the experimental data ($\sigma_{xx}(B_j)$ and $\sigma_{xy}(B_j)$).

An example of the sheet conductivity in the carrier mobility domain as extracted from mobility spectrum analysis techniques (e.g., HR-MSA) is provided in Figure 3.11, in which each conductivity peak represents a distinct carrier species in a sample. Thus, from a magnetic-field-dependent Hall Effect measurement, electron and hole spectra can be unambiguously determined.

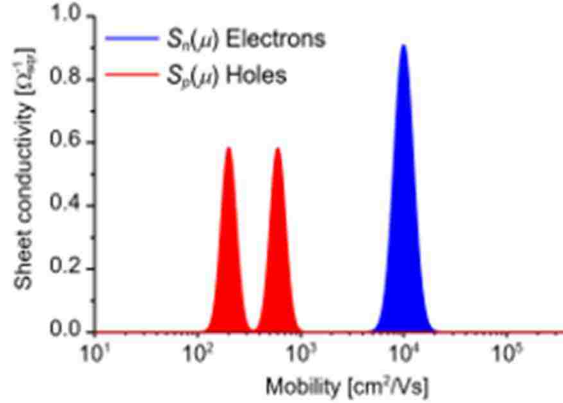

Figure 3.11: Sheet conductivity in the carrier mobility domain as extracted from mobility spectrum analysis techniques (e.g., HR-MSA), in which each peak conductivity represents a distinct carrier species. **Image adapted from* [28].

Several tests have demonstrated that HR-MSA can resolve closely spaced mobility peaks arising from separate carriers [28]. An optimized magneto-resistance version of HR-MSA was developed to analyze the geometrical magneto-resistance characteristics, and extract vertical transport parameters, from *p*-type InAs/GaSb Type-II Superlattices for Long-Wavelength Infrared (LWIR) detectors, and was later instrumental in providing experimental evidence of sub-band carrier modulation effects in nanostructured silicon-on-insulator field-effect transistors [29], [30].

A limitation of multi-carrier analysis algorithms such as MCF, QMSA and HR-MSA, is that the vertical and horizontal mobilities cannot be decoupled; such algorithms extract effective mobilities in which the true vertical and horizontal mobilities are convolved. Without properly decoupling the vertical and lateral mobilities, a geometric average of the two mobilities is extracted, which possibly results in an inaccurate vertical mobility estimation [31]. Due to the sophistication of the HR-MSA algorithm and the ability to extract vertical mobility in anisotropic material such as T2SL, the vertical transport mobilities presented in Chapter 6 of this dissertation were extracted using HR-MSA as a collaborative effort with UWA and mentorship of Dr. Gilberto Umana-

Membreno. To finalize, Table 3.1 summarizes the MSA fitting methods in chronological order and contribution.

Table 3.1. Summary of the history of Mobility Spectrum Analysis (MSA) in chronological order and contribution.

Year	Author & Reference	Contribution
1956	McClure *et al*. [20]	Derives equations from first principles
1987	Beck & Anderson [16]	Introduces the Mobility Spectrum Analysis (MSA)
1992	Dziuba & Gorska [17]	First iterative solution of MSA
1993	Meyer *et al.* [21]	Hybrid Mix Conduction Analysis (HMCA)
1995	Brugger & Kosser [22]	Combination of MSA & MCF
1995	Antoszewski *et al*. [32]	Quantitative Mobility Spectrum Analysis (QMSA)
1997	Meyer *et al*. [24]	QMSA optimized based on experimental feedback
1998	Vurgaftman *et al.* [19]	Improved-Quantitative Mobility Spectrum Analysis (i-QMSA)
2002	Kiatgamolchai *et al.* [26]	Maximum-Entropy Mobility Spectrum Analysis (ME-MSA)
2006	Rothman *et al.* [33]	full-Maximum Entropy-MSA (f-MEMSA), can deal with mobilities below 100 cm^2/Vs
2010	Umana-Membreno *et al.* [27]	High-Resolution Mobility Spectrum Analysis (HR MSA)
2015	Cui *et al.* [34]	Fourier-domain MSA (FMSA)
2018	Beck W. [35]	Multicarrier MSA (patented new approach)

3.7 Summary

This chapter describes the primary growth technique, optical measurements, and fabrication as well as the equipment employed to implement temperature- and magnetic-field-dependent transport measurements. First, the NRL MULTIBANDS® software employed to obtain band-diagrams plus estimate carrier concentration build-up at the samples interfaces is described. Secondly, multi-carrier fitting programs are presented with an emphasis on Multiple-Carrier Fit (MCF) used in Chapter 4-5, and High-Resolution Mobility Spectrum Analysis (HR-MSA) used in Chapter 6.

3.8 References

[1] L. Esaki and R. Tsu, “Superlattice and Negative Differential Conductivity in Semiconductors,” *IBM J. Res. Dev.*, vol. 14, no. 1, 1970.

[2] “Bragg’s Law.” [Online]. Available: https://byjus.com/physics/braggs-law/. [Accessed: 11-Apr-2019].

[3] E. A. Kadlec, “Progress Towards Competitive III-V Infrared Detectors : Fundamental Material Characterization and Techniques,” University of New Mexico, 2017.

[4] O. Dier, C. Lin, M. Grau, and M.-C. Amann, “Selective and non-selective wet-chemical etchants for GaSb-based materials,” *Semicond. Sci. Technol.*, vol. 19, no. 11, 2004.

[5] A. E. Brown, N. Baril, D. Zuo, L. A. Almeida, J. Arias, and S. Bandara, “Characterization of n-Type and p-Type Long-Wave InAs/InAsSb Superlattices,” *J. Electron. Mater.*, vol. 46, no. 9, pp. 5367–5373, 2017.

[6] S. P. Svensson *et al.*, “Background and interface electron populations in InAs 0.58 Sb 0.42,” *Semicond. Sci. Technol.*, vol. 30, no. 3, 2015.

[7] E. M. Lysczek, J. A. Robinson, and S. E. Mohney, “Ohmic contacts to p-type InAs,” *Mater. Sci. Eng. B*, vol. 134, no. 1, 2006.

[8] S. Myers, “Mid-Wave and Long-Wave Single Uni-polar Barrier Infrared Detectors Based on Antimonide Material Systems,” 2013.

[9] E. J. Renteria, “Integration of Thin Film TPV Cells to CVD Diamond Heat Spreaders,” University of New Mexico, 2017.

[10] K. Lee, K. Shiu, J. D. Zimmerman, C. K. Renshaw, R. Stephen, and S. R. Forrest, “Multiple growths of epitaxial lift-off solar cells from a single InP substrate,” *Appl. Phys. Lett.*, vol. 97, no. 10, 2017.

[11] A. E. Brown, “Application of Mobility Spectrum Analysis to Modern Multi-layered IR Device Material,” University of Illinois at Chicago, 2015.

[12] Lake Shore, “Lake Shore 7500/9500 Series Hall System User’s Manual.” [Online]. Available: https://www.lakeshore.com.

[13] L.J van der PAUW, “A method of measuring specific resisitivity and hall effect of discs of arbitrary shape,” *Philips Res. Reports*, vol. 13, no. 1, 1958.

[14] M. P. Lumb *et al.*, “Quantum wells and superlattices for III-V photovoltaics and photodetectors,” *Proc. SPIE*, vol. 8471, 2012.

[15] J. Singh, *Electronic and Optoelectronic Properties of Semiconductor Structures*. Cambridge University Press, 2003.

[16] W. A. Beck and J. R. Anderson, “Determination of electrical transport properties using a novel magnetic field-dependent Hall technique,” *J. Appl. Phys.*, vol. 62, no. 2, 1987.

[17] Z. Dziuba and M. Gorska, “Analysis of the electrical conduction using an iterative method,” *J. Phys. III*, vol. 2, 1992.

[18] J. Antoszewski, D. J. Seymour, L. Faraone, J. R. Meyer, and C. A. Hoffman, “Magneto-transport characterization using quantitative mobility-spectrum analysis,” *J. Electron. Mater.*, vol. 24, no. 9, pp. 1255–1262, 1995.

[19] I. Vurgaftman *et al.*, “Improved quantitative mobility spectrum analysis for hall characterization,” *J. Appl. Phys.*, vol. 84, no. 9, pp. 4966–4973, 1998.

[20] J. W. McClure, “Field dependence of magnetoconductivity,” *Phys. Rev.*, vol. 101, no. 1642, 1956.

[21] J. R. Meyer, C. a Hoffman, F. J. Bartoli, D. a Arnold, S. Sivananthan, and J. P. Fauri, “Methods for magnetotransport characterization of IR detector materials,” *Semicond. Sci. Technol.*, vol. 8, no. 6S, 1993.

[22] H. Brugger and H. Koser, “Variable-Field: Hall Technique,” *III-Vs Rev.*, vol. 8, no. 3, 1995.

[23] Z. Dziuba and M. Gorska, “Analysis of the electrical conduction using an iterative method,” *J. Phys. III 2*, vol. 2, no. 1, pp. 99–110, 1992.
[24] J. R. Meyer and C. A. Hoffman, “Quantitative mobility spectrum analysis of multicarrier conduction in semiconductors,” *J. Appl. Phys.*, vol. 81, no. 2, 1997.
[25] T. V. Chandrasekhar Rao, J. Antoszewski, J.-B. Rodriguez, E. A. Plis, S. Krishna, and L. Faraone, “Quantitative mobility spectrum analysis of carriers in GaSb/InAs/GaSb superlattice,” *J. Vac. Sci. Technol. B Microelectron. Nanom. Struct.*, vol. 26, no. 3, 2008.
[26] S. Kiatgamolchai, M. Myronov, O. A. Mironov, V. G. Kantser, E. H. C. Parker, and T. E. Whall, “Mobility spectrum computational analysis using a maximum entropy approach,” *Phys. Rev. E*, vol. 66, no. 036705, 2002.
[27] G. A. Umana-Membreno *et al.*, “Investigation of Multicarrier Transport in LPE-Grown Hg1-xCdxTe Layers,” *J. Electron. Mater.*, vol. 39, no. 7, 2010.
[28] J. Antoszewski, G. A. Umana-Membreno, and L. Faraone, “High-resolution mobility spectrum analysis of multicarrier transport in advanced infrared materials,” *J. Electron. Mater.*, vol. 41, no. 10, pp. 2816–2823, 2012.
[29] G. A. Umana-Membreno *et al.*, “Vertical minority carrier electron transport in p-type InAs/GaSb type-II superlattices,” *Appl. Phys. Lett.*, vol. 101, no. 25, 2012.
[30] G. A. Umana-Membreno, S. J. Chang, M. Bawedin, J. Antoszewski, S. Cristoloveanu, and L. Faraone, “Evidence of Sub-band Modulated Transport in Planar Fully Depleted Silicon-on-Insulator MOSFETs,” *IEEE Electron Device Lett.*, vol. 35, no. 11, 2014.
[31] C. H. Swartz and T. H. Myers, “Method for the simultaneous determination of vertical and horizontal mobilities in superlattices,” *Phys. Rev. B*, vol. 89, no. 7, 2014.
[32] J. Antoszewski, D. J. Seymour, L. Faraone, J. R. Meyer, and C. A. Hoffman, “Magneto-Transport Characterization using Quantitative Mobility-Spectrum Analysis,” *J. Electron. Mater.*, vol. 24, no. 9, 1995.
[33] Rothman, Johan, et al. "Maximum entropy mobility spectrum analysis of HgCdTe heterostructures." *Journal of electronic materials*, vol. 35, no. 6, 2006.
[34] Cui, Boya, Yang Tang, and M. Grayson. "Introducing Fourier-domain mobility spectrum analysis (FMSA) to deduce multi-component carrier mobility and density." *Quantum Sensing and Nanophotonic Devices XII*. vol. 9370, International Society for Optics and Photonics, 2015.
[35] W. Beck, *US Patent* US2018/0231602A1 (2018)

Chapter 4

p-type InAsSb Lateral Transport

4.1 Introduction

Accurate *p*-type doping of the active region in III-V infrared detectors is essential for optimizing the detector design and overall performance. While most III-V detector absorbers are *n*-type (e.g., nBn), the minority carrier devices with *p*-type absorbers would be expected to have relatively higher quantum efficiencies due to the higher mobility of minority carrier electrons. However, there are added challenges to determining the hole carrier concentration in narrow bandgap InAsSb alloys and InAs/InAsSb type-II Strained Layer Superlattices (T2SLs) due to the potential for electron accumulation at the surface of the material and at its interface with the layer grown directly below it. Electron accumulation layers form high conductance electron channels that can dominate both resistivity and Hall Effect transport measurements.

Hence, to correctly determine the bulk hole concentration and mobility, temperature- and magnetic-field-dependent transport measurements in conjunction with Multi-Carrier Fit (MCF) analysis were utilized on a series of *p*-doped $InAs_{0.91}Sb_{0.09}$ samples grown on GaSb substrates. To attribute each carrier species suggested by MCF with a corresponding physical conduction process of the InAsSb samples at 77 and 300 K, the samples are etched to different thicknesses, and variable-field measurements are

utilized to assist in confirming whether a carrier species represents bulk, interface or surface conduction. Then, a surface treatment experiment is conducted to correlate one of the electron conducting populations with conducting electrons at the surface of the mesa. The concentrations of two interface carriers are compared to the experimental data using the NRL MULTIBANDS® model. Variable temperature measurements (15 – 390 K) enabled the confirmation of the different carrier species and resulted in further extraction of bulk hole carrier and surface electron transport properties as a function of temperature. Finally, a substrate removal attempt is presented which serves as the foundation for the processing technique presented in Chapter 6 employed for vertical transport measurements. The work presented in this chapter can be found in Casias *et al.* [1] Infrared Physics and Technology Journal publication.

4.2 Sample and Methods

4.2.1 Device Structures, Fabrication and Characterization

For this study, the sample was grown on an *n*-type (*Te*-doped) GaSb substrate using Molecular Beam Epitaxy (MBE). The structure is shown in Figure 4.1 (a), which consists of a 2 μm thick lattice-matched $InAs_{0.91}Sb_{0.09}$ bulk layer with a target *p*-type Be-doping concentration of ~2×10^{18} cm^{-3} grown on top of a 0.01 μm thick undoped GaSb layer on a 0.5 μm thick lattice-matched and undoped $AlAs_{0.08}Sb_{0.92}$ insulating layer. The 2-dimensional and 3-dimensional fabricated sample diagrams are shown in Figure 1 (a) and (b) with Van der Pauw (VDP) configuration.

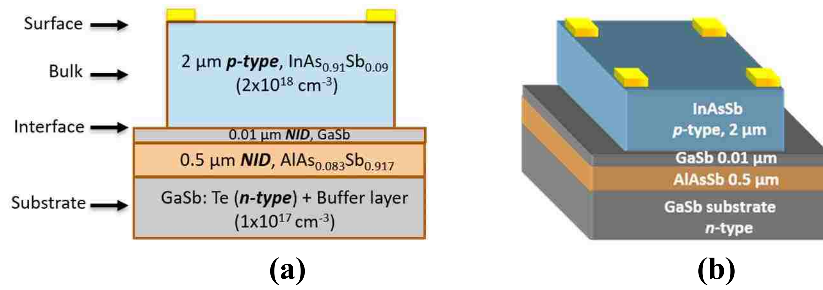

Figure 4.1: Schematics of the fabricated samples in Van der Pauw (VDP) configuration: (a) 2-dimensional InAsSb sample cross section with distinct conductive paths indicated (b) 3-dimensional etched InAsSb sample structure [1].

The wide-bandgap AlAsSb insulating layer acts to effectively remove the conductive pathway of the substrate. The 0.01 μm thick GaSb layer was necessary to produce high-quality InAsSb, which exhibited significantly poorer minority carrier lifetimes when grown directly on the AlAsSb barrier. The wafer was diced, and pieces from the wafer were wet-etched to different thicknesses using a citric acid based etch (citric acid:H_2O_2(30%) = 5:1) at room temperature. This citric acid-based etch had a repeatable 0.09-0.098 μm/minute etch rate for InAsSb and selectively stops at the GaSb buffer layer as depicted in Figure 4.1 (a) and (b).

Stylus profilometry measured four different InAsSb bulk thicknesses (1.6 μm, 1.4 μm, 0.8 μm, 0.3 μm) in addition to the original 2 μm thick sample. Standard optical photolithography was employed to define 5 mm × 5 mm square mesas in the VDP configuration. Then, 300 μm × 300 μm corner contacts were defined and contact formation with Ti/Pt/Au was used as previously shown to make suitable ohmic *p*-type contacts for similar material [2]. Contacts were verified to be ohmic for all samples and temperatures of interest. In addition to etching the InAsSb film thicknesses, a surface chemical treatment method was employed to identify the surface component of the 2 μm sample.

Dark variable-field Hall Effect measurements are performed using a current of 100 μA. The LakeShore Hall Measurement System (HMS) software controlled the electrical

equipment for each run and provided current-voltage (I-V) characterization of contacts, sheet resistivity, and Hall coefficients that were needed as inputs for the MCF analysis.

4.2.2 Optical Characterization

Photoluminescence (PL) measurements were provided by Sandia National Laboratories (SNL) using double modulation Fourier-transform infrared spectroscopy (FTIR) with a pump laser at 1550 nm and a 2.4 μm long pass to filter out the pump beam. A skewed gaussian was employed to fit the PL spectra. To build the *x-y* wafer map shown in Figure 4.2, the measurements were taken in 5 mm increments. Figure 4.2 shows the 80 K PL wavelength range across the wafer from 4.35 – 4.85 μm which confirmed MWIR operation with an average bandgap energy of $E_g \sim 270$ meV.

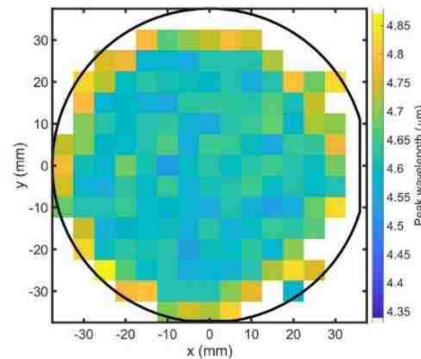

Figure 4.2: Photoluminescence (PL) map at 80 K provided by SNL that shows the peak wavelength of every measurement across the whole *p*-type InAsSb wafer. Mid-Wavelength (MW) operation was confirmed across the wafer, ranging from 4.35-4.85 μm.

4.2.3 Multi-Carrier Analysis

Although conventional Hall Effect analysis at a single magnetic field is routinely employed to characterize transport properties in III-V materials such as InAsSb, the need for a multiple-carrier analysis is evident when the magnetic-field-dependent resistivity and Hall coefficient characteristics indicate the presence of more than one carrier species. As discussed and summarized in Chapter 3, Section 3.6.2, Multi-Carrier Fit (MCF), Mobility

Spectrum Analysis (MSA), and Quantitative Mobility Spectrum Analysis (QMSA) are some of the widely used techniques for analyzing variable-magnetic-field Hall Effect data [3], [4]. In MSA and MCF, the experimental Hall coefficient (R_H), and resistivity (ρ_{xx}) are related to the longitudinal and transverse conductivity tensor components (σ_{xx} and σ_{xy}). However, the disadvantage of the MCF technique is that it requires prior knowledge of the number of electron and hole carriers, whereas MSA or QMSA does not.

Initially, LakeShore QMSA was employed, but the fit did not identify the low mobility/high conductivity carrier properties, but it did display the peak for a low mobility carrier as shown in Figure 4.3. Figure 4.3 illustrates the mobility spectrum for the 1.4 µm InAsSb sample at 300 K, which identified four carrier peaks, two electrons and two holes, however, the low mobility hole carrier concentration and mobility were incompletely resolved due to the upper magnetic field limit of the equipment. A representative threshold is below approximately *1/B_{max},* where B_{max} is the maximum applied magnetic field (9 T in the work reported here). In our case, this implies that the QMSA software may not be able to resolve mobilities below ~1100 cm^2/Vs.

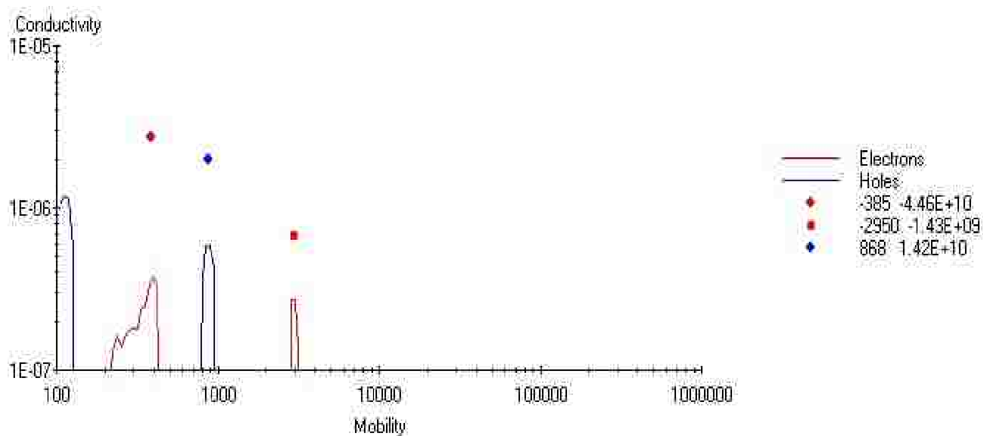

Figure 4.3: LakeShore QMSA mobility spectrum for the *p*-type 1.4 µm InAsSb sample at 300 K. The figure demonstrates how the fit is unable to resolve the low mobility/high conductivity hole due the maximum magnetic field intensity limit.

The LakeShore QMSA method was initially used to determine the number of carriers present in the samples, and the MCF method was used thereafter to quantify the carrier species. Due to the unresolved transport properties of the low hole mobility carrier using QMSA, MCF was utilized as it demonstrated reliable fit trends. MCF was set up to allow for eight total possible carrier populations and identified the same four carrier populations (two electrons and two holes) at both temperatures (77 K and 300 K). Furthermore, the fit quality severely diminished when the MCF analysis was executed using fewer than four carriers. As mentioned, the analysis in this work was completed using MCF to extract both the number of carriers present with mobility and concentration values for each sample. Finally, both mobility and concentration values were employed to calculate the sheet conductivity for each of the four carriers in each sample using the equation $\sigma = \mu pq$, where μ, p, and q represent the mobility, sheet carrier concentration, and electron charge, respectively.

4.3 Simulations

NRL MULTIBANDS® was employed to simulate the band structure and concentration at the interfaces. Figure 4.4 shows the band edge diagram and Figure 4.5 shows the carrier concentration profile of the sample structure. Figure 4.4 inset (i) zooms in to the sample surface to demonstrate Fermi level pinning, and the resulting surface electron accumulation can be seen in Figure 4.5 inset (i). Similarly, Figure 4.4, inset (ii) zooms in on the electron and hole wells formed at the InAsSb/GaSb/AlAsSb interface, and Figure 4.5, inset (ii) plots the resultant carrier concentration profile which shows the electron and hole well accumulations at the InAsSb/GaSb/AlAsSb interface.

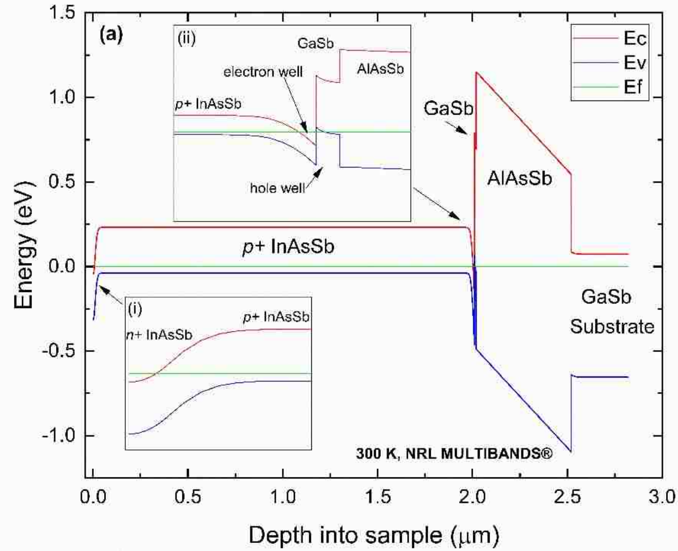

Figure 4.4: Energy band diagram vs. sample depth modeled using NRL MULTIBANDS® at 300 K [1]. Inset (i) zooms in to the surface Fermi level pinning and inset (ii) provides a closer look of the electron and hole wells formed at the InAsSb/GaSb/AlAsSb interface. Figure 2 (b), inset (i) shows the concentration diagram at the surface while inset (ii) shows the electron and hole accumulations at the InAsSb/GaSb/AlAsSb interface.

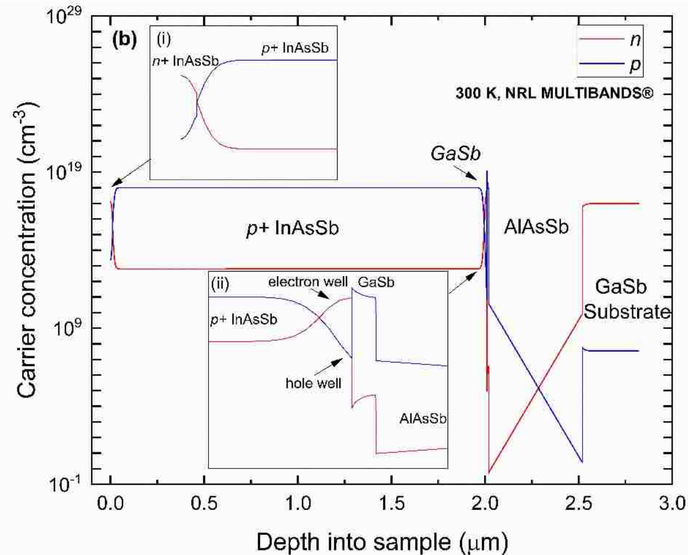

Figure 4.5: Carrier concentration vs. sample depth showing the different layers in the sample structure modeled using NRL MULTIBANDS® at 300 K [1]. Inset (i) shows the concentration diagram at the surface while inset (ii) shows the electron and hole accumulations at the InAsSb/GaSb/AlAsSb interface.

The undoped GaSb interface layer was modeled as *p*-type with a concentration of 1×10^{16} cm^{-3} [5]. InAsSb suffers from a strong surface accumulation layer due to the fact that the surface Fermi level is approximately 200 meV above the conduction band

minimum [6]. Since this known surface electron accumulation that has been widely reported for *n*- and *p*-type InAs [7]–[12], a similar effect is expected in InAsSb. However, NRL MULTIBANDS® does not directly model the surface conditions, so the Fermi level pinning effect is simulated by including a 10 nm thin *n*-type InAsSb layer at the structure model's surface. Therefore, the doping and thickness of this n^{+}-InAs layer is fit to yield a surface electron accumulation layer equal to that which was measured earlier [9], [11].

In addition to the surface electron accumulation, it is known that there is an intrinsic 2DEG at an InAs/AlSb interface [13]. In the *p*-type InAsSb structure used, the inclusion of the 0.01 μm thin GaSb between InAsSb and AlAsSb, has the consequence of forming an additional hole conduction channel as seen in the insets (ii) of Figures 4.4-4.5. Using NRL MULTIBANDS® at 300 K, the calculated area under the electron well gives a sheet concentration of 4.2×10^{11} cm^{-2}, while the area under the hole well gives a sheet concentration of 1.2×10^{12} cm^{-2}. Finally, the bandgap modeled provides an approximate ~ 5 μm cutoff wavelength at 300 K.

4.4 Results and Analysis

4.4.1 Sheet Resistivity Characterization

Sheet resistivity measurements are utilized to demonstrate multi-carrier conduction in the samples. The classic linear magneto-resistance is expected to follow Equation 4.1 for a single discrete carrier:

$$\rho_s(B) = \rho_s(0)(1 + \mu^2 B^2) \quad (4.1)$$

whereas ρ_s is the measured sheet resistivity, μ is the single discrete carrier mobility contributing to conduction, and B is the applied magnetic field intensity. If only a single

carrier is present in the material under test, then Equation 4.1 predicts $\rho_s(B)$, sheet resistivity as a function of magnetic field intensity to be linear with respect to B^2 [14]. Figure 4.6 (a) and (b) shows the non-linear behavior of measured sheet resistivity with respect to B^2 at 77 and 300 K, respectively. The non-linear behavior indicates multiple-carrier conduction which demands a variable-magnetic-field measurement and the use of advanced multiple-carrier analysis methodologies (MCF or MSA) to measure transport characteristics.

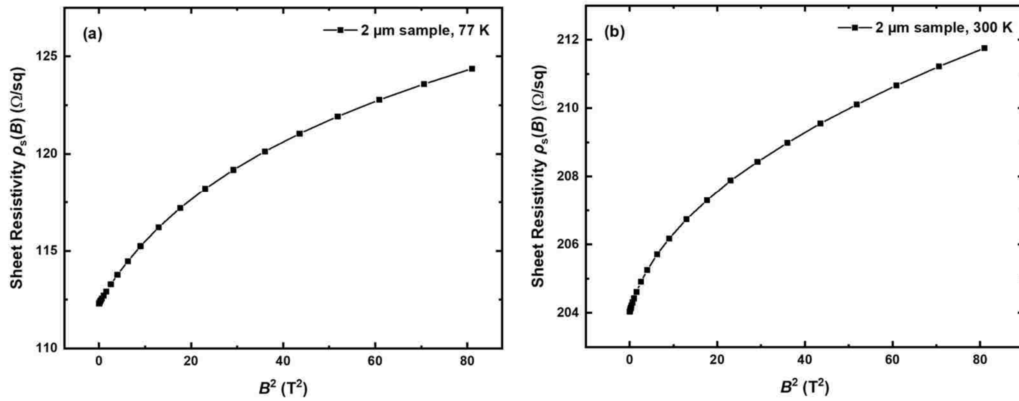

Figure 4.6: Sheet resistivity vs. B^2 for the 2 μm *p*-type InAsSb sample at (a) 77 K and (b) 300 K [1]. The non-linear behavior indicates multiple-carrier conduction.

Sheet resistivity is measured for the five sample thicknesses (2.0 μm, 1.6 μm, 1.4 μm, 0.8 μm, and 0.3 μm) at 77 and 300 K. Figure 4.7 (a) and (b) show the measured sheet resistivity as a function of magnetic field at 77 and 300 K, respectively. Sheet resistivity (ρ_s) increases with decreasing film thickness (t) which is consistent with the expression for resistivity:

$$\rho_s = (tqp\mu_p)^{-1} \tag{4.2}$$

whereas q is the electronic charge, p is the concentration and μ_p is the hole mobility. Also, Figure 4.7 (a) and (b) demonstrates that the sheet resistivities are higher for all sample thicknesses at 300 K compared to 77 K. This indicates that the increase in dopant activation

from 77 to 300 K is not significant enough to overcome the decrease in mobility due to increased phonon scattering.

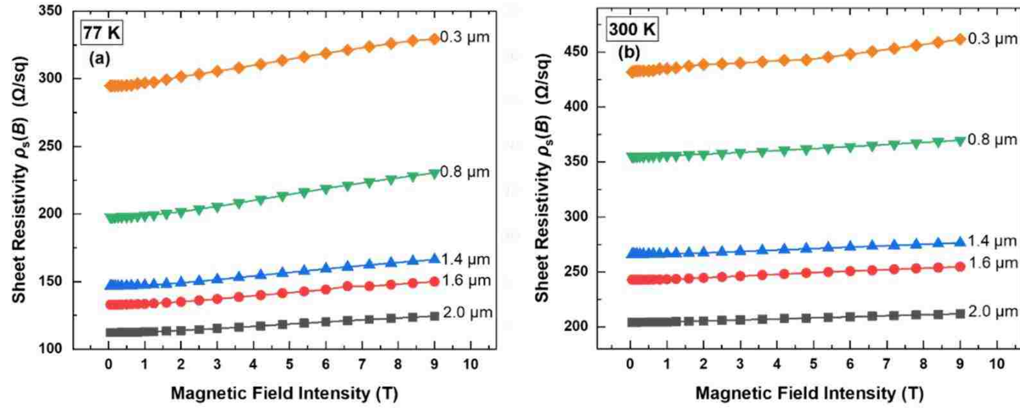

Figure 4.7: Sheet resistivity as a function of magnetic field intensity for different InAsSb layer thickness at (a) 77 K and (b) 300 K [1].

4.4.2 Variable Field Characterization

MCF was set up to allow for eight total possible carrier populations and identified the same four carrier populations (two electrons and two holes) at 77 and 300 K temperatures. Therefore, the analysis in this study was completed using MCF to extract both the number of carriers present with mobility and concentration values for each sample. Finally, both mobility and concentration values were employed to calculate the sheet conductivity for each of the four carriers in each sample.

Samples of thickness 2.0 µm 1.6 µm, 1.4 µm, 0.8 µm, and 0.3 µm are tested at 77 K. The sheet conductivity is plotted as a function of InAsSb layer thickness in Figure 4.8 (a) and (b) in linear and semilog scales, respectively. MCF extracted four carrier populations: a high-conductivity hole population (*h1*), a secondary hole population (*h2*) with higher mobility than *h1*, and two electron populations (*e1* and *e2*).

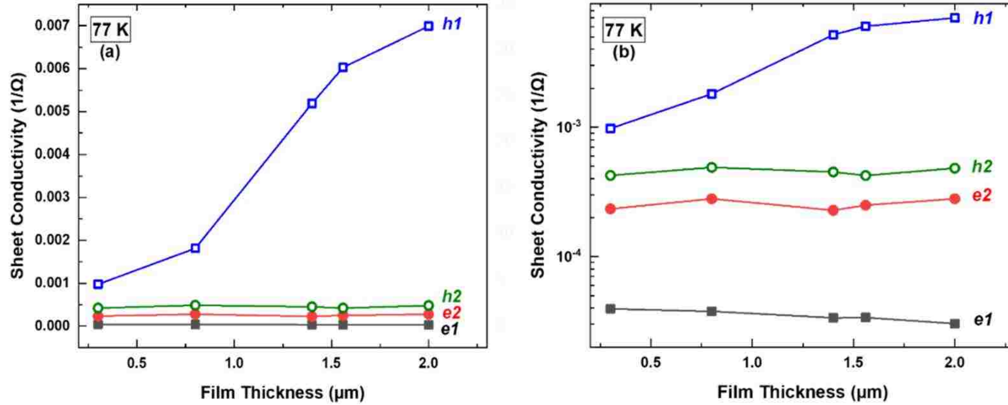

Figure 4.8: The sheet conductivity of the four carrier populations present in the *p*-type InAsSb structure at 77 K as a function of etched thickness on a (a) linear scale and (b) semilog scale [1].

At 300 K, five samples of the 2.0 μm thickness and three samples of thickness 1.6 μm, 1.4 μm, 0.8 μm, and 0.3 μm are tested. The average sheet conductivity as a function of bulk layer thickness is shown in Figure 4.9 (a) and (b) on linear and semilog scales, respectively. Figure 4.9 (b) includes conductivity error bars calculated using mean and standard deviation for reference. Similar to the results at 77 K, MCF also extracted four carrier populations at 300 K: a high-conductivity hole population (*h1*), a secondary hole population (*h2*) with higher mobility than (*h1)*, and two electron populations (*e1* and *e2*). As shown in Figure 4.9 (a) and (b), the *h2* carrier showed non-monotonic behavior.

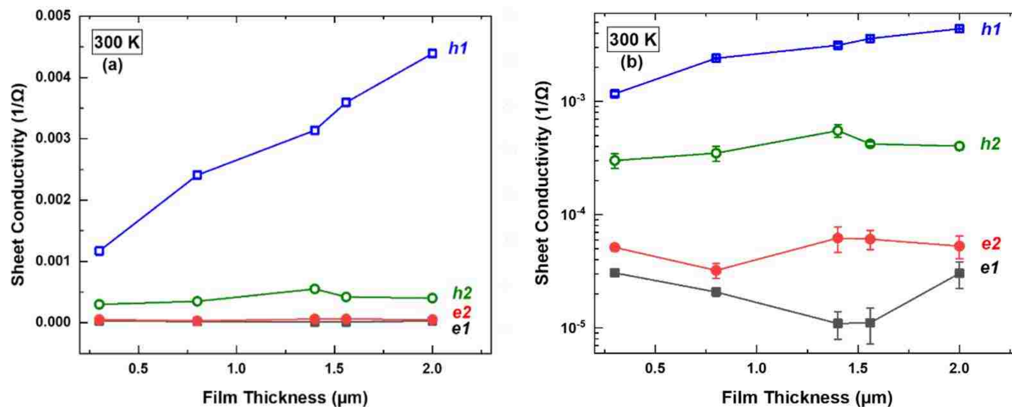

Figure 4.9: The average conductivity of the four carrier populations present in the *p*-type InAsSb structure at 300 K as a function of etched thickness on (a) linear scale and (b) semilog scale with error bars [1].

At both 77 K (Figures 4.8 (a) and (b)) and 300 K (Figure 4.9 (a) and (b)), the *h1* hole population had the highest sheet conductivity out of all four carriers and is shown to linearly increase with increasing thickness, whereas the other three carriers' sheet conductivities are relatively insensitive to the InAsSb layer thickness. This thickness-dependence suggests that *h1* is the bulk hole carrier for the *p*-type InAsSb layer whereas the other three carriers may not be associated with the bulk film.

At 77 K, the bulk *p*-type sheet carrier concentration and mobility are 3.2×10^{14} cm^{-2} and 125 cm^2/Vs for the 2.0 μm sample, and the corresponding bulk carrier concentration is 1.6×10^{18} cm^{-3}. At room temperature (300 K), the bulk *p*-type sheet carrier concentration and mobility obtained are 4.6×10^{14} cm^{-2} and 60 cm^2/Vs for the 2.0 μm sample, and the corresponding bulk carrier concentration is 2.3×10^{18} cm^{-3}.

It is worth emphasizing that identifying the bulk carrier in a multiple-carrier structure by modifying the thickness of the sample has been previously published for *n*-type InAs and $InAs_{0.58}Sb_{0.42}$ material [12], [15]. For instance, using QMSA, the bulk electron conduction for InAs *n*-doped at a concentration of 1×10^{18} cm^{-3}, was extracted by changing the thickness of the sample from 1 to 2 μm. Due to this change, the calculated sheet carrier density changed proportionally with layer thickness for a constant doping, noting that no change would be expected if this was a surface accumulation effect [12]. Also, using MSA, *n*-type $InAs_{0.58}Sb_{0.42}$ sample was doped at a concentration of 8×10^{16} cm^{-3} and etched to remove part of the bulk film to attribute each carrier to its corresponding layer [15]. However, presumably, there has not been studies on *p*-type InAsSb that use a similar method. Hence, the motivation for the work reported here.

4.4.2.1 Surface and Interface Components at 300 K

The Fermi level pinning effect causes an electron accumulation layer on both *p*-type and *n*-type InAs and InAsSb surfaces [6], [16]. Surface currents related to this layer can be successfully minimized using unipolar barriers such as the nBn device architectures for *n*-type absorbers [17]. However, in *p*-type material, such as that studied here, the conductivity type of the bulk and the surface layer differ, making it difficult to extract the majority carrier hole and surface electron accumulation currents independently. To differentiate which of the three unknown carriers belonged to the surface, the 2.0 μm sample surface is dipped in 5.25% sodium hypochlorite (NaClO) and rinsed in deionized water in order to disturb or change the sample surface. The 2.0 μm sample is used so that the experiment was only affecting the conductivity of the carrier related to the surface and not the bulk film carrier affected by etching.

Room temperature variable-field measurements and MCF analysis are then repeated under similar conditions prior to the NaClO treatment. Svensson *et al.* [15] employed a similar chemical treatment on *n*-type $InAs_{0.58}Sb_{0.42}$ surfaces to identify the surface carrier population. The advantage of such treatment is that it does not etch InAsSb [15]. Sodium hypochlorite treatment has also been used as an etching passivant in GaAs and for chemical polishing of InAs/GaSb T2SL material [18], [19]. The exact reaction of the solution on the surface of InAsSb is unknown, but the free sodium ions in the solution may bring negative charges to the surface of the sample which causes it to affect the electron accumulation surface layer.

Pre- and post- surface treatment analysis of the same 2.0 μm sample is compared in Table 4.1. The mobility and concentration results for the four different carrier

populations (pre- to post-treatment) are shown. The *e1* carrier population exhibits a significant change in mobility (4260 ± 100 to 468 ± 30 cm^2/Vs) as well as sheet concentration (6.00×10^{10} to 6.67×10^{12} cm^{-2}) whereas the other three carrier species are not severely impacted by the surface treatment, supporting the conclusion that *e1* is the surface electron carrier in InAsSb. Concentration in Table 4.1 is only shown for the bulk carrier as the exact thickness of the bulk layer is known; the other carrier components are expressed using sheet concentrations.

Table 4.1: Pre- and post- surface treatment mobility and carrier concentration results for the 2.0 µm *p*-type InAsSb at 300 K. Concentration is listed for the bulk hole carrier only.

Carrier	Mobility Pre- (cm^2/Vs)	Mobility Post- (cm^2/Vs)	Sheet Concentration Pre- (cm^{-2})	Sheet Concentration Post- (cm^{-2})	Concentration Pre- (cm^{-3})	Concentration Post- (cm^{-3})
e1 = surface	4260 ± 100	468 ± 30	6.0×10^{10}	6.67×10^{12}		
e2 = interface	1370 ± 50	1600 ± 70	2.40×10^{11}	2.17×10^{11}		
h1 = bulk	60 ± 10	65 ± 20	4.58×10^{14}	4.61×10^{14}	2.29×10^{18}	2.31×10^{18}
h2 = interface	789 ± 20	800 ± 50	3.00×10^{12}	3.01×10^{12}		

To confirm that the remaining two carrier populations (*e2* and *h2*) belong to the InAsSb/GaSb/AlAsSb interface, the experimental values for sheet concentration listed in Table 4.1 are compared to calculated sheet concentrations from Figure 4.5, inset (ii). For interface electron (*e2*) at 300 K, the measured sheet concentration was 2.4×10^{11} cm^{-2} compared to a value of 4.2×10^{11} cm^{-2} determined using the NRL MULTIBANDS®. For an interface hole (*h2*) at 300 K, the measured sheet concentration was 3.0×10^{12} cm^{-2} compared to the modeled value of 1.2×10^{12} cm^{-2}. The model confirms that electrons and holes are expected to accumulate at the InAsSb/GaSb/AlAsSb interface noted in Figure

4.5, and close agreement of these calculated sheet densities with the experimental results supports the hypothesis that these are the electron (*e2*) and hole interface (*h2*) populations.

4.4.2.2 Variable Temperature

Temperature (15 – 390 K) and magnetic-field-dependent measurements in conjunction with MCF analysis are employed to further characterize the transport properties of the 2.0 μm *p*-type $InAs_{0.91}Sb_{0.09}$ sample. The analysis involves an individual variable-magnetic-field measurement at each temperature followed by MCF analysis to identify the different carriers present. From 15 – 60 K, the MCF identifies only three carriers (two holes and one electron) when set up to allow for eight total possible carrier populations. However, from 60 – 390 K, the MCF identified four carriers (two holes and two electrons) when set up to allow for eight total possible carrier populations.

The extracted carrier mobilities and concentrations for each of the carrier populations are presented as a function of temperature in Figure 4.10 (a) and (b), respectively. The carrier assignments shown in Figure 4.10 (a) and (b) are identified based on the following considerations: (1) For 77 and 300 K, the carrier concentration and mobility of the lowest mobility carrier (*h1* or the bulk hole) is consistent with the mobilities extracted previously in the etch experiment for the 2.0 μm thick samples and with the intended Be-doping (~2×10^{18} cm^{-3}), (2) the *h1* bulk carrier population appeared to be dominated by lattice scattering ($T^{-3/2}$) at high temperatures while *h2* and *e2* do not demonstrate a clear scattering dependence, (3) the *e1* (surface electron) carrier population exhibits an approximately temperature-independent concentration which is indicative of surface electron accumulation commonly found in narrow-bandgap materials [20], and (4) the *e2* interface carrier dropped from the fitting at temperatures lower than 63 K and higher than 240 K.

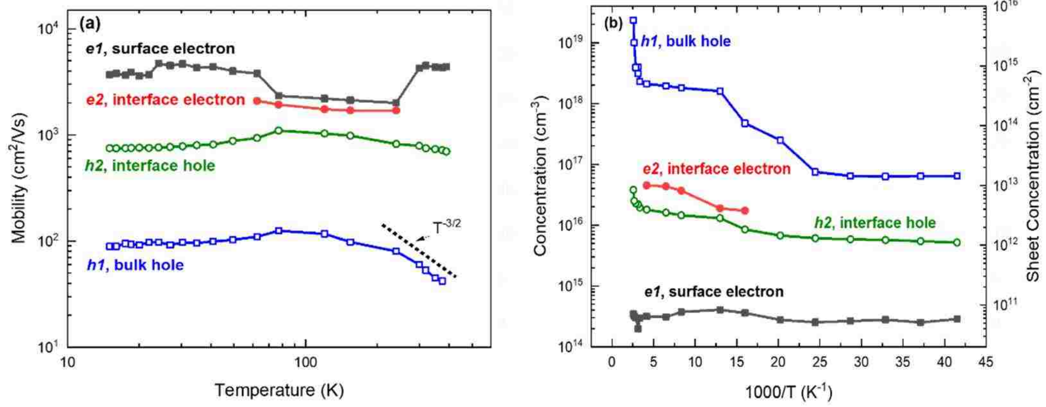

Figure 4.10: Variable-temperature analysis of the four resolved carrier populations in the *p*-type 2 µm thick InAsSb sample vs. (a) mobility and (b) carrier concentration [1].

The *n*-type carrier population *e1* shown in Figure 4.10 (a) and (b), result in surface carrier mobilities and sheet concentrations at 30 K (300 K) of 4500 cm^2/Vs (4300 ± 100 cm^2/Vs) and 5.6×10^{10} cm^{-2} ($6\times10^{10} \pm 2\times10^{10}$ cm^{-2}), which are similar to the surface electron mobility reports for InAs/InAsSb superlattices, InAsSb and InAs surfaces [15], [21], [22]. For specific comparison, the surface electron mobility and concentration found in un-passivated *p*-type InAs/InAsSb superlattices reported previously [21] at 30 K was found to be 4690 cm^2/Vs and 4.71×10^{11} cm^{-2}, respectively. In addition, from 4-77 K, the surface of *p*-type InAs was found to be strongly *n*-type with mobilities ranging from 3000-5000 cm^2/Vs with a concentration of 5.00×10^{11} cm^{-2} [22].

Figure 4.11 plots the natural log of $h1$ carrier concentration ($p_{h1=bulk\ hole}$) as a function of temperature $(1/k_BT)$ on the lower horizontal axis, whereas k_B is the Boltzmann constant (8.62×10^{-5} eV/K). Intrinsic, extrinsic and freeze-out regions of $h1$ are indicated.

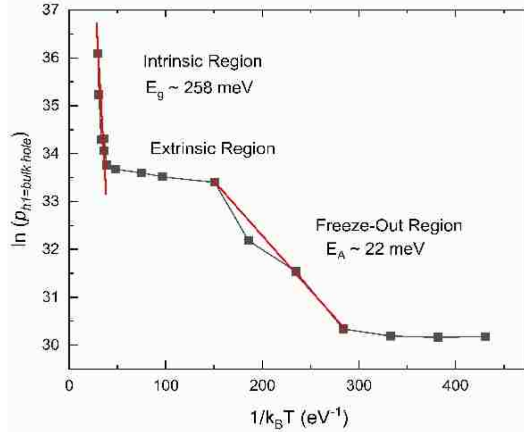

Figure 4.11: Bandgap and activation energy analysis for the bulk carrier hole ($h1$) in the p-type 2 µm thick InAsSb sample. Intrinsic, extrinsic and freeze-out regions of $h1$ are indicated.

The sharp increase of hole concentration observed as the temperature increased from 300 to 390 K is due to increased thermal excitation across the bandgap as the material begins to enter the intrinsic region. The onset of the intrinsic regime (300 – 390 K) is defined by the bandgap energy, and the analysis of the slope fit in Figure 4.11 indicates that there is a thermal activation of intrinsic carriers at a bandgap energy of $E_g \sim 258$ meV.

The fitted experimental bandgap extracted from Figure 4.11 is slightly smaller than the room temperature $InAs_{0.91}Sb_{0.09}$ bandgap energy of 270 meV (NRL MULTIBANDS®), which is consistent with the observation that intrinsic carriers only begin to become significant above room temperature. The material is in the extrinsic regime from 240 – 300 K, as the bulk hole carrier ($h1$) concentration is constant at ~1.8-2.3×10^{18} cm^{-3} in agreement with the intended doping level (2×10^{18} cm^{-3}). Below 240 K, the free holes begin to freeze out. Arrhenius analysis of the p-type concentration for the $h1$ carrier ($\ln(p_{h1=bulk\ hole})$) vs. $1/k_BT$ indicates that there is an activation energy of $E_A \sim 22$ meV for the Be-doping. At temperatures below 30 K, the bulk carrier concentration flattens out to a sheet value of ~ 1.4×10^{13} cm^{-2} suggesting a possible background impurity level in the material.

The sheet conductance was calculated using the mobility and sheet concentration results at each temperature and is shown in Figure 4.12. The bulk carrier (*h1*) showed the highest sheet conductivity out of the four carriers with the surface electron (*e1*) having the lowest. These conductance results are consistent with the etching experiment where bulk carriers (*h1*) dominated and surface electrons (*e1*) were the least conductive. The *e2* carrier (electron interface carrier) increased in sheet conductivity from 63 – 240 K and could not be uniquely resolved in the fitting at temperatures below 63 K and above 240 K.

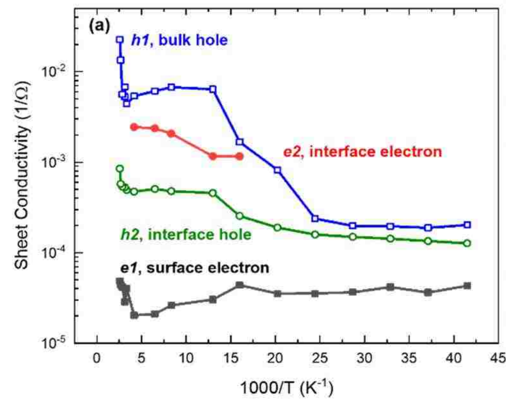

Figure 4.12: Sheet conductivity vs. temperature of the four carrier populations present in the *p*-type 2 μm thick InAsSb sample [1].

4.5 Substrate Removal Attempt

Although substrate removal is covered in detail in Chapter 6, Section 6.4.3, for vertical transport measurements, this section describes an attempt to remove the GaSb substrate on the VDP *p*-type InAsSb samples for lateral transport measurements. The goal was to remove the GaSb substrate, AlAsSb etch-stop, and the GaSb layer to obtain more information about the carriers present in the *p*-type InAsSb absorber layer only. In the substrate removal techniques used for detectors [23] and solar cells [24], the epitaxial layers are separated from their growth substrate by lapping and wet-etching the substrate [25], [26]. Usually, the epitaxial layers are protected with a high bandgap etch stop layer

(e.g., AlAsSb). Typically, the substrate is thinned down, and then, the remaining is wet-etched. The solution employed to etch the substrate must have a higher selectivity compared to the etch-stop layer. Then, if the etch-stop layer needs to be removed, a highly selective etchant must be used to avoid damage to the epilayer material of interest.

Electrical transport measurements in InAsSb and InAs/InAsSb T2SLs are challenging due to the semiconducting nature of the native growth substrate, namely GaSb. The substrate removal of InAsSb and the transfer to insulating substrates can enable a thorough investigation of electrical transport via variable-field VDP measurements and MCF analysis. While the GaSb substrate provides mechanical support during device fabrication, the substrate is undesirable in infrared detector cameras due to the highly conductive nature. For instance, GaSb substrates absorb much of the incoming radiation in the infrared range, thus reducing the Signal-to-Noise Ratio (SNR) [27]. Although a wide-bandgap layer is employed to prevent carrier injection from the substrate (e.g., insulating layer), it is still unclear which carriers identified by the multiple-carrier analysis belong to substrate, AlAsSb insulation layer, or interfaces [21].

The 2.0 µm *p*-type InAsSb sample processed with VDP configuration was cleaned and protected with photoresist (AZ4330, baked at 120°C for five minutes). Anything that etches AlAsSb will etch GaSb; therefore, AlAsSb and GaSb will both be etched by the HF solution. However, during the HF wet-etch, the InAsSb epilayer needs to be protected from the etchant. Figure 4.13 illustrates how if the *p*-type InAsSb sample sidewalls are not protected with photoresist, the epilayer will start to etch after about 11 minutes in the HF solution. The five steps taken for such work are shown in Figure 4.14 and summarized here.

Figure 4.13: *p*-type InAsSb VDP processed sample in the HF-based solution. The HF-based solution will etch away the GaSb substrate, the AlAsSb etch-stop, the GaSb buffer layers, and begin to etch the InAsSb epilayer since no photoresist sidewall protection was used.

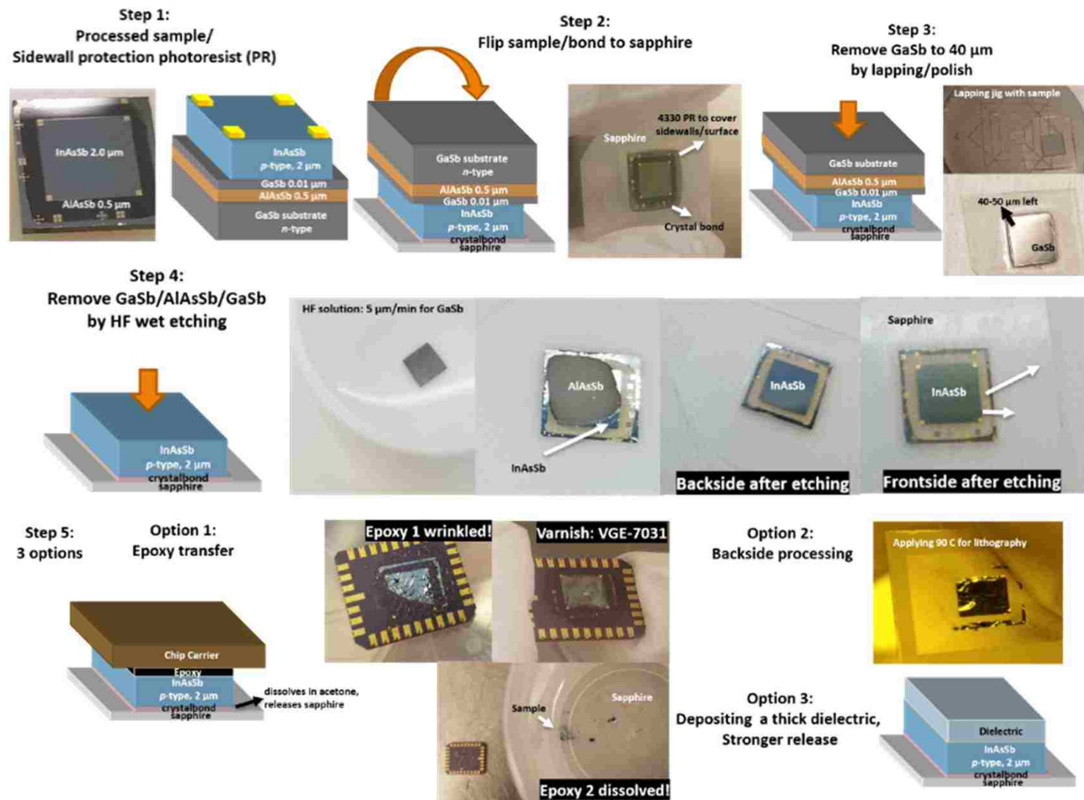

Figure 4.14: Steps and pictures taken on an attempt to remove the GaSb substrate, AlAsSb etch-stop, and the GaSb buffer for the *p*-type InAsSb lateral transport samples.

As shown in Figure 4.14, Step 2, the sample was bonded (substrate side up) to a sapphire carrier with Crystalbond^{TM} 509 adhesive on a hot plate at a temperature of 120°C. Once the sample cools down, the lapping/polishing process starts. As shown in Figure 4.14, Step 3, the sample is lapped/polished to 40-50 µm prior to HF acid wet-etching. In Figure 4.14, Step 4, the GaSb substrate is then fully removed using the HF solution [28] which

also etches the AlAsSb/GaSb layers but selectively stops at InAsSb. At this point, the sample is fragile since only the thin 2.0 μm InAsSb epilayer is left on the sapphire carrier. Soaking the sample in acetone will release the InAsSb layer, because the Crystalbond adhesive dissolves; however, it is troublesome to handle such a thin sample with tweezers. Therefore, several epoxies (T7110, VGE-7031) were employed in order to attempt to bond the InAsSb layer as shown in Figure 4.14, Step 5. The epoxies were supposed to be acetone resistant and be able to hold the sample uniformly. However, wrinkles, breaks, and unsuccessful InAsSb layer releases demonstrated a failed epoxy option.

Step 5, Option 2, shown in Figure 4.14, consisted of processing the back-side in order to deposit a dielectric layer in an effort to make the sample stronger for release, but the Crystalbond adhesive wrinkled when 90°C was applied for lithography patterning. Finally, Step 5, Option 3 was based on Renteria *et al.* [24] work which released InGaAs solar cells after removal of InP substrate by depositing a thick layer of metal before soaking and releasing the sample in acetone. However, the option for the *p*-type InAsSb sample would be to deposit a dielectric instead of metal. Due to the failed attempts to perform photolithography of such samples, the dielectric deposition option was not further pursued. The failed attempt provided the background for the successful substrate removal method reported in Chapter 6 for vertical transport samples or Metal-Semiconductor-Metal (MSM) structures.

4.6 Conclusions

Temperature and magnetic-field-dependent measurements in conjunction with Multi-Carrier Fit (MCF) analysis were used to characterize the transport properties of Be-doped lattice-matched $InAs_{0.91}Sb_{0.09}$ grown on a GaSb substrate. The MCF analysis was employed

to uniquely identify the different conducting carrier populations and their respective mobilities in the structure. The primary hole conductivity was confirmed to be that of the bulk hole in InAsSb. The bulk hole concentrations and mobilities at 77 K (300 K) are 1.6×10^{18} cm^{-3} (2.3×10^{18} cm^{-3}) and 125 cm^2/Vs (60 cm^2/Vs) indicating that the Be dopants are 100% ionized at room temperature and are 70% ionized at 77 K.

A surface treatment experiment was conducted and correlated one of the electron conducting populations to the surface. The two remaining carriers are native to the InAsSb/GaSb/AlAsSb interface, as the experimentally measured sheet charge concentrations are consistent with the carrier concentrations modeled using the NRL MULTIBANDS® model. Variable temperature (15 – 390 K) measurements confirmed the different carrier species present in the sample and enabled the extraction of the bulk hole, interface carriers, and surface electron transport properties. For the bulk carrier, thermal activation of intrinsic carriers at high temperatures (320 – 390 K) with a bandgap of $E_G \sim$ 258 meV was found, which was comparable to the modeled room temperature $InAs_{0.91}Sb_{0.09}$ bandgap of ~270 meV. Also, the low-temperature slope suggested a Be-doping activation energy of $E_A \sim 22$ meV. Temperature analysis confirmed a surface carrier electron with resulting mobilities and sheet concentrations at 30 K (300 K) of 4500 cm^2/Vs (4300 ± 100 cm^2/Vs) and 5.6×10^{10} cm^{-2} ($6\times10^{10} \pm 2\times10^{10}$ cm^{-2}), respectively. Finally, a substrate removal attempt for the lateral *p*-type InAsSb samples is presented which serves as the foundation for the processing technique presented in Chapter 6 for vertical transport.

4.7 References

[1] L. K. Casias *et al.*, “Carrier concentration and transport in Be-doped InAsSb for infrared sensing applications,” *Infrared Phys. Technol.*, vol. 96, pp. 184–191, 2019.

[2] E. M. Lysczek, J. A. Robinson, and S. E. Mohney, “Ohmic contacts to p-type InAs,” *Mater. Sci. Eng. B*, vol. 134, no. 1, 2006.

[3] W. A. Beck and J. R. Anderson, “Determination of electrical transport properties using a novel magnetic field-dependent Hall technique,” *J. Appl. Phys.*, vol. 62, no. 2, 1987.

[4] Z. Dziuba and M. Gorska, “Analysis of the electrical conduction using an iterative method,” *J. Phys. III*, vol. 2, 1992.

[5] A. E. Brown, “Application of Mobility Spectrum Analysis to Modern Multi-layered IR Device Material,” University of Illinois at Chicago, 2015.

[6] D. Lackner *et al.*, “InAsSb and InPSb Materials for Mid Infrared Photodetectors,” in *22nd International Conference on Indium Phosphide and related Materials (IPRM), IEEE*, 2010.

[7] H. . Wieder, “Transport coefficients of InAs epilayers,” *Appl. Phys. Lett.*, vol. 25, no. 4, 1974.

[8] S. . Watkins, C. . Tran, R. Ares, and G. Soerensen, “High mobility InAs grown on GaAs substrates using tertiarybutylarsine and trimethylindium,” *Appl. Phys. Lett. 66*, vol. 66, no. 7, 1995.

[9] M. Noguchi, K. Hirakawa, and T. Ikoma, “Intrinsic electron accumulation layers on reconstructed clean InAs (100) surfaces,” *Phys. Rev. Lett.*, vol. 66, no. 17, 1991.

[10] L. Ö. Olsson, C. B. M. Andersson, M. C. Håkansson, J. Kanski, L. Ilver, and U. O. Karlsson, “Charge Accumulation at InAs Surfaces,” *Phys. Rev. Lett.*, vol. 76, no. 19, 1996.

[11] G. R. Bell, T. S. Jones, and C. F. McConville, “Accumulation layer profiles at InAs polar surfaces,” *Appl. Phys. Lett.*, vol. 71, no. 25, 1997.

[12] Y. Lin, A. R. Arehart, A. M. Carlin, and S. A. Ringel, “Separation of bulk and surface electron transport in metamorphic InAs layers using quantitative mobility spectrum analysis,” *Appl. Phys. Lett.*, vol. 93, no. 6, 2008.

[13] G. Tuttle, H. Kroemer, and J. H. English, “Effects of interface layer sequencing on the transport properties of InAs/AlSb quantum wells: Evidence for antisite donors at the InAs/AlSb interface,” *J. Appl. Phys.*, vol. 67, no. 6, 1990.

[14] G. a. Umana-Membreno *et al.*, “Vertical transport in InAs/GaSb type-II strained-layer superlattices for infrared focal plane array applications,” *Proc. SPIE*, vol. 80120Y, 2011.

[15] S. P. Svensson *et al.*, “Background and interface electron populations in InAs 0.58 Sb 0.42,” *Semicond. Sci. Technol.*, vol. 30, no. 3, 2015.

[16] L. F. J. Piper, T. D. Veal, M. J. Lowe, and C. F. Mcconville, “Electron depletion at InAs free surfaces : Doping-induced acceptorlike gap states,” *Phys. Rev. B*, vol. 73, no. 19, 2006.

[17] J. B. Rodriguez *et al.*, “nBn structure based on InAs/GaSb type-II strained layer superlattices,” *Appl. Phys. Lett.*, vol. 91, no. 4, 2007.

[18] R. Chaghi, C. Cervera, H. Aït-Kaci, H. Grech, J. . Rodriguez, and P. Christol, “Wet etching and chemical polishing of InAs / GaSb superlattice photodiodes,” *Semicond. Sci. a*, vol. 24, no. 6, 2009.

[19] L. Mcghee, I. Nicol, R. D. Peacock, M. I. Robertson, R. Stevenson, and J. M. Winfield, “Halogen etching of group 13 – 15 (3 – 5) semiconductors and its relevance to chemical – mechanical polishing. The reactions of dibromine, dichlorine and sodium hypochlorite with gallium arsenide and related materials,” *J. Mater. Chem.*, vol. 7, no. 12, 1997.

[20] G. A. Umana-Membreno *et al.*, “Vertical minority carrier electron transport in p-type InAs/GaSb type-II superlattices,” *Appl. Phys. Lett.*, vol. 101, no. 25, 2012.

[21] A. E. Brown, N. Baril, D. Zuo, L. A. Almeida, J. Arias, and S. Bandara, "Characterization of n-Type and p-Type Long-Wave InAs/InAsSb Superlattices," *J. Electron. Mater.*, vol. 46, no. 9, pp. 5367–5373, 2017.
[22] S. Kawaji and H. C. Gatos, "Electric field effect on the magnetoresistance of Indium Arsenide surfaces in high magnetic fields," *Surf. Sci.*, vol. 7, no. 2, 1967.
[23] B. Klein, J. Montoya, N. Gautam, and S. Krishna, "Selective InAs / GaSb strained layer superlattice etch stop layers for GaSb substrate removal," *Appl. Phys. A*, vol. 111, no. 2, 2013.
[24] E. J. Renteria, "Integration of Thin Film TPV Cells to CVD Diamond Heat Spreaders," University of New Mexico, 2017.
[25] P.-Y. Delaunay, B. M. Nguyen, D. Hofman, and M. Razeghi, "Substrate removal for high quantum efficiency back side illuminated type-II InAs/GaSb photodetectors," *Appl. Phys. Lett.*, vol. 91, no. 23, 2007.
[26] R. Rehm *et al.*, "Substrate removal of dual-colour InAs/GaSb superlattice focal plane arrays," *Phys. Status Solidi*, vol. 9, no. 2, 2012.
[27] S. M. Zamiri, "Antimonide-based superlattice membranes for infrared applications," University of New Mexico, 2016.
[28] J. Fastenau, E. Ozbay, G. Tuttle, and F. Laabs, "Epitaxial Lift-Off of Thin InAs Layers," *J. Electron. Mater.*, vol. 24, no. 6, 1995.

Chapter 5

n-type InAsSb and InAs/InAsSb Type-II Strained Layered Superlattices (T2SLs) Lateral Transport

5.1 Introduction

This chapter is devoted to the lateral transport measurements of Mid-Wavelength Infrared (MWIR) *n*-type $InAs_{0.91}Sb_{0.09}$ alloys and $InAs/InAs_{0.65}Sb_{0.35}$ Type-II Strained Layered Superlattices (T2SLs). III-V materials such as InAsSb and T2SL, offer an alternative to the Mercury Cadmium Telluride (MCT) technologies and their fundamental lateral transport properties will be investigated in this chapter, beginning with ternary alloy materials, and later InAs/InAsSb T2SLs. The lateral transport properties of all the carriers (bulk, surface, and interface) of *n*-doped InAsSb alloys and InAs/InAsSb MWIR T2SLs grown on GaSb substrates were determined using temperature- and magnetic-field-dependent transport measurements in conjunction with Multi-Carrier Fit (MCF). Results are presented for alloy and T2SL structures with absorber regions grown with doping concentrations: (1) 1×10^{15} cm^{-3} or Non-Intentionally Doped (*NID*); and, (2) 1×10^{16} cm^{-3} intentionally Si-doped (*n*-type).

The aim of this chapter is to gain a better understanding of lateral transport properties in III-V material systems used in infrared (IR) photodetectors, as well as the determination of ways that multiple-carrier analysis may aid in deducing the different carriers present in such systems. Finally, using the T2SL lateral transport mobility results presented in this chapter, the true vertical transport mobility was calculated in Chapter 6. To the best of our knowledge, there has been only a few reports [1]–[3] on the extraction of all the different lateral carriers (bulk, interface, and barrier-interface) contributing to transport in *n*-type InAsSb and *n*- plus *p*-type InAs/InAsSb T2SL material systems using Mobility Spectrum Analysis (MSA), which served as an important reference for the work reported here.

A surface treatment experiment conducted in this work correlated one of the electron conducting populations to the surface of the samples. The remaining carriers are native to the InAsSb/GaSb/AlAsSb interface, as the experimentally measured sheet charge concentrations are close to the carrier concentrations modeled using the NRL MULTIBANDS® at 300 K. Variable temperature (20 – 375 K) measurements extracted the different carrier species present in the samples and enabled the extraction of the bulk electron, interface carriers, and surface electron transport properties. Transport properties extracted for the *n*-type InAsSb alloy and the InAs/InAsSb T2SL samples are summarized in Tables 5.5-5.8 and Tables 5.9-5.12 for temperatures 77 and 300 K, respectively. Finally, minority carrier (hole) lateral diffusion lengths are extracted using lifetime and mobility measurements for the *NID* InAs/InAsSb T2SL sample at 100 K.

The lateral transport properties reported in this work for isotropic (InAsSb alloys) and anisotropic (InAs/InAsSb T2SLs) materials can be used to decouple bulk carrier

vertical transport properties. Conventional transport measurements such as variable-field Hall Effect can suffice for lateral transport diagnostics; however, vertical transport is a more challenging task that is undertaken in Chapter 6.

5.2 Surface Conductivity

One of the major issues that impedes the development of III-V Sb-based IR materials is surface passivation [4]. For infrared detectors, poor mesa sidewall passivation leads to unwanted *n*-type surface leakage currents which act as another source of dark-current [5]. Many groups have tried to tackle the passivation issue throughout the years [6]. However, presently, the surface electron layer has not been eliminated with any simple passivation process and thus remains a challenge. The issue of surface passivation for III-V Sb-based IR materials also plagues simple material characterization work, such as transport measurements where surface conduction is a strong contributor to the total conduction. In the lateral transport measurements reported in this dissertation, to mitigate the effects of the surface layer, the separation of such conduction proved to be sufficient. This separation is accomplished using variable temperature- and magnetic-field-dependent measurements in conjunction with a multi-carrier fitting routine.

In *p*-type InAs material, charge carrier sign-inversion in *p*-doped samples has occurred [7]. Due to the surface electron accumulation layer, *p*-type layers appear *n*-type below a certain carrier concentration as the surface layer dominates the conduction [8], [9]. In addition to *p*-type material, there will be surface electrons in *n*-type material. Therefore, for both *p*- and *n*-type material, performing a simple single -field and -temperature measurement will result in a measured conductivity affected by the surface conduction, which provides an erroneous bulk carrier concentration and mobility result.

The surface conductivity in InAs and $InAs_{1-x}Sb_x$ has been studied for several decades as shown in Table 5.1. Surface charge effects are due to the formation of an electron accumulation layer in the near-interface region, which causes an unusual tendency of InAs to adjust its energy bands in such a way that the Fermi level becomes located above the conduction band minimum (CBM) [7]. The electrical properties of the surface accumulation layer have not shown any significant dependence on temperature [1], [9], [10]. In nBn barrier structures, a similar electron accumulation layer at the surface remains. For instance, it was reported that for III – V infrared barrier detectors composed of T2SL material, when an absorbing layer possessed opposite conductivity types in its bulk and at its surface layer, unipolar barriers were insufficient to eliminate surface leakage [11]. Hence, the existence of surface Fermi level pinning in III–V infrared detector materials require that careful consideration is given to the surface conductivity type and the relation between surface and bulk conductivities.

Table 5.1 provides a summary of the electron surface accumulation layers found in InAs, InAsSb, and InAs/InAsSb T2SLs using different measurement techniques. Some of the techniques listed are magneto-transport (Magneto), High-Resolution-Electron-Energy-Loss-Spectroscopy (HREELS), Angle-Resolved Photoemission Spectroscopy (ARPES), and a two-layer model (two-layer) [12]. Surface concentration and mobility are denoted as n_s and μ_s. The average surface layer results shown for InAsSb and InAs/InAsSb T2SL in Table 5.1 served as the basis for the NRL MULTIBANDS® simulations presented in this work.

Table 5.1: Summary of surface properties reported for InAs, $InAs_{1-x}Sb_x$ and InAs/ $InAs_{1-x}Sb_x$ T2SLs using different measurement techniques. Surface concentration and mobility are denoted as n_s and μ_s.

Material	Type	Substrate	Temp. K	Concentration n_s cm^{-2}	Mobility μ_s cm^2/Vs	Method	Reference
InAs	*p*		4.2 - 77	5.0×10^{11}	5×10^3	Magneto	Kawaji *et al.* [13]
InAs	*n*	GaAs	77, 300	1.1×10^{12}	1.5×10^4	Magneto	Brown [1]
InAs	*n*	InAs	77	5.0×10^{11} - 1.0×10^{12}		HREELS	Noguchi *et al.* [14]
InAs	*n*	InAs		4.0×10^{11} - 7.5×10^{11}		HREELS	Bell *et al.* [15]
InAs	*p*	InAs		1.0×10^{12}		ARPES	Olson *et al.* [7]
InAs	*n*	InP	300	4.0×10^{12}	2.4×10^3	Magneto	Lin *et al.* [16]
InAs	*n*	GaAs	77	1.0×10^{12}	2×10^4	Magneto	Holmes *et al.* [17]
$InAs_{1-x}Sb_x$ x=0.9	*n*	GaSb	77	5.7×10^{11}	1.3×10^4	Magneto	Brown [1]
InAsSb x=0.42	*n*	GaSb	77	5.5×10^{11}	4.5×10^3	Magneto	Svensoon *et al.* [3]
InAsSb x=0.1	*n*	GaAs	77	1.0×10^{13}	2.0×10^3	two-layer	Krug *et al.* [9]
InAsSb x=0.9	*p*	GaSb	77	6.0×10^{10}	4.3×10^3	Magneto	Casias *et al.* [18]
InAs/InAsSb x = 0.5	*n*	GaSb	77	5.3×10^{12}	1.0×10^4	Magneto	Brown [1]
InAs/InAsSb x = 0.5	*n*	GaSb	77	6.3×10^{11}	1.3×10^4	Magneto	Brown [1]
InAs/InAsSb x = 0.5	*p*	GaSb	77	3.9×10^{11}	8.5×10^3	Magneto	Brown [1]

5.3 Samples and Methods

5.3.1 Device Structures

For the study presented here, four samples were grown on *n*-type (*Te*-doped) GaSb substrates using Molecular Beam Epitaxy (MBE). Each pair of structures is demonstrated in Figure 5.1 (a) and (b), where each structure is shown with two doping concentrations. Figure 5.1 (a) consists of a 2 µm thick lattice-matched $InAs_{0.91}Sb_{0.09}$ bulk layer with undoped (*NID* or *n*-type 1×10^{15} cm^{-3}) and with an *n*-type Si-doping concentration of 1×10^{16} cm^{-3}. The InAsSb layers are grown on top of a 0.01 µm thick undoped GaSb layer on a 0.5 µm thick lattice-matched and undoped $AlAs_{0.08}Sb_{0.92}$ insulating layer. Figure 5.1 (b) consists of a 2 µm thick lattice-matched InAs/$InAs_{0.65}Sb_{0.35}$ T2SL layer with undoped (*NID* or *n*-type 1×10^{15} cm^{-3}) and with an *n*-type Si-doping concentration of 1×10^{16} cm^{-3}. The superlattice layer consists of 4.63 nm of InAs plus 1.06 nm of $InAs_{0.65}Sb_{0.35}$. The superlattice layers are grown on top of a 0.01 µm thick undoped GaSb layer on a 0.5 µm thick lattice-matched and undoped $AlAs_{0.08}Sb_{0.92}$ insulating layer. The fabricated sample diagrams are provided in Figure 5.1 (a), (b) with Van der Pauw (VDP) configuration.

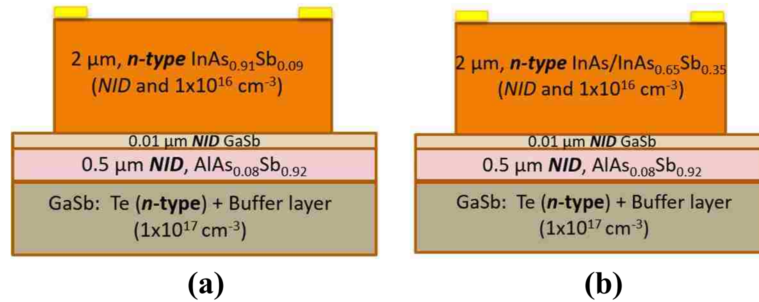

Figure 5.1: Schematics of the fabricated *n*-type samples in Van der Pauw (VDP) configuration, (a) 2-dimensional InAsSb sample cross section (b) 2-dimensional InAs/InAsSb T2SL sample cross section with two doping concentrations (*NID* and Si-doped at 1×10^{16} cm^{-3}).

The wide-bandgap AlAsSb insulating layer acts to remove the conductive pathway of the substrate effectively. The 0.01 μm thick GaSb layer was necessary to produce high-quality InAsSb and InAs/InAsSb T2SL samples.

5.3.2 Material Characterization

X-Ray Diffraction (XRD) performed at Sandia National Laboratories (SNL) assessed the structural quality of as-grown InAsSb alloy and InAs/InAsSb T2SL materials. Representative XRD plots provided by SNL for the four samples (two InAsSb and two InAs/InAsSb T2SLs) are shown in Figure 5.2. As shown in Figure 5.2 (a) and (b), the overall periodicity of the absorber material, the full width at half maximum (FWHM) value of the 1st satellite T2SL peak, and the lattice mismatch between the GaSb substrate and the T2SL were extracted from the XRD measurements. Also, SNL provided Nomarski images to verify the clean surface morphology for all four *n*-type samples used in this work, as shown in Figure 5.3 (a) - (d).

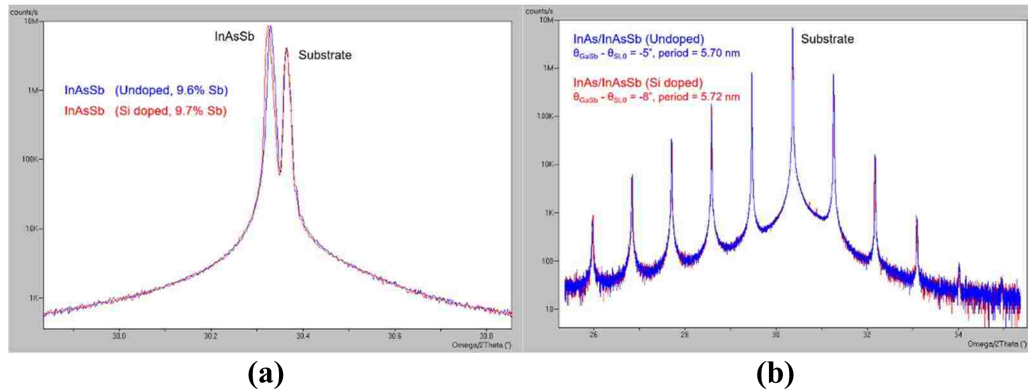

Figure 5.2: XRD characterization for the *n*-type samples (a) InAsSb undoped (blue) and Silicon-doped (red), (b) InAs/InAsSb T2SL undoped (blue) and Silicon-doped (red).
**Data provided by Sandia National Laboratories (SNL)*

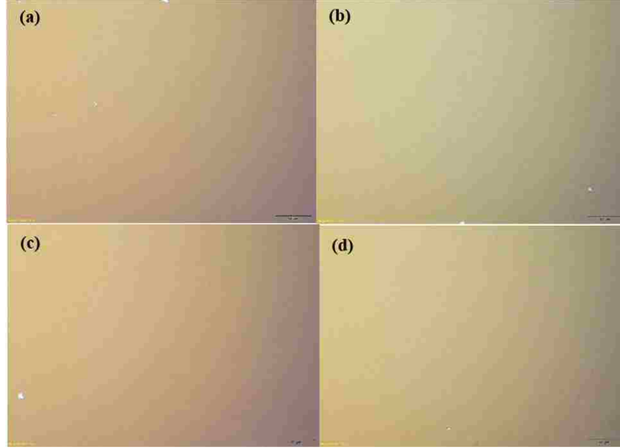

Figure 5.3: Nomarski images comparing surface morphology of (a) Non-Intentionally Doped (*NID*) InAsSb (b) Si-doped InAsSb (c) *NID* InAs/InAsSb T2SL (d) Si-doped InAs/InAsSb T2SL. **Images provided by SNL*

The optical quality of the as-grown structures was evaluated by photoluminescence (PL) and lifetime (LT) measurements at SNL. PL maps were done using double modulation Fourier-Transform Infrared Spectroscopy (FTIR) with a pump laser at 1550 nm and a 2.4 μm long pass to filter out the pump beam. A skewed Gaussian function was employed to fit the PL spectra. LT maps were obtained using Time-Resolved Microwave Reflectance (TMR) at 94 GHz with a pump laser at 1535 nm. The TMR signal was averaged over 5,000-30,000 waveforms to generate the final data for the fit. Then, an automated fitting routine for the lifetimes is performed. For the PL and LT maps, measurements are performed in 5mm increments. For illustration, Figure 5.4 shows the PL and LT results for the *n*-type InAsSb Non-Intentionally Doped (*NID*) sample. The other PL/LT maps provided by SNL are included in Appendix A for reference.

Four *n*-type samples were grown for lateral transport studies and are summarized in Table 5.2: Sample 1 (InAsSb *NID*-1×10^{15} cm^{-3}), Sample 2 (InAsSb Si-doped-1×10^{16} cm^{-3}), Sample 3 (InAs/InAsSb T2SL *NID*-1×10^{15} cm^{-3}) and sample 4 (InAs/InAsSb T2SL Si-doped-1×10^{16} cm^{-3}).

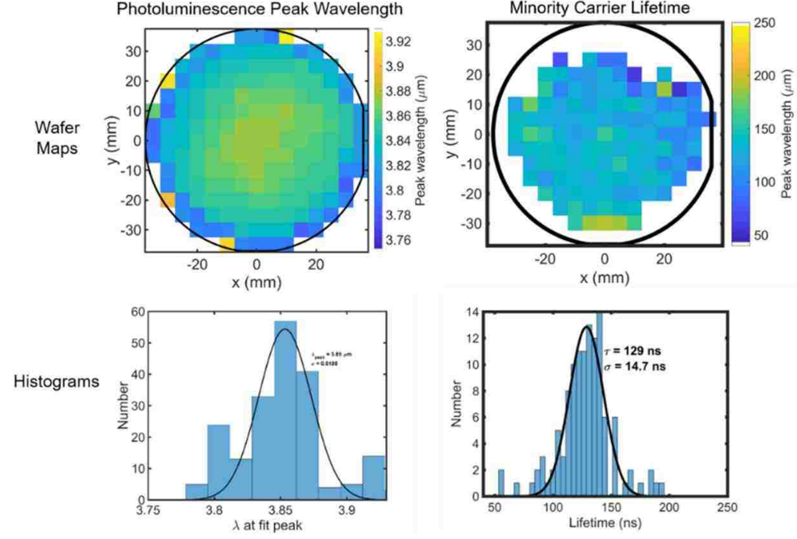

Figure 5.4: Photoluminescence (PL) and Lifetime (LT) measurements for Non-Intentionally Doped (*NID*) InAsSb sample, (top) *x*-*y* wafer maps and (bottom) histograms. **Data provided by SNL*

Table 5.2: Four *n*-type InAsSb alloy and InAs/InAsSb T2SL samples grown by MBE for lateral transport measurements with structure, doping, lifetime at 100 K and PL peak wavelength at 80 K summarized.

	Structure	#	Doping (cm^{-3})	Lifetime @ 100K (μs)	PL peak @ 80 K (μm)	Run #
***n*-type**	Bulk InAsSb: Lateral Transport	1	1×10^{15} cm^{-3} (*NID*)	0.129	3.88	GN1302
		2	1×10^{16} cm^{-3} (Si-doped)	0.047	3.91	GN1298
	InAs/InAsSb: Lateral Transport	3	1×10^{15} cm^{-3} (*NID*)	1.45	5.14	GN1288
		4	1×10^{16} cm^{-3} (Si-doped)	0.25	5.2	GN1287

5.3.3 Fabrication and Electrical Characterization

Standard optical photolithography was employed to define 5 mm × 5 mm square mesas in the Van der Pauw (VDP) configuration. Wet-etching was used to create mesas using a citric acid based etch (citric acid:H_2O_2(30%) = 5:1) at room temperature. The resulting mesa etch depth was 2.0 μm confirmed with stylus profilometry for all four samples. Any native oxide film grown on the sidewalls of the mesas was removed by a 30-second etch in a diluted hydrochloric solution (HCl:$H_2$0= 1:20). Finally, 300 μm × 300 μm corner contacts were

defined with a 25 µm offset from the edge of the mesa as shown in Figure 5.5 (a) microscope and (b) SEM images. The 25 µm offset employed on this lithography step accounted for any edge non-uniformities from wet-etching. Contact formation with Ti (500 Å)/Pt (500 Å) /Au (3000 Å) was used followed by top-surface wire-bonding.

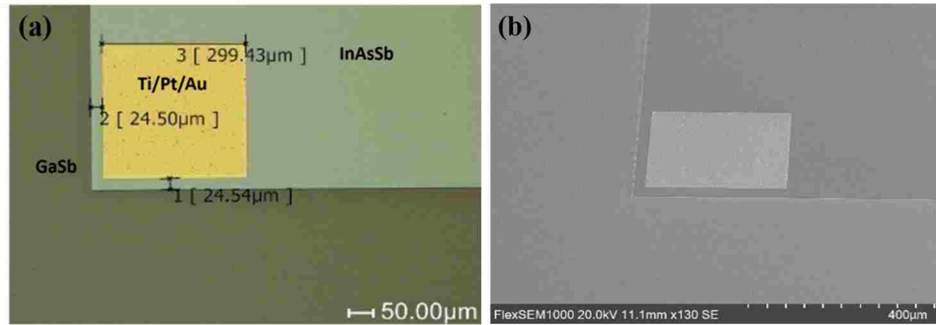

Figure 5.5: (a) Microscope and (b) SEM images of the *n*-type Si-doped InAsSb sample, showing sample edge with 300 µm × 300 µm corner lateral contact placement and a 25 µm offset from the edge of the mesa.

Figure 5.6 shows the SEM image of over-the-side (lateral) contacts deposited using e-beam evaporation in the *n*-type Si-doped (1×10^{16} cm^{-3}) InAsSb sample, with lighter areas indicating Au (gold) and inset showing the mesa sidewall depth of 2 µm.

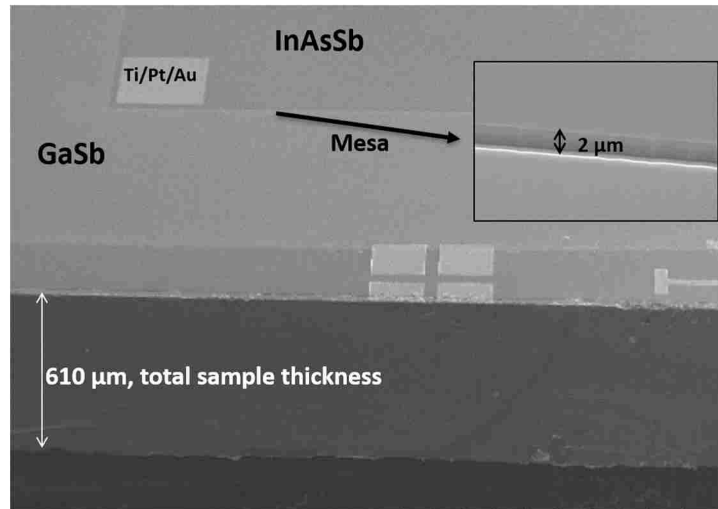

Figure 5.6: SEM image of over-the-side (lateral) contacts deposited using e-beam evaporation on the Si-doped (1×10^{16} cm^{-3}) InAsSb sample, with lighter areas indicating Au (gold) and inset showing the mesa sidewall depth of 2 µm.

After fabrication, contacts need to be verified to be ohmic by applying current across a pair of contacts and reading the voltage across the same contacts ($R_{1212} = R_{I+I-V+V-}$). If the contacts are ohmic, the current-voltage (I-V) curves are straight lines for all configurations. The contacts were verified to be ohmic for all samples and temperatures of interest. Figure 5.7 shows the I-V behavior for the four n-type samples at 300 K for (a) InAsSb and (b) InAs/InAsSb T2SL samples under the two different absorber doping concentrations (*NID* and Si-doped).

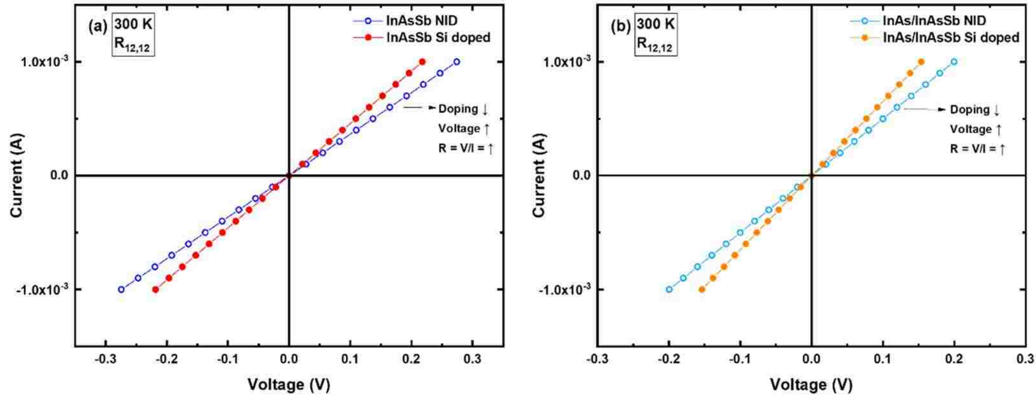

Figure 5.7: Current-voltage (I-V) behavior for the four n-type samples at 300 K, (a) InAsSb and (b) InAs/InAsSb T2SL samples under the two different absorber doping concentrations (*NID* and Si-doped).

As shown in Figure 5.7 (a) and (b), resistance ($R = \frac{V}{I}$), increases with lower doping concentration ($n = N_d$) if all other parameters are kept constant, which is consistent with the equation for resistance:

$$R = \frac{1}{qn\mu_n}\frac{L}{wt} \tag{5.1}$$

whereas q is the electronic charge, μ_n is the mobility, and L, w, t are the length, width, and thickness of the sample. The resistance change with doping lends some confidence to the fact that a device is being measured and not attributed to a cable or fixture leakage.

After I-V measurements and confirmation of ohmic contacts, variable-field Hall Effect measurements are performed on the LakeShore 9509 Hall Measurement System (HMS) with a 9-Tesla maximum magnetic field intensity at a current of 100 μA. As summarized in Chapter 3, current reversal, field reversal, and two distinct Hall Effect configuration techniques are employed to minimize measurement errors. The HMS software controlled the electrical equipment for each run and provided sheet resistivity and Hall coefficients that were needed as inputs for the Multiple-Carrier Fit (MCF) analysis. All the analysis in this chapter was completed using MCF to extract both the number of carriers present with mobility and concentration values for each sample. Finally, both mobility and concentration values extracted were employed to calculate the sheet conductivity for each of the carriers in each sample using the equation $\sigma = \mu nq$, where μ, n and q represent the mobility, sheet carrier concentration, and electron charge, respectively. The MCF technique is discussed in more detail in Chapter 3, Section 3.6.2.2.

5.4 Simulations

Simulations are performed using the 8 x 8 k·p model software known as Naval Research Laboratory (NRL) MULTIBANDS®. This model was employed to extract the interface concentrations for InAsSb and InAs/InAsSb T2SL samples. The undoped GaSb interface layer was modeled as *p*-type with a concentration of ~ 8×10^{15} cm^{-3} as previously measured at 77 K [1]. In addition to the surface accumulation layer, the inclusion of the 0.01 μm GaSb layer between the epilayer (InAsSb or InAs/InAsSb T2SL) and AlAsSb insulating layer has the consequence of forming additional interface carriers, which are modeled in the following sections using NRL MULTIBANDS® at 300 K.

5.4.1 Undoped and Doped InAsSb Alloy Samples

For the $InAs_{0.91}Sb_{0.09}$ samples, Figure 5.8 (a) shows the band edge diagram and (b) shows the carrier concentration profile of the *NID* sample.

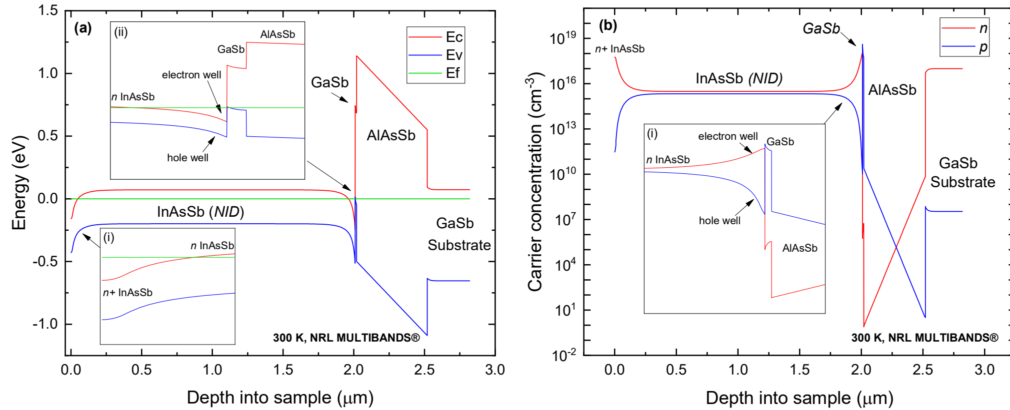

Figure 5.8: Non-Intentionally Doped (*NID)* InAsSb sample, (a) Energy band diagram vs. sample depth (b) Carrier concentration vs. sample depth showing the different layers in the sample structure, modeled using NRL MULTIBANDS® at 300 K. Figure 5.8 (a), inset (i) zooms in to the surface Fermi level pinning and inset (ii) provides a closer look of the electron and hole wells formed at the InAsSb/GaSb/AlAsSb interface. Figure 5.8 (b), inset (i) shows the electron and hole accumulations at the InAsSb/GaSb/AlAsSb interface.

Additionally, Figure 5.9 (a) shows the band edge diagram and (b) shows the carrier concentration profile of the Si-doped InAsSb sample.

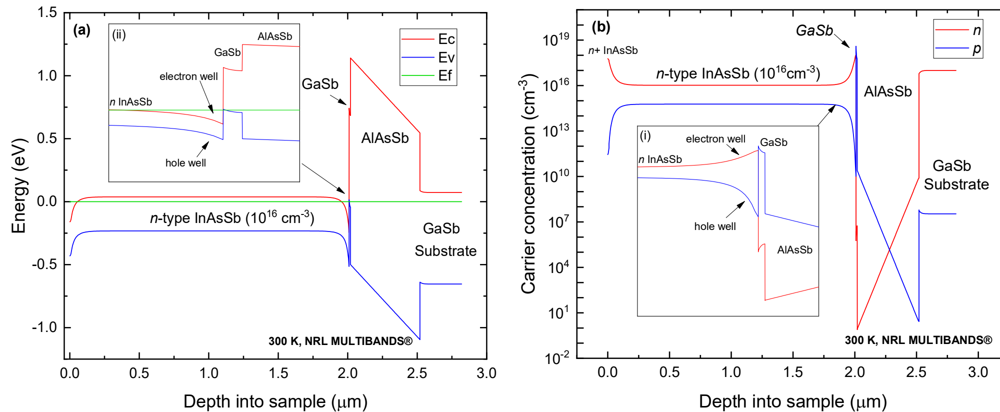

Figure 5.9: Silicon-doped InAsSb sample, (a) Energy band diagram vs. sample depth (b) Carrier concentration vs. sample depth showing the different layers in the sample structure, modeled using NRL MULTIBANDS® at 300 K. Figure 5.9 (a), inset (i) provides a closer look of the electron and hole wells formed at the InAsSb/GaSb/AlAsSb interface. Figure 5.9 (b), inset (i) shows the electron and hole accumulations at the InAsSb/GaSb/AlAsSb interface.

It is possible to combine information from different sources to get a self-consistent idea of the simulated parameters for the surface accumulation layer or Fermi level pinning. For instance, Bell *et al.* [15] provided insight into the thickness of the surface accumulation layer on InAs, reporting that the *n*-type layer was located in the top 10 nm. Then, combining information summarized in Table 5.1, a surface sheet concentration of 5.0×10^{11} - 1.0×10^{12} cm^{-2} is expected. Therefore, with the assumption that the surface accumulation length is the same as in InAs (10 nm) with a sheet concentration of 5.0×10^{11} cm^{-2}, then, a concentration of 5.0×10^{17} cm^{-3} can be used to model Fermi level pinning. These assumptions are employed to model the accumulation layer on each sample simulation presented.

5.4.2 Undoped and Doped InAs/InAsSb T2SLs

For the InAs/$InAs_{0.65}Sb_{0.35}$ T2SL samples, the energy band alignment modeled with NRL MULTIBANDS® at 300 K is shown in Figure 5.10. Electrons in the conduction band are confined to the InAs layer, while the heavy holes are confined to the InAsSb layer.

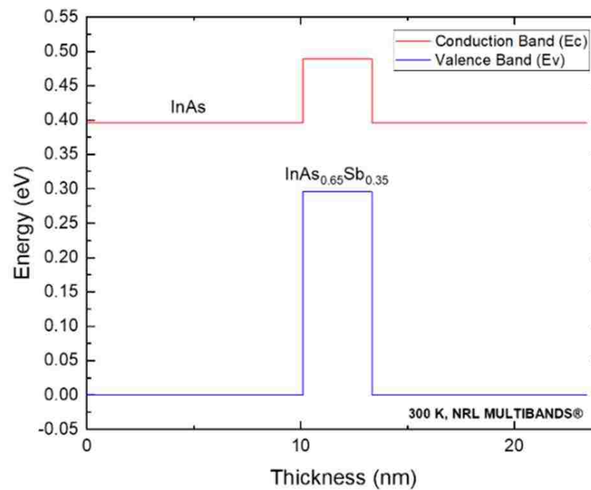

Figure 5.10: Energy band alignment for the InAs/$InAs_{0.65}Sb_{0.35}$ T2SL sample. Modeled using NRL MULTIBANDS® at 300 K.

Figure 5.11 presents the E vs. k dispersion relation which provides the electronic band structure of the $InAs/InAs_{0.65}Sb_{0.35}$ T2SL along the growth-axis (left portion) *z*-direction and lateral *x-y* direction (right portion). The C1, HH, and LH are the conduction, heavy hole, and light hole bands, respectively. The simulation shown in Figure 5.11 resulted in an effective superlattice bandgap, which is the separation between Conduction band - Heavy Hole (C1-HH) minibands, of 0.180 eV which equals a 6.9 µm cutoff at 80 K, confirming MWIR operation.

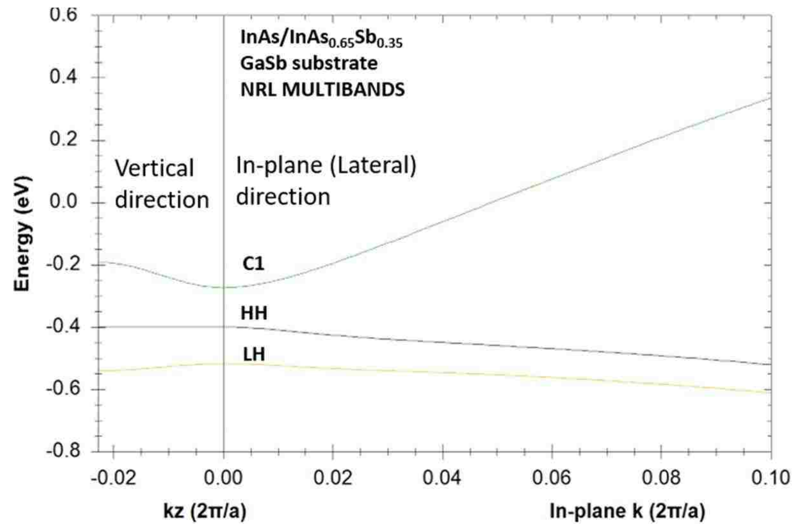

Figure 5.11: Energy band structure of MWIR $InAs/InAs_{0.65}Sb_{0.35}$ T2SL showing the vertical *z*-direction (left portion) and lateral *x-y* direction (right portion) using NRL MULTIBANDS®.

Effective mass anisotropy can be seen in Figure 5.11 for the *n*-type InAs/InAsSb T2SL samples in the lateral and vertical directions. A small band curvature translates into a heavier mass (lower mobility) while a large curvature translates into lighter mass (higher mobility). The heavy-holes (HH) tend to dominate the properties of the valence-band, their heavier effective mass results in much larger density of states compared to the light holes (LH).

As seen in Figure 5.11, the heavy-hole (HH) band in MWIR InAs/InAsSb T2SL shows very small band curvature behavior in the vertical direction, leading to a conclusion that a very low vertical hole mobility is expected. Finally, mobility values are dependent on the transport direction, with lateral mobilities exceeding mobilities in the vertical direction [1]. In this chapter, the focus will be on lateral transport properties of the InAs/InAsSb T2SL, whereas Chapter 6 will further discuss vertical transport properties.

Once the superlattice absorber layer was modeled, the entire *n*-type InAs/InAsSb T2SL structures are modeled and interface carrier concentrations estimated using NRL MULTIBANDS® at 300 K. Figure 5.12 (a) shows the band edge diagram and (b) shows the carrier concentration profile of the *NID* InAs/$InAs_{0.65}Sb_{0.35}$ T2SL sample. Then, Figure 5.13 (a) shows the band edge diagram and (b) shows the carrier concentration profile of the Si-doped InAs/$InAs_{0.65}Sb_{0.35}$ T2SL sample.

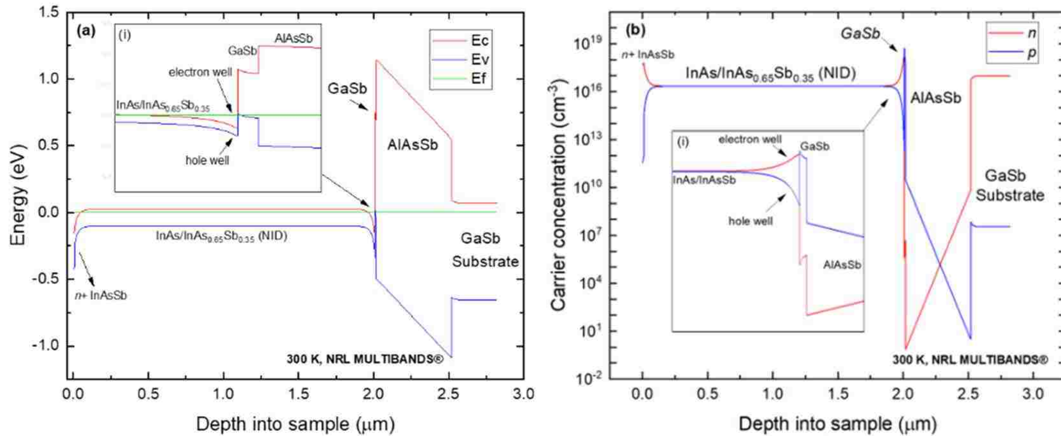

Figure 5.12: *NID* InAs/$InAs_{0.65}Sb_{0.35}$ T2SL sample, (a) Energy band diagram vs. sample depth (b) Carrier concentration vs. sample depth showing the different layers in the sample structure, modeled using NRL MULTIBANDS® at 300 K. Figure 5.12 (a), inset (i) zooms in to the surface Fermi level pinning and inset (ii) provides a closer look of the electron and hole wells formed at the T2SL/GaSb/AlAsSb interface. Figure 5.12 (b), inset (i) shows the electron and hole accumulations at the T2SL/GaSb/AlAsSb interface.

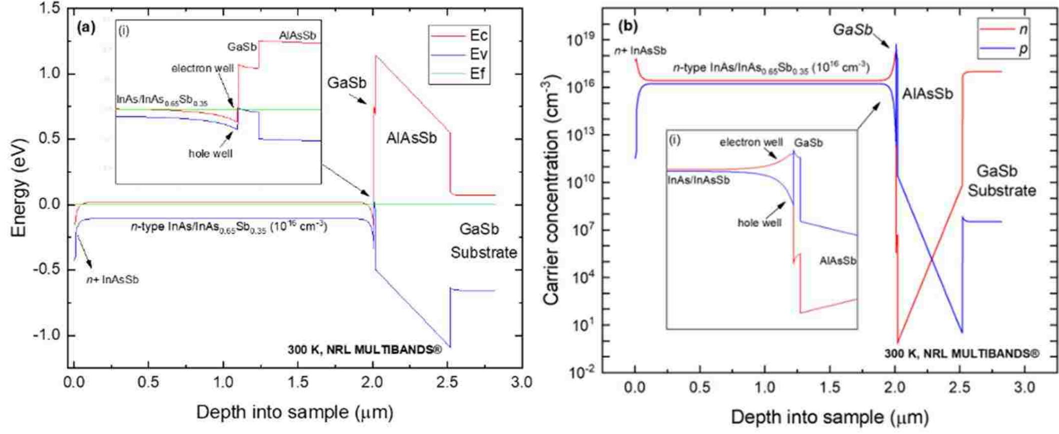

Figure 5.13: Silicon-doped $InAs/InAs_{0.65}Sb_{0.35}$ T2SL sample, (a) Energy band diagram vs. sample depth (b) Carrier concentration vs. sample depth showing the different layers in the sample structure, modeled using NRL MULTIBANDS® at 300 K. Figure 5.13 (a), inset (i) provides a closer look of the electron and hole wells formed at the T2SL/GaSb/AlAsSb interface. Figure 5.13 (b), inset (i) shows the electron and hole accumulations at the T2SL/GaSb/AlAsSb interface.

5.4.3 Interface Carriers Summary

As previously mentioned, the inclusion of the 0.01 μm GaSb layer between the absorber ($InAs_{0.91}Sb_{0.09}$ or $InAs/InAs_{0.65}Sb_{0.35}$ T2SL) and AlAsSb insulating layer has the consequence of forming additional interface carriers. The interface sheet concentrations of InAsSb/GaSb/AlAsSb and T2SL/GaSb/AlAsSb were modeled using NRL MULTIBANDS® at 300 K and summarized in Table 5.3.

Table 5.3: Summary of interface carrier concentrations for the *n*-type InAsSb and InAs/InAsSb T2SL samples modeled using NRL MULTIBANDS® at 300 K.

Sample	Interface electron Sheet concentration (cm^{-2})	Interface hole Sheet concentration (cm^{-2})
2 μm *NID* $InAs_{0.91}Sb_{0.09}$	1.6×10^{12}	1.16×10^{12}
2 μm Si-doped (10^{16} cm^{-3}) $InAs_{0.91}Sb_{0.09}$	1.7×10^{12}	1.15×10^{12}
2 μm *NID* $InAs/InAs_{0.65}Sb_{0.35}$	2.2×10^{12}	1.4×10^{12}
2 μm Si-doped (10^{16} cm^{-3}) $InAs/InAs_{0.65}Sb_{0.35}$	2.16×10^{12}	1.4×10^{12}

5.5 Results and Analysis

In the following sections, temperature- and magnetic-field-dependent transport measurements in conjunction with MCF analysis enabled the identification of the different carrier species in the four *n*-type $InAs_{0.91}Sb_{0.09}$ and $InAs/InAs_{0.65}Sb_{0.35}$ T2SL samples summarized in Table 5.2. The measurements resulted in the extraction of lateral transport properties for the bulk electron, surface electron, and interface carriers as a function of temperature. In addition, a bulk minority hole carrier is identified for the T2SL samples. A surface treatment experiment is conducted to correlate one of the electron conducting populations with conducting electrons at the surface of the samples. For each of the four samples, the concentrations of the interface carriers summarized in Table 5.3 are compared to the MCF results.

5.5.1 Sheet Resistivity Characterization

Before any multiple-carrier analysis, it is worth noting that all four *n*-type samples considered and summarized in Table 5.2, demonstrated a clear indication of the presence of multiple electrical carriers at all temperatures of interest. Magnetic-field dependent sheet resistivity measurements were utilized to demonstrate multi-carrier conduction in the samples; this is shown in Figures 5.14-5.15 (a)-(b).

When a single carrier is present in a sample, the plot of sheet resisitivity versus square of magnetic field ($\rho_S(B)$ vs. B^2) should be a straight line with a slope equivalent to the square of the carrier mobility. Thus, non-linear $\rho_S(B)$ vs. B^2 characteristics show a clear indication that more than one carrier is present. Figure 5.14 illustrates the sheet resistivity vs. B^2 results for the 2 μm $InAs_{0.91}Sb_{0.09}$ samples at 77 and 300 K for (a) *NID* and (b) Si-doped at 1×10^{16} cm^{-3}.

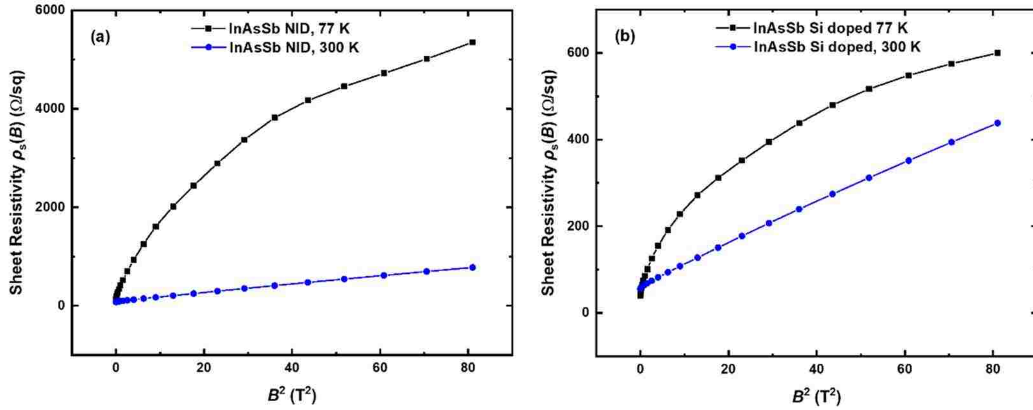

Figure 5.14: Sheet resistivity vs. B^2 results for the 2 µm *n*-type InAsSb samples at 77 K and 300 K for (a) *NID* and (b) Si-doped at 1×10^{16} cm^{-3}. The non-linear behavior indicates multiple-carrier conduction. *Note: Y-axis scaling obscures the fact that higher temperature (300 K) exhibit non-linear resistance behavior as a function of B^2.*

Figure 5.15 illustrates the sheet resistivity vs. B^2 results for the 2 µm *n*-type $InAs/InAs_{0.65}Sb_{0.35}$ T2SL samples at 77 and 300 K for (a) *NID* and (b) Si-doped at 1×10^{16} cm^{-3}. The non-linear behavior of sheet resistivity vs. B^2 shown in $InAs_{0.91}Sb_{0.09}$ and $InAs/InAs_{0.65}Sb_{0.35}$ T2SL samples indicate multiple-carrier conduction and motivate the use of MCF to measure transport characteristics precisely.

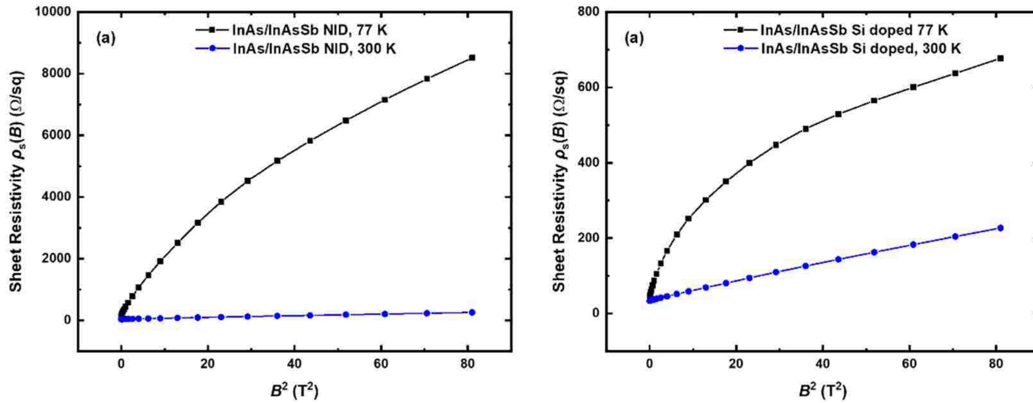

Figure 5.15: Sheet resistivity vs. B^2 results for the 2 µm *n*-type $InAs/InAs_{0.65}Sb_{0.35}$ T2SL samples at 77 K and 300 K for (a) *NID* and (b) Si-doped at 1×10^{16} cm^{-3}. The non-linear behavior indicates multiple-carrier conduction. *Note: Y-axis scaling obscures the fact that higher temperature 300 K exhibit non-linear resistance behavior as a function of B^2.*

Resistivity measurements can also be compared as a function of doping and as a function of temperature. For an n-type semiconductor, with $n = N_d$ representing the donor doping concentration, the sheet resistivity (ρ_s) is expressed as:

$$\rho_s = (tqN_d\mu_n)^{-1} \tag{5.2}$$

whereas t is the thickness, q is the electronic charge, and μ_n is the electron mobility. From Equation 5.2, it is expected that sheet resistivity (ρ_s) decrease with increasing doping concentration (N_d). Figure 5.14 (a) and (b) and Figure 5.15 (a) and (b) show the measured sheet resistivity decreasing as the doping concentration increases from *NID* to Silicon-doped. These results are expected as higher doping leads to higher conductivity or lower resistivity. In all the four samples, sheet resistivity is higher at 77 K compared to 300 K, indicating that the increase in dopant activation from 77 to 300 K is significant enough to overcome the decrease in mobility due to increased phonon (lattice) scattering.

5.5.2 Variable Field-Temperature Results for InAsSb

InAsSb alloy materials have been extensively studied throughout decades; the isotropic transport properties make the material straightforward to investigate and a prevailing candidate used for infrared detector applications. Still, the electron accumulation layer at the surface makes the identification of the bulk conductivity challenging. InAsSb material possesses the narrowest bandgap of ternary III-V detectors [19]. Two n-type $InAs_{0.91}Sb_{0.09}$ alloy structures were characterized: (1) *NID* and (2) Si-doped at 1×10^{16} cm^{-3}.

For both alloy structures, MCF was set up to allow for eight total possible carrier populations and identified four carrier populations: three electrons (*e1*, *e2*, *e3*) and one hole (*h1*). Temperature (15 – 390 K) and magnetic-field-dependent measurements in conjunction with MCF analysis were employed to characterize the transport properties of

the $InAs_{0.91}Sb_{0.09}$ samples. All the respective graphs shown in this section are compared for *NID* vs. Si-doped samples on the same *x-y* scales to emphasize their differences and similarities.

The sheet concentrations for each of the four carrier populations found in both $InAs_{0.91}Sb_{0.09}$ alloy samples are plotted as a function of temperature for *NID* and Si-doped in Figures 5.16 (a) and (b), respectively. For the *NID* alloy sample shown in Figure 5.16 (a), *e2* carrier dropped from the fitting at temperatures higher than 85 K, while *e2* does not drop from fitting in the Si-doped alloy sample results shown in Figure 5.16 (b).

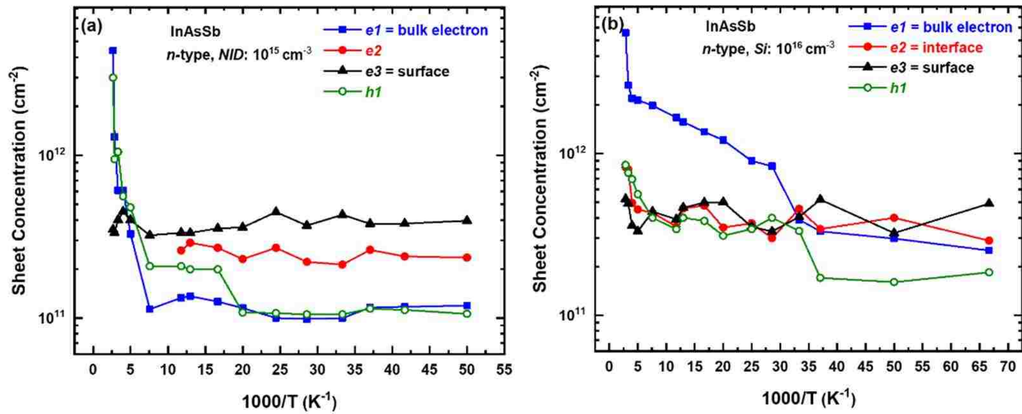

Figure 5.16: Sheet concentrations of the four resolved carrier populations in the *n*-type $InAs_{0.91}Sb_{0.09}$ alloy samples as a function of temperature for (a) *NID* and (b) Si-doped at 1×10^{16} cm^{-3}.

The carrier mobilities for each of the four carrier populations present in both $InAs_{0.91}Sb_{0.09}$ alloy samples are plotted as a function of temperature for *NID* and Si-doped in Figures 5.17 (a) and (b), respectively. Reference guidelines have been added to the mobility plots ($T^{-3/2}$) to represent lattice (phonon) scattering behavior.

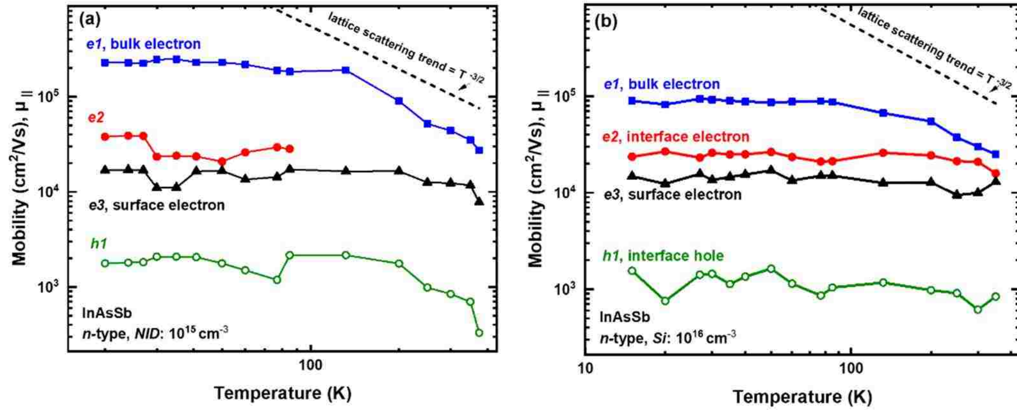

Figure 5.17: Mobilities of the four resolved carrier populations in the *n*-type $InAs_{0.91}Sb_{0.09}$ alloy samples as a function of temperature for (a) *NID* and (b) Si-doped at 1×10^{16} cm^{-3}. Reference guidelines have been added to the mobility plots ($T^{-3/2}$) to represent lattice (phonon) scattering behavior.

The sheet conductance was calculated using the mobility and sheet concentration results at each temperature. The calculated sheet conductivities for each of the four carrier populations present in both $InAs_{0.91}Sb_{0.09}$ alloy samples are plotted as a function of temperature for *NID* and Si-doped in Figures 5.18 (a) and (b), respectively.

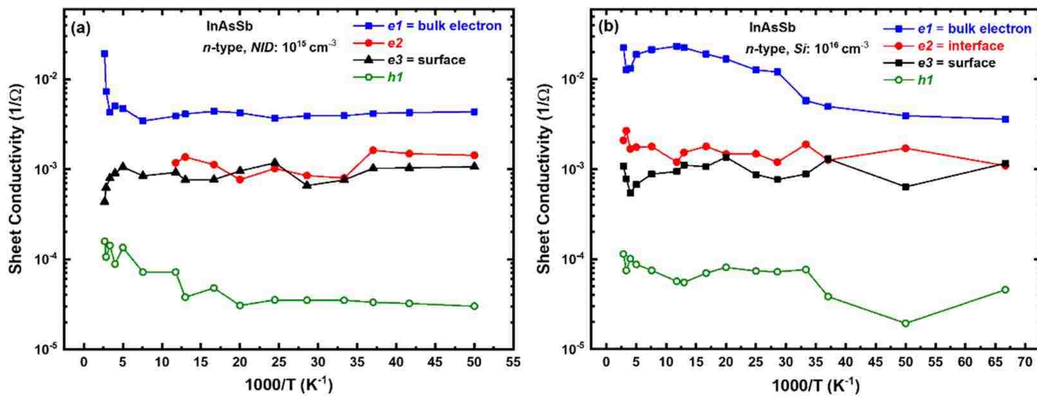

Figure 5.18: Sheet conductivities of the four resolved carrier populations in the *n*-type $InAs_{0.91}Sb_{0.09}$ alloy samples as a function of temperature for (a) *NID* and (b) Si-doped at 1×10^{16} cm^{-3}.

The carrier assignments for the InAsSb alloy samples shown in Figures 5.16, 5.17, and 5.18 are identified based on the following considerations.

Bulk electron carrier (*e1*)

Comparing InAsSb alloy material shown in Figures 5.16 (a) *NID* and (b) Si-doped, both samples are found to be *n*-type with a noticeable increase in sheet concentration for electron carrier (*e1)* as a function of doping. For instance, the *n*-type *e1* carrier population shown in Figures 5.16 (a) and (b) at 300 K resulted in sheet concentrations of *NID* (Si-doped) at 6.09×10^{11} cm^{-2} (3.00×10^{12} cm^{-2}) which translate into concentrations of 3.05×10^{15} cm^{-3} (1.50×10^{16} cm^{-3}) when taking the 2 μm bulk thickness into account. Hence, electron *e1* is the only carrier that demonstrates a considerable increase in sheet concentration as a function of doping, and closely matches the predicted concentrations at 300 K for *NID* at 3.05×10^{15} cm^{-3} and Si-doped at 1.50×10^{16} cm^{-3}.

Then, comparing mobility results in Figures 5.17 (a) *NID* and (b) Si-doped samples, the *e1* carrier population appears to be dominated by lattice scattering ($T^{-3/2}$) at high temperatures while *e2*, *e3,* and *h1* do not demonstrate a clear scattering dependence. Thus, *e1* is identified as the sole bulk electron carrier. At 77 K, mobility (concentration) results for carrier *e1* for the *NID* InAsSb sample are 1.89×10^{5} cm^2/Vs (7.00×10^{14} cm^{-3}). At 77 K, mobility (concentration) results for carrier *e1* for the Si-doped InAsSb sample are 8.90×10^{4} cm^2/Vs (8.00×10^{15} cm^{-3}).

Comparing previously reported values of *NID* (*n*-type) $InAs_{0.91}Sb_{0.09}$ at 77 K, Brown *et al.* [1] found a bulk electron with mobility (concentration) of 1.20×10^{5} cm^2/Vs (1.40×10^{15} cm^{-3}). Also, Svensson *et al.* [3] reported that for *n*-type doped (~8.00×10^{16} cm^{-3}) $InAs_{0.58}Sb_{0.42}$ at 77 K a bulk electron with mobility (concentration) of 1.40×10^{5} cm^2/Vs (2.40×10^{15} cm^{-3}) was found. Both InAs and InSb have relatively high electron mobilities, even at room temperature, due to the relatively small electron effective masses in the

compounds [20]. Hence, it is reasonable that the InAsSb alloy material will exhibit high mobility. Previously reported mobility values for *n*-type *NID* InAsSb bulk electron were found to be higher than 10^5 cm^2/Vs at low temperature [1] while for *n*-type doped (1.00×10^{16} cm^{-3}) at 77 K, the mobilities were found to exceed ~10^4 cm^2/Vs [3]. A similar mobility trend is seen in Figures 5.17 (a) and (b) for the bulk electron carrier *e1*. The closely reported transport values for the bulk electron found in similar alloy material further confirms that *e1* is associated with the bulk layer.

Comparing Figures 5.17 (a) and (b), as the doping is increased, the mobility of the bulk electron *e1* decreases while the other carrier populations stay relatively flat. The mobility reduction in the bulk electron carrier can be associated with an increase of Coulomb scattering. Finally, comparing sheet conductivity in Figures 5.18 (a) *NID* and (b) Si-doped, carrier *e1* showed the highest sheet conductivity out of the four carriers with the hole carrier *h1* having the lowest for both alloy samples.

Based on the listed comparisons, *e1* is identified as the bulk carrier electron, and Arrhenius analysis of the carrier concentration is performed in Figures 5.19 (a) *NID* and (b) Si-doped. The sharp increase of electron concentration for *e1* as the temperature increases from 300 to 390 K is likely to be due to increased thermal excitation across the bandgap as the material begins to enter the intrinsic regime.

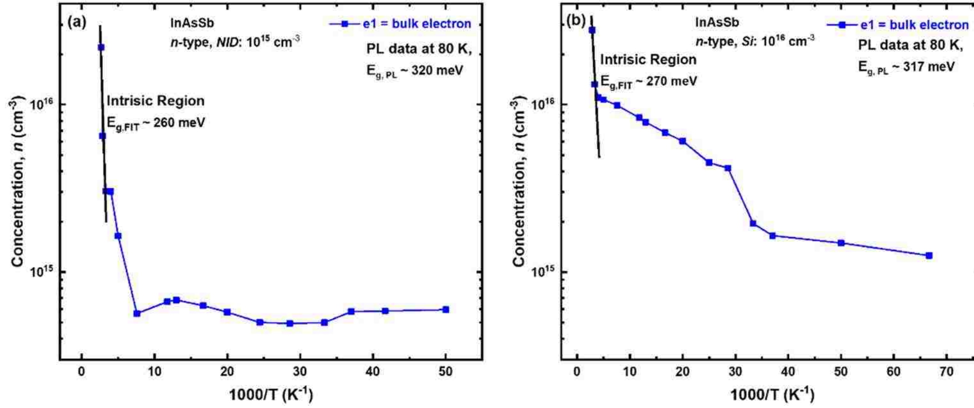

Figure 5.19: Bandgap and activation energy analysis of the intrinsic region for the bulk electron carrier (*e1*) in the InAsSb alloy samples for (a) *NID* and (b) Si-doped at 1×10^{16} cm^{-3}.

The intrinsic regime is indicated in Figures 5.19 (a) and (b) with a line fit at high temperatures that enables the extraction of the bandgaps, labeled E_{gFIT}. Arrhenius analysis at high temperatures of the *n*-type concentration for the *e1* bulk electron carrier (e.g., $\ln(n_{e1})$ vs. $1/k_B T$) indicates a thermal activation of intrinsic carriers at a bandgap energy of E_{gFIT} ~ 260 meV (*NID* InAsSb) and E_{gFIT} ~ 270 meV (Si-doped InAsSb). The fitted high-temperature bandgaps found are in the MWIR range, but slightly smaller than the bandgap energies of $E_{g,PL}$ ~ 320 meV (*NID* InAsSb) and $E_{g,PL}$ ~ 317 meV (Si-doped InAsSb) extracted from the PL measurements at 80 K, consistent with the observation that the energy bandgap of III-V semiconductors tends to decrease ~ 50-60 meV as temperature is increased to room temperature [21].

Surface (*e3*) and Interface carriers (*e2* and *h1*)

To differentiate which of the three unknown carriers (*e2*, *e3,* and *h1*) belonged to the surface of the sample, the *NID* InAsSb 2 μm alloy sample is dipped in 5.25% sodium hypochlorite (NaClO) and rinsed in deionized water in order to modify the surface properties as shown in Chapter 4, Section 4.4.2.1. Room temperature variable-field

measurements and MCF analysis are then repeated under the same conditions after the NaClO treatment. Similar chemical treatment has been employed on *n*-type and *p*-type InAsSb surfaces to identify the surface carrier population [3], [18]. At 300 K, for the *NID* InAsSb sample, only the *e3* carrier population exhibits a significant change in mobility and concentration pre- and post- chemical treatment from 1.24×10^{4} to 8250 cm^2/Vs and 4.00×10^{11} to 3.00×10^{12} cm^{-2}, respectively. The other carrier species are not severely impacted by the surface treatment, supporting a conclusion that *e3* is associated with the surface accumulation layer in the InAsSb samples. The sheet concentration values for the surface electron carrier (*e3*) are fairly consistent with previous reports [1], [3], [13], [14], and mobilities [1] found in similar materials. Also, the *e3* carrier population exhibits an approximately temperature-independent concentration which is indicative of surface electron accumulation commonly found in narrow-bandgap materials [10].

To investigate if the remaining two carrier populations (*e2* and *h1*) belonged to the InAsSb/GaSb/AlAsSb sample interface, the modeled sheet concentration values listed in Table 5.3 at 300 K are compared to experimental sheet concentrations from Figures 5.16 (a) and (b). Interface electron carrier (*e2*) for the Si-doped InAsSb sample at 300 K; the MCF extracted sheet concentration of 1.10×10^{12} cm^{-2} compared to a value of 1.70×10^{12} cm^{-2} determined using the NRL MULTIBANDS® software. For the Si-doped InAsSb sample at 300 K, the MCF extracted sheet concentration of 7.60×10^{11} cm^{-2} for an interface hole (*h1*) carrier compared to the modeled value of 1.15×10^{12} cm^{-2}. Hence, the NRL MULTIBANDS® simulations confirmed that electrons and holes are expected to accumulate at the InAsSb/GaSb/AlAsSb interface for both InAsSb alloy samples (see Table 5.3). Close agreement of the modeled interface sheet concentrations with the MCF

results supports the hypothesis that these unknown carriers may be related to the electron (*e2*) and hole interface (*h1*) populations.

5.5.3 Variable Field-Temperature Results for T2SLs

The minority carrier lifetime in InAs/InAsSb T2SL materials has shown improvement compared to InAs/GaSb T2SLs [22]. Nevertheless, similar to InAsSb alloys, the electron accumulation layer at the surface and interface carriers in InAs/InAsSb T2SL offer a challenge for the proper identification of the bulk conductivity. Hence, lateral transport measurements reported in such materials are limited. Two MWIR *n*-type $InAs/InAs_{0.65}Sb_{0.35}$ T2SL structures were investigated in this work: (1) *NID* and (2) Si-doped at 1×10^{16} cm^{-3}.

For each T2SL structure, MCF was set up to allow for eight total possible carrier populations and identified five carrier populations, three electrons (*e1*, *e2*, *e3*) and two holes (*h1, h2*). Temperature (15 – 390 K) and magnetic-field-dependent measurements in conjunction with MCF analysis are employed to characterize the transport properties of the $InAs/InAs_{0.65}Sb_{0.35}$ T2SL samples. All the respective graphs shown in this work are compared for *NID* and Si-doped T2SL samples on the same *x-y* scales to emphasize their differences and similarities.

The sheet concentrations for each of the five carrier populations present in both $InAs/InAs_{0.65}Sb_{0.35}$ T2SL samples are plotted as a function of temperature for *NID* and Si-doped in Figures 5.20 (a) and (b), respectively.

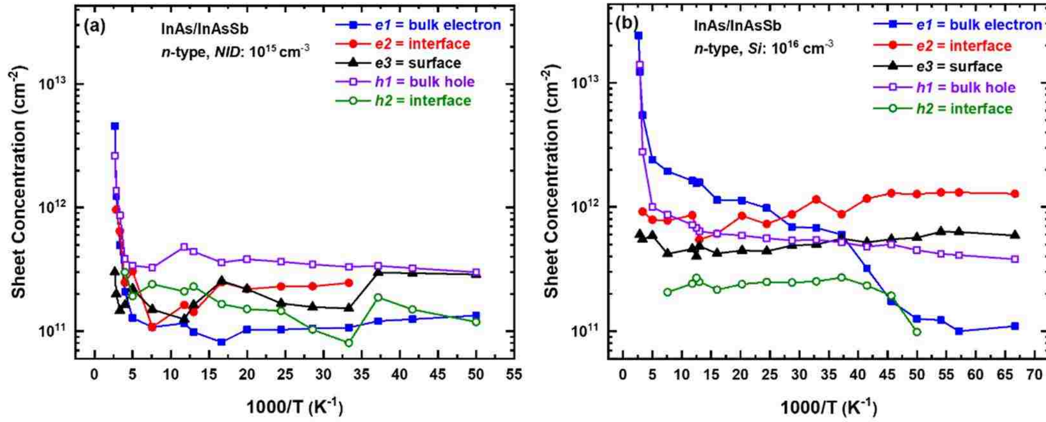

Figure 5.20: Sheet concentrations of the five resolved carrier populations in the *n*-type InAs/InAs$_{0.65}$Sb$_{0.35}$ T2SL samples as a function of temperature for (a) *NID* and (b) Si-doped at 1×10^{16} cm^{-3}.

The carrier mobilities for each of the five carrier populations present in both InAs/InAs$_{0.65}$Sb$_{0.35}$ T2SL samples are plotted as a function of temperature for *NID* and Si-doped in Figures 5.21 (a) and (b), respectively. Reference guidelines have been added to the mobility plots ($T^{-3/2}$) to represent lattice (phonon) scattering behavior.

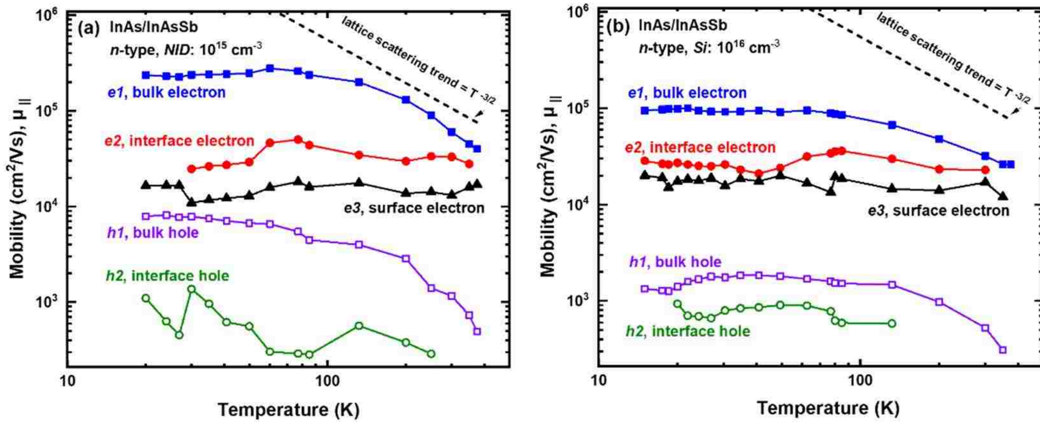

Figure 5.21: Mobilities of the five resolved carrier populations in the *n*-type InAs/InAs$_{0.65}$Sb$_{0.35}$ T2SL samples as a function of temperature for (a) *NID* and (b) Si-doped at 1×10^{16} cm^{-3}. Reference guidelines have been added to the mobility plots ($T^{-3/2}$) to represent lattice (phonon) scattering behavior.

The calculated sheet conductivities for each of the five carrier populations present in both InAs/InAs$_{0.65}$Sb$_{0.35}$ T2SL samples are plotted as a function of temperature for *NID* and Si-doped in Figures 5.22 (a) and (b), respectively.

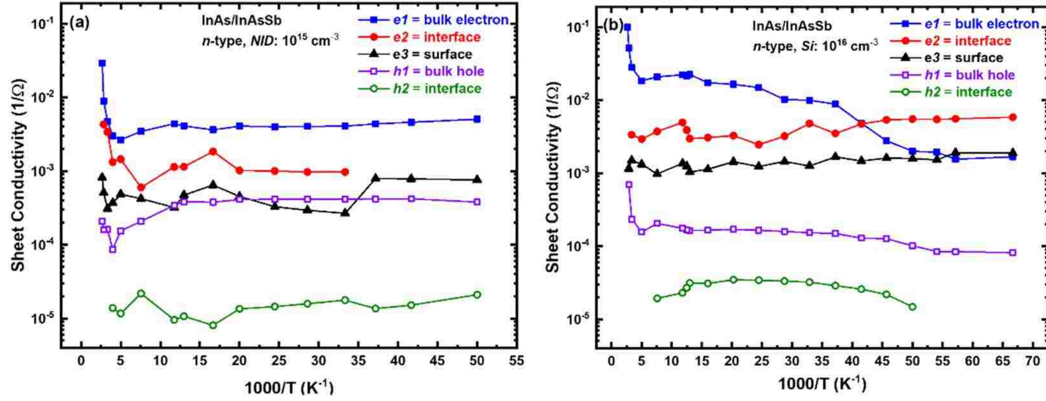

Figure 5.22: Sheet conductivities of the five resolved carrier populations in the *n*-type $InAs/InAs_{0.65}Sb_{0.35}$ T2SL samples as a function of temperature for (a) *NID* and (b) Si-doped at 1×10^{16} cm^{-3}.

The carrier assignments for the InAs/InAsSb T2SL samples shown in Figures 5.20, 5.21 and 5.22 are identified based on the following considerations.

Bulk electron and hole carriers (*e1* and *h1*)

Comparing $InAs/InAs_{0.65}Sb_{0.35}$ T2SLs, Figures 5.20 (a) *NID* and (b) Si-doped at 1×10^{16} cm^{-3}, both samples are found to be *n*-type with a noticeable increase in sheet concentration for electron carrier (*e1*) as a function of doping. For instance, at 300 K the *n*-type population for carrier *e1* shown in Figures 5.20 (a) and (b), resulted in sheet concentrations of *NID* (Si-doped) of 4.96×10^{11} cm^{-2} (5.48×10^{12} cm^{-2}), which translate into concentrations of 2.48×10^{15} cm^{-3} (2.74×10^{16} cm^{-3}) when accounting for the 2 μm bulk thickness. Electron carrier *e1* demonstrates a considerable increase in sheet concentration as a function of doping, and closely matches the predicted concentrations at 300 K for *NID* at 2.48×10^{15} cm^{-3} and Si-doped at 2.74×10^{16} cm^{-3}.

Comparing mobility results in Figures 5.21 (a) *NID* and (b) Si-doped T2SL samples, *e1* and *h1* carrier populations appear to be dominated by lattice scattering ($T^{-3/2}$) at high temperatures while *e2*, *e3,* and *h2* do not demonstrate a clear scattering dependence. When comparing Figures 5.21 (a) and (b), as the doping is increased (*NID* to Silicon-

doped), the mobility of the bulk carriers (*e1* and *h1*) decreases while the other carrier mobilities (*e2*, *e3,* and *h2*) stay relatively constant. The mobility reduction in the bulk carriers of the T2SL samples is similar to the reduction seen in the alloy samples and can be associated with an increase of Coulomb scattering as a function of doping. Hence, the electron *e1* and hole carrier *h1* are assigned as bulk carriers for the T2SL samples due to their intrinsic behavior and scattering dependence. At 77 K for the *NID* InAs/InAsSb T2SL sample, mobility (concentration) results for the bulk electron carrier *e1* are found at 2.60×10^{5} cm^{2}/Vs (4.92×10^{14} cm^{-3}). At 77 K for the Si-doped InAs/InAsSb T2SL sample, mobility (concentration) results for the bulk electron carrier *e1* are found at 8.87×10^{4} cm^{2}/Vs (7.90×10^{15} cm^{-3}).

Previously reported measurements of electron mobility in *n*-type *NID* Long-Wavelength Infrared (LWIR) $InAs/InAs_{0.5}Sb_{0.5}$ T2SL at 77 K revealed a bulk electron mobility of 1.28×10^{5} cm^{2}/Vs and a bulk hole mobility at 4307 cm^{2}/Vs [1]. For *NID* MWIR $InAs/InAs_{0.65}Sb_{0.35}$ T2SLs, a bulk electron mobility of 2.06×10^{5} cm^{2}/Vs at 10 K was reported [23]. For the *NID* MWIR $InAs/InAs_{0.65}Sb_{0.35}$ T2SLs structures reported here, at 77 K, the mobility of the bulk electron carrier *e1* is found to be 2.60×10^{5} cm^{2}/Vs while the bulk hole carrier *h1* mobility is 5450 cm^{2}/Vs. The closely reported concentration and mobility values for the bulk carriers found in similar T2SL material further confirms that *e1* and *h1* are the bulk carriers for the T2SLs (e.g., majority electron and minority hole). Figure 5.20 (a) shows that for the *NID* InAs/InAsSb T2SL sample, the bulk hole sheet concentration is higher than the bulk electron at temperatures below 200 K, while the sheet concentration is similar for both bulk carriers at temperatures above 200 K. A similar effect

was reported in *NID* LWIR InAs/InAsSb T2SL [1], but the exact nature remains unknown and requires further investigation.

Comparing sheet conductivity results in Figures 5.22 (a) *NID* and (b) Si-doped, bulk carrier *e1* showed the highest sheet conductivity out of the five carriers, while the interface hole carrier *h2* had the lowest. Based on the listed comparisons, *e1* and *h1* are identified as the bulk carriers, and Arrhenius analysis of the slope fit is performed. Figures 5.23 (a) *NID* and (b) Si-doped show the *e1* and *h1* bulk carrier concentrations as a function of inverse temperature (*1000/T*).

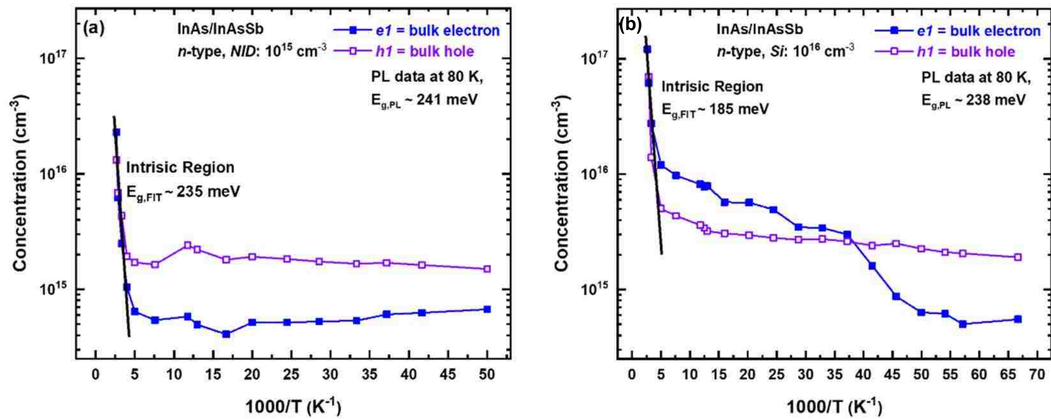

Figure 5.23: Bandgap and activation energy analysis for the bulk carriers *e1* and *h1* found in $InAs/InAs_{0.65}Sb_{0.35}$ T2SL samples for (a) *NID* and (b) Si-doped at 1×10^{16} cm^{-3}.

In Figures 5.23 (a) and (b), the sharp increase in concentrations for bulk carriers *e1* and *h1* as the temperature is increased from 300 to 390 K is likely due to increased thermal excitation across the bandgap as the material begins to enter the intrinsic regime. A similar effect for the bulk electron carrier in the alloy InAsSb samples was seen. The intrinsic regime is indicated in Figures 5.23 (a) and (b) with a line fit at high temperatures that enables the extraction of the bandgaps, labeled E_{gFIT}. Arrhenius analysis at high temperatures of the *n*- and *p*-type concentration for the *e1*/*h1* bulk electron/hole carriers (e.g., $\ln(n_{e1})\,/\,\ln(p_{h1})$ vs. $1/k_BT$) indicates that there is a thermal activation of intrinsic

carriers at an energy of E_{gFIT} ~ 235 meV (*NID* InAs/InAsSb T2SL) and E_{gFIT} ~ 185 meV (Si-doped InAs/InAsSb T2SL). The experimental bandgaps found are in the MWIR range, but smaller than the 80 K bandgap energies of $E_{g,PL}$ ~ 241 meV (*NID* InAs/InAsSb T2SL) and $E_{g,PL}$ ~238 meV (Si-doped InAs/InAsSb T2SL) extracted from the PL measurements, consistent with the observation that the energy bandgap of III-V semiconductors tends to decrease as temperature is increased [21].

Surface (*e3*) and interface carriers (*e2* and *h2)*

To differentiate which of the three unknown carriers (*e2*, *e3*, *h2*) belonged to the surface of the T2SL sample, *e3* electron carrier had a similar concentration and mobility to previously reported surface conductivities for *n*-type InAs/InAsSb T2SLs listed in Table 5.1, and to the surface accumulation layer found for the InAsSb alloy in this study. The electron carrier *e3* found for the *NID* InAs/InAsSb T2SL resulted in mobilities and sheet concentrations at 77 K (300 K) of 1.81×10^{4} cm^2/Vs (1.30×10^{4} cm^2/Vs) and 1.63×10^{11} cm^{-2} (1.47×10^{11} cm^{-2}), respectively. This extracted values for carrier *e3*, are like the mobilities and sheet concentrations found for the surface accumulation layers in similar materials and remain temperature-independent. In addition, the electron carrier *e3* for Si-doped InAs/InAsSb T2SL resulted in mobilities and sheet concentrations at 77 K (300 K) of 1.34×10^{4} cm^2/Vs (1.70×10^{4} cm^2/Vs) and 4.84×10^{11} cm^{-2} (5.50×10^{11} cm^{-2}), respectively. Hence, the *e3* (surface electron carrier) sheet concentration values are fairly consistent with previous reports [1], [3], [13], [14] and mobilities [1] found in similar materials and closely match the surface carrier population found in InAsSb alloys in Section 5.5.2.

To investigate if the remaining two carrier populations (*e2* and *h2*) belonged to the T2SL/GaSb/AlAsSb sample interface, the modeled sheet concentration values listed in

Table 5.3 at 300 K are compared to MCF sheet concentrations from Figures 5.20 (a) *NID* and (b) Si-doped. For the Si-doped InAs/InAsSb T2SL sample at 300 K, the MCF extracted sheet concentration for electron carrier *e2* was found at 9.18×10^{11} cm^{-2} compared to a value of 2.16×10^{12} cm^{-2} determined using the NRL MULTIBANDS® software (Table 5.3). This comparison alludes to a possible interface electron carrier (*e2*), which leaves an unknown hole carrier (*h2*) that cannot be compared to the modeled hole interface carrier concentration at 300 K due to the unresolved MCF values of *h2* at high temperatures. However, the expected hole T2SL/GaSb/AlAsSb interface model provided in Figures 5.12-5.13, and the non-intrinsic behavior of the *h2* hole carrier suggest that this unresolved carrier may be related to the T2SL sample interface.

5.5.3.1 Diffusion Length of Minority Carriers in T2SLs

Transport in semiconductors can be expressed with the average distance that the relevant charge moves in the structure before it recombines. This distance is usually referred to as the diffusion length (L_p) and is related to diffusion coefficient (D_p) and lifetime (τ_p) for minority holes:

$$L_p = \sqrt{D_p \tau_p} \tag{5.3}$$

The carrier drift mobility and diffusion coefficient are related through the Einstein relations:

$$D_p = \frac{k_B T \mu_p}{q} \tag{5.4}$$

whereas k_B is the Planck's constant, T is the temperature, q is the fundamental charge of an electron, and μ_p is the mobility of the minority carrier holes in *n*-type material. The combination of the variable-magnetic field mobility measurement performed, and the

optical lifetime measurement taken enables the extraction of the minority hole diffusion length by using Equation 5.3 and 5.4 at 100 K.

The electron effective masses for an InAs/InAsSb T2SL are reported to be two orders of magnitude and one order of magnitude lighter than the hole masses in the vertical and lateral directions, respectively [24]. This anisotropic characteristic results in the hole mobility being much lower than electrons, and therefore the ambipolar diffusion coefficient (D_A) becomes highly dependent on holes. However, for n-type T2SL material under low-level excitation such as the one studied here, the ambipolar diffusion coefficient and mobility equal the minority hole diffusion coefficient ($D_A = D_p$) and mobility ($\mu_A = \mu_p$). Hence, the excess electron and hole motion is governed by the hole diffusion coefficient.

Results presented in Section 5.5.3 for the *NID* and Si-doped InAs/InAsSb T2SL samples extracted a minority bulk hole $h1$ carrier. Using the measured minority carrier lifetime and mobility extracted at 100 K for both T2SL samples, the lateral minority carrier diffusion length was calculated. For the *NID* InAs/InAsSb T2SL sample at 100 K, the lifetime calculated was 1.450 μs (Table 5.2) with a lateral mobility of 3980 cm^2/Vs (from Figure 5.21 (a)). This results translate into a hole minority carrier diffusion length of L_p = 70.5 μm with a diffusion coefficient of D_p = 34.32 cm^2/s. For the n-type Si-doped (1×10^{16} cm^{-3}) InAs/InAsSb T2SL sample at 100 K, the lifetime calculated was 0.250 μs (Table 5.2) with a lateral mobility of 1400 cm^2/Vs (from Figure 5.21 (b)), this results translate into a minority carrier diffusion length of L_p = 17.4 μm with a diffusion coefficient of D_p = 12.08 cm^2/s.

A higher absorber doping can lead to lower diffusion dark-currents in nBn III-V detectors, but the diffusion length also shortens due to lower Shockley-Read-Hall (SRH)

lifetime [25], which increases the dark-current. In the MWIR $InAs/InAs_{0.65}Sb_{0.35}$ T2SL samples characterized in this work, the diffusion length shortens as absorber doping is increased (*NID* to Silicon-doped) due to a mutual drop in mobility and lifetime. The calculated minority hole lateral diffusion lengths for the $InAs/InAs_{0.65}Sb_{0.35}$ T2SL samples are summarized in Table 5.4.

Table 5.4: Minority hole lateral diffusion lengths for the $InAs/InAs_{0.65}Sb_{0.35}$ T2SL samples.

n-type T2SL Sample	Doping (cm^{-3})	Lifetime @ 100 K (µs)	Mobility @ 100 K (cm^2/Vs)	Lateral Diffusion Length @ 100 K (µm)	Lateral Diffusivity @ 100 K (cm^2/s)
$InAs/InAs_{0.65}Sb_{0.35}$ Lateral Transport	1×10^{15} cm^{-3} (*NID*)	1.45	3980	70.5	34.32
	1×10^{16} cm^{-3} (Si-doped)	0.25	1400	17.4	12.08

5.6 Conclusions

Section 5.5 described the individual temperature- and magnetic-field-dependent results extracted using MCF for InAsSb alloys (Section 5.5.2) and for $InAs/InAs_{0.65}Sb_{0.35}$ T2SLs (Section 5.5.3) with *NID* and Si-doped absorbers. A comparison of the bulk (intrinsic) carrier results is presented to provide further insight into the lateral transport properties of III-V materials. The lateral bulk electron mobilities vs. temperature found for the alloy and T2SL samples are shown in Figure 5.24 (a) under both doping concentrations. Figures 5.24 (b) and (c) show the *NID* and Si-doped bulk electron mobility results vs. temperature, respectively, displaying the single-field mobility values at 77 and 300 K at a magnetic field (*B*) of 0.5 Tesla for each sample.

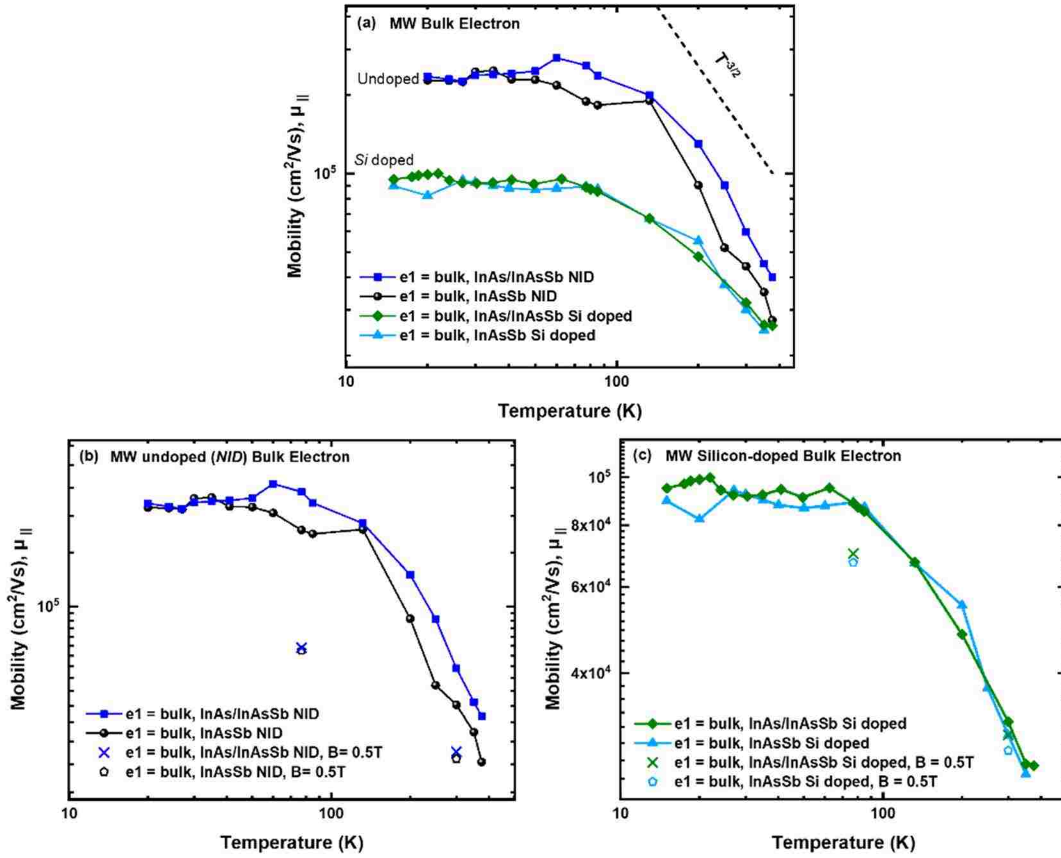

Figure 5.24: Lateral bulk (intrinsic) electron mobilities vs. temperature results for (a) *NID* and Si-doped InAsSb alloys and InAs/InAsSb T2SL samples. Figures (b) and (c) show the *NID* and Si-doped bulk electron mobility results vs. temperature, respectively, displaying the single-field mobility values at 77 and 300 K at a magnetic field (B) of 0.5 Tesla for each sample. Reference guidelines have been added to the mobility plot ($T^{-3/2}$) to represent lattice (phonon) scattering.

The lateral bulk electron concentrations vs. temperature results found for the alloy and T2SL samples are shown in Figure 5.25 (a) under both doping concentrations. Figures 5.25 (b) and (c) show the *NID* and Si-doped bulk electron concentration results vs. temperature, respectively, displaying the single-field concentration values at 77 and 300 K at a magnetic field (B) of 0.5 Tesla for each sample.

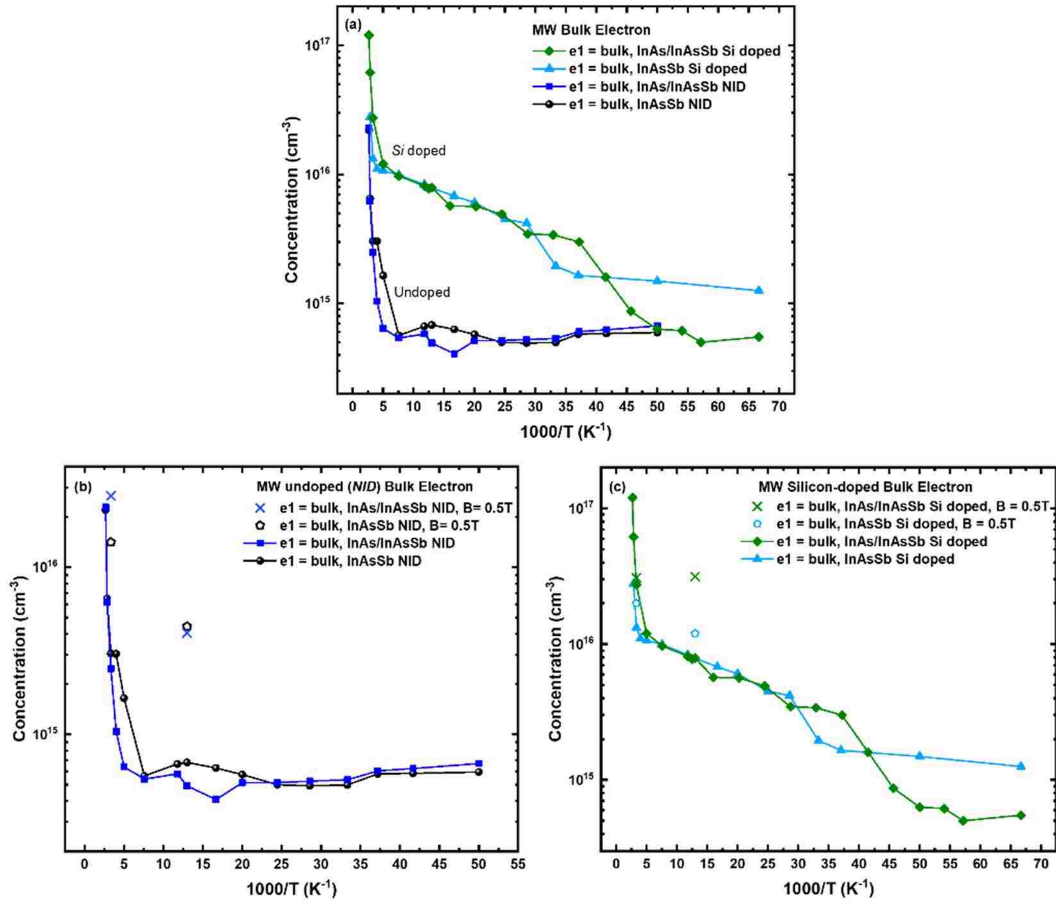

Figure 5.25: Lateral bulk (intrinsic) electron concentrations vs. temperature results for (a) *NID* and Si-doped InAsSb alloys and InAs/InAsSb T2SL samples. Figures (b) and (c) show the *NID* and Si-doped bulk electron concentration results vs. temperature, respectively, displaying the single-field concentration values at 77 and 300 K at a magnetic field (*B*) of 0.5 Tesla for each sample.

Comparing the results shown in Figure 5.24 (a) and Figure 5.25 (a), similar magnitude and temperature dependence of the bulk electron mobilities and concentrations are found for MWIR InAsSb alloys and InAs/InAsSb T2SL samples as a function of doping (*NID* to Si-doped). In addition, all mobility trends for the electron bulk carrier found in the four samples show a similar lattice scattering dependence. InAsSb-like properties of the bulk electron seen in InAs/InAsSb T2SL samples are an indication of strong electron-hole wave function overlap [26].

Figures 5.24 (b) *NID* and (c) Si-doped show the single-field bulk electron mobilities at 77 and 300 K for each of the samples (alloy and T2SL). The single-field bulk electron mobility values are lower than the MCF extracted mobilities under both temperatures, most likely due to the multi-carrier conduction nature of the samples, which traditional single-field Hall Effect measurement do not consider. Similarly, Figures 5.25 (b) *NID* and (c) Si-doped show the single-field bulk electron concentrations at 77 and 300 K for each of the samples (alloy and T2SL). The single-field concentrations are higher than the MCF extracted concentrations. The single-field bulk electron concentration values are higher than the MCF extracted concentrations. These results demonstrate the need for variable-field measurements with multi-carrier analysis to accurately determine the bulk carrier mobilities and concentrations for III-V material.

In section 5.5.3, a bulk (intrinsic) minority hole for the InAs/InAsSb T2SL samples was extracted and diffusion lengths calculated under two doping concentrations (*NID* and Si-doped). Figures 5.26 (a) and (b) combines the minority hole mobilities and concentrations found for the T2SL samples, respectively.

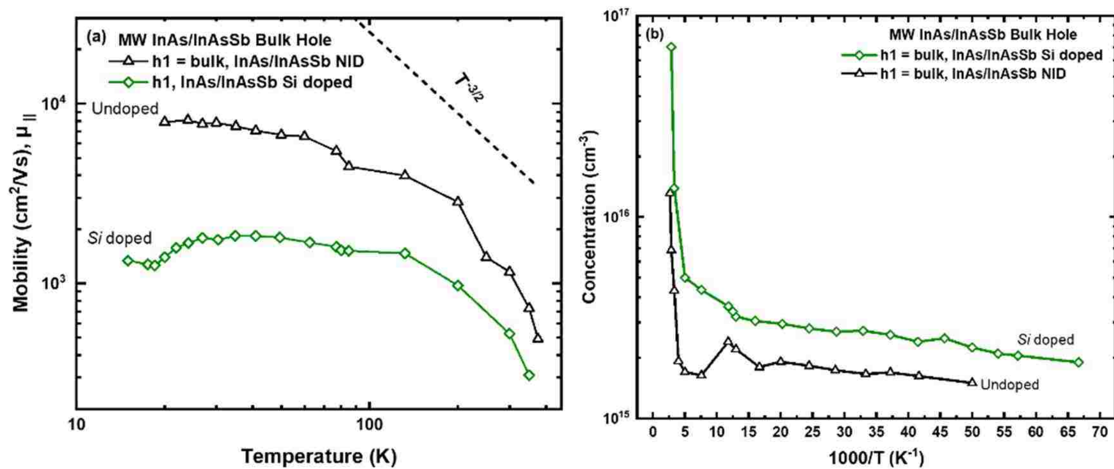

Figure 5.26: Lateral (a) mobilities and (b) concentration vs. temperature results for minority hole found in *NID* and Si-doped InAs/InAsSb T2SL samples. Reference guidelines have been added to the mobility plot ($T^{-3/2}$) to represent lattice (phonon) scattering.

As seen in Figures 5.26 (a) and (b), silicon doping decreases the mobility and increases the concentration for the minority hole in InAs/InAsSb T2SLs. Due to Coulomb scattering, it was expected to see a reduction in minority carrier hole mobility due to doping. However, Figure 5.26 (b) shows that the Si-doped T2SL minority carrier hole possessed higher concentrations throughout the temperature range compared to the minority hole carrier in the *NID* T2SL sample, which is an unexpected result that requires further investigation.

All of the extracted transport properties (e.g., mobilities and concentrations) from the temperature- and magnetic-field measurements in conjunction with MCF presented in this chapter are listed in Tables 5.5-5.8 for the *n*-type InAsSb alloy samples under both doping concentrations for temperatures at 77 and 300 K. Likewise, Tables 5.9-5.12 summarize the transport properties found for the *n*-type InAs/InAsSb T2SL samples under both doping concentrations for temperatures at 77 and 300 K.

Table 5.5: Summary of mobility and carrier concentration results found for the different carriers in the undoped (*NID*) $InAs_{0.91}Sb_{0.09}$ at 77 K.

Sample: InAsSb **Doping:** 1.0×10^{15} cm^{-3}	Mobility (cm^2/Vs)	Sheet Concentration (cm^{-2})	Concentration (cm^{-3})
e1 = bulk	1.89×10^{5}	1.36×10^{11}	7.00×10^{14}
e2	2.94×10^{4}	2.90×10^{11}	
e3= surface	1.43×10^{4}	3.33×10^{11}	
h1	1186	1.99×10^{11}	

Table 5.6: Summary of mobility and carrier concentration results found for the different carriers in the undoped (*NID*) $InAs_{0.91}Sb_{0.09}$ at 300 K.

Sample: InAsSb **Doping:** 1.0×10^{15} cm^{-3}	Mobility (cm^2/Vs)	Sheet Concentration (cm^{-2})	Concentration (cm^{-3})
e1 = bulk	4.40×10^{4}	6.09×10^{11}	3.05×10^{15}
e2	unresolved	unresolved	
e3= surface	1.24×10^{4}	4.00×10^{11}	
h1	844	1.05×10^{12}	

Table 5.7: Summary of mobility and carrier concentration results found for the different carriers in the *n*-type Si-doped (1.0×10^{16} cm^{-3}) $InAs_{0.91}Sb_{0.09}$ at 77 K.

Sample: InAsSb **Doping:** 1.0×10^{16} cm^{-3}	Mobility (cm^2/Vs)	Sheet Concentration (cm^{-2})	Concentration (cm^{-3})
e1 = bulk	8.90×10^{4}	1.60×10^{12}	8.00×10^{15}
e2 = interface	1.84×10^{4}	4.60×10^{11}	
e3= surface	1.50×10^{4}	4.50×10^{11}	
h1	859	4.00×10^{11}	

Table 5.8: Summary of mobility and carrier concentration results found for the different carriers in the *n*-type Si-doped (1.0×10^{16} cm^{-3}) $InAs_{0.91}Sb_{0.09}$ at 300 K.

Sample: InAsSb **Doping:** 1.0×10^{16} cm^{-3}	Mobility (cm^2/Vs)	Sheet Concentration (cm^{-2})	Concentration (cm^{-3})
e1 = bulk	3.00×10^{4}	3.00×10^{12}	1.50×10^{16}
e2 = interface	2.00×10^{4}	1.10×10^{12}	
e3= surface	1.00×10^{4}	4.90×10^{11}	
h1	614	7.60×10^{11}	

Table 5.9: Summary of mobility and carrier concentration results found for the different carriers in the undoped (*NID*) $InAs/InAs_{0.65}Sb_{0.35}$ T2SL at 77 K.

Sample: InAs/InAsSb **Doping:** 1.0×10^{15} cm^{-3}	Mobility (cm^2/Vs)	Sheet Concentration (cm^{-2})	Concentration (cm^{-3})
e1 = bulk	2.60×10^5	9.84×10^{10}	4.92×10^{14}
e2 = interface	5.00×10^4	1.43×10^{11}	
e3= surface	1.81×10^4	1.63×10^{11}	
h1 = bulk	5450	4.41×10^{11}	2.20×10^{15}
h2 = interface	290	2.30×10^{11}	

Table 5.10: Summary of mobility and carrier concentration results found for the different carriers in the undoped (*NID*) $InAs/InAs_{0.65}Sb_{0.35}$ T2SL at 300 K.

Sample: InAs/InAsSb **Doping:** 1.0×10^{15} cm^{-3}	Mobility (cm^2/Vs)	Sheet Concentration (cm^{-2})	Concentration (cm^{-3})
e1 = bulk	5.97×10^4	4.96×10^{11}	2.48×10^{15}
e2 = interface	3.30×10^4	6.44×10^{11}	
e3= surface	1.30×10^4	1.47×10^{11}	
h1 = bulk	1160	8.64×10^{11}	4.32×10^{15}
h2 = interface	unresolved	unresolved	

Table 5.11: Summary of mobility and carrier concentration results found for the different carriers in the Si-doped (1.0×10^{16} cm^{-3}) $InAs/InAs_{0.65}Sb_{0.35}$ T2SL at 77 K.

Sample: InAs/InAsSb **Doping:** 1.0×10^{16} cm^{-3}	Mobility (cm^2/Vs)	Sheet Concentration (cm^{-2})	Concentration (cm^{-3})
e1 = bulk	8.87×10^4	1.58×10^{12}	7.90×10^{15}
e2 = interface	3.40×10^4	5.46×10^{11}	
e3= surface	1.34×10^4	4.84×10^{11}	
h1 = bulk	1600	6.40×10^{11}	3.20×10^{15}
h2 = interface	780	2.5×10^{11}	

Table 5.12: Summary of mobility and carrier concentration results found for the different carriers in the Si-doped (1.0×10^{16} cm^{-3}) $InAs/InAs_{0.65}Sb_{0.35}$ T2SL at 300 K.

Sample: InAs/InAsSb **Doping:** 1.0×10^{16} cm^{-3}	Mobility (cm^2/Vs)	Sheet Concentration (cm^{-2})	Concentration (cm^{-3})
e1 = bulk	3.20×10^4	5.48×10^{12}	2.74×10^{16}
e2 = interface	2.30×10^4	9.18×10^{11}	
e3= surface	1.70×10^4	5.50×10^{11}	
h1 = bulk	526	2.78×10^{12}	1.40×10^{16}
h2 = interface	unresolved	unresolved	

Regarding the interface carriers, the four samples (InAsSb alloys and InAs/InAsSb T2SLs) had interface electron mobilities ranging from ~ 20,000-50,000 cm^2/Vs under variable temperature. For instance, the interface electron mobility and sheet concentration found for the *NID* InAsSb sample at 77 K are 2.94×10^4 cm^2/Vs and 2.90×10^{11} cm^{-2}, respectively. It is known that an intrinsic 2DEG at InAs/AlSb interface exists, for example, Brown *et al.* [1] reported an interface/barrier electron population found in *NID* InAsSb/AlSb interface with mobilities ranging from ~ 28,000-48,000 cm^2/Vs under variable temperature and a sheet concentration of 1.20×10^{11} cm^{-2} at 77 K. This result nicely agrees with the electron interface (*e2*) values found in this work for the InAsSb alloy samples. In addition, for the LWIR *NID* InAs/InAsSb T2SL as a function of absorber thickness (0.5 - 3.3 μm) at 77 K, it was previously reported that interface/barrier electron population had a mobility of 2.37×10^4 - 2.18×10^4 cm^2/Vs and a sheet concentration of 4.60×10^{11} - 1.30×10^{12} cm^{-2} [1]. In the work reported here, for the MWIR *NID* InAs/InAsSb T2SL as a function of doping (*NID* to Si-doped) at 77 K, interface electron mobilities and sheet concentrations of 5.00×10^4 - 3.40×10^4 cm^2/Vs and 1.43×10^{11} - 5.46×10^{11} cm^{-2} were found, respectively.

Finally, the inclusion of the 0.01 μm thin GaSb layer between the absorber (alloy or T2SL) and the AlAsSb insulating layer had the consequence of forming an additional hole interface in all the samples presented. Using temperature- and magnetic-field dependent measurements with MCF, the four samples (InAsSb alloys and InAs/InAsSb T2SLs) resulted in a hole population that did not possess evident intrinsic behavior. This hole population had mobilities and sheet concentrations vs. temperature ranging from 300 - 1000 cm^2/Vs and 1.00×10^{11} - 1.00×10^{12} cm^{-2}, respectively. Finally, the surface electron

layer found for all four samples (InAsSb alloys and InAs/InAsSb T2SLs) had mobilities and sheet concentrations vs. temperature results ranging from 1.00×10^4 - 2.00×10^4 cm^2/Vs and 1.50×10^{11} - 6.00×10^{11} cm^{-2}, respectively.

5.7 Summary

Chapter 5 reports on the extraction and comparison of all the lateral carriers (bulk, surface, and interface) present in the MWIR $InAs_{0.91}Sb_{0.09}$ alloy and $InAs/InAs_{0.65}Sb_{0.35}$ T2SL samples under two doping concentrations: (1) *NID* and (2) *n*-type Si-doped (1×10^{16} cm^{-3}) using temperature- and magnetic-field-dependent measurements in conjunction with MCF. A surface treatment experiment conducted correlated one of the electron conducting populations to the surface of *NID* InAsSb. The interface carriers are related to the InAsSb/GaSb/AlAsSb or T2SL/GaSb/AlAsSb interfaces as the MCF extracted sheet concentrations are consistent with the carrier concentrations modeled using NRL MULTIBANDS® at 300 K.

MCF transport properties extracted for the carriers present in the *n*-type InAsSb alloy and InAs/InAsSb T2SL samples are summarized in Tables 5.5-5.8 and Tables 5.9-5.12 at 77 and 300 K, respectively. The lateral transport properties reported in this chapter for isotropic (InAsSb alloys) and anisotropic (InAs/InAsSb T2SLs) materials can be used to decouple bulk carrier vertical transport properties. Conventional transport measurements such as variable-field Hall Effect can suffice for lateral transport diagnostics; however, vertical transport is a more challenging task that is undertaken in Chapter 6.

5.8 References

[1] A. E. Brown, "Application of Mobility Spectrum Analysis to Modern Multi-layered IR Device Material," University of Illinois at Chicago, 2015.

[2] A. E. Brown, N. Baril, D. Zuo, L. A. Almeida, J. Arias, and S. Bandara, "Characterization of n-Type and p-Type Long-Wave InAs/InAsSb Superlattices," *J. Electron. Mater.*, vol. 46, no. 9, pp. 5367–5373, 2017.

[3] S. P. Svensson *et al.*, "Background and interface electron populations in InAs 0.58 Sb 0.42," *Semicond. Sci. Technol.*, vol. 30, no. 3, 2015.

[4] A. Hood, M. Razeghi, E. Aifer, and G. J. Brown, "On the performance and surface passivation of type II superlattice photodiodes for the very-long-wavelength infrared," *Appl. Phys. Lett.*, vol. 87, no. 15, 2005.

[5] S. Maimon and G. W. Wicks, "nBn detector, an infrared detector with reduced dark current and higher operating temperature," *Appl. Phys. Lett.*, vol. 89, no. 15, 2006.

[6] H. S. Kim *et al.*, "Reduction of surface leakage current in InAs/GaSb strained layer long wavelength superlattice detectors using SU-8 passivation," *Appl. Phys. Lett.*, vol. 97, no. 14, 2010.

[7] L. Ö. Olsson, C. B. M. Andersson, M. C. Håkansson, J. Kanski, L. Ilver, and U. O. Karlsson, "Charge Accumulation at InAs Surfaces," *Phys. Rev. Lett.*, vol. 76, no. 19, 1996.

[8] D. Lackner, "InAsSb / InAs STRAIN BALANCED SUPERLATTICES FOR PHOTODETECTOR APPLICATIONS," Simon Fraser University, 2011.

[9] T. Krug, L. Botha, P. Shamba, T. R. Baisitse, and A. Venter, "Electrical properties of undoped and doped MOVPE-grown InAsSb," *J. Cryst. Growth*, vol. 298, 2007.

[10] G. A. Umana-Membreno *et al.*, "Vertical minority carrier electron transport in p-type InAs/GaSb type-II superlattices," *Appl. Phys. Lett.*, vol. 101, no. 25, 2012.

[11] D. E. Sidor, G. R. Savich, and G. W. Wicks, "Surface Leakage Mechanisms in III – V Infrared Barrier Detectors," vol. 45, no. 9, pp. 4663–4667, 2016.

[12] A. Nedoluha and K. M. Koch, "Zum Mechanismus der Widerstandsiinderung in Magnetfeld," *Zeitschrift fur Phys.*, vol. 132, no. 5, 1952.

[13] S. Kawaji and H. C. Gatos, "Electric field effect on the magnetoresistance of Indium Arsenide surfaces in high magnetic fields," *Surf. Sci.*, vol. 7, no. 2, 1967.

[14] M. Noguchi, K. Hirakawa, and T. Ikoma, "Intrinsic electron accumulation layers on reconstructed clean InAs (100) surfaces," *Phys. Rev. Lett.*, vol. 66, no. 17, 1991.

[15] G. R. Bell, T. S. Jones, and C. F. McConville, "Accumulation layer profiles at InAs polar surfaces," *Appl. Phys. Lett.*, vol. 71, no. 25, 1997.

[16] Y. Lin, A. R. Arehart, A. M. Carlin, and S. A. Ringel, "Separation of bulk and surface electron transport in metamorphic InAs layers using quantitative mobility spectrum analysis," *Appl. Phys. Lett.*, vol. 93, no. 6, 2008.

[17] S. Holmes, R. A. Stradling, P. D. Wang, R. Droopad, S. D, Parker, and R. L. Williams, "Magneto-optical and transport studies of ultrahigh mobility films of InAs grown on GaAs by molecular beam epitaxy," *Semicond. Sci. Technol*, vol. 4, no. 4, 1989.

[18] L. K. Casias *et al.*, "Carrier concentration and transport in Be-doped InAsSb for infrared sensing applications," *Infrared Phys. Technol.*, vol. 96, 2019.

[19] D. Lackner *et al.*, "InAsSb and InPSb Materials for Mid Infrared Photodetectors," in *22nd International Conference on Indium Phosphide and related Materials (IPRM), IEEE*, 2010.

[20] W. L. C. Vincent, R. J. Egan, and T. L. Tansley, "Electron mobility in InAs1 − x Sb x and the effect of alloy scattering," *J. Appl. Phys.*, vol. 69, no. 6, 1990.

[21] P. T. Webster *et al.*, “Measurement of InAsSb bandgap energy and InAs / InAsSb band edge positions using spectroscopic ellipsometry and photoluminescence spectroscopy,” *J. Appl. Phys.*, vol. 118, no. 24, 2015.
[22] E. H. Steenbergen *et al.*, “Significantly improved minority carrier lifetime observed in a long-wavelength infrared III-V type-II superlattice comprised of InAs/InAsSb,” *Appl. Phys. Lett.*, vol. 99, no. 25, pp. 1–4, 2011.
[23] E. H. Steenbergen, S. Elhamri, W. C. Mitchel, S. Mou, and G. J. Brown, “Carrier transport properties of Be-doped InAs / InAsSb type-II infrared superlattices,” *Appl. Phys. Lett.*, vol. 104, no. 1, 2014.
[24] Y. Aytac, “Time-Resolved Measurements of Charge Carrier Dynamics in MWIR to LWIR InAs/InAsSb Superlattices,” University of Iowa, 2016.
[25] D. Z. Ting, D. Z. Ting, A. Soibel, A. Khoshakhlagh, and S. D. Gunapala, “Theoretical analysis of nBn infrared photodetectors,” *SPIE Opt. Eng. Appl.*, vol. 56, no. 9, 2017.
[26] D. Lackner, M. Steger, M. L. W. Thewalt, O. J. Pitts, and Y. T. Cherng, “InAs / InAsSb strain balanced superlattices for optical detectors : Material properties and energy band simulations,” *J. Appl. Phys.*, vol. 111, no. 3, 2012.

Chapter 6

n-type InAs/InAsSb Type-II Strained Layered Superlattice (T2SL) Vertical Transport

6.1 Introduction

In Chapter 5, the lateral transport measurements of *n*-type Mid-Wavelength Infrared (MWIR) $InAs_{0.91}Sb_{0.09}$ alloys and $InAs/InAs_{0.65}Sb_{0.35}$ Type-II Strained Layered Superlattices (T2SLs) materials were presented and compared. It was proven in Chapter 4 (*p*-type $InAs_{0.91}Sb_{0.09}$) and Chapter 5 that by performing lateral Hall Effect and resistivity measurements over a range of temperature and magnetic fields, it is possible to separate contributions from different carrier species using Multi-Carrier Fit (MCF) analysis. This Chapter presents a new test-structure processing technique to characterize vertical transport properties on T2SL absorber materials (e.g., $InAs/InAs_{0.65}Sb_{0.35}$) equivalent to those characterized previously in this work. The test-structure developed, is configured as a vertical Metal-Semiconductor-Metal (MSM) structure, that requires removal of the GaSb substrate on which the T2SL active region was epitaxially grown. The MSM fabrication enables geometrical magneto-resistance measurements on T2SL structures after the GaSb substrate and etch stop layers have been mechanically and chemically

removed, with the purpose that only the carriers from the absorber materials are considered. Thus, the MSM test-structure configuration used for the first time, enables better insight into the vertical transport properties of InAs/InAsSb T2SLs.

This Chapter provides details and background on the substrate removal technique employed. A review of vertical transport characterization is summarized, including a discussion of the limitations of test-structure configurations previously used. Next, a summary of the as-grown samples, including optical measurements is provided. MSM fabrication and electrical characterization methodology are detailed prior to the presentation of experimental results from geometrical magneto-resistance measurements. Finally, vertical transport mobility is obtained from magneto-resistance measurements of an $InAs/InAs_{0.65}Sb_{0.35}$ T2SL sample using High-Resolution Mobility Spectrum Analysis (HR-MSA). The lateral transport data presented in Chapter 5 was then employed to decouple the true vertical mobility characteristics of the $InAs/InAs_{0.65}Sb_{0.35}$ T2SL sample. Access to HR-MSA was facilitated via collaboration links with the Microelectronic Research Group, headed by Prof. Faraone, at the University of Western Australia (UWA) [1] .

The aim of this chapter is to demonstrate, for the first time, a novel vertical MSM test-structure that allows accurate extraction of vertical transport parameters from T2SL anisotropic materials. It is anticipated that the processes and test-structure design details herein provided will serve as a foundation for future improvements. Since currently there is no truly direct or effective methodology to measure vertical mobility, it is anticipated that the vertical MSM structure is a significant contribution to addressing this characterization challenge. Employing the vertical MSM structure, the vertical transport

properties of n-type ($n^+n^-n^+$) lattice-matched and strain-balanced MWIR $InAs/InAs_{0.65}Sb_{0.35}$ T2SLs grown on GaSb substrates were determined using temperature-dependent magneto-resistance measurements. The samples were grown by molecular beam epitaxy (MBE), and in order to isolate the effect of the conducting substrate from the electrical measurements, samples were fabricated and transferred to metal-coated sapphire substrates. Results are presented for two T2SL epitaxial structures with absorber-like regions grown with doping concentrations: (1) 1×10^{15} cm^{-3} or Non-Intentionally Doped (*NID*) and (2) 1×10^{16} cm^{-3} intentionally Si-doped (n-type).

6.2 Substrate Removal Background

One of the major challenges for accurate vertical transport measurements of III-V Sb-based infrared (IR) materials is the parasitic effects of the GaSb substrate on which such materials are typically grown. In order to circumvent the effects of the highly-conducting GaSb substrate, and its substrate/epilayer heterojunction, on vertical transport measurements, it would be ideal to remove completely the substrate and transfer the as-grown sample active epitaxial regions to suitable alternative substrate material. In this way the fundamental properties of T2SL absorbers, such as lateral and vertical carrier mobility can be accurately characterized. This approach has not been previously used to fully characterize vertical transport in Sb-based IR materials.

Thus, lateral or vertical transport measurements can be characterized by transferring the absorber material (alloy or T2SL) to an insulating or conducting substrate then using standard Van der Pauw (VDP) or geometrical magneto-resistance measurements, respectively. In this approach, the removal of the GaSb substrate and AlAsSb etch-stop layer without affecting the III-V material absorber layer is the key and

crucial process step that enables accurate electronic transport characterization, and thus the motivation for the substrate removal process used in this work. Taking into account that many substrate removal approaches have been previously reported [2]–[4], this section provides a brief summary of some of the substrate removal techniques used in III-V materials, which provided a basis upon which our approach was developed.

Cervera *et al.* [5] removed the GaSb substrate on InAs/GaSb T2SL material by including an InAsSb etch-stop layer between the substrate and the T2SL absorber. After mechanical polishing, the substrate was selectively wet-etched in a diluted $Cr0_3$: HF-based solution which selectively stops at InAsSb. Similarly, for the removal of the GaSb substrate in T2SLs, a similar CrO_3:HF:H_2O solution was used by Delaunay *et al.* [2]. Although CrO_3:HF:H_2O is considered to be a selective etchant between InAsSb and GaSb, there is no report of how selective it is [6]. Since the CrO_3:HF:H_2O solution can slightly etch InAsSb, the thickness of the InAsSb etch-stop layer is required to be thick (micron range). However, for the work presented in this dissertation, this solution posed safety hazards due to CrO_3 disposal, and alternative approaches were explored.

Fastenau *et al.*[7] reported a high etching selectivity between AlSb and InAs material using an HF:H_20_2:H_20 solution. As it is known, anything that etches AlSb-based layers will etch GaSb [6]. Consequently, for this work, the use of the HF:H_20_2:H_20 (2:1:20) solution was pursued to etch the GaSb substrate, the AlAsSb layer, and the GaSb layer down to the InAs/InAsSb superlattice absorber layer.

6.3 Vertical Transport Review

6.3.1 Limitations

$InAs/InAs_{1-x}Sb_x$ and InAs/GaSb T2SLs have been shown to exhibit minority carrier lifetimes limited by Shockley-Read-Hall (SRH) and carrier mobility limited by interface roughness (IRS). However, the T2SL material system has been significantly hampered by: (1) the lack of a straightforward experimental technique to gain insight into the fundamental properties of carrier transport in the direction perpendicular to the superlattice plane (vertical transport), (2) the difficulties of making in-plane (lateral) transport measurements when an electrically conductive buffer or substrate is employed, and (3) the lack of insight or knowledge into correlations between lateral and vertical transport properties. In particular, T2SL vertical transport properties such as carrier mobility are not well understood yet.

Additionally, carrier localization in InAs/InAsSb T2SLs is another concern for vertical transport. For instance, it has been shown, that specific defects and localized states can result in carrier localization in InAs/InAsSb T2SLs [8]. As demonstrated by the dispersion relation for the $InAs/InAs_{0.65}Sb_{0.35}$ T2SL shown in Chapter 5, Section 5.4.2, localization of minority holes is expected due to the very large effective mass in the heavy-hole (HH) band (dispersion-less band curvature behavior) along the vertical direction. Further details of the vertical transport measurements and limitations are provided in Chapter 2, Section 2.8.

6.3.2 Vertical Transport Configuration for Magneto-Resistance

MSA algorithms provide a means to extract transport parameters of multiple carriers without a priori knowledge or assumptions about the number of carrier species [1], [9]. Experimental investigation into T2SL vertical carrier transport has been conducted recently using mesa devices with on-mesa top contacts and off-mesa bottom contacts [10], [11]. Using this processing method, collaborative research conducted in 2012 by UWA and the University of New Mexico (UNM) became the first published report of a MSA-based technique to extract vertical transport properties from Long-Wavelength Infrared (LWIR) InAs/GaSb ($p^+p^-p^+$) T2SL [10].

A limitation of multi-carrier analysis algorithms is that the vertical and horizontal mobilities cannot be decoupled; such algorithms extract effective mobilities in which the true vertical and horizontal mobilities are convolved [12]. In 2014, Swartz *et al.*[11], motivated by the vertical and horizontal mobility coupling issues and concern with the effects of neglecting series resistance in the bottom contact layer, reported on the decoupling technique in anisotropic InAs/GaSb ($n^+n^-n^+$) T2SLs. It was concluded that both lateral and vertical transport parameters are required to decouple the true vertical mobility. Without properly decoupling the vertical and lateral mobilities, a geometric average of the two mobilities is extracted, which possibly results in an inaccurate mobility estimation. Figure 6.1 (a) illustrates the device structure and the typical T2SL device cross-section used for previously reported magneto-resistance measurements [10], [11]. The typical structure consists of a lightly doped "absorber" region, sandwiched between two heavily doped contact layers of the same superlattice design. Figure 6.1 (b) shows the top view of the same device structure, where the center gold square is the mesa

top contact, and the encompassing gold ring is the bottom contact. The processed device structure shown in Figures 6.1 (a) and (b) is used because it resembles a typical photodetector pixel; however, carrier conduction through the bottom contact layer adds a parasitic series resistance element to any current-voltage measurement. If this parasitic resistance is not negligible, it can significantly affect the reliability of the parameters extracted, since they would correspond not solely to the absorber region but to a combination of the absorber and the bottom contact layer.

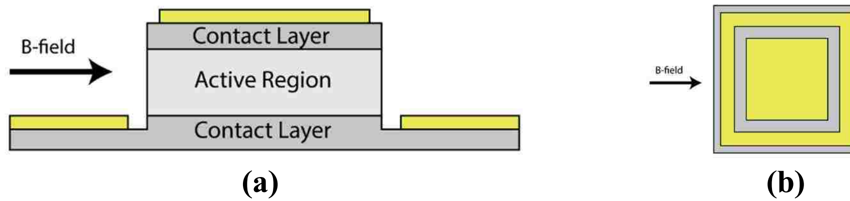

Figure 6.1: Typical device cross-section used for vertical transport measurements in T2SLs where an active region is sandwiched between two heavily doped contact layers, (a) device cross-section and (b) top view of typical device.

As shown in Figure 6.1 (a) and (b), investigation of the bottom contact layer resistance requires an approximation to a Corbino disk device geometry. A Corbino disk is a particular case device geometry that shorts the Hall voltage [13]. Figure 6.2 shows the top view of a Corbino disk. The typical T2SL device structure is like the Corbino disk geometry when comparing Figures 6.1 (b) and 6.2. Hence, for previously reported vertical magneto-resistance measurements, the Corbino disk geometry approximation was used [10], [11].

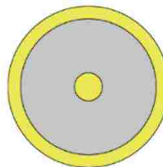

Figure 6.2: Top view of a Corbino disk device geometry. A Corbino disk is a special case device geometry that shorts the Hall voltage, typical T2SL device structure is like the Corbino disk.

In the Corbino disk configuration, the electric current from the bottom contact must travel through the bottom contact layer and enter the active region. The distance over which most of the current transfers from the bottom contact layer to the active region is defined as the transfer length. This means that the current is 'crowded' at the mesa edges where essentially all voltage is dropped [14]. As a result, the middle region below the active region may not have any voltage across it. Hence, transfer length becomes an issue for such configuration. Figure 6.3 represents the same idea in a circuit diagram whereas R_{sh} represents the bottom contact layer sheet resistance, and ρ_c represents the specific contact resistivity (interface), which is the resistivity of the interface formed by the bottom contact layer and active region. When current flows from the semiconductor to metal, it encounters the resistances R_{sh} and ρ_c [15]. The transfer length (L_T) equation is:

$$L_T = \sqrt{\frac{\rho_c}{R_{sh}}} \tag{6.1}$$

In terms of the circuit diagram, the current will choose the path of least resistance which is usually significantly less than the contact length.

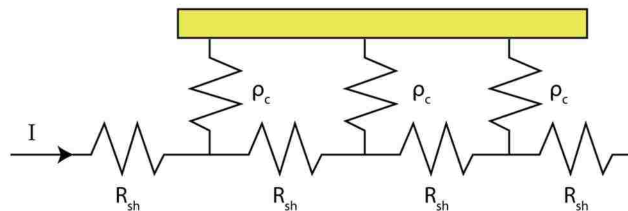

Figure 6.3: Circuit diagram, R_{sh} represents the bottom contact layer sheet resistance and ρ_c represents the specific contact resistivity, which is the resistivity of the interface formed by the bottom contact layer and active region. In terms of the circuit diagram, the current will choose the path of least resistance which is usually significantly less than the contact length.

Finally, application of a current crowding model indicated a transfer length of ~ 10 μm from the mesa edge which is less than the typical mesa diameter [11]. Hence, Swartz *et al.* concluded that series contact resistance could not be neglected with such a short transfer length and with such configuration. A new approach is required to overcome this problem, and this is the main motivation for the proposal and development of the novel Metal-Semiconductor-Metal (MSM) test-structure for vertical transport measurements detailed below.

6.4 Samples and Methods

6.4.1 Device Structures

For this vertical transport study, two $(n^{+}n^{-}n^{+})$ samples were grown on an n-type (*Te*-doped) GaSb substrates using MBE. The epitaxial structure is shown in Figure 6.4, where two doping concentrations for the absorber layer are used: (1) 1×10^{15} cm^{-3} or Non-Intentionally Doped (*NID)*, and (2) 1×10^{16} cm^{-3} Si-doped. The absorber consists of a 2 μm thick lattice-matched $InAs/InAs_{0.65}Sb_{0.35}$ T2SL layer of 4.63 nm of InAs plus 1.06 nm of $InAs_{0.65}Sb_{0.35}$. The absorber layer is sandwiched between the top and bottom $InAs_{0.91}Sb_{0.09}$ contact layers, which are heavily n-type doped to a concentration of 1 x 10^{18} cm^{-3}. The bottom contact layer is grown on top of a 0.01 μm thick undoped GaSb layer on a 0.1 μm thick lattice-matched $AlAs_{0.08}Sb_{0.92}$ etch-stop layer.

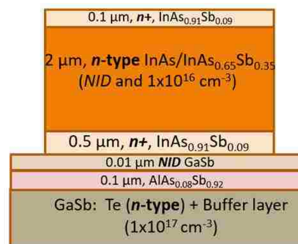

Figure 6.4: Cross-section of the MBE grown $(n^{+}n^{-}n^{+})$ $InAs/InAs_{0.65}Sb_{0.35}$ T2SL samples. The structure is shown with two doping concentrations for the absorber layer.

The intention of including the wide-bandgap AlAsSb insulating layer is to serve as an etch-stop layer, and thus was grown to be thinner (0.1 µm) compared to the samples for lateral transport measurements in which the AlAsSb layer served as insulating layer and needed to be thicker (~0.5 µm). The 10 nm thick GaSb layer was necessary to produce high-quality InAs/InAsSb T2SL material, which can exhibit significantly poorer minority carrier lifetimes when grown directly on the AlAsSb layer.

6.4.2 Material Characterization

The structural quality of as-grown InAs/InAsSb superlattice material was assessed by X-Ray Diffraction (XRD) characterization performed by Sandia National Laboratories (SNL). A representative plot of the XRD characteristics of the two samples is shown in Figure 6.5. As shown in Figure 6.5, the overall periodicity of the absorber material, the full width at half maximum (FWHM) value of the 1st satellite T2SL peak, and the lattice mismatch between the GaSb substrate and the absorber were extracted from the XRD measurements. Also, SNL provided Nomarski images to that demonstrate a specular and defect-free surface morphology as shown in Figures 6.6 (a) and (b) for the two superlattice samples.

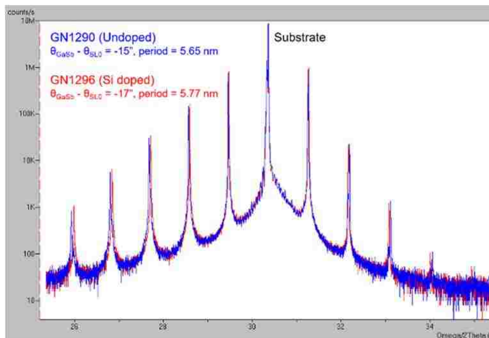

Figure 6.5: XRD characterization for the two $(n^{+}n^{-}n^{+})$ InAs/$InAs_{0.65}Sb_{0.35}$ T2SL samples, (blue) Non-Intentionally Doped (*NID)* and (red) Silicon-doped (Si-doped).
**Data provided by Sandia National Laboratories (SNL)*

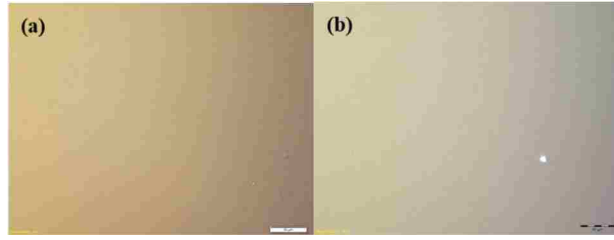

Figure 6.6: Nomarski images comparing surface morphology of the two $InAs/InAs_{0.65}Sb_{0.35}$ T2SL samples, (a) Non-Intentionally Doped (*NID)* (b) Silicon-doped (Si-doped). **Images provided by SNL*

The optical quality of the as-grown structures was evaluated by photoluminescence (PL) and lifetime (LT) measurements at SNL. PL maps were done using double modulation Fourier-Transform Infrared Spectroscopy (FTIR) with a pump laser at 1550 nm and a 2.4 μm long pass to filter out the pump beam. A skewed Gaussian function was employed to fit the PL spectra. LT maps were obtained using Time-Resolved Microwave Reflectance (TMR) at 94 GHz, with a pump laser at 1535 nm. The TMR signal was averaged over about 5,000-30,000 waveforms to generate the final data for the fit. Then, an automated fitting for the lifetimes is performed. For the PL and LT maps, measurements are performed in 5mm increments. The PL and LT maps for the two superlattice samples can be found in Appendix A.

The optical characterization of the two *n*-type $(n^{+}n^{-}n^{+})$ samples is summarized in Table 6.1, where the samples are labeled 5-6 to differentiate from the *n*-type lateral T2SL samples in Chapter 5. Table 6.1 illustrates: sample 5 (InAs/InAsSb *NID*-1×10^{15} cm^{-3} T2SL) and sample 6 (InAs/InAsSb Si-doped-1×10^{16} cm^{-3} T2SL).

Table 6.1: Two n-type $(n^{+}n^{-}n^{+})$ InAs/InAsSb T2SL samples grown by MBE for vertical transport measurements with structure, doping, lifetime (LT) at 100 K and Photoluminescence (PL) peak wavelength at 80 K summarized.

Structure	#	Doping (cm^{-3})	Lifetime @ 100K (μs)	PL peak @ 80 K (μm)	Run #
InAs/InAsSb: Vertical Transport	5	1×10^{15} cm^{-3} (*NID*)	1.550	5.12	GN1290
	6	1×10^{16} cm^{-3} (Si-doped)	0.300	5.10	GN1296

6.4.3 Metal-Semiconductor-Metal (MSM) Fabrication

The critical fabrication steps necessary for realizing a vertical Metal-Semiconductor-Metal (MSM) structure using the $(n^{+}n^{-}n^{+})$ T2SL samples are: (a) the removal of the thick (> 600 μm) GaSb substrate, and (b) transfer of the thin $(n^{+}n^{-}n^{+})$ layer unto a host substrate (e.g., a metalized non-conductive substrate such as sapphire). The success of this process step allowed testing of MSM structures for vertical transport measurements as the one shown in Figure 6.7 (a) and (b).

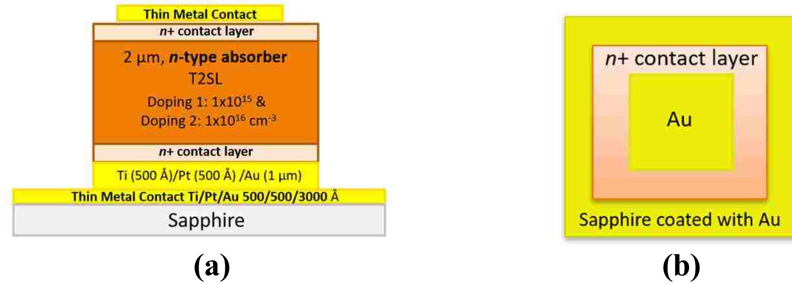

Figure 6.7: Metal-Semiconductor-Metal (MSM) structure for vertical transport measurements (a) cross-section schematic and (b) top view. The 2 μm absorber region is composed of $InAs/InAs_{0.65}Sb_{0.35}$ T2SL.

In order to fabricate the MSM structure, the epilayers must be isolated from the growth substrate, requiring also processing of the top and bottom metallic contacts, and the subsequent transfer to a metalized non-conductive substrate.

After epitaxial growth, the as-grown wafers were diced into 8 mm x 8 mm square pieces for ease of handling and to preserve and ensure uniformity during lapping and etching. The samples were cleaned to remove surface contaminants by rinsing them in subsequent baths of acetone, isopropanol, methanol, and deionized (DI) water. This was done at the beginning of sample processing and during the fabrication steps. The fabrication process steps required to obtain the vertical MSM structures developed in this work are schematically depicted in Figure 6.8. Additional details for each step are presented in Sections 6.4.3.1 - 6.4.3.7.

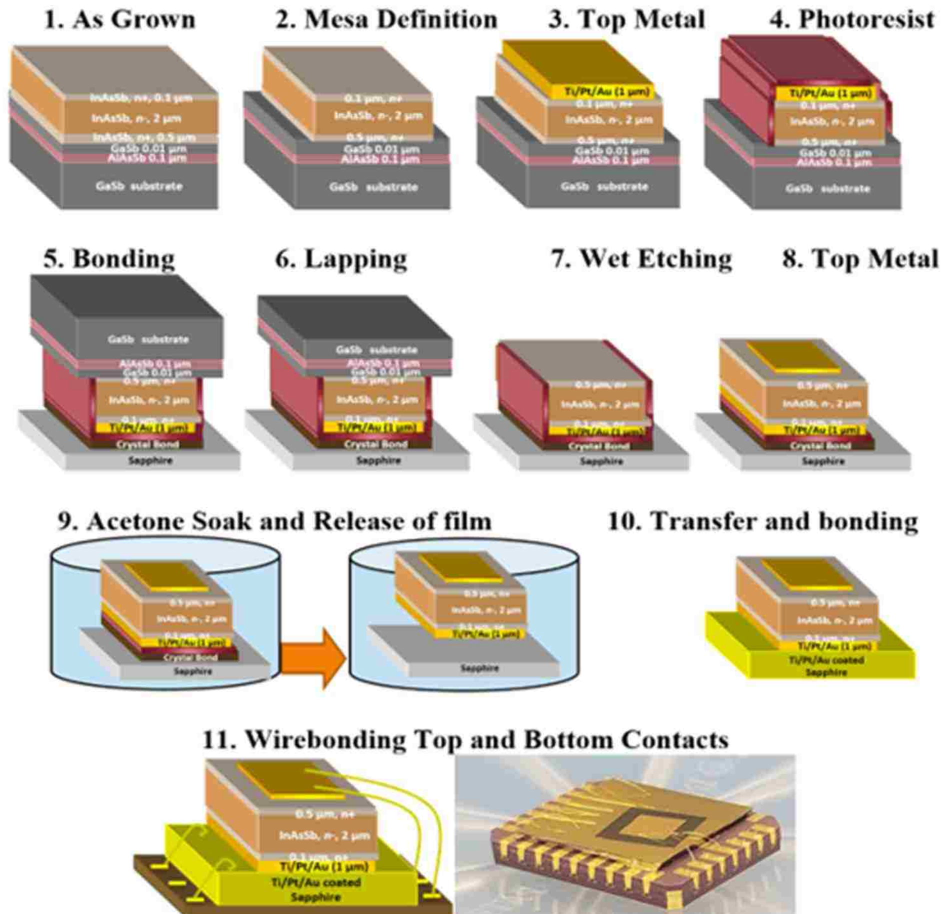

Figure 6.8: Schematic of the fabrication steps used for the Metal-Semiconductor-Metal (MSM) structure used for vertical transport measurements. Details for each step are provided in Sections 6.4.3.1 - 6.4.3.7.

6.4.3.1 Mesa Definition and Top Metal

Before substrate removal, the surface of the samples is processed to define the mesas and to deposit a thick metal layer. The thick metal layer is required to provide sufficiently robust support to the epitaxial film after the substrate is removed. Standard optical photolithography was used to define 5 mm × 5 mm square mesas. Wet-etching was used to define mesas using a citric acid based etch (citric acid:H_2O_2(30%) = 5:1) at room temperature. The resulting mesa etch height was 2 μm, as measured using stylus profilometry. After mesa etching, a 4.7 mm × 4.7 mm square was defined photolithographically for the deposition of the thick metal layer. The offset used on this lithography step accounted for any edge uniformities from wet-etching; alignment marks were used to ensure proper alignment as shown in Figure 6.9 (b). Prior to the deposition of thick metal (by e-beam evaporation), the unintentional native oxide on the mesa side walls was removed using a 30-second etch in a diluted hydrochloric solution (HCl:H_20= 1:20). Metal contact formation consisted of Ti (500 Å)/Pt (500 Å) /Au (1 μm) to form the top ohmic contact. As mentioned previously, at least 1 μm thick metal must be deposited on the sample surface to have enough support for the epilayer to stand free after substrate removal [6].

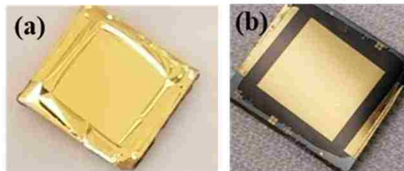

Figure 6.9: Photolithography defined a 4.7 mm × 4.7 mm square for thick top metal application on the surface. Metal contact formation consisted of Ti (500 Å)/Pt (500 Å) /Au (1 μm) to form ohmic contact, (a) shows the sample during the metal liftoff and (b) sample with surface metal after liftoff.

6.4.3.2 Photoresist Protection

To protect the sample before lapping and wet-etching steps required to remove the substrate, photoresist (PR) was used to protect the sidewalls and sample surface. AZ 4330 PR was spun on the surface of the sample, at a speed of 3000 RPM for 30 seconds (final PR thickness of ~ 3.0 µm). Photoresist spinning was followed by a bake at 120ºC for 5 minutes on a hot plate. Once the mesa surface and sidewalls were protected, the samples were ready for lapping and etching. The PR protection was necessary not only for mechanical protection but also to ensure that the absorber layer is unaffected by any chemicals used in the wet etching.

6.4.3.3 Bonding to a Carrier

For substrate lapping and polishing, the processed samples were first mounted (substrate side up) on a sapphire carrier wafer using Crystalbond™ 509 adhesive at 120ºC on a hot plate, as shown in Figure 6.10 (a) and (b). Crystalbond™ 509 was used because of its solvability with acetone and its resistance to most chemicals. Slight pressure was applied to the sample to avoid/remove bubbles between adhesive and sample. The adhesive held the sample firmly during the lapping/polishing process and served also as a protection layer from the wet-chemical etchant. The mechanical lapping process removed most of the GaSb substrate, leaving about ~ 50 µm left. The 50µm thick sample mounted on the lapping carrier was robust enough to be handled with tweezers and to be not affected by the heat used to remove it from the lapping puck.

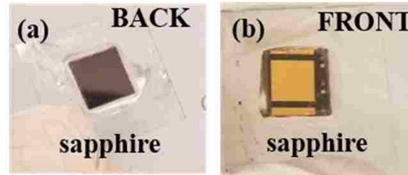

Figure 6.10: Bonded sample to a sapphire carrier for lapping/polishing of the GaSb substrate, (a) shows the sample back (substrate side up) with Crystalbond™ 509 adhesive and (b) sample front showing through the sapphire carrier.

6.4.3.4 Lapping and Wet-Etching for Substrate Removal

The task was to etch three layers in our samples: (1) the GaSb substrate, (2) AlAsSb etch-stop and (3) GaSb layer, while leaving the $n^{+}n^{-}n^{+}$epilayers unaffected – in particular, the T2SL absorber layer (n^{-}). As mentioned earlier, any chemical solution that etches AlAsSb or AlSb will also etch GaSb, so the three layers present in the samples studied in this work can be etched away together if the solution is sufficiently selective over the InAsSb-based layers. Fastenau *et al.* reported a hydrofluoric recipe ($HF:H_20_2:H_20$, 2:1:20) with a highly selective etching ratio of AlSb over InAs [7]. Since anything that etches GaSb will also etch AlAsSb, the etch stop layer should be InAs-based. Hence, after careful consideration, the HF ($HF:H_20_2:H_20$, 2:1:20) recipe was adopted to remove the three layers (GaSb substrate/AlAsSb/GaSb layer), with the “etch-stop” layers being effectively the $n^{+}n^{-}n^{+}$ structure composed of n^{+}(InAsSb)/n^{-}(T2SL)/ n^{+}(InAsSb). The high Indium (In) content of the layers deemed to be sufficient to ensure a low etch rate.

The first step in the substrate removal process consisted of lapping the GaSb substrate, while the second step consisted of etching the sample in the selective HF-based wet-etching solution described above. Figure 6.11 (a)-(c) shows photos of partially processed samples. The GaSb substrates with initial thickness ~ 600-700 µm were carefully lapped. Next, the substrate was further thinned by a final polish to its final thickness of approximately 50 µm. Polishing was essential to ensure that the subsequent

etching step produced a uniform and specular surface. After this stage, the samples were removed from the lapping puck. However, the sample in process remained attached to the sapphire carrier holder with Crystalbond™ 509, thus facilitating handling of the sample during the wet-etching (substrate removal) step.

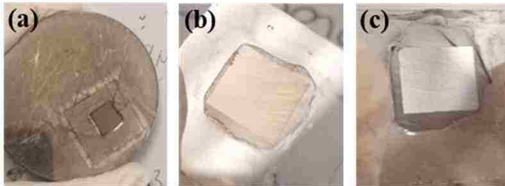

Figure 6.11: Sample lapping and polishing, (a) shows the sample mounted on the lapping puck, (b) and (c) show the sample lapped and slightly polished and unmounted from lapping puck. Crystalbond™ 509 adhesive holds the sample onto the sapphire carrier.

After lapping and mechanical polishing of the substrate, the sample could be then moved onto the second step in the GaSb and AlAsSb removal process: the wet-chemical etching using the highly selective HF-based solution. In this step, the GaSb was fully removed. The etching rate of the GaSb substrate was measured to be ~ 5 μm/min. It should be noted that mechanical thinning of the substrate down ~ 50 μm prior to wet-etching was necessary because prolonged immersion in the solution can result in non-uniform etching and thus result in localized disappearance of the etch stop AlAsSb layer [2]. The removal of the remaining 50 μm substrate, at an etch rate of ~ 5 um/min took approximately, 10-13 minutes.

As previously mentioned, in addition to etching the GaSb substrate, the HF-based solution also etches the AlAsSb etch-stop layer and the thin GaSb layer. The complete etching of the GaSb substrate/AlAsSb/GaSb layer structure took an average of about 15 minutes at room temperature without agitation. As shown in Figure 6.12 (a), (b) and (c), during etching the sample color changed from a grey-dark tint after a few seconds in the solution, to a lighter blue when it reaches the InAsSb-based layer. The sample was left an

additional of 1 minute in the HF solution to ensure that all the GaSb and Al-layer were fully removed. The final sample mounted on the sapphire carrier after substrate removal is shown in 6.8 (f). After the removal of the GaSb substrate, AlAsSb, and GaSb layer, the sample was cleaned with acetone, isopropanol and methanol.

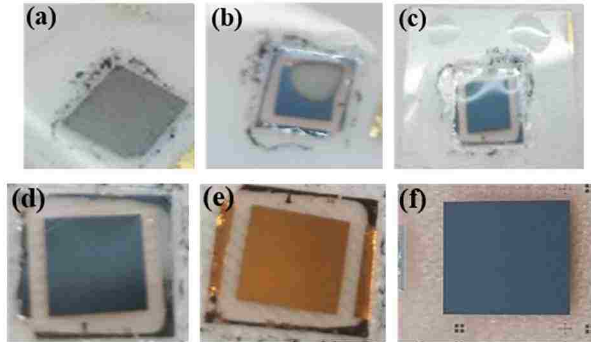

Figure 6.12: Substrate removal by HF wet-etching, (a) seconds in the HF solution bath, (b) after 12 minutes in the solution the color signals removal of the substrate, etch stop layers, (c) after 15 minutes the grey-tint disappears, (d) sample is rinsed in DI water and removed from acid bath, (e) front side of the sample, looking through the sapphire carrier and (f) substrate side after removal process and post- acetone, IPA and methanol rinse. The sample remains on sapphire carrier in all the processes shown.

6.4.3.5 Top Contacts

The remaining steps to be performed to form the top contacts were contact area definition by photolithography, and top metal layer deposition. However, it was found that application of heat applied to such a thin sample induced significant deformation of the thin T2SL film ("wrinkling"), that effectively destroyed the sample, an effect that is likely to be due to significant differences in thermal expansion coefficients of sapphire, Crystalbond, and the thin T2SL membrane. A sample thus damaged is shown in Figure 6.13, which occurred after exposure to the 90 ºC bake required during lithography patterning of the contact area.

Figure 6.13: Sample "wrinkles" during an attempt to perform photolithography after substrate removal to fabricate top contacts. The sample is shown as it looks through the sapphire carrier (substrate side down).

Hence, in order to avoid any lithography steps, a shadow mask was used as an alternative to deposit top contact and thus avoid any heat treatment on the sample in-process.

A shadow mask is a patterning mask that does not require any photolithography patterning, but can be directly positioned in the sample to cover the areas where metal should not be evaporated [16]. For our purposes, a 6 mm × 6 mm square frame with a 2 mm × 2 mm square hole in the middle was used as a shadow mask, as shown in Figure 6.14. These were fabricated on aluminum sheets. The shadow masks were positioned such that its 2 mm × 2 mm hole opening was centered on the sample, so that metal was deposited only through this opening (as shown in Figure 6.14a). This step served to form the top metal on the substrate-removed side of the sample. Prior to top metal e-beam evaporation, any native oxide film unintentionally formed on the mesa surface was removed by a 30-second etch in a diluted hydrochloric solution ($HCl:H_20$= 1:20). The deposited metal layer consisted of Ti (500 Å)/Pt (500 Å) /Au (3000 Å), forming ohmic top contacts as shown in Figure 6.14 (b).

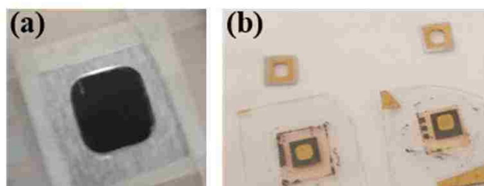

Figure 6.14: The use of a 6 mm × 6 mm square shadow mask with a 2 mm × 2 mm hole in the middle was used, (a) shadow masks were made from aluminum sheets and positioned before top metal evaporation, (b) samples after top metal e-beam evaporation held by sapphire carriers with shadow mask shown on the top.

6.4.3.6 Acetone Release

After substrate removal and thin top metal deposition, the sample was still being held by the Crystalbond™ 509 adhesive on the sapphire carrier. In order to release the remaining $n^+n^-n^+$ layers from the carrier and adhesive, the sample was left in acetone overnight to fully dissolve the adhesive and detach the sample from the sapphire carrier. Once the adhesive was dissolved, the isolated thin sample naturally floated in the acetone bath as shown in Figures 6.15 (a)-(c).

Thanks to the thick metal deposited, the thin layers could be carefully handled using tweezers, albeit they curled a little in the direction of the thick metal. Renteria *et al*. demonstrated that the extra support that the thick metal layer gives to a released thin film facilitates the transferring process [6]. Upon release, the samples were rinsed in acetone, IPA, and methanol before being transferred to a host sapphire substrate coated with metal.

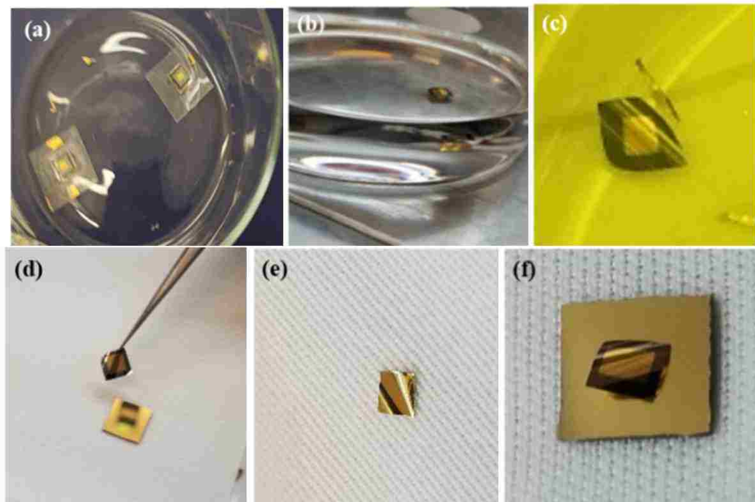

Figure 6.15: Release in acetone bath and transfer to a sapphire carrier coated with metal, (a) samples held by adhesive onto the sapphire carriers placed in acetone bath, (b) sample in acetone bath after 10 hours dissolves, (c) released thin film (d) transfer of the thin sample using tweezers, (e) backside of the thin sample after release with thick bottom metal and, (f) thin sample transferred to a sapphire carrier coated with Ti/Pt/Au ready for the bonding process step.

6.4.3.7 Bonding to a Host Substrate

After release, the sample were bonded to a 10 mm × 10 mm sapphire carrier coated with Ti/Pt/Au by using an Au-to-Au cold-welding technique that is commonly used in solar-cell processing [17], [18]. For this bonding process, a sapphire substrate was first cleaned in a BOE solution for 5 minutes, to remove residues or contaminants from the substrate surface. The clean sapphire substrate was then coated with Ti (500 Å)/Pt (500 Å) /Au (3000 Å) via e-beam evaporation. Next, the thin sample was transferred to the Au coated sapphire substrate (thick metal side down) as shown in Figure 6.15 (f). This sample-substrate combination was then placed in a graphite press, as shown in Fig 6.16 (a) and (b), which was then placed inside an oven at 250 ºC for 30 minutes; this process uses the applied pressure and the diffusion of gold (Au-Au) to fuse the bottom contact of the sample to the metal surface of the sapphire substrate. The sample is shown after the Au-Au bonding in Figures 6.16 (c) - (e) and SEM picture is provided in Figure 6.16 (f).

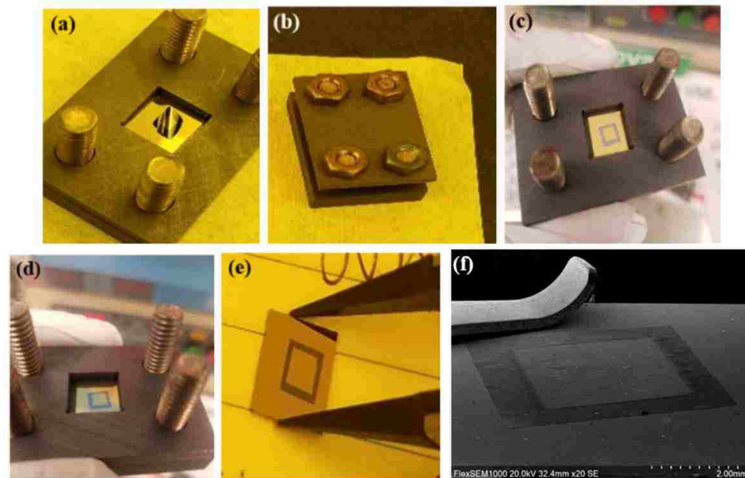

Figure 6.16: Au-Au bonding process of the released sample to sapphire substrate coated with Ti/Pt/Au, (a) sample in graphite press, (b) graphite press is screwed on, then placed in an oven 250 ºC for 30 minutes, (c)-(d) sample after bonding process, (e) final 5 mm × 5 mm sample with top contact and bonded to metal coated-sapphire substrate and (f) SEM image of the bonded sample.

Finally, upon complete MSM fabrication, manual wire-bonding using a silver-loaded epoxy was used to connect the top and bottom contacts for electrical characterization.

6.4.4 Electrical Characterization

Unlike lateral transport in $InAs/InAs_{0.65}Sb_{0.35}$ T2SLs studied in Chapter 5, which was shown to be similar to that of $InAs_{0.91}Sb_{0.09}$ alloy materials, vertical transport is significantly different from bulk charge transport due to the presence of the nanometer scale and periodic potential wells along the vertical direction [19], [20]. As previously emphasized, there is currently no method to directly measure transport properties for carriers traveling in the direction parallel to the growth axis (vertical direction).

Vertical transport of carriers is parallel to the epitaxial growth axis (z-direction) while lateral transport is parallel to the growth plane (x-y direction). Vertical transport characterization is particularly important because this is the direction of photogenerated carrier flow in infrared (IR) detectors, thus the need for a direct measurement of vertical mobility in IR detector materials. The MSM processing technique described in Section 6.4.3, provides a new approach to overcome challenges of vertical transport measurement.

By fabricating a pair of heavily doped contact layers (n^+) on each face of a thin absorber region composed of (n^-) T2SL material, without the substrate, the measured contact-to-contact resistance should be dominated by the active region [11]. The vertical geometrical magneto-resistance configuration is shown in Figures 6.17 (a) and (b), a current is applied vertically between the two contact layers and a magnetic field is applied horizontally, the conducting contact layers serve to short out the horizontal electric field in the active region. That is, the symmetry of the structure forces the Hall

Effect voltage to become zero in the (n^{-}) active region. Hence, in this configuration, the measured Hall coefficient (R_H) and the transverse component of the conductivity tensor (σ_{xy}) become zero $(R_H = 0, \sigma_{xy} = 0)$. Consequently, info about carrier type is lost in vertical geometrical magneto-resistance measurements.

Since the Hall Effect technique is not applicable for vertical transport measurements, the magneto-resistance approach is used. The first step is to obtain the current-voltage (I-V) characteristics of each sample to check the ohmic nature of the contacts. The second step is to measure resistance as a function of magnetic field at a specific temperature. There were four resistance configurations used in this work.

Figure 6.17 illustrates the four-wire experimental setup with an applied electric field (*E field*) and the magnetic field (*B field*). Figure 6.17 (a) demonstrates the 3-dimensional and (b) the 2-dimensional four-wire setup used on the MSM structures. As seen in Figure 6.17 (b) the top contacts are labeled as 1 and 2, while bottom contacts are labeled 3 and 4. The magneto-resistance setup measures the sheet resistance (R_s) as a function of magnetic field. For this work, the experimental data was obtained by measuring resistance (R) using top (1,2) and bottom (3,4) contact configurations. Figures 6.17 (a) and (b) illustrates the measurement arrangement, the four resistance configurations ($R_{I+I-V+V-}$) were measured by applying a 700 μA current and sensing the voltage, the four resistances are thus labeled R_{1324}, R_{1423}, R_{2314}, R_{2413}.

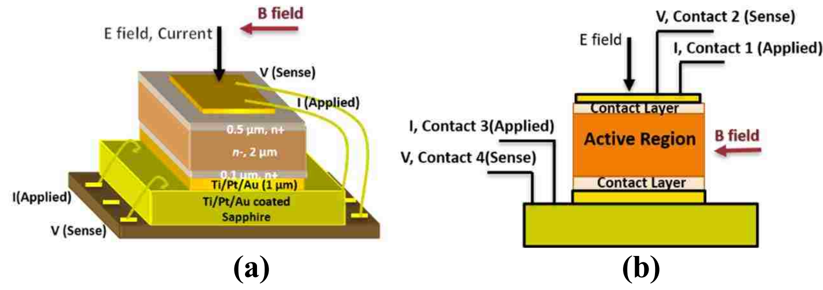

(a) **(b)**

Figure 6.17: Experimental setup used with applied electric field (*E field*) and magnetic field (*B field*), (a) demonstrates the 3-dimensional and (b) the 2-dimensional four-wire setup used on the MSM structures. The top contacts are labeled as 1 and 2, while bottom contacts are 3 and 4.

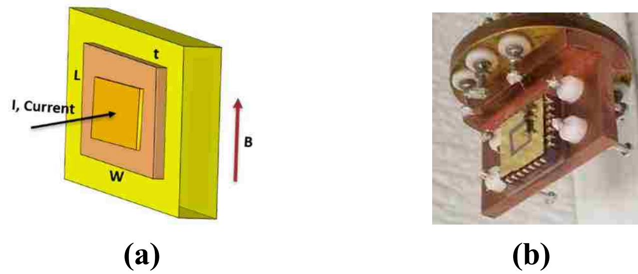

(a) **(b)**

Figure 6.18: Testing configurations used with (a) applied current I (*E field*) and magnetic field (*B field*); where w, t and L are the width, thickness, and length of the sample under test and (b) a picture of the sample mounted for testing.

Figures 6.18 (a) and (b) illustrate the testing configuration used for magneto-resistance measurements, with Figure 6.18 (a) showing the current I (*E field*) and magnetic field (*B field*) arrangement; and where w, t, and L are the width, thickness and length of the sample under test. Figure 6.18 (b) shown how the sample was mounted for testing. The experimental resistance (R) is converted to sheet conductance (inverse of sheet resistance R_s) using the following equations:

$$R = \frac{R_s t}{w} \tag{6.2}$$

$$R_s = \frac{Rw}{t} \tag{6.3}$$

$$\sigma_{xx} = \frac{1}{R_s} \tag{6.4}$$

whereas σ_{xx} is the longitudinal conductivity tensor component, and w, t, and L are the width, thickness, and length of the sample under test as shown in Figure 6.18 (a).

The measured magneto-resistance characteristics indicated multi-carrier conduction. Before proceeding to multiple-carrier analysis, it is worth noting that both MSM fabricated samples considered in this work, and summarized in Table 6.1, clearly indicated the presence of multiple electrical carriers at all temperatures of interest. Magnetic-field dependent resistance measurements were utilized to demonstrate multi-carrier conduction in the samples. Here, it should be noted that when a single carrier is present in a sample, a plot of resistance versus the square of magnetic field intensity should be a straight line with a slope equivalent to the square of the carrier mobility. Thus, non-linear $R(B)$ vs. B^2 characteristics are a clear indication that more than one carrier is present in a sample. These results are summarized in Section 6.5.

Consequently, and since conventional single-carrier analysis could not be employed, the measured magneto-resistance characteristics were analyzed using High-Resolution Mobility Spectrum Analysis (HR-MSA) as a collaborative effort with UWA. Using HR-MSA, the sheet resistance *($R_s(B)$)* gets converted to longitudinal conductivity tensor component (σ_{xx}) that assumes the presence of *N* distinct carriers:

$$\sigma_{xx}(B) = \frac{1}{R_s(B)} = \sum_{i=1}^{N} \frac{q n_i \mu_i}{1+(\mu_i B)^2} \tag{6.5}$$

whereas $R_s(B)$ is the sheet resistance as a function of magnetic field, q is electron charge, and n_i, μ_i are the electron concentration and mobility values for the i_{th} carrier [9], [10]. Further details regarding conductivity tensors and HR-MSA can be found in Chapter 3, Sections 3.6.2.1 and 3.6.2.3, respectively.

6.5 Results

In the following sections, temperature- and magnetic field-dependent measurements are used to extract the magneto-resistance results in the MSM processed samples. Variable temperature analysis was performed from 20-350 K and magneto-resistance measurements under four resistance configurations ($R_{I+I-V+V-}$: R_{1423}, R_{1324}, R_{2413}, R_{2314}). A magnetic field ranging from -9T to 9T and a sample current of 700 μA was used. Then, the magneto-resistance data for the *NID* InAs/InAsSb T2SL was further analyzed by HR-MSA at UWA to extract vertical transport mobility versus temperature. The analysis indicates the presence of two dominant carriers: an electron and a hole carrier species. In order to extract the decoupled vertical mobility results for the *NID* InAs/InAsSb T2SL carriers, the lateral mobility results found in Chapter 5 for such structure were used.

6.5.1 Variable Temperature Magneto-Resistance

The ($n^+n^-n^+$) MSM fabricated devices contain an $InAs/InAs_{0.65}Sb_{0.35}$ T2SL anisotropic narrow gap absorber with two different *n*-type doping concentrations: (1) *NID* and (2) Si-doped (1×10^{16} cm^{-3}). Magneto-resistance measurements were utilized to demonstrate multi-carrier conduction in the samples. Figure 6.19 illustrates the experimentally measured resistance versus square of magnetic field (B^2) for the *NID* InAs/InAsSb T2SL sample at temperatures (a) 20, (b) 50, (c) 130, (d) 250, (e) 300, and (f) 350 K under the four resistance configurations; average resistance of the configurations displayed as a solid line. The sign of the magnetic field is kept and only the magnitude is squared to enable evaluation of the symmetry characteristics with magnetic field polarity.

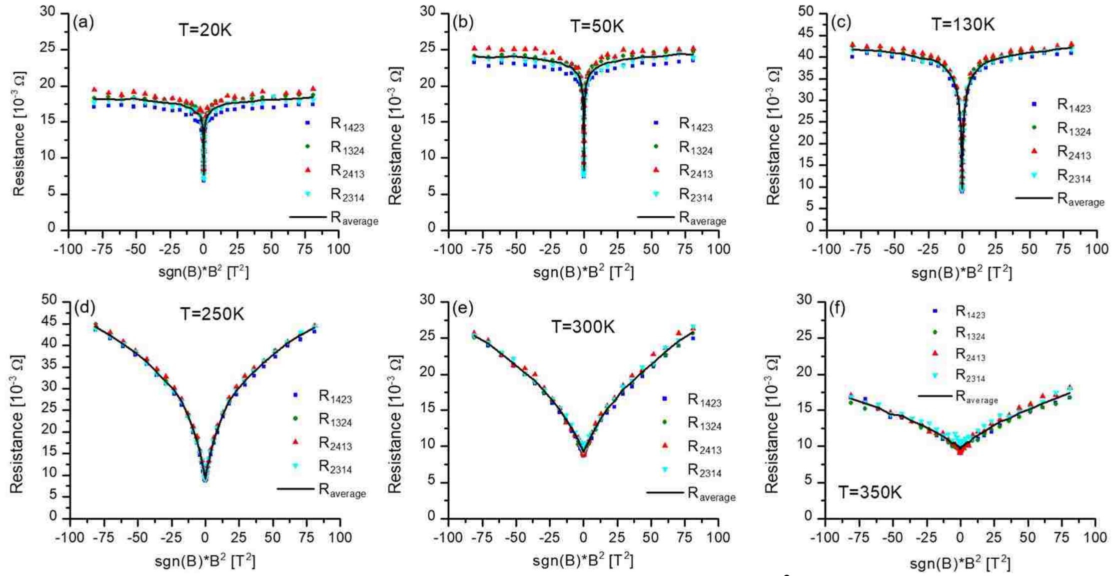

Figure 6.19: Resistance versus square of magnetic field (B^2) for the *NID* InAs/InAsSb T2SL sample at temperatures (a) 20, (b) 50, (c) 130, (d) 250, (e) 300, and (f) 350 K under four resistance configurations; average resistance of the configurations displayed as a solid line. The sign of the magnetic field is kept and only the magnitude is squared to enable evaluation of the symmetry characteristics with magnetic field polarity.

Under variable-temperature, the non-linear resistance behavior of all four resistance configurations with respect to B^2 indicate multiple-carrier species (conduction paths).

Defining the Signal-to-Noise Ratio (*SNR*) figure of merit of a measurement as $\mathrm{std}(R(B))/\overline{R(B)}$, where std($R$(B)) and $\overline{R(B)}$ are the standard deviation and average values obtained from different measurements of the resistance $R(B)$ at a given magnetic field intensity, it can be seen in Figure 6.19 that SNR in this sample was worse at low temperatures. This is the case even when there is a rapid change in resistance from the high mobility electrons. It is important to note that the resistance values in this sample configuration are in the milliohms range, an aspect which poses great difficulties in obtaining good SNR from a single measurement, and thus requiring the averaging employed in this study. On the other hand, it should also be noted that although the MSM structure circumvents the parasitic series resistance problems posed by the spreading resistance of the bottom contact layer encountered in prior reports, the series resistance

presented by metal-semiconductor contacts remains to be quantified. This contact resistance, albeit very low, is likely to be higher at lower temperature.

Figure 6.20 illustrates the experimentally measured resistance versus square of magnetic field (B^2) for the Si-doped InAs/InAsSb T2SL sample at temperatures (a) 20, (b) 50, (c) 77, (d) 130, (e) 250, and (f) 300 K under the four resistance configurations; average resistance of the configurations displayed as a solid line. Again, the sign of the magnetic field is kept and only the magnitude is squared to enable evaluation of the symmetry characteristics with magnetic field polarity. As with the sample with *NID* absorber layer, the non-linear resistance behavior of all four resistance configurations with respect to B^2 indicate multiple-carrier conduction in the Si-doped InAs/InAsSb T2SL sample at all temperatures of interest. However, the characteristics approach linear-like characteristics above 250 K.

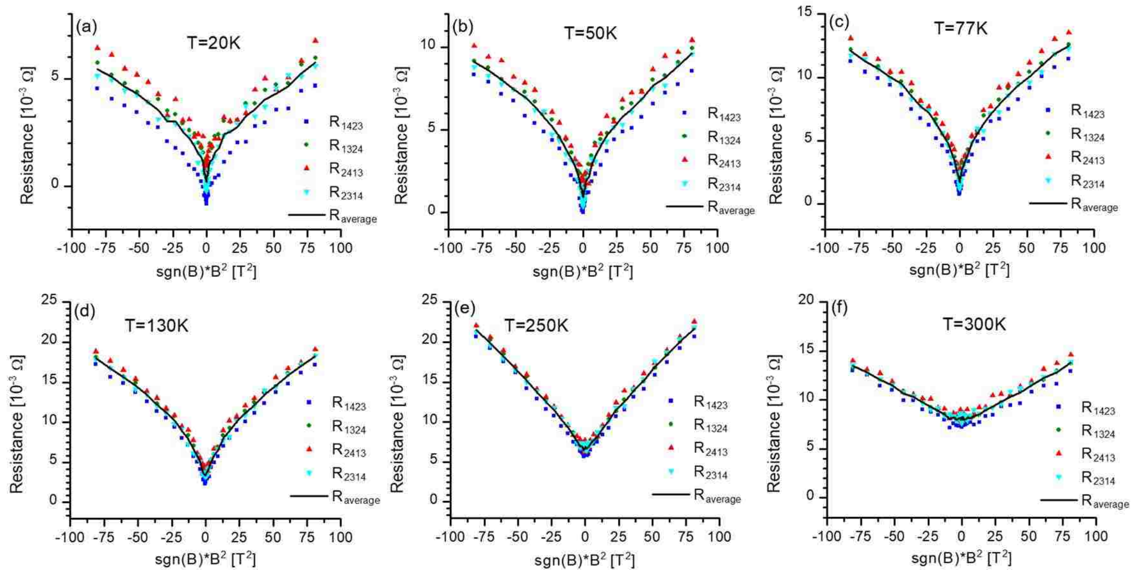

Figure 6.20: Resistance versus square of magnetic field (B^2) for the Si-doped InAs/InAsSb T2SL sample at temperatures (a) 20, (b) 50, (c) 77, (d) 130, (e) 250, and (f) 300 K under the four resistance configurations; average resistance of the configurations displayed as a solid line. The sign of the magnetic field is kept and only the magnitude is squared to enable evaluation of the symmetry characteristics with magnetic field polarity.

As seen in Figure 6.20, the relative *SNR* is also worse at low temperatures, the same effect that was previously observed in Figure 6.19 for the *NID* T2SL sample. However, when comparing variable temperature magneto-resistance in Figures 6.19 (*NID*) and Figures 6.20 (Si-doped), it is evident that the Si-doped T2SL sample exhibited higher noise levels. It is important to note that, the zero-field resistance values in the Si-doped sample were lower than ~ 3mΩ for temperatures below 77 K, and thus challenging to characterize employing the available instrumentation set up. Hence, the results for the (*NID)* InAs/InAsSb T2SL sample were deemed to be "cleaner" and much easier to interpret, and thus more amenable for HR-MSA to extract vertical transport mobilities.

6.5.2 InAs/InAsSb T2SL HR-MSA Vertical Transport

The *NID* $InAs/InAs_{0.65}Sb_{0.35}$ T2SL magneto-resistance characteristics were analyzed using HR-MSA approach at UWA. Figure 6.21 illustrates the sheet conductance versus magnetic field (B) for the average magneto-resistance dataset, together with the fit obtained from HR-MSA, at (a) 20, (b) 77, and (c) 300 K. Analysis of the longitudinal conductivity tensor ($\sigma_{xx}(B)$) or sheet conductance was done using Equation 6.5.

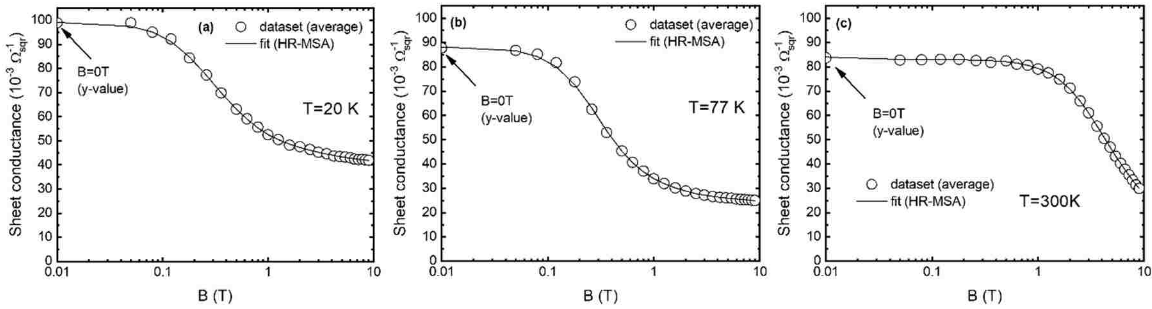

Figure 6.21: Sheet conductance for *NID* InAs/InAsSb T2SL versus magnetic field (B) for the average magneto-resistance dataset, together with the fit obtained from HR-MSA, at (a) 20, (b) 77 and (c) 300 K.

Finally, the mobility spectra for selected temperatures from 20 to 350 K using HR-MSA is shown in Figure 6.22. The high mobility/conductance carriers are assigned to an electron species and the low mobility/conductance carriers to a hole carrier species. As mentioned, SNR was found to be worse at low temperatures, which was evident not only as random noise but also asymmetry with respect to magnetic-field direction, the impact of such non-idealities appears as minor additional conductivity peaks in the mobility spectra.

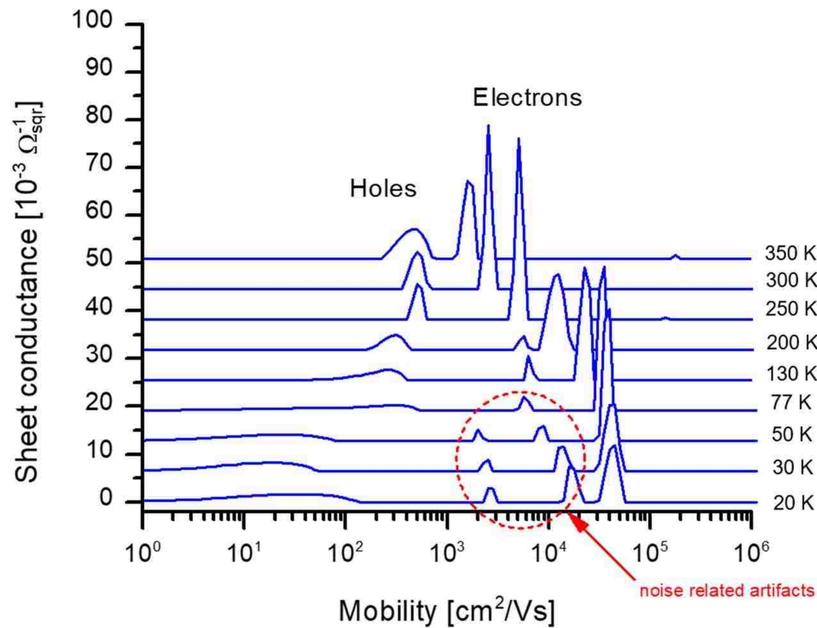

Figure 6.22: Mobility spectra for the *NID* InAs/InAsSb T2SL sample at selected temperatures from 20 to 350 K extracted using HR-MSA. High mobility/conductance carrier is assigned to an electron and low mobility/conductance to a hole. SNR is worse at low temperatures, evident not only as random noise but also asymmetry with respect to magnetic-field direction, their effect appears as minor additional conductivity peaks pointed out in the mobility spectra as noise-related artifacts.

As shown in Figure 6.22, a vertical electron (high mobility/conductance) and a hole (low mobility/conductance) were identified. Figure 6.23 illustrates the coupled vertical mobility for (a) electron and (b) hole mobility as a function of temperature extracted from HR-MSA. The vertical mobility extracted from HR-MSA is a coupled

vertical mobility that contains both the lateral and true vertical mobility components. A reference guideline has been added to the mobility plot in Figure 6.23 (a) to indicate the temperature dependence of the mobility when dominated by lattice scattering ($T^{-3/2}$). The coupled vertical electron mobility exhibits intrinsic behavior which is consistent with mobility dominated by lattice scattering at high temperatures (Figure 6.23 (a))). In contrast, the coupled vertical hole mobility decreases rapidly at lower temperatures, and effect that appears to be consistent with carrier localization effects (Figure 6.23 (b)).

The conductance and mobility behavior as a function of temperature shown in Figure 6.23 (a) and (b), point to a vertical majority electron carrier and a minority hole carrier, with the conductance dominated at all temperatures by electron transport. At 77 K, the coupled vertical electron and hole mobilities are 3.4×10^4 cm^2/Vs and 143 cm^2/Vs, respectively.

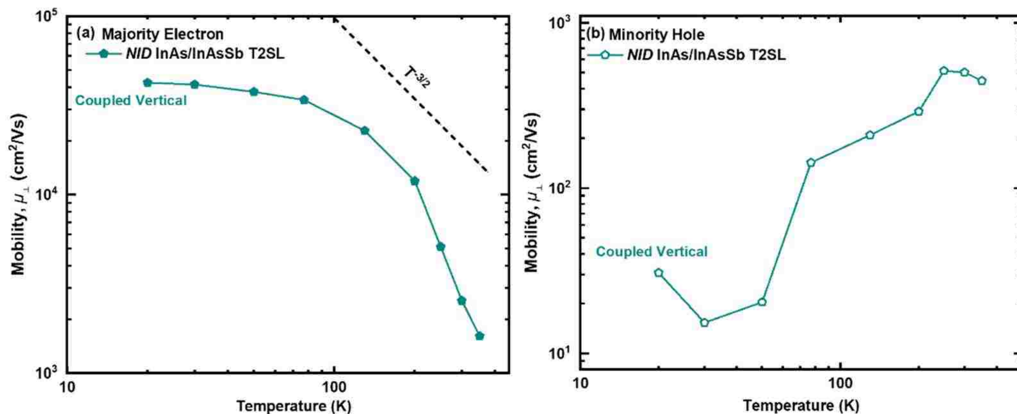

Figure 6.23: HR-MSA extracted coupled vertical mobility for (a) majority electron and (b) minority hole as a function of temperature for the *NID* InAs/InAsSb T2SL sample. The coupled vertical mobility contains both the lateral and vertical components of mobility. Reference guideline has been added to the mobility plot (a) to represent lattice scattering behavior ($T^{-3/2}$). **No extraction of the lateral mobility component in coupled results.*

As mentioned in Section 6.3.2, both lateral and vertical transport parameters are required in order to decouple vertical mobility from the lateral mobility. Without properly

decoupling the vertical mobility, a geometric average of the lateral and vertical mobilities is extracted (coupled results). Hence, using the lateral mobility versus temperature results extracted in Chapter 5 for the *NID* InAs/InAsSb T2SL sample, the decoupled vertical mobility ($\mu_{decoupled}$) was calculated using the equation [11]:

$$\mu_{decoupled} = \frac{(\mu_{\perp coupled})^2}{(\mu_{||measured})} \tag{6.6}$$

whereas $\mu_{\perp coupled}$ is the measured coupled vertical mobility and $\mu_{||measured}$ is the measured lateral mobility. Figure 6.24 illustrates the lateral, coupled vertical and decoupled vertical electron mobility versus temperature (T) results for the *NID* InAs/InAsSb T2SL sample.

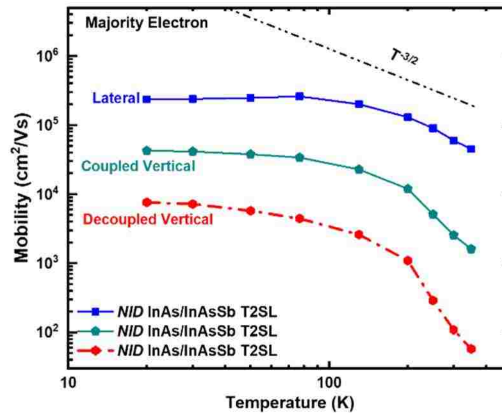

Figure 6.24: Majority carrier electron comparison for lateral ($\mu_{||measured}$), coupled vertical ($\mu_{\perp coupled}$), and decoupled vertical ($\mu_{decoupled}$) results of mobility versus temperature for the *NID* InAs/InAsSb T2SL sample. Reference guideline has been added to the mobility plot to represent lattice scattering behavior ($T^{-3/2}$).

In Figure 6.24, lateral electron mobility is higher than the decoupled vertical electron mobility. Unlike lateral mobility, vertical carrier transport is defined by the nanometer-scale periodic potential wells along the vertical direction, which results in a band structure with higher effective masses in the vertical direction and, consequently, very high conductivity anisotropy. Thus, higher lateral carrier mobilities are expected in T2SL samples. At 77 K, the calculated decoupled vertical electron mobility is found to be

4.4×10^3 cm^2/Vs using the lateral electron mobility of 2.6×10^5 cm^2/Vs (lateral results found in Chapter 5, Table 5.9) for the *NID* InAs/InAsSb T2SL.

Figure 6.25 (a) shows the minority carrier hole comparison for lateral ($\mu_{||measured}$), coupled vertical ($\mu_{\perp coupled}$), and decoupled vertical ($\mu_{decoupled}$) results of mobility versus temperature (T) for the *NID* InAs/InAsSb T2SL sample. The lateral hole mobility shows lattice scattering dependence at high temperatures. Figure 6.25 (b) shows the mobility versus temperature $(1/k_BT)$ of the vertical hole carrier (coupled and decoupled), where k_B is the Boltzmann constant (8.62×10^{-5} eV/K).

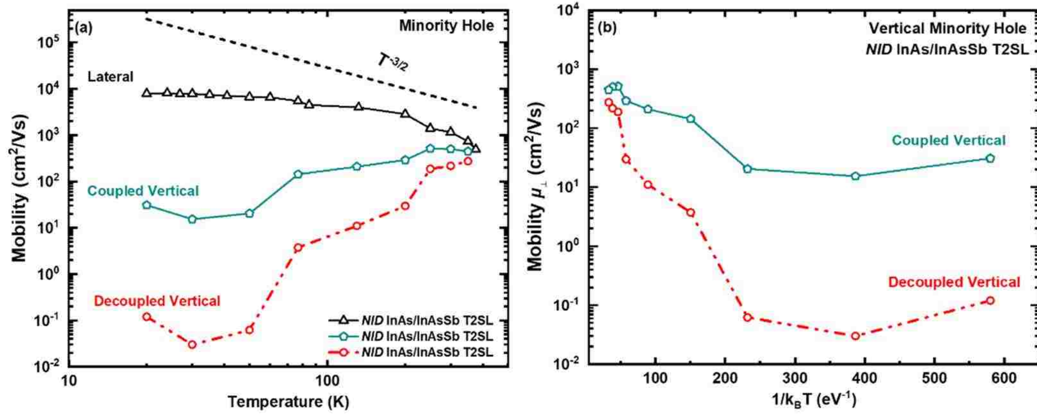

Figure 6.25: (a) Minority carrier hole comparison for lateral ($\mu_{||measured}$), coupled vertical ($\mu_{\perp coupled}$), and decoupled vertical ($\mu_{decoupled}$) results of mobility versus temperature (T) for the *NID* InAs/InAsSb T2SL sample; (b) mobility versus temperature $(1/k_BT)$ results for the vertical hole carrier (coupled and decoupled), where k_B is the Boltzmann constant (8.62×10^{-5} eV/K). Reference guideline has been added to the mobility plot (a) to represent lattice scattering behavior ($T^{-3/2}$).

In Figures 6.25 (a) and (b), the decoupled vertical hole mobility appears to be primarily dominated by localization/hopping at low temperatures. Olson *et al.* [20] reported a similar vertical hole mobility trend as the one shown in Figure 6.25 (b) for *NID* *n*-type InAs/$InAs_{0.55}Sb_{0.45}$ T2SL using Heterojunction Bipolar Transistors (HBTs) and Photoluminescence (PL) measurements. Their results indicated carrier localization to play a critical role in the vertical hole transport and suggested that defect centers play a

significant role in the hopping transport [20]. In addition to localization/hopping transport effects, the low vertical hole mobility can be attributed to the Heavy-Hole (HH) band curvature in the InAs/InAsSb T2SL. For instance, in Chapter 5, Figure 5.11, the HH band showed a dispersion-less or a very small curvature behavior in the vertical direction; hence, a vanishingly low vertical hole mobility has been anticipated. Thus, the mobility trend and low-mobility values suggest that this carrier is the intrinsic minority vertical hole.

Extracted from Chapter 5 results (Tables 5.19-5.10), for the *NID* InAs/$InAs_{0.65}Sb_{0.35}$ T2SL, the lateral minority hole mobility values found at 77 K (300 K) were 5450 cm^2/Vs (1160 cm^2/Vs), while the measured coupled vertical hole mobilities found using HR-MSA in this study were 143 cm^2/Vs (501 cm^2/Vs) at 77 K (300 K). Using this values and employing Equation 6.6, for the *NID* InAs/$InAs_{0.65}Sb_{0.35}$ T2SL, the decoupled true vertical hole mobilities calculated at 77 K (300 K) are 3.75 cm^2/Vs (216 cm^2/Vs). For InAs/InAsSb T2SLs at 77 K, the lateral hole mobility results closely agree with the work reported by Brown *et. al* [21] using magneto-transport and MSA on *NID* material (1×10^{15} cm^{-3}), while the vertical hole mobility results agree with work reported by Yon *et al.* [22], [23] using Electron Beam Induced Current (EBIC) and Time-Resolved Photoluminescence (TRPL) on *n*-doped material (2×10^{16} cm^{-3}).

The extracted decoupled vertical hole mobilities reported in this dissertation are of particularly importance for the modeling and characterization of nBn InAs/InAsSb T2SL photodetector technology, since such devices rely primarily on vertical hole transport for photodetector operation. Finally, Table 6.2 chronologically summarizes the vertical transport mobility results reported for III-V material (InAsSb alloy, InAs/GaSb,

and InAs/InAsSb T2SLs) using different methods, including the results presented in this dissertation from magneto-resistance characteristics of T2SL samples using the vertical MSM test-structures configuration, at 77 and 130 K. In Table 6.2, μ_e and μ_h are the vertical $(\mu_\perp)$ electron and hole mobilities, respectively. The cited works reference the original studies wherein the results were reported, to aid the reader access such information and details.

Table 6.2: Chronological summary of the vertical transport mobility results reported for III-V material (InAsSb alloy, InAs/GaSb, and InAs/InAsSb T2SLs), including the results presented in this dissertation from magneto-resistance characteristics of T2SL samples using the vertical MSM test-structures configuration, at 77 and 130 K.

Method	Material	Vertical $\mu_\perp$ (cm^2/Vs)	Temperature (K)	Ref., Year
Cyclotron Resonance	MWIR *p*-type InAs/GaSb	$\mu_e = 7.6\times10^3$	4	[24],
	LWIR *p*-type InAs/GaSb	$\mu_e = 1.5\times10^4$	4	2011
Magneto-Resistance	LWIR *p*-type InAs/GaSb	$\mu_h = 280 \pm 27$	80-150	[10],
		$\mu_e = 2.4\times10^3 \pm 75$	80-150	2012
TRDT	MWIR *n*- & *p*-type InAs/GaSb	$\mu_e = 700 \pm 80$	77	[25],
		$\mu_h = 6 \pm 5$		2013
Transient Response	LWIR *n*-type $InAs_{0.60}Sb_{0.40}$	$\mu_h = 800$	77	[26], 2014
EBIC/TRPL	MWIR *n*B*n* $InAs/InAs_{0.81}Sb_{0.19}$	$\mu_h = 60$	6	[27], 2015
EBIC/TRPL	MWIR *n*B*n* $InAs/InAs_{0.65}Sb_{0.35}$	$\mu_h = 4.0$	80	[22], [23],
		$\mu_h = 1.2$	80	2016-17
HBT/PL	MWIR *NID* *n*-type $InAs/InAs_{0.55}Sb_{0.45}$	$\mu_h = 360$	120	[20],
		$\mu_h = 2$	30	2017
EBIC/TMR	MWIR *n*B*p* InAs/GaSb	$\mu_e = 150\text{-}200$	80	[28], 2019
Magneto-Resistance (MSM)	MWIR *NID* *n*-type $InAs/InAs_{0.65}Sb_{0.35}$	$\mu_h = 3.75$	77	**This work, 2019**
		$\mu_e = 4.4\times10^3$	77	
		$\mu_h = 11$	130	
		$\mu_e = 2.6\times10^3$	130	

6.6 Summary

The intent of this chapter was to demonstrate, for the first time, a Metal-Semiconductor-Metal (MSM) test-structure process to enable vertical transport measurements of III-V materials. Using the MSM processing and variable-temperature, the magneto-resistance properties of *n*-type ($n^+n^-n^+$) $InAs/InAs_{0.65}Sb_{0.35}$ Type-II Strained Layered Superlattices (T2SLs) grown on GaSb substrates were determined. The samples were fabricated and transferred onto metal-coated sapphire substrates. The T2SL structures studied had different impurity concentrations: (1) 1×10^{15} cm^{-3} Non-Intentionally Doped (*NID*) and (2) 1×10^{16} cm^{-3} Silicon-doped (Si-doped).

For the *NID* InAs/InAsSb T2SL, the magnetic field dependent magneto-resistance characteristics measured at different temperatures were analyzed using the High-Resolution Mobility Spectrum Analysis (HR-MSA) methodology, which allow the identification of two distinct carriers contributing to vertical conduction: a high conductance/mobility electron and a low conductance/mobility hole. The extraction and decoupling of vertical transport mobilities in the *NID* $InAs/InAs_{0.65}Sb_{0.35}$ T2SL was performed using the lateral transport results presented in Chapter 5. The comparison of lateral and vertical mobilities (coupled and decoupled) for both carriers confirms that mobility values are dependent on transport direction, with lateral mobilities higher than vertical mobilities. For the vertical decoupled electron (hole) at 77 K, mobility is found at 4.4×10^3 cm^2/Vs (3.75 cm^2/Vs).

6.7 References

[1] G. A. Umana-Membreno *et al.*, "Investigation of Multicarrier Transport in LPE-Grown Hg1-xCdxTe Layers," *J. Electron. Mater.*, vol. 39, no. 7, 2010.

[2] P.-Y. Delaunay, B. M. Nguyen, D. Hofman, and M. Razeghi, "Substrate removal for high quantum efficiency back side illuminated type-II InAs/GaSb photodetectors," *Appl. Phys. Lett.*, vol. 91, no. 23, 2007.

[3] B. Klein, J. Montoya, N. Gautam, and S. Krishna, "Selective InAs / GaSb strained layer superlattice etch stop layers for GaSb substrate removal," *Appl. Phys. A*, vol. 111, no. 2, 2013.

[4] R. Rehm *et al.*, "Substrate removal of dual-colour InAs/GaSb superlattice focal plane arrays," *Phys. Status Solidi*, vol. 9, no. 2, 2012.

[5] C. Cervera, J. B. Rodriguez, J. P. Perez, R. Chaghi, and L. Konczewicz, "Unambiguous determination of carrier concentration and mobility for InAs / GaSb superlattice photodiode optimization," *J. Appl. Phys.*, vol. 106, no. 3, 2009.

[6] E. J. Renteria, "Integration of Thin Film TPV Cells to CVD Diamond Heat Spreaders," University of New Mexico, 2017.

[7] J. Fastenau, E. Ozbay, G. Tuttle, and F. Laabs, "Epitaxial Lift-Off of Thin InAs Layers," *J. Electron. Mater.*, vol. 24, no. 6, 1995.

[8] Y. Aytac, "Time-Resolved Measurements of Charge Carrier Dynamics in MWIR to LWIR InAs/InAsSb Superlattices," University of Iowa, 2016.

[9] I. Vurgaftman *et al.*, "Improved quantitative mobility spectrum analysis for hall characterization," *J. Appl. Phys.*, vol. 84, no. 9, pp. 4966–4973, 1998.

[10] G. A. Umana-Membreno *et al.*, "Vertical minority carrier electron transport in p-type InAs/GaSb type-II superlattices," *Appl. Phys. Lett.*, vol. 101, no. 25, 2012.

[11] C. H. Swartz and T. H. Myers, "Method for the simultaneous determination of vertical and horizontal mobilities in superlattices," *Phys. Rev. B*, vol. 89, no. 7, 2014.

[12] M. C. Malone, C. P. Morath, S. Fahey, V. M. Cowan, and S. Krishna, "Progress towards vertical transport study of proton- irradiated InAs / GaSb type-II strained-layer superlattice materials for space-based infrared detectors," *SPIE Opt. Eng. Appl.*, vol. 9616, pp. 1–10, 2015.

[13] D. . Kleinman and A. . Schawlow, "Corbino Disk," *J. Appl. Phys.*, vol. 31, no. 12, 1960.

[14] D. K. Schroder, *Semiconductor material and device characterization*, 3rd Editio. John Wiley & Sons, Inc, 2006.

[15] H. H. Berger, "Contact Resistance and Contact Resistivity," *J. Electrochem. Soc*, vol. 119, 1972.

[16] A. Tixier, "A silicon shadow mask for deposition," *J. Micromechanics*, vol. 157, no. 10, 2000.

[17] K. Lee, K. Shiu, J. D. Zimmerman, C. K. Renshaw, R. Stephen, and S. R. Forrest, "Multiple growths of epitaxial lift-off solar cells from a single InP substrate," *Appl. Phys. Lett.*, vol. 97, no. 10, 2010.

[18] Y. H. Lee *et al.*, "Fabrication and analysis of thin- film GaAs solar cell on fl exible thermoplastic substrate using a low-pressure cold-welding," *Curr. Appl. Phys.*, vol. 15, no. 11, 2015.

[19] B. Deveaudt, J. Shah, C. Damen, B. Lambert, and A. Regreny, "Bloch Transport of Electrons and Holes in Superlattice Minibands: Direct Measurement by Subpicosecond Luminescence Spectroscopy Luminescence Spectroscopy," *Phys. Rev. Lett.*, vol. 58, no. 2582, 1987.

[20] B. V. Olson *et al.*, “Vertical Hole Transport and Carrier Localization in InAs/InAs1−xSbx Type-II Superlattice Heterojunction Bipolar Transistors,” *Phys. Rev. Appl.*, vol. 7, no. 2, 2017.
[21] A. E. Brown, “Application of Mobility Spectrum Analysis to Modern Multi-layered IR Device Material,” University of Illinois at Chicago, 2015.
[22] N. Yoon, C. J. Reyner, G. Ariyawansa, J. E. Scheihing, J. Mabon, and D. Wasserman, “Diffusion Characterization of In (Ga) As / InAsSb Type-II Superlattices via Electron Beam Induced Current and Time- Resolved Photoluminescence,” *2016 IEEE Photonics Conf.*, vol. 2, 2016.
[23] N. Yoon *et al.*, “Modified electron beam induced current technique for in(Ga)As/InAsSb superlattice infrared detectors,” *J. Appl. Phys.*, vol. 122, no. 7, 2017.
[24] S. Suchalkin *et al.*, “In-plane and growth direction electron cyclotron effective mass in short period InAs/GaSb semiconductor superlattices,” *J. Appl. Phys.*, vol. 110, no. 4, 2011.
[25] B. V. Olson, L. M. Murray, J. P. Prineas, M. E. Flatte, J. T. Olesberg, and T. F. Boggess, “All-optical measurement of vertical charge carrier transport in mid-wave infrared InAs/GaSb type-II superlattices,” *Appl. Phys. Lett.*, vol. 102, no. 20, 2013.
[26] Y. Lin, D. Wang, D. Donetsky, and G. Kipshidze, “Transport properties of holes in bulk InAsSb and performance of barrier long-wavelength infrared detectors,” *Semicond. Sci. Technol*, vol. 29, no. 11, 2014.
[27] D. Zuo *et al.*, “Direct minority carrier transport characterization of InAs / InAsSb superlattice nBn photodetectors,” *Appl. Phys. Lett.*, vol. 106, no. 7, 2015.
[28] Z. Taghipour *et al.*, “Temperature-Dependent Minority-Carrier Mobility in p -Type InAs / GaSb Type-II-Superlattice Photodetectors,” *Phys. Rev. Appl.*, vol. 11, no. 2, 2019.

Chapter 7

Conclusions and Future Work

7.1 Transport to Improve III-V Detector Performance

Infrared (IR) sensing applications are dominated by Mercury Cadmium Telluride (MCT) photodetectors. However, there are several fundamental technological material challenges such as low electron effective mass (~0.009m_o) resulting in sizeable dark-currents due to tunneling [1] and expensive Cadmium Zinc Telluride (CdZnTe) substrates for epitaxial growth [2]. Regardless of its drawbacks, MCT material remains as a prominent, mature material for IR detector applications although younger technologies utilizing quantum confinement and heterostructure engineering exist.

Antimonide-based Type-II Strained Layer Superlattices (T2SLs) have gained significant attention since first proposed in the late 70s and 80s by Esaki and other researchers [3], [4]. III-V IR detector materials of interest include ternary alloy $InAs_{1-x}Sb_x$ [5], InAs/GaSb T2SLs [6] and $InAs/InAs_{1-x}Sb_x$ T2SLs [7], [8] . Some of the potential benefits of using III-V materials compared to MCT detectors include reduced Auger recombination [9] and the larger effective mass (~ 0.04m_o) in T2SLs which leads to a reduction of tunneling currents compared with MCT detectors of similar bandgap [10].

Auger recombination is a prominent source of noise in MCT detectors; however, it has been reduced in T2SLs due to light and heavy-hole bands splitting and larger effective masses. The InAs/InAsSb T2SL has demonstrated considerable potential as an IR detector material due to its longer carrier lifetime [7]. The absorber materials explored in this dissertation were the III-V Mid-Wavelength Infrared (MWIR) $InAs_{0.91}Sb_{0.09}$ alloys and $InAs/InAs_{0.65}Sb_{0.35}$ T2SLs.

Understanding carrier transport parameters are fundamentally crucial in advancing III-V IR photodetectors. Electrical transport studies on III-V IR materials are the subject of continued research [11]–[15], and are this dissertation's topic of investigation. To comprehend carrier transport in III-V materials, lateral (in-plane) transport measurements need to be addressed. Lateral transport properties are usually extracted using Hall Effect measurements. They can be challenging to perform in InAsSb alloys and InAs/InAsSb T2SLs due to the parallel conduction in the highly conductive GaSb substrate as well as surface and interface accumulation layers. In addition, a key parameter desired among the infrared community is the vertical mobility in the T2SL material, which is a highly anisotropic system. However, the T2SL material system has been significantly hindered by: (1) the lack of a straightforward experimental technique to gain insight into the fundamental properties of carrier transport in the direction perpendicular to the superlattice plane (vertical transport), (2) the difficulties of making lateral transport measurements when an electrically conductive buffer or substrate is employed, and (3) the lack of insight or knowledge into correlations between lateral and vertical transport properties.

7.2 Conclusions

This dissertation tackles the transport challenge of III-V absorber material (alloy InAsSb and InAs/InAsSb T2SLs). The experiments performed in this work verified the hypothesis that temperature- and magnetic-field-dependent measurements are needed to correctly report the transport properties of InAsSb and InAs/InAsSb T2SLs due to the multi-carrier behavior of the samples. All the different carriers present in each sample were extracted, and the transport properties of InAsSb and InAs/InAsSb T2SLs were determined using theoretical modeling, Van der Pauw (VDP) processing, a novel vertical Metal-Semiconductor-Metal (MSM) test-structure, and experimental verification. Multi-Carrier Fitting (MCF) and High-Resolution Mobility Spectrum Analysis (HR-MSA) were used to deduct the lateral and vertical carrier species, respectively. In addition, the theoretical modeling using NRL MULTIBANDS® confirmed the bandstructure and identified the interface carriers for lateral transport measurements.

In this dissertation, carrier transport is addressed in three major steps: Step 1 (Chapter 4) incorporates a theoretical and experimental lateral transport investigation of MWIR *p*-type InAsSb using different bulk layer thicknesses, MCF, NRL MULTIBANDS®, and sodium hypochlorite (NaClO) solution to identify surface carriers. Step 2 (Chapter 5) shadows a similar method, but the lateral transport measurements are performed and compared on *n*-type InAsSb alloys and InAs/InAsSb T2SLs detectors. As previously mentioned, lateral transport measurements are performed to understand the different conduction paths (surface, interface, and bulk) present in an isotropic (InAsSb) and anisotropic material (InAs/InAsSb T2SL).

Finally, Step 3 (Chapter 6) demonstrates for the first time, a novel vertical MSM test-structure that allows accurate extraction of vertical transport parameters from T2SL anisotropic materials. It is anticipated that the processes and test-structure design details provided will serve as a foundation for future improvements. Since there is no direct or effective methodology to measure vertical mobility, it is anticipated that the vertical MSM test-structure is a significant contribution to addressing this characterization challenge.

In Chapter 4, temperature and magnetic-field-dependent measurements in conjunction with MCF were used to characterize the transport properties of Beryllium-doped (*p*-type), lattice-matched, $InAs_{0.91}Sb_{0.09}$. The bulk hole concentrations and mobilities at 77 K (300 K) are 1.6×10^{18} cm^{-3} (2.3×10^{18} cm^{-3}) and 125 cm^2/Vs (60 cm^2/Vs) indicating that the Be dopants are 100% ionized at room temperature and are 70% ionized at 77 K.

In Chapter 5, *n*-type lateral transport measurements of $InAs_{0.91}Sb_{0.09}$ and $InAs/InAs_{0.65}Sb_{0.35}$ T2SL materials were determined using temperature- and magnetic-field-dependent measurements in conjunction with MCF. Transport properties extracted for the carriers found in *n*-type InAsSb alloy samples and for the InAs/InAsSb T2SLs are summarized in Tables 5.5-5.8 and Tables 5.9-5.12 (Chapter 5) for temperatures 77 and 300 K, respectively. The surface electron found for all the four samples (InAsSb alloys and InAs/InAsSb T2SLs) had mobilities and sheet concentrations vs. temperature results ranging from ~ 1.00×10^4 - 2.00×10^4 cm^2/Vs and ~ 1.50×10^{11} - 6.00×10^{11} cm^{-2}, respectively. Finally, a minority carrier hole was identified for the *n*-type InAs/InAsSb T2SL samples, using the measured minority carrier lifetime and mobility extracted at 100 K, the lateral minority carrier diffusion length was calculated.

In Chapter 6, using the MSM processing and variable-temperature, the magneto-resistance properties of n-type ($n^+n^-n^+$) $InAs/InAs_{0.65}Sb_{0.35}$ T2SLs were determined. For the *NID* InAs/InAsSb T2SL, the magnetic field dependent magneto-resistance characteristics measured at different temperatures were analyzed using the High-Resolution Mobility Spectrum Analysis (HR-MSA) methodology, which allow the identification of two distinct carriers contributing to vertical conduction: a high conductance/mobility electron and a low conductance/mobility hole. The extraction and decoupling of vertical transport mobilities in the *NID* $InAs/InAs_{0.65}Sb_{0.35}$ T2SL was performed using the lateral transport bulk-carrier results presented in Chapter 5. The comparison of lateral and vertical mobilities (coupled and decoupled) for both carriers confirms that mobility values are dependent on transport direction, with lateral mobilities higher than vertical mobilities. For the vertical decoupled electron (hole) at 77 K, mobility is found at 4.4×10^3 cm^2/Vs (3.75 cm^2/Vs).

The extracted decoupled vertical hole mobilities reported in this dissertation are of importance for the modeling and characterization of nBn InAs/InAsSb T2SL photodetector technology, since such devices rely primarily on vertical hole transport for photodetector operation. Finally, Table 6.2 in Chapter 6, chronologically summarizes the vertical transport mobility results reported for III-V material (InAsSb alloy, InAs/GaSb, and InAs/InAsSb T2SLs) using different methods, including the results presented in this dissertation from magneto-resistance characteristics of T2SL samples using the vertical MSM test-structure configuration.

7.3 Future Work

7.3.1 Radiation Effects

MCT technology dominates the space-based IR sensors regime. Compared to MCT technology, III-V materials such as InAs/InAsSb T2SLs have low radiation tolerance. Proton irradiation has been shown to degrade carrier lifetime, thus increasing dark current and decreasing quantum efficiency (QE) [16]; however, the effects of proton irradiation on carrier mobility are currently questionable. Therefore, understanding the effects of radiation on T2SLs materials is important. As a follow-up, a future work option considered is to measure the degradation of carrier mobility as a function of proton irradiation. InAs/InAsSb T2SLs material can be characterized via magneto-resistance measurements pre- and post-irradiance with 63 MeV protons. The goal of a future proton irradiation study is to determine if carrier mobility, specifically in the vertical direction, is degraded by proton irradiation.

7.3.2 Passivation in *p*-type Material

Further research regarding the passivation of the InAsSb and InAs/InAsSb T2SLs surface should be carried out, as promising concepts such as Atomic Layer Deposition (ALD) and SU-8 have recently been published [17], [18], and should be tested on IR detectors for lateral and vertical transport characterization. The most significant effect is expected on magneto-resistance measurements, since the passivation of the surface accumulation layer should enable the direct observation of *p*-type properties by eliminating the surface electron conduction channel without the need of any other external experiments. Therefore, the same temperature- and magnetic-field dependent transport experiments reported in this

dissertation should be repeated on *p*-type alloy and T2SL material with a passivation technique included.

7.3.3 SdH Study and MSM Test-Structure

To provide further confirmation of the multi-carriers found in *n*-type or p-type III-V material, an analysis of Shubnikov-de Haas (SdH) oscillations can provide a detailed picture of the free carrier spatial distribution. In addition, the vertical transport MSM test-structure reported in this dissertation can be further explored by (1) studying the series resistance effect on such structures, (2) further investigating the Signal-To-Noise Ratio (SNR) seen in the magneto-resistance data at low temperatures, and (3) comparing isotropic and anisotropic material results. It should be noted that although the MSM test-structure circumvents the parasitic series resistance problems posed by the spreading resistance of the bottom contact layer encountered in prior reports [19], the series resistance presented by metal-semiconductor contacts remains to be quantified. This contact resistance, albeit very low, is likely to be higher at lower temperature and can be further investigated.

Another interesting study can include a comparison between MSM test-structure and single-pixel detector processing [20] using (1) variable-area arrays, (2) thicker structures to facility substrate removal process, and (3) plotting current density versus periphery/area. It is anticipated that the MSM processes and test-structure design details provided in this work, will serve as a foundation for future improvements. Since currently there is no truly direct or effective methodology to measure vertical mobility, it is anticipated that the vertical MSM test-structure is a significant contribution to addressing this characterization challenge.

7.4 References

[1] A. Rogalski, "HgCdTe infrared detector material: History, status and outlook," *Reports Prog. Phys.*, vol. 68, no. 10, pp. 2267–2336, 2005.

[2] M. Kopytko and A. Rogalski, "HgCdTe barrier infrared detectors," *Prog. Quantum Electron.*, vol. 47, pp. 1–18, 2016.

[3] G. A. Sai-Halasz, R. Tsu, and L. Esaki, "A new semiconductor superlattice," *Appl. Phys. Lett.*, vol. 30, no. 12, 1977.

[4] D. L. Smith and C. Mailhiot, "Proposal for strained type II superlattice infrared detectors," *J. Appl. Phys.*, vol. 62, no. 6, 1987.

[5] Y. Lin, D. Wang, D. Donetsky, and G. Kipshidze, "Transport properties of holes in bulk InAsSb and performance of barrier long-wavelength infrared detectors," *Semicond. Sci. Technol*, vol. 29, no. 11, 2014.

[6] C. Cervera *et al.*, "Transport measurements on InAs/GaSb superlattice structures for mid-infrared photodiode," *J. Phys. Conf. Ser.*, vol. 193, no. 012030, 2009.

[7] E. H. Steenbergen *et al.*, "Significantly improved minority carrier lifetime observed in a long-wavelength infrared III-V type-II superlattice comprised of InAs/InAsSb," *Appl. Phys. Lett.*, vol. 99, no. 25, pp. 1–4, 2011.

[8] H. S. Kim *et al.*, "Long-wave infrared nBn photodetectors based on InAs/InAsSb type-II superlattices," *Appl. Phys. Lett.*, vol. 101, no. 16, pp. 1–4, 2012.

[9] C. H. Grein, M. E. Flatté, J. T. Olesberg, S. A. Anson, L. Zhang, and T. F. Boggess, "Auger recombination in narrow-gap semiconductor superlattices incorporating antimony," *J. Appl. Phys.*, vol. 92, no. 12, pp. 7311–7316, 2002.

[10] A. G. Thompson and J. C. Woolley, "Energy-Gap Variation in Mixed III–V Alloys," *Can. J. Phys.*, vol. 45, no. 2, 1967.

[11] J. Antoszewski, G. A. Umana-Membreno, and L. Faraone, "High-resolution mobility spectrum analysis of multicarrier transport in advanced infrared materials," *J. Electron. Mater.*, vol. 41, no. 10, pp. 2816–2823, 2012.

[12] Y. Lin *et al.*, "Effect of hole transport on performance of infrared type-II superlattice light emitting diodes," *J. Appl. Phys.*, vol. 117, no. 16, pp. 1–5, 2015.

[13] D. Zuo *et al.*, "Direct minority carrier transport characterization of InAs/InAsSb superlattice nBn photodetectors," *Appl. Phys. Lett.*, vol. 106, no. 7, pp. 2–6, 2015.

[14] E. H. Steenbergen, S. Elhamri, W. C. Mitchel, S. Mou, and G. J. Brown, "Carrier transport properties of Be-doped InAs / InAsSb type-II infrared superlattices," *Appl. Phys. Lett.*, vol. 104, no. 1, 2014.

[15] A. E. Brown, N. Baril, D. Zuo, L. A. Almeida, J. Arias, and S. Bandara, "Characterization of n-Type and p-Type Long-Wave InAs/InAsSb Superlattices," *J. Electron. Mater.*, vol. 46, no. 9, pp. 5367–5373, 2017.

[16] C. P. Morath, V. M. Cowan, L. A. Treider, G. D. Jenkins, and J. E. Hubbs, "Proton Irradiation Effects on the Performance of," *IEEE Trans. Nucl. Sci.*, vol. 62, no. 2, 2015.

[17] T. Specht *et al.*, "Side Wall Passivation of LWIR P-type Superlattice Detectors Using Atomic Layer Deposition," *2018 IEEE Res. Appl. Photonics Def. Conf.*, 2018.

[18] H. S. Kim *et al.*, "Reduction of surface leakage current in InAs/GaSb strained layer long wavelength superlattice detectors using SU-8 passivation," *Appl. Phys. Lett.*, vol. 97, no. 14, 2010.

[19] C. H. Swartz and T. H. Myers, "Method for the simultaneous determination of vertical and horizontal mobilities in superlattices," *Phys. Rev. B*, vol. 89, no. 7, 2014.

[20] G. A. Umana-Membreno *et al.*, "Vertical minority carrier electron transport in p-type InAs/GaSb type-II superlattices," *Appl. Phys. Lett.*, vol. 101, no. 25, 2012.

APPENDIX A

OPTICAL MEASUREMENTS

A.1 Lateral Transport Samples

Four *n*-type samples (Lateral transport, Chapter 5) were grown, and optical measurements are summarized in Table A.1. Samples are composed of Mid-Wavelength Infrared (MWIR) $InAs_{0.91}Sb_{0.09}$ and $InAs/InAs_{0.65}Sb_{0.35}$ Type-II Strained Layered Superlattice (T2SL) materials. Table A.1 summarizes the optical measurements for: sample 1 (InAsSb Non-Intentionally Doped (*NID)*-1×10^{15} cm^{-3}), sample 2 (InAsSb Silicon-doped-1×10^{16} cm^{-3}), sample 3 (InAs/InAsSb T2SL *NID*-1×10^{15} cm^{-3}) and sample 4 (InAs/InAsSb T2SL Silicon-doped-1×10^{16} cm^{-3}). Photoluminescence/Lifetime (PL/LT) maps provided by Sandia National Laboratories (SNL) are included in Figure A.1 with the extracted lifetime and peak wavelengths listed in Table A.1. Non-Intentionally Doped sample doping is abbreviated as *NID* and Silicon doped samples as Si-doped.

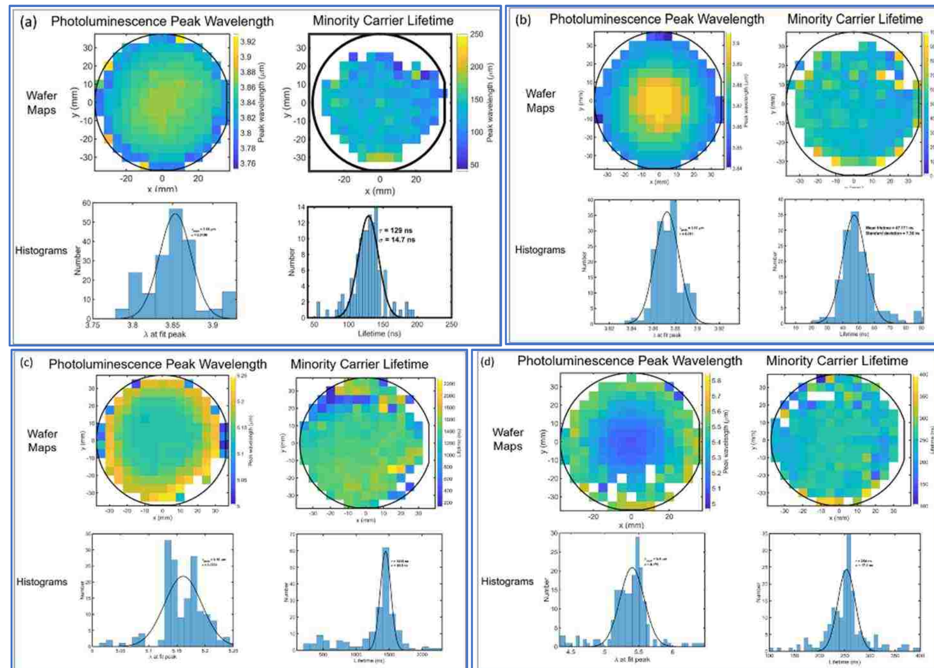

Figure A.1: Photoluminescence (PL) and Lifetime (LT) measurements, (top) *x-y* wafer maps and (bottom) histograms for lateral transport samples: (a) *n*-type *NID* InAsSb (b) *n*-type Si-doped InAsSb (c) *n*-type *NID* InAs/InAsSb T2SL and (d) *n*-type Si-doped InAs/InAsSb T2SL. **Data provided by SNL, Samples used in Chapter 5*

Table A.1: Four n-type InAsSb and InAs/InAsSb T2SL samples grown by MBE for lateral transport measurements with structure, doping, lifetime at 100 K and PL peak wavelength at 80 K summarized. **Samples used in Chapter 5 for lateral transport measurements*

	Structure	#	Doping (cm^{-3})	Lifetime @ 100K (μs)	PL peak @ 80 K (μm)	Run #
***n*-type**	Bulk InAsSb: Lateral Transport	1	1×10^{15} (*NID*)	0.129	3.88	GN1302
		2	1×10^{16} (Si-doped)	0.047	3.91	GN1298
	InAs/InAsSb: Lateral Transport	3	1×10^{15} (*NID*)	1.45	5.14	GN1288
		4	1×10^{16} (Si-doped)	0.25	5.2	GN1287

A.2 Vertical Transport Samples

The optical characterization of the two n-type ($n^+n^-n^+$) samples grown for vertical transport measurements (Chapter 6) are summarized in Table A.2, where the samples are labeled 5-6 to differentiate from n-type lateral superlattice samples in Chapter 5. Samples are composed of MWIR $InAs/InAs_{0.65}Sb_{0.35}$ Type-II Strained Layered Superlattice (T2SL) absorber material. The superlattice absorber layer is sandwiched between the top and bottom $InAs_{0.91}Sb_{0.09}$ contact layers with n-type highly doped concentrations (1 x 10^{18} cm^{-3}). Table A.2 summarizes the optical properties of the two vertical transport samples: sample 5 (InAs/InAsSb T2SL *NID*-1×10^{15} cm^{-3}) and sample 6 (InAs/InAsSb T2SL Si-doped-1×10^{16} cm^{-3}). Non-Intentionally Doped sample doping is abbreviated as *NID* and Silicon doped samples as Si-doped. The two sample PL/LT maps provided by SNL are included in Figure A.2 with extracted lifetime and peak wavelengths listed in Table A.2.

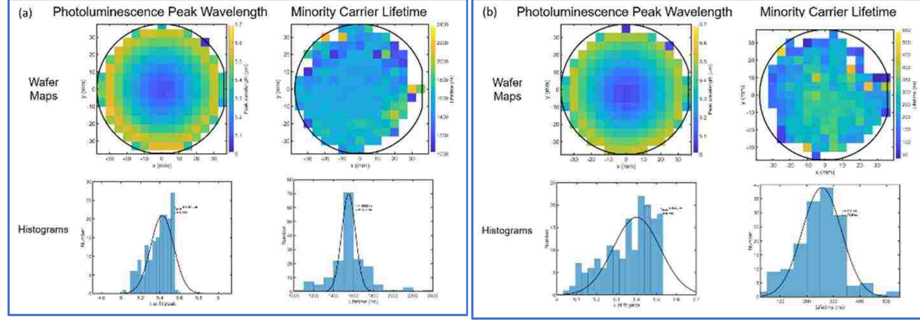

Figure A.2: Photoluminescence (PL) and Lifetime (LT) measurements, (top) *x-y* wafer maps and (bottom) histograms of two vertical transport samples: (a) *n*-type *NID* InAs/InAsSb T2SL and (b) *n*-type Si-doped InAs/InAsSb T2SL. **Data provided by SNL, Samples used in Chapter 6*

Table A.2: Two *n*-type ($n^+n^-n^+$) InAs/InAsSb T2SL samples grown by MBE for vertical transport measurements with structure, doping, lifetime (LT) at 100 K and Photoluminescence (PL) peak wavelength at 80 K summarized. **Samples used in Chapter 6 for vertical transport measurements*

Structure	#	Doping (cm^{-3})	Lifetime @ 100K (µs)	PL peak @ 80 K (µm)	Run #
InAs/InAsSb: Vertical Transport	5	1×10^{15} (*NID*)	1.550	5.12	GN1290
	6	1×10^{16} (Si-doped)	0.300	5.10	GN1296